**Trinity College Dublin**
Coláiste na Tríonóide, Baile Átha Cliath
The University of Dublin

# Mesoporous Silica Nanocarriers for triggered drug delivery in the treatment of cancer

A thesis submitted for the degree of

Doctor of Philosophy

at the School of Pharmacy & Pharmaceutical Sciences,

Trinity College Dublin,

The University of Dublin, Ireland

by Sara Toselli

Under the supervision of

Dr Eduardo Ruiz-Hernandez and Dr Maria J Santos-Martinez

2024

## Declaration

I declare that this thesis has not been submitted as an exercise for a degree at this or any other University. A small proportion of the work described in this thesis was carried out in collaboration with other researcher and this is duly acknowledged in the text wherever relevant. This includes the *in vitro* experiments on a 3D model of Glioblastoma Multiforme outlined in Chapter 5, which were conducted by Dr Amelia Ultimo and Ph.D. students Mila Djisalov and Teodora Knezic, and the *in vivo* experiments outlined in Chapter 6, which were conducted by Dr Maria Manuela Jesus Guilherme Gaspar. I declare that all other work is entirely my own.

I agree to deposit this thesis in the University's open access institutional repository or allow the library to do so on my behalf, subject to Irish Copyright Legislation and Trinity College Library conditions of use and acknowledgement.


*Sara Toselli*
_____

Sara Toselli

# Table of Contents

# Abstract

Cancer is the second leading cause of death globally, accounting for 10 million deaths in 2020.

Cancer chemotherapy is currently limited by a high systemic toxicity that occurs as a result of high systemic dosing and the failure of non-targeted drugs to reach therapeutic doses at the target site. There is an urgent need for improved carrier systems able to deliver diagnostic agents and anti-cancer drugs to the tumour. One of the most promising approaches is based on the design of site-specific and stimuli-responsive controlled drug delivery systems (DDSs), which is of major interest for researchers worldwide. Basically, a DDS is a formulation that controls the rate and period of drug delivery and targets specific areas in the body. Mesoporous silica nanocarriers (MSNs) have received growing attention as drug carriers. Due to their stable and rigid framework under extreme conditions compared to organic DDSs, silica carriers may not suffer from uncontrollable drug release owing to an accelerated degradation in a physiological environment but release the drugs in a sustained way when suitably functionalised.

The overall aim of this research project is to develop biocompatible nanoparticles based on mesoporous silica for the delivery of contrast agent(s) and/or chemotherapeutic drug(s) for the diagnosis and/or therapy of lung cancer, that can serve as a starting step to build libraries of nanoparticles for improving the diagnosis and treatment of multiple cancers.

The objective is to detect abnormal cells with high specificity and sensitivity. The MSNs will respond promptly to the presence of known specific biomarker(s), by releasing the contrast agent(s) and consequently providing a warning signal. In a similar fashion, the MSNs could be loaded with chemotherapeutic agent(s) to provide a stimuli-responsive release triggered by the presence of the tumour biomarker(s).

The present work focused on the development of MSNs using a sol-gel method, resulting in nanoparticles (NPs) with typical features of MCM-41 type MSNs, including a spherical shape and uniform size distribution of around 100 nm, hexagonal mesopore order, and pores with a size of 2-3 nm. The NPs were loaded with paclitaxel, which showed higher toxicity towards human and murine lung cancer cells (A549 and

LLC1, respectively), when compared to doxorubicin hydrochloride. To achieve selective release in the tumour environment and protect the loaded drug from premature release, the NPs were functionalized by coating their surface with two different polymers: one type had a layer of poly- (ethylene glycol) methyl ether thiol (PEG), and another type a gelatine shell (GEL). The surface functionalization improved the particles' colloidal stability and dispersibility, as well as their biocompatibility towards cancer cells (when unloaded). Moreover, it allowed for a controlled release of the payload in response to specific stimuli (glutathione for PEG-functionalised MSNs, and metalloproteinases for GEL-functionalised MSNs).

*In vitro* release assays and cytotoxicity studies with A549 and LLC1 lung cancer cells confirmed the ability of the functionalized NPs to protect the payload from premature release and selectively deliver to the cancer cells. Flow cytometry and confocal analysis demonstrated that the PEG- and GEL-functionalised MSNs were taken up by lung cancer cells after only one hour. Preliminary hemocompatibility studies showed low toxicity of the synthesised NPs towards red blood cells and platelets.

PEG- and GEL-functionalised MSNs loaded with DOX were tested *in vitro* on a well-established 3D cell model of glioblastoma multiforme in order to analyse their toxicity and internalization capabilities in a system that better mimics the complexity and three-dimensional (3D) architecture of a tumour found *in vivo*. This study provided evidence of the successful penetration and distribution of the NPs within the spheroids structure, and the effectiveness of both PEG- and GEL-functionalised MSNs in delivering DOX.

*In vivo* studies in C57/BL6 male mice bearing lung cancer demonstrated that MSNs-PEG were well tolerated, as opposed to MSNs-GEL which accumulated in liver, spleen and lungs causing tissue inflammation and a possible increase in oxidative stress. Efficacy studies with the PTX loaded NPs demonstrated an improved delivery of the drug to the tumour site, as opposed to the free drug in cremophor/ethanol (CrEL).

In summary, the present study aimed to create a stimuli-responsive nanoparticle-based system that can enhance the detection and treatment of cancer, while minimizing the impact on healthy cells. This approach could have significant implications for improving cancer therapy by mitigating the issue of non-targeted cytotoxic drug release.

# Acknowledgements

I would like to start by thanking my primary Supervisor, Dr Eduardo Ruiz-Hernandez. Without your help, support, and guidance I would not be here. You gave me the opportunity to pursue this Ph.D. and always pushed me a little further. I have grown so much as a researcher and as an individual during this long, hard and rewarding journey, I will be forever thankful. Next, I would like to thank my Co-Supervisor, Dr Maria J Santos-Martinez. Thank you for your help, support, and kindest words, always. It helped me a lot. I could have not asked for better supervisors, thank you for believing in me.

A special thanks to Dr Oliviero Gobbo. You were not my supervisor, but your guidance and suggestions made the difference. Thank you for always offering a "tazzina di caffè".

Thanks to Dr Maria Manuela de Jesus Guilherme Gaspar for helping out in this research project by carrying out the *in vivo* experiments.

I would like to say a special thanks to Luiza and Amelia, the first two colleagues I had. Thank you for the support and the help you always gave me, no matter what, and thank you for the pints and the food we had together after the long hours in the lab. It was a pleasure to spend those years together.

A special thanks to Vicente too, who worked with us for a short time only, but who has also helped me a lot in those few months.

Thanks to Almudena, who joined the group halfway through my journey, but whose experience and knowledge were very helpful during my last months. And thank you for all the coffees we shared.

I would like to mention Binh, Shubhrima, Gulfam and Rebecca as well. You all helped a lot one way or another. You are all great researchers, thank you guys.

Thanks to Anushka. You have been a great help as well and a very good friend.

Thanks to Rosemary, who has had a similar journey to mine and was always very supportive. Thanks for always listening to me and giving me tons of advice.

v

## Presentations and Certificates

<u>Poster Presentations:</u>

1. Poster presentation at the **1st CA17140 TRAINING SCHOOL, Trieste, Italy (April 2019).**
   Sara Toselli, Maria Santos-Martinez, Eduardo Ruiz-Hernandez
   Silica-Based Multifunctional Nanomedicine for Targeted Drug Delivery.

2. Poster presentation at the **41st All Ireland Schools of Pharmacy Conference, Trinity College Dublin, Ireland (April 2019).**
   Sara Toselli, Maria Santos-Martinez, Eduardo Ruiz-Hernandez
   Silica-Based Multifunctional Nanomedicine for Targeted Drug Delivery.

3. Poster presentation at the **Controlled Release Society Virtual Annual Meeting, (June 2020).**
   Sara Toselli, Maria Santos-Martinez, Eduardo Ruiz-Hernandez
   Mesoporous Silica Nanocarriers for sustained drug delivery in the treatment of lung cancer.

<u>Oral Presentations:</u>

1. Oral presentation at the **1st COST Action CA17140 Conference - Cancer Nanomedicine: from the bench to the bedside, Riga, Latvia (October 2019).**
   Sara Toselli, Maria Santos-Martinez, Eduardo Ruiz-Hernandez
   Silica-Based Multifunctional Nanomedicine for Targeted Drug Delivery.

2. Oral presentation at the **5th International Caparica Symposium on Nanoparticles/Nanomaterials and Applications, Caparica, Portugal (January 2022).**
   Sara Toselli, Maria Santos-Martinez, Eduardo Ruiz-Hernandez

Mesoporous Silica Nanocarriers for sustained drug delivery in the treatment of lung cancer.

<u>Certificates:</u>

1. **Statistics (Online) P.Grad.Cert., Trinity College Dublin, Ireland (Academic Year 2020/2021).**
   Postgraduate Certificate in Statistics. Part-time one year module providing a broad introduction to the statistical ideas and methods relevant to data gathering and analysis.

# List of Figures

# List of Tables

# List of Abbreviations

**A549 -** Human non-small-cell lung cancer

**ACN –** Acetonitrile

**AdenoCA -** Adenocarcinoma

**ALT -** Alanine transaminase

**APMA -** 4-Aminohenylmercuric Acetate

**APS -** Ammonium persulfate

**APTES -** (3-Aminopropyl)triethoxysilane

**AST -** Aspartate aminotransferase

**ATCC -** American Type Culture Collection

**AUC -** Area under the ROC Curve

**BBB -** Blood Brain Barrier

**BCA -** Bicinchoninic acid

**BET -** Brunauer–Emmett–Teller analysis

**BJH -** Barrett-Joyner-Halenda analysis

**BM -** Basement Membrane

**BSA -** Bovine Serum Albumin

**CaCl$_2$ -** Calcium Chloride

**cAMP -** Cyclic adenosine monophosphate

**CCK-8 –** Cell Counting Kit-8 assay

**CdS -** cadmium sulphide

**CNHs –** Carbon Nanohorns

**CNPs -** Carbon Nanoparticles

**CNTs –** Carbon Nanotubes

**CO$_2$ –** Carbon dioxide

**CrEL -** Cremophor/ethanol

**CSV –** Cancer Surveillance Branch

**CTAB -** Cetyltrimethylammonium Bromide

**CTAC -** Cetyltrimethylammonium Chloride

**Cys -** Cysteine

**DCM -** Dichloromethane

**dd H$_2$O –** double distilled water

**DDS(s) –** Drug Delivery System(s)

**DLS –** Dynamic Light Scattering

**DMEM -** Dulbecco's Modified Eagle Medium

**DNA -** Deoxyribonucleic acid

**DOX –** Doxorubicin Hydrochloride

**ECACC -** European Collection of Authenticated Cell Cultures

**ECM –** Extracellular Matrix

**EE –** Encapsulation Efficiency

**EPR -** Enhanced Permeability and Retention effect

**EtOH –** Ethanol

**Fe$_3$O$_4$ –** Iron Oxide

**FBS –** Foetal Bovine Serum

**FDA -** Food and Drug Administration

**Fol –** Folic acid

**FTIR -** Fourier transform infrared

**GBM –** Glioblastoma Multiforme

**GCL -** Glutamate Cysteine Ligase

**GEL –** Gelatine

**GGT -** γ-Glutamyl Transpeptidase

**GRAS -** Generally Recognized As Safe

**GS -** Glutathione Synthetase

**GSH –** Glutathione

**GTA –** Glutaraldehyde

**GTP -** Guanine Triphosphate

**Hb -** Haemoglobin

**HCl –** Hydrochloric Acid

**HMSN -** Hollow MSNs

**HPLC -** High-performance liquid chromatography

**HSPG -** Heparan Sulphate Proteoglycan

**HT1080 -** Human fibrosarcoma cells

**IARC –** International Agency for Research

**IC$_{50}$ -** Half Maximal Inhibitory Concentration

**IUPAC -** International Union of Pure and Applied Chemistry

**LAC -** Lung Adenocarcinoma

**LC –** Loading Capacity

**LD$_{50}$ -** Median Lethal Dose

**LDH -** lactate Dehydrogenase

**LLC1 –** Lewis Lung Carcinoma Cells

**LTA –** Light transmission aggregometry

**MCM –** Mobile Composition of Matter

**MCM-41 –** Mobile Composition Of Matter No 41

**MCM-48 –** Mobile Composition Of Matter No 48

**MCM-50 –** Mobile Composition Of Matter No 50

**MDR –** Multiple Drug Resistance

**MEM -** Minimum Essential Medium Eagle

**MHz -** Megahertz

**MMP(s) –** Matrix Metalloproteinase(s)

**M-MSNs -** Magnetic MSNs

**MNPs –** Magnetic Nanoparticles

**MPS -** Mononuclear Phagocyte System

**MRI -** Magnetic Resonance Imaging

**MSN(s) –** Mesoporous Silica Nanoparticle(s)

**MSNs-CHO+DOX -** MSNs functionalised with aldehyde groups and loaded with DOX

**MSNs+DOX -** MSNs loaded with DOX

**MSNs+DOX-GEL -** MSNs loaded with DOX functionalised with GEL

**MSNs+DOX-PEG -** MSNs loaded with DOX functionalised with PEG

**MSNs-CHO+PTX -** MSNs functionalised with aldehyde groups and loaded with PTX

**MSNs+PTX -** MSNs loaded with PTX

**MSNs+PTX-GEL -** MSNs loaded with PTX functionalised with GEL

**MSNs+PTX-PEG -** MSNs loaded with PTX functionalised with PEG

**MSNs-RhBITC –** Rhodamine B Isothiocyanate functionalised MSNs

**MSNs-CHO –** Aldehyde functionalised MSNs

**MSNs-CHO-RhBITC –** Rhodamine B Isothiocyanate Aldehyde functionalised MSNs

**MSNs-GEL –** Gelatine functionalised MSNs

**MSNs-GEL-RhBITC –** Rhodamine B Isothiocyanate Gelatine functionalised MSNs

**MSNs-PEG -** Poly-(ethylene glycol) functionalised MSNs

**MSNs-PEG-RhBITC -** Rhodamine B Isothiocyanate Poly-(ethylene glycol) functionalised MSNs

**MTD –** Maximum Tolerated Dose

**MT-MMP -** Membrane-Type Metalloproteinases

**NaCl –** Sodium chloride

**nAChR** - nicotinic Acetylcholine Receptors

**NAD -** Nicotinamide Adenine Dinucleotide

**NaN$_3$ -** Sodium azide

**NaOH –** Sodium hydroxide

**NIR -** Near Infrared

**NLCs -** Nanostructured Lipid Carriers

**NPs –** Nanoparticles

**NRP-1** - Neuropilin 1

**NSCLC –** Non-small Cell Lung Cancer

**ORMOSIL -** Multimodal Organically Modified Silica

**OS –** Overall Survival

**PAH -** Polycyclic Aromatic Hydrocarbons

**PBS -** Phosphate-buffered saline

**PC –** Polystyrene Coated

**PDI -** Polydispersity Index

**PEG -** Poly-(ethylene glycol)

**PEI -** Polyethylenimine

**PFS –** Progression Free Survival

**pI** - Isoelectric point

**PMA -** Phorbol 12-myristate 13-acetate

**PPP –** Platelet Poor Plasma

**PRP –** Platelet Rich Plasma

**PS –** Performance Status

**PTX -** Paclitaxel

**QCM-D -** Quartz Crystal Microbalance with Dissipation

**RBC –** Red Blood Cell

**RCF (g) -** Relative Centrifugal Force

**RES -** Reticuloendothelial System

**RhBITC –** Rhodamine B Isothiocyanate

**RNA -** Ribonucleic acid

**ROC curve -** Receiver operating characteristic curve

**ROS -** Reactive Oxygen Species

**RPM -** Revolutions Per Minute

**RT -**  Room Temperature

**SCLC –** Small Cell Lung Cancer

**SDA –** Structure Directing Agent

**SDS -** Sodium Dodecyl Sulphate

**SEM –** Scanning Electron Microscopy

**SHp -** Stroke Homing peptide

**siRNA -** Small interfering RNA

**SLNs –** Solid Lipid Nanoparticles

**TAM –** Tamoxifen

**TCGA -** The Cancer Genome Atlas

**TEM –** Transmission Electron Microscopy

**TEMED -** N,N,N′,N′ -Tetramethyl ethylenediamine

**TEOS -** Tetraethyl orthosilicate

**Tf -** Transferrin

**TGA –** Thermogravimetric Analysis

**TIMP -** Tissue inhibitor of metalloproteinase

**TMOS -** Tetramethyl Orthosilicate

**TNM Staging System -** TNM Classification of Malignant Tumours

**TPP –** Triphenylphosphine

**TSNAs** - Tobacco-Specific N-Nitrosamines

**U-87 –** Human glioblastoma cell line

**U.S. –** United States

**US -** Ultrasound

**UV –** Ultraviolet

**Vis –** Visible spectrum

**WHO –** World Health Organization

**WST-8 -** Water-Soluble Tetrazolium Salt

**XRD -** X-ray Diffraction Analysis

*"No matter how cold the winter, there is a springtime ahead".*

*(Pearl Jam, 2002)*

# 1 CHAPTER 1: GENERAL INTRODUCTION

## 1.1 Cancer

Cells can divide and grow forming lumps or growths of tissue (benign tumours) due to the accumulation of cells. However, when cells don't go through the regular "cell division process" and start growing without control due to genetic changes, premalignant lesions, and then malignant tumours (cancer) can be developed. From this primary tumour, cancer cells can then spread to other parts of the body including not only nearby tissues, but also lymph nodes and other organs by travelling through either the blood or the lymphatic system (metastasis). [1-3] Cancer was reported for the first time by the Greek physician Hippocrates who used the Greek word καρκίνος ("Karkinos" which means crab) for describing the disease. [4]

Cancer cells form from normal cells during a multi-stage process during which a pre-cancerous lesion becomes a malignant tumour because of changes to genes which usually control cell functions. Cells genetic changes related to cancer can be inherited, caused by errors during the cell division process and/or triggered by external factors like physical, chemical and biological carcinogens. [2, 5] Under physiological conditions our body eliminates any mutation/cell that could lead to cancer. However, as we grow older, this ability decreases, increasing the incidence of tumours amongst the older population. Most of the diagnosed cancers are related to environmental factors, and risk factors include tobacco smoke, unhealthy diet and alcohol consumption, the lack of physical activity and air pollution. [5, 6]

Data published by the World Health Organization (WHO) in 2019, showed that cancer (diagnosed before the age of 70) was the first and/or second leading cause of death in 112 of 183 countries, and the third or fourth cause in further 23 countries. [7]

The Cancer Surveillance Branch (CSU) at the International Agency for Research on Cancer (IARC) regularly provides statistics of cancer incidence and mortality by age and sex in 85 countries for 36 types of cancers (as well as all

cancers combined); GLOBOCAN is an online database that provides data on cancer incidence, prevalence, and mortality. GLOBOCAN estimates for year 2020 showed that 1 in 5 people will get cancer during their lifetime, and 1 in 10 will die from it. Based on their data, 19.3 million new cancer cases were diagnosed worldwide in 2020 and, in the same year, 10 million cancer deaths were recorded. [8, 9]

The highest diagnosis numbers were recorded for female breast cancer, while the highest deaths numbers were recorded for patients suffering from lung cancer (**Fig. 1.1**).

**ESTIMATED NUMBER OF NEW CASES IN 2020, WORLD, BOTH SEXES, ALL AGES**



BREAST
2,261,419 (11.72 %)

LUNG
2,206,771 (11.44 %)

COLORECTUM
1,931,590 (10.01 %)

PROSTATE
1,414,259 (7.33 %)

STOMACH
1,089,103 (5.65 %)

LIVER
905,677 (4.69 %)

CERVIX UTERI
604,127 (3.13 %)

OTHER CANCERS
8,879,843 (46.03 %)

**Total = 19,292,789**
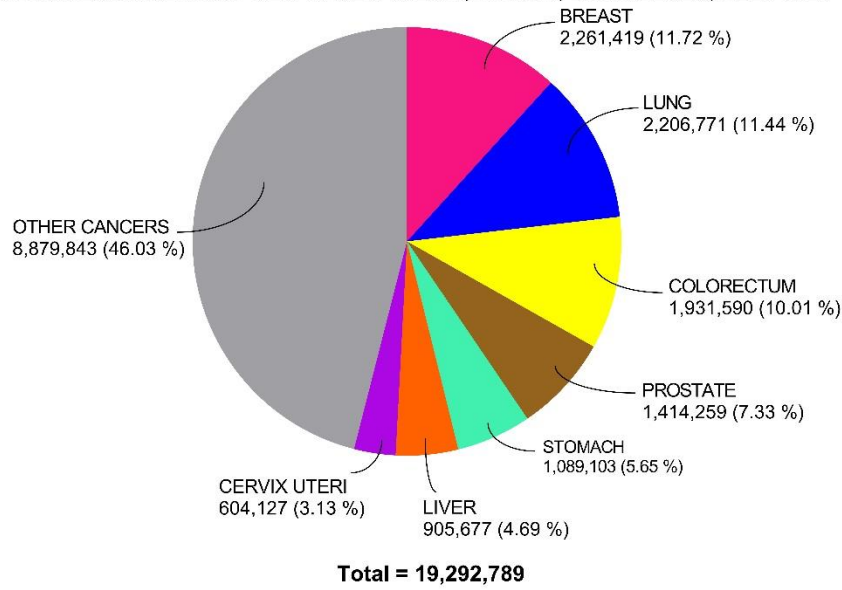
**ESTIMATED NUMBER OF DEATHS IN 2020, WORLD, BOTH SEXES, ALL AGES**



LUNG
1,796,144 (18.04 %)

COLORECTUM
935,173 (9.39 %)

LIVER
830,180 (8.34 %)

STOMACH
768,793 (7.72 %)

BREAST
684,996 (6.88 %)

OESOPHAGUS
544,075 (5.46 %)

PANCREAS
466,003 (4.68 %)

OTHER CANCERS
3,932,768 (39.49 %)

**Total = 9,958,133**
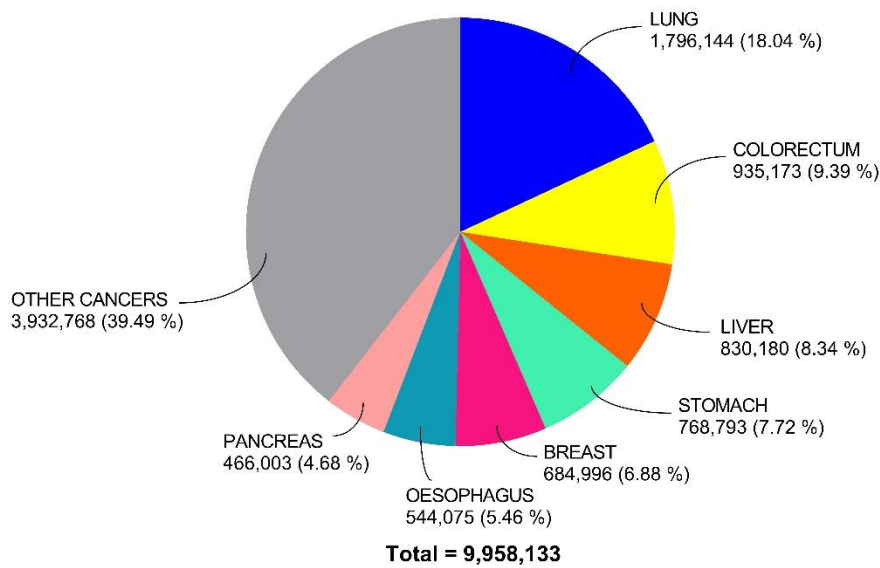
**Figure 1.1:** Number of new cases and deaths from cancer in 2020 (*Adapted from GLOBOCAN 2020, IARC, WHO*).

Malignant tumours are a complex structure made up of cancer cells lodged in vasculature and surrounded by a dynamic tumour stroma composed of a variety of non-cancerous cells like fibroblasts and myeloid cells. The tumour microenvironment mimics the inflammatory response in a healing wound,

promoting angiogenesis, extracellular matrix (ECM) turnover, and tumour cell motility and plays a crucial role during tumour growth and progression. [10]

Cancer staging is a crucial step in the diagnosis process, and it serves for a variety of purposes, such as:

1) Assisting the clinician in recommending a treatment plan.
2) Providing some indication of prognosis.
3) Assisting in the evaluation of treatment results.
4) Facilitating the exchange of information between treatment centers.
5) Contributing to the ongoing investigation of human cancer. [11]

The anatomical extent of the malignancy (in the case of solid tumours) is described using the international TNM-based staging system. The "T" classification defines the primary tumour's size and extent (from T0-no evidence of tumour present to T4); the "N" classification indicates the degree of involvement of regional lymph nodes (from N0-no involvement to N4), and the "M" classification reflects the absence (M0) or presence (M1) of distant metastatic spread. TNM subsets and stages (from stage I-localized to stage IV- metastasised) are  defined using combinations of the T, N, and M categories. [11, 12]


1.2   Types of Cancer


More than 100 different cancers exist. Typically, cancer types are named after the organs or tissues in which they first appeared, where the "primary cancer" has formed. For instance, brain cancer begins in the brain and lung cancer begins in the lung. The type of cell that gave rise to a cancer can also be used to describe the condition:

- carcinoma, when the cancer originates from the epithelial tissues (like the skin, the layer of cells covering the outer surface of internal organs, blood vessels and the inner surface of many internal organ cavities). There are further sub-classifications of carcinomas depending on the type of epithelial cells the cancer originated from.

- Sarcoma, when the malignancy originates in the connective or supportive tissues.

- Leukaemia, the tumour of white blood cells, which originates in the bone marrow's blood-forming tissue. In this case there is no solid tumour, but on the contrary abnormal white blood cells grow and multiply in the bloodstream. It may be more difficult for the body to manage bleeding, fight infections, or deliver oxygen to its tissues due to fewer regular blood cells present. Leukaemia presents four main types, categorised according to the type of blood cell the malignancy first appears in (lymphoblastic or myeloid) and if the condition worsens quickly (acute or chronic).

- Lymphoma and myeloma, cancers of the immune system cells. The cancer that starts in lymphocytes is called lymphoma (T cells or B cells); these aberrant white blood cells accumulate in the body's lymph nodes, lymph arteries, and other organs. The two primary kinds of lymphoma are the Hodgkin lymphoma and non-Hodgkin lymphoma.

- Brain and spinal cord cancers, also known as central nervous system cancers. [1, 2]

### 1.2.1  Carcinoma

Carcinoma is the most common type of cancer. This cancer is named after the type of epithelial cells it originated from:

- squamous cell carcinoma, from squamous cells which are surface-covering cells that for example line the skin and the lung's alveoli among other places (intestines, stomach, kidneys, bladder).

- Adenocarcinoma, from glandular cells (they secrete fluid or mucus to preserve the moisture of tissues).

- Transitional cell carcinoma, from transitional epithelium, or urothelium, which consists of numerous layers of epithelial cells; these cells can adjust by changing shape (contracting and extending) as the organ they are a part

of stretches (they make up the epithelium that lines the urinary system's organs).

- Basal cell carcinoma, from the basal (base) layer of the epidermis, which is a person's outer layer of skin. [2, 3]

## 1.2.2  Lung Cancer

Lung cancer has become over the past century (from a rare and unknown condition) the most prevalent cancer worldwide and the leading cause of cancer-related mortality. In fact, its incidence keeps growing internationally most likely due to an increased tobacco use and industrialisation in emerging countries. [13-16]

Lung cancer is a very diverse disease that can develop in a variety of locations throughout the bronchial tree and the lung parenchyma, resulting in a wide range of symptoms depending on the anatomic location. This malignancy is detected in around 70% of cases at an advanced stage (stage III meaning locally advanced cancer, or stage IV meaning presence of metastasis). [11] Under these circumstances only half of the patients survive up to one year after diagnosis and the 5-year survival rate is of approximately 16%. Yet, lung cancer has a greater chance of being successfully treated if diagnosed early, with a 5-year survival rate of 70%. [13-15]

According to the GLOBOCAN 2020 estimates (**Fig. 1.1**), with a predicted 1.8 million fatalities (18%) and 2.2 million new cancer cases, lung cancer continues to be the most common type of cancer worldwide, followed by colorectal (9.4%), liver (8.3%), stomach (7.7%) and female breast (6.9%) cancers. Lung cancer accounts for about one in ten (11.4%) new cases of cancer and one in five (18.0%) fatalities, making it the second most prevalent disease all over the world. Lung cancer ranks third in incidence and second in terms of mortality in women, and the most common cause of cancer morbidity and mortality in men. Men have nearly double the incidence and fatality rates than women, although the male-to-female ratio varies greatly among areas. [8, 9]

## 1.2.2.1 Modifiable risk factors

### 1.2.2.1.1 Tobacco smoking

Smoking is the single biggest risk factor for lung cancer. Lung cancer affects one out of every nine smokers and long-term smokers have a 10-fold to 30-fold increased risk of lung cancer compared to lifetime non-smokers. The cumulative risk of lung cancer in heavy smokers can reach 30%, compared to a lifetime risk of less than 1% in non-smokers. [13, 14, 17, 18]

The likelihood of developing lung cancer rises with the time spent smoking or with the daily pack counts. [19, 20] At least 80% of lung cancer deaths in the Western world are brought on by smoking. However, it is worth mentioning that the risk of developing lung cancer for those who never smoked, but lived with smokers, has increased by 20-30% according to the U.S. Surgeon General. [21] When compared to filtered mainstream cigarette smoke (mainstream smoke is formed by inhaling air via the cigarette and is the smoker's principal source of smoke exposure), side-stream smoke (created by the cigarette slow burning between puffs: the primary source of environmental tobacco smoke) contains four times higher concentration of the carcinogen benzo[a]pyrene due to the presence of filters on the cigarettes' end. In addition, studies have demonstrated that the urine of non-smokers who have been passively exposed to tobacco smoke contains nicotine, its metabolite cotinine and DNA adducts (sequence of DNA that has been damaged by the covalent bond to a chemical) from tobacco carcinogens. [22] In fact, in a meta-analysis published in 2018, [23] from 12 separate investigations, it was reported that second-hand smoke exposure was linked to a 25% higher risk of lung cancer compared to never smokers without such exposure. [13, 14, 16, 17, 24]

Exposure during pregnancy or in young infants is linked to chronic illnesses including asthma, sudden infant death syndrome and developmental delays. [16, 25-27]

With smoking accounting for around two-thirds of all lung cancer deaths globally, the condition could be substantially forestalled by comprehensive tobacco-control policies and regulations; the WHO Framework Convention on Tobacco Control developed the MPOWER package, which consists of six policy

intervention strategies to assist countries in implementing effective interventions to reduce tobacco demand:

- monitor cigarette use and preventative measures.
- Protect people from tobacco smoke.
- Offer aid to stop tobacco use.
- Warn about the hazards of tobacco.
- Enforce restrictions on tobacco advertising, promotion, and sponsorship.
- Raise taxes on tobacco. [9]

Tobacco was introduced to Europe at the end of the 15th century. It was initially chewed or smoked in pipes but following the introduction of cigarette wrapping machines in the mid-1800s, it was readily available in the form of cigarettes. During the two World Wars, cigarette smoking significantly grew in the US and Europe, first among males and then among women. Free cigarettes were distributed to soldiers to relieve their anxiety, who later became addicted to nicotine and brought the habit home with them after the war. Many doctors and other medical professionals smoked back then since there was little information available about the negative effects of tobacco use or nicotine addiction. [13, 17]

Doll and Hill [28] and Wynder and Graham [29] conducted large epidemiological studies in 1950 that provided strong evidence linking cigarette smoking to lung cancer. According to Wynder and Graham's estimation, the average adult smoked fewer than 100 cigarettes per year in 1900. However, over the next 50 years, the number of cigarettes smoked per person per year increased significantly. By the middle of the 1960s, it peaked at approximately 4400 cigarettes per person per year. In response to the growing evidence of the dangers of smoking, several authoritative bodies took action to raise public awareness. The Royal College of Physicians in the United Kingdom, and the US Surgeon General issued reports in 1962 and in 1964 respectively, to warn the public about the dangers of smoking. [13, 16, 17]

The tobacco component which is responsible for its addiction is nicotine, a natural alkaloid which binds to nicotinic acetylcholine receptors (nAChR) in the brain, affecting gene and receptor expression, as well as neurotransmitter (like

dopamine, serotonin, norepinephrine, endorphins, gamma-aminobutyric acid) levels in the bloodstream, promoting dependency. Even though nicotine is not a carcinogen, the upregulation of nicotinic receptors and changes in gene expression are linked to the progression of existing lung tumours. [30-32] More than 4000 chemicals can be found in tobacco smoke; [33] carcinogens and other toxicants are produced by the combustion of tobacco, and more than 60 are known nowadays, of which the most relevant include polycyclic aromatic hydrocarbons (PAH), nitrates and tobacco-specific N-nitrosamines (TSNAs). [34-37] Tobacco carcinogenesis mechanisms include the formation of DNA adducts by carcinogens and their metabolites, as well as free radical damage. [38] Cells with damaged DNA may go through apoptosis, or repair processes may remove these DNA adducts and return the DNA to its original state. However, failure of the ordinary DNA repair processes to eliminate DNA adducts might result in irreversible mutations and formation of cancer cells. [17, 39-41] To become carcinogenic, PAHs and N-nitrosamines must undergo metabolic activation. These substances can also undergo metabolic detoxification, and the equilibrium between their activation and detoxification probably influences each person's chance of developing cancer. The percentage of nitrates and TSNAs in cigarettes has grown since 1978, and various studies have demonstrated the relationship between these chemicals (specifically 4-(methylnitrosamino)-1-(13-pyridyl-1-butanone) or also called NNK, which has shown to induce lung cancer in animal studies) and adenocarcinoma; [42] a variety of signalling pathways, including the regulation of important oncogenes and tumour suppressor genes, can be mediated by NNKs, which can eventually lead to unregulated cellular proliferation and carcinogenesis. NNK is linked to DNA mutations that result in the activation of K-ras oncogenes; its activity has been discovered in 24% of human lung adenocarcinomas [43] and is also present in ex-smokers' lung adenocarcinoma, indicating that such mutations do not necessarily reverse with tobacco smoking discontinuance. This may help to explain why ex-smokers' lung cancer risk remains elevated many years after quitting smoking. [44] Furthermore, a particular chemical element of tobacco smoke, benzo[a]pyrene metabolite, has been shown to damage multiple p53 tumour-suppressor gene loci known to be aberrant in around 60% of primary lung cancer cases. [45] Other TSNAs have been associated to oesophageal, bladder, pancreatic, oral cavity, and

laryngeal cancer. NNK shows carcinogenic effects with both topical and systemic exposure. Inhaling tobacco smoke directly delivers TSNAs to the lungs; TSNAs are also absorbed systemically, and hematogenous distribution to the lung via the pulmonary circulation is possible. The increased content of NNK in cigarette smoke is most likely related to the increase in squamous non-small cell lung cancer in recent years. [13, 16, 17, 24]

The worldwide variance in lung cancer rates is due to regional differences in tobacco usage and air quality. The overall incidence is declining in men from developed nations due to tobacco control policies (rates of lung cancer in males are significantly higher in developed countries than in less-developed ones). In the industrialised nations, lung cancer in women is likewise more common and associated with cigarette smoking. Lung cancer numbers in females are rising worldwide; for instance, female lung cancer incidence in Europe has been increasing in the 21st century, and for the first time lung cancer mortality rates outnumbered breast cancer mortality rates in 2017 (14.6 lung cancer deaths per 100,000 compared to 14 for breast cancer). [13]

The cessation of tobacco use is thought to have the potential to prevent up to 20% of all cancer deaths globally. It is also undeniable that personal susceptibility plays a role in the development of cancer. Less than 20% of smokers develop lung cancer, even though tobacco use accounts for more than 80% of lung cancer cases. It is likely that genetic predisposition or other environmental variables contribute to this variability in cancer risk. [17]

1.2.2.1.2  Chronic obstructive pulmonary disease

Chronic obstructive pulmonary disease (COPD) is one of the non-malignant diseases that has been linked to lung cancer. [16, 17, 46, 47]

Smoking is the leading cause of COPD, [48] and this disease might raise the risk of lung cancer by increasing oxidative stress, which causes DNA damage, prolonging exposure to inflammatory cytokines, suppressing DNA repair processes and boosting cellular proliferation. COPD is the most prevalent independent risk factor for lung cancer, other than smoking, increasing the risk by 6- to 13-fold. [49,

50] Studies have found a statistically significant link between the existence of airflow restriction and the development of lung cancer in those who have never smoked but have been diagnosed with the disease. This shows that, regardless of smoking, airflow restriction is a risk factor for lung cancer. [51-53] There is more evidence supporting the latter statement, like the Lung Health Study [54], which followed a large group of smokers with spirometric signs of mild to moderate COPD for 5 years, found that lung cancer was the leading cause of mortality, accounting for 38% of all deaths in the study population. In this study, lung cancer fatalities outnumbered cardiovascular disease deaths by almost 50%. More recent large-scale investigations have shown the substantial link between COPD and an increased risk of lung cancer, particularly in males. [55, 56] These findings add to the evidence that COPD, in addition to smoking, is an independent risk factor for lung cancer. [16, 17, 46, 47]

In another recent study [57], which examined 602 lung cancer patients, it was found that half of them presented prebronchodilator pulmonary function test results consistent with a diagnosis of COPD. Since the prevalence of COPD in newly diagnosed lung cancer patients was six times higher than that in matched smokers, this finding raised the possibility that COPD may play a role in the pathogenesis of lung cancer as an important independent risk factor. [17]

A list of different risk factors for lung cancer is presented in **table 1.1**. [13, 14, 16, 58]

**Table 1.1**: Risk factors for lung cancer, both established and suspected. *(Adapted with permission from "AACR")* [24]

| RISK FACTOR | MAGNITUDE OF ASSOCIATION |
| --- | --- |
| Tobacco smoking | 20-fold increased risk vs. never smoker |
| Second-hand smoke | 25% to 28% increased risk vs. never smoker |
| Electronic cigarettes | Presently unknown |

| | |
|---|---|
| Other tobacco use (cigars, pipes, water pipes) | 1.9 to 4.6-fold increased risk |
| Smoked cannabis | Presently no known risk |
| Radon | 14% to 29% increased risk |
| Asbestos | 12% to 24% increased risk |
| History of COPD, emphysema, or chronic bronchitis | 2 to 3-fold increased risk |
| History of asthma | 28% to 44% increased risk |
| History of pneumonia | 30% to 57% increased risk |
| History of *Chlamydia pneumoniae* | 1.2 to 2.4-fold increased risk |
| History of tuberculosis | 48% to 76% increased risk |
| HIV | 2-fold increased risk |

## 1.2.2.2 Non-modifiable risk factors

Non-modifiable risk factors for developing lung cancer are factors that cannot be changed or controlled by an individual. These risk factors may increase the likelihood of developing lung cancer but cannot be altered through personal behaviour or lifestyle changes.

The factors which are considered to serve as risk factors for an individual to develop lung malignancies are:

- Family history/genetic factors: there are various chromosomes and genes that have been associated with a higher risk of lung cancer. [14] Not all tobacco smokers acquire lung cancer, confirming a hereditary

predisposition to lung cancer. Studies on familial aggregation (it refers to clustering of disease(s) within families) have reinforced the concept that lung cancer risk has a genetic component. A 1.7-fold increased risk of developing lung cancer has been linked to a family history of the disease; some studies have found that the risk of lung cancer is enhanced 2 to 4 times among first degree relatives of lung cancer patients, with an increased risk present in non-smoker too. [13, 16, 17] In a study conducted by Spitz and colleagues [59, 60] it has been demonstrated the impact of a cancer family history on the risk of lung cancer in never smokers, past and current smokers. Another study, from Cassidy and colleagues, [61] also emphasized the greatly elevated risk of lung cancer in people with a family history of early-onset lung cancer (< 60 years of age). [17]

- Gender: in the late 1980s, lung cancer overtook breast cancer as the top cause of cancer deaths in women. Today, lung cancer claims about twice as many female lives as breast cancer. It has been hypothesised that there might be a relation between the observed gender variations in susceptibility, and differences in nicotine metabolism and metabolic activation or detoxification of lung carcinogens. Ryberg and co-workers [62] reported that women with lung cancer present more DNA adducts than males; considering this, such individuals may be more vulnerable to carcinogens, and this could justify why women appear to acquire lung cancer with lower-intensity cigarette use. [13, 16, 17]

- Ethnicity and socioeconomic status: when talking about lung cancer incidence, cigarette smoking most certainly does contribute to the high heterogeneity among ethnicity and nations, but other genetic and environmental variables are also likely to have a role and need to be considered. Disparities in lung cancer incidence, mortality and survival outcomes are recorded and attributed to wealth status differences, which lead to variations in exposure to risk factors and barriers to high-quality prevention, early detection, and treatment. There have been disparities reported in the United States, where minorities and patients with lower incomes are less likely to receive aggressive lung cancer therapy and less likely to be included in clinical trials. [63] Despite having a substantially lower

incidence of reported cigarette usage, Chinese women are just as likely as Western European women to be diagnosed with lung cancer. Air pollution and exposure to smoke from charcoal burning are considered to contribute to the elevated risk among Chinese women. [16, 24]

- Age: tumorigenesis in the lungs appears to develop decades after first mutagen exposure, explaining the disease's delayed onset. The median age of populations in industrialised countries is increasing and cancer is defined as a disease of the elderly; the median age for lung cancer diagnosis is 70 years for both men and women. Due to biological variables biological aging is also likely a factor since, as we age, telomeres shorten, levels of the metabolite NAD+ drop, and cells lose the capacity to tolerate and repair DNA damage as well as detect abnormal cells. [13, 16, 17]

## 1.2.2.3 Lung cancer histological classification

As shown in **Fig. 1.2**, lung cancer malignancies are broadly classified into two primary histologic groups:

- Non-small cell lung cancer (NSCLC) is the most common type responsible for more than 80% to 85% of lung malignancies. It includes adenocarcinoma (AdenoCA) the most common histologic subtype regardless of age, in smokers and non-smokers and in men and women, that accounts for around 40% of lung cancers; squamous cell carcinoma, second in frequency (25% to 30%), and large cell carcinoma, the less common one accounting for 10% to 15%.
- Small cell lung cancer (SCLC) is a less frequent type of lung cancer, but it spreads more quickly than NSCLC.
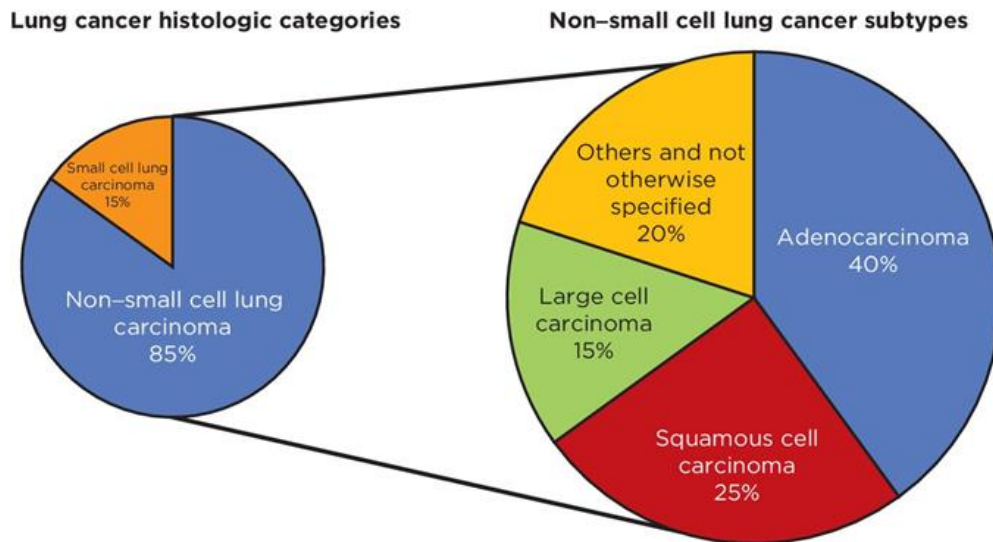
**Figure 1.2:** Lung cancer histologic classification. The two primary histologic classifications of lung cancer (NSCLC and small cell lung carcinoma), as well as the three most prevalent histologic subtypes of NSCLC. *(Reprinted with permission from "AACR")* [24]

**Table 1.2** summarises the prevalence and main characteristics/origin of the small and non-small cell lung cancer.

Table 1.2: Types of lung cancer. *(Adapted with permission from Elsevier)* [11]

| Lung cancer type | % Of all lung cancer | Anatomic location/Main characteristics |
|---|---|---|
| Squamous cell lung cancers (SQCLC) | 25–30% | Arise in main bronchi and advance to the carina |
| Adenocarcinomas (AdenoCA) | 40% | Arise in peripheral bronchi |
| Large cell anaplastic carcinomas (LCAC) | 10% | Tumours lack of the classic glandular or squamous morphology |
| Small cell lung cancers (SCLC) | 10–15% | Derive from the hormonal cells of the lung Cells disseminate into submucosal lymphatic vessels and regional lymph nodes almost without a bronchial invasion |

1.2.2.4 The biology of lung cancer

15

The regulatory circuits that regulate normal cell growth and homeostasis are defective in lung cancer cells. The progression from a normal to malignant lung cancer phenotype is believed to occur in stages, with a succession of epigenetic and genetic modifications eventually leading to invasive cancer via clonal propagation. The processes of invasion, metastasis, and resistance to cancer therapy are influenced by the ongoing accumulation of genetic and epigenetic aberrations acquired during clonal expansion after the onset of the primary cancer. A tailored prognosis and the selection of the best treatment for each patient can be considerably improved by knowing the patient's tumour features and genetics. [11]

In **table 1.3** are summarised the main somatic mutations and alterations detected in NSCLC.

**Table 1.3:** Frequency of somatic mutations and alterations in NSCLC. *(Reprinted with permission from "AACR")* [24]

| Gene | Alteration type | Frequency in NSCLC |
|:---:|:---:|:---:|
| **EGFR** | Mutation | 10%–35% |
| **KRAS** | Mutation | 15%–25% |
| **FGFR1** | Amplification | 20% |
| **PTEN** | Mutation | 4%–8% |
| **DDR2** | Mutation | ~4% |
| **ALK** | Rearrangement | 3%–7% |
| **HER2** | Mutation | 2%–4% |
| **MET** | Amplification | 2%–4% |
| **BRAF** | Mutation | 1%–3% |
| **PIK3CA** | Mutation | 1%–3% |
| **AKT1** | Mutation | 1% |

| | | |
|---|---|---|
| **MEK1** | Mutation | 1% |
| **NRAS** | Mutation | 1% |
| **RET** | Rearrangement | 1% |
| **ROS1** | Rearrangement | 1% |

1.2.2.5  Signs and symptoms of lung cancer

There are no distinct symptoms or indicators that may be useful to diagnose lung cancer. Some of the symptoms associated with lung cancer are also present in smokers and those with other illnesses, such as upper respiratory tract infections. Both the presence of metastatic disease and the size and location of the initial tumour can define the occurrence of specific signs and symptoms. [64]

Coughing, haemoptysis, wheezing, and dyspnoea are common symptoms, yet it is not rare for a lesion to be found by chest radiography in a patient who is asymptomatic. As the lesions grow and start to spread, new symptoms can emerge. Growth inside a bronchus frequently causes coughing and wheezing and sometimes stridor. Haemoptysis often manifests as moderate blood-stained sputum. Pneumonia and fever can also be developed from airway obstruction. Pleural involvement may result in pleuritic pain and pleural effusion. Additional symptoms associated to local spread are the Pancoast's syndrome (shoulder or arm discomfort), brought on by the compression of the brachial plexus by extension of an apical tumour, and the superior vena cava syndrome (characterised by oedema in the face, neck, and shoulders) due to the compression of the superior vena cava by an expanding tumour. Hoarseness may result from pressure on the laryngeal nerve caused by an enlarged tumour or mediastinal nodes. Fatigue and weight loss are nonspecific signs of metastatic illness. [64]

The liver, brain, bones, and adrenal glands are the most typical locations for distant metastases. When the metastasis is present in the brain, patients may have headaches, impaired mental function, seizures, and even encephalopathy

17

symptoms. Bone lesions are typically excruciatingly painful and liver lesions can cause abdominal discomfort and eventually jaundice. [64]

## 1.2.2.6  Management of NSCLC

NSCLCs are addressed by a combination of surgery and adjuvant treatment, whereas SCLCs exhibit aggressive behaviour and are often treated non-surgically. [65]

❖ **Stage I and II:** about 15% of newly diagnosed episodes of NSCLC qualify for surgical resection, which provides the highest chance for long-term survival. Due to concomitant comorbidities, some patients with localized cancer may not be candidates for surgical resection (some patients might refuse surgery too) and in these cases radiation treatment with a curative goal may be administered. High-energy beams are used in radiotherapy to disrupt cancer cells' DNA, ultimately killing them. Survival rates following this treatment vary between 15-20%. [11, 14, 64]

Some individuals who have had lung cancer resection surgery may benefit from adjuvant treatment to reduce the chance of recurrence. Radiation, chemotherapy, and targeted treatment may be used as adjuvant therapy and prolong survival. [14]

❖ **Stage III:** over 70% of NSCLC patients have progressed or metastatic illness when they are first diagnosed (stages III and IV). The degree of nodal involvement and the degree of the resection are the main predictors of survival in these individuals. [11, 64]

Treatment options, such as radiation, chemotherapy, and surgical resection, are dictated by the tumour site and whether it is possible to surgically remove it. Chemotherapy and radiation treatment can be delivered sequentially or simultaneously; which is the optimum schedule is unknown. Different trials [66-69] have demonstrated an improved survival when lung cancer patients at stage III were treated with both chemotherapy and radiation.  In one trial [70] it has been observed that the occurrence of distant

metastases was significantly reduced when the two treatments were used in succession. [11, 64]

❖ **Stage IV:** 40% of newly diagnosed NSCLC patients present advanced metastatic disease (stage IV NSCLC). Treatment for stage IV NSCLC patients is determined by a variety of criteria, including comorbidities, patient's performance status (PS), histology, and molecular genetic characteristics of the tumour. Patients with advanced lung cancer are unlikely to be cured by chemotherapy; improved survival and a reduction of adverse disease-related events are the aims of treatment for these individuals. Chemotherapy has demonstrated to improve the 1-year overall survival (OS) rate. [71] Cytotoxic combination chemotherapy is the first-line treatment for stage IV NSCLC. [11, 14, 64]

According to the American Society of Clinical Oncology, a platinum (cisplatin, or carboplatin) regimen combined with either taxanes (paclitaxel, docetaxel, or vinorelbine), antimetabolites (gemcitabine, or pemetrexed), vinca alkaloids (vinblastine) or irinotecan is the recommended first-line course of therapy. [11, 14]

Bevacizumab, an anti-VEGF antibody, is now recommended for use in first-line doublet combination chemotherapy, with some exceptions due to concerns of lethal bleeding. [11]

Agents that specifically block EGFR, such as erlotinib and gefitinib, are the first of the approved targeted medications for NSCLC patients and they are not indicated for use as first-line treatment in conjunction with cytotoxic chemotherapy. [11]

1.2.2.7   Maintenance therapy

A malignancy that has not progressed after receiving first-line therapy is treated with what is called "maintenance therapy" until the illness progresses with the aim to minimize cancer-related symptoms and, ideally, extend survival time over what is achieved by first-line therapy. [11]

The two drugs that have so far received FDA approval for use as maintenance treatment for advanced lung cancer are pemetrexed and erlotinib. It was demonstrated in two randomised clinical trials [72, 73] that the use of pemetrexed as maintenance treatment after conventional first-line platinum-based combination chemotherapy improved the progression-free survival (PFS). Another major randomized controlled clinical study [74] found that erlotinib maintenance treatment after platinum-based chemotherapy enhanced survival (both PFS and OS) in NSCLC patients without progressing disease. [11]

### 1.2.2.8   Second- and third-line therapies

Authorized second-line therapies for patients with advanced NSCLC who have not responded to first-line platinum-based treatment include docetaxel, pemetrexed, erlotinib, and gefitinib. [11]

### 1.2.2.9   Recurrent NSCLC

Recurring/relapsing NSCLC is the malignancy that returns or spreads after the primary treatment (surgery, radiotherapy and/or chemotherapy). It might reappear in the lung, brain, or other regions of the body. It is very common for patients with lung cancer to get brain metastases, which are a major source of morbidity and mortality. At two years after diagnosis, 30% of NSCLC and 80% of SCLC patients with the disease had brain metastases. [11]

The treatment of spreading tumours and tumour metastases often requires extensive chemotherapy. Low specificity, quick drug clearance and biodegradation, and restricted targeting are current issues in the treatment of cancer. One of the main problems of chemotherapeutic drugs is that they are non-selective and for this reason they can also damage other rapidly growing healthy cells (i.e., cells in hair follicles, nail etc), causing severe unintended and undesirable side effects. Some common side effects of chemotherapy include nephrotoxicity (kidney damage), neurotoxicity (nerve damage), ototoxicity

(damage to the ears and hearing), and many others. These side effects can vary depending on the specific drugs used and the individual patient. On top of that the bioavailability of chemotherapeutics to tumour sites/tissues is poor and higher doses are usually required. All these factors can potentially contribute to cause high toxicity in healthy cells, in addition to an increased incidence of multiple drug resistance (MDR), one of the major challenges in cancer treatment. For all the above stated reasons, it is of great importance to develop chemotherapies that will specifically target cancer cells. [75-77]

1.2.3   Glioblastoma multiforme (GBM)

Glioblastoma multiforme (GBM) is a type of primary brain malignant tumour that originates from the glial cells, specifically the astrocytes. It is classified as a grade IV astrocytoma by the WHO [78] and it is the most common and aggressive form of malignant primary brain tumour in adults, with a very poor prognosis and a median survival time of less than a year for most patients. [79-81] The incidence rate of GBM varies, and it is typically stated as the number of new cases per 100,000 people per year, which is generally age-adjusted to account for changes in age distributions between populations: depending on the report, it can range between 0.59 and 3.69 per 100,000 people. [82, 83] GBM is more commonly diagnosed in older individuals. The incidence of GBM increases with age, and it is most frequently found in people over the age of 60. The highest incidence tends to be in the 75–84-year-old age group. [84, 85] The frequency is greater among Caucasians than in other ethnic groups, as well as in men than in women. [85, 86] GBM is known for its ability to rapidly invade and infiltrate surrounding healthy brain tissues, making difficult their complete removal through surgery. The tumour is also highly vascularized, which means it has a significant amount of blood vessels that supply it with nutrients and oxygen. This can hinder the success of traditional therapies, such as chemotherapy and radiation. On top of that, the significant intra- and inter-heterogeneity of the tumour mass, which consists of a variety of different cell types with different genetic and molecular characteristics, makes difficult to identify treatment targets. In recent years, significant research efforts, led by initiatives like

The Cancer Genome Atlas (TCGA) network and the paediatric neurooncological community, have focused on investigating the molecular biology underlying GBM. [87, 88] These efforts have resulted in the generation of detailed catalogues of genomic and epigenomic alterations associated with GBM, identifying distinct biological subgroups within GBM characterized by specific molecular features, and therefore providing valuable information for understanding the heterogeneity of the disease which have implications for prognosis, treatment response, and the development of targeted therapies tailored to specific molecular profiles.


## 1.3   Drug Delivery Systems (DDSs)

The term Drug Delivery Systems is referred to the macro-/micro-/nanocarriers used for the administration of therapeutic/diagnostic agents into the patient body, in order to improve drugs safety, patient compliance, and convenience. [89-91]

Delivering therapeutic compounds to the target site is indeed a major challenge in the treatment of many diseases. Drugs often present limitations such as low efficacy, uneven distribution throughout the body, and inability to specifically target the affected area. The pharmacological action of anti-cancer drugs involves not only the targeting of cell surfaces but also reaching specific cellular organelles such as endosomes, lysosomes, mitochondria, endoplasmic reticulum, and the nucleus. The low water solubility of certain drugs frequently limits their delivery to the tumour as they can be eliminated from the bloodstream before reaching the targeted tissue: the reticuloendothelial system (RES) can detect hydrophobic elements as foreign and remove them from the circulation accumulating them in the liver or spleen. A targeted delivery can be achieved through the use of DDSs, which can offer an improved option for cancer chemotherapy. DDSs aim to overcome chemotherapy limitations by precisely controlling the delivery of drugs to the desired location allowing for a more targeted and effective treatment. By encapsulating these molecules in DDSs their transport through the bloodstream can be enhanced, limiting rapid clearance, and enhancing the bioavailability and efficacy, without the need of using higher doses. [76, 77, 92]

Several advantages are achieved from encapsulating drug(s) in a carrier, leading to an improvement in both pharmacokinetics and pharmacodynamics of chemotherapeutics drugs, including:

1. Protection from rapid degradation or clearance: by encapsulating or formulating the drug within a delivery system, it can be shielded from enzymatic degradation or a quick elimination from the body. This protection ensures that a sufficient concentration of the drug is maintained over an extended period, increasing its efficacy.

2. Enhancing the drug concentration in target tissues: by specifically targeting the affected site or organ, the drug can accumulate in higher concentrations at the desired location. The ability to obtain a targeted delivery consequently increases the local therapeutic effect while minimizing the drug's exposure to non-target tissues, reducing the potential for adverse side effects.

3. Controlled Release: by designing the DDS to release the drug in a controlled manner. This controlled release feature allows for a sustained and prolonged drug release at the tumour site, ensuring a more continuous and effective exposure of cancer cells to the drug. This can also help reduce the frequency of drug administration.

4. Allow the use of lower doses of the drug: the possibility to lower the administered doses can reduce the overall toxicity of the drug, as it is concentrated in the desired area and less of it circulates throughout the body. It can help improve the patient's compliance and quality of life by reducing potential side effects associated with higher doses, and it can also help mitigate any potential cost implications associated with high drug quantities.

5. Overcoming multiple drug resistance: cancer cells can become resistant to multiple drugs, which makes chemotherapy less effective. DDSs can potentially overcome MDR by improving drug uptake in resistant cells, bypassing efflux pumps, or using specific mechanisms to enhance drug sensitivity. [75, 92-96]

## 1.3.1 Delivery/Targeting mechanisms

The controlled release of the loaded medication(s) may be facilitated by the use of internal and external triggers as well as targeted modifications in order to guarantee selective toxicity to the tumour tissues while protecting normal tissues. [76]

Different delivery/targeting mechanisms can be used in order to make the DDS reach the tumour tissues (**Fig. 1.3**):

- Passive targeting.
- Active targeting.
- The use of stimuli-responsive systems for a triggered release. [76]
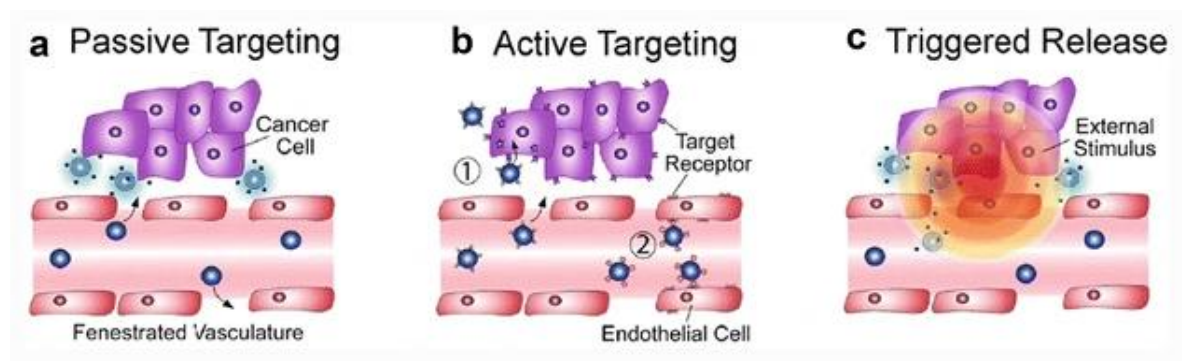


**Figure 1.3:** Delivery/targeting mechanisms of DDSs. *(Adapted with permission from Elsevier)* [97]

## 1.3.1.1 Passive targeting

Cancer cells grow very rapidly and, therefore, new blood vessels (angiogenesis) from the surrounding capillaries need to be developed for keeping the supply of nutrients and oxygen at the tumour site. Angiogenesis is a very fast and uncontrolled process under these circumstances, and for this reason the newly formed vessels are irregular, with discontinuous endothelium and fenestrations with sizes between 200 and 2000 nm. On top of that, in solid tumours, the lymphatic drainage is also deficient. Therefore, when comparing with normal tissues, tumour

tissues present hypervascularization, aberrant vascular architecture, an excessive production of vascular permeability factors and they lack an efficient lymphatic drainage. This phenomenon is called "Enhanced Permeability and Retention effect" (EPR). Passive targeting takes advantage of these pathological and immunochemical characteristics of the tumour tissues, allowing DDSs of appropriate sizes to escape the blood circulation and accumulate in the tumour interstitium. In fact, and due to the presence of a discontinuous endothelium with fenestrations, DDSs can accumulate and be retained for days due to the deficient lymphatic drainage of solid tumours and exert their activity releasing the drugs into the vicinity of the tumour cells. [93, 98-101]

However, although the EPR effect can be used to passively target DDSs to the tumour site(s), DDSs can re-enter the blood circulation by diffusion and for this reason they may not stay for prolonged periods of time in the target site(s). In addition, passive targeting cannot completely rule out the possibility of nanocarriers accumulating in tissues like the liver or spleen that typically have fenestrated blood vessels and, on top of that, the permanence of DDSs in the bloodstream can be affected by the interaction with circulating blood components such as opsonins. These interactions are strongly dependent on the surface properties of the DDSs and can induce the removal of the latter from the bloodstream through the RES and Kupffer cells (phagocytic macrophages located in the liver) and may also trigger inflammation following the release of cytokines from phagocytic cells. It is well known that the surface coating of the DDSs with hydrophilic polymers ("stealth" systems) can prolong their circulating time, and for this reason polymeric-based DDSs have been developed and used in order to obtain prolonged retention times at the tumour site. [76, 102-108]

## 1.3.1.2  Active targeting

Active targeting can be achieved by modification of the surface of DDSs with small molecules (i.e., folic acid), antibodies and antibody fragments, glycoproteins, nucleic acids, growth factors, peptides, and vitamins, which will specifically bind to specific receptors (i.e., antigens, folic acid receptors, transferrin receptors,

epidermal growth factor receptors) overexpressed by tumour cells and vasculature.
[93, 102, 108]

It is also possible to functionalize the surface of DDSs with two targeting agents in order to obtain what is called "dual targeting" with the aim of improving selectivity. Some examples of dual targeting are:

1. The Janus type MSNs (MSNs) (**Fig. 1.4**) synthesized by López V. *et al.*, [109] Those MSNs are functionalised with both folic acid (Fol, in order to interact with folate receptors) and triphenylphosphine (TPP, able to bind to mitochondria membrane), enhancing the therapeutic efficiency of MSN for antitumor therapies.

2. Li Y. *et al.*, [110] synthesised a DDS using both transferrin (Tf, a protein that binds to transferrin receptors, which are overexpressed on the surface of the blood brain barrier (BBB) endothelial cells) and tamoxifen (TAM, a drug that specifically recognizes and inhibits MDR proteins, which are overexpressed on the BBB and glioma cells) as the targeting groups in order to strengthen the ability to transport across the BBB and consequently concentrate drugs in glioma cells.

3. Hu Q. *et al.*, in their work [111] functionalised their DDS with two peptides: ATWLPPR and CGKRK in order to enhance antiglioma therapy. The first sequence is able to bond to NRP-1 receptors ("shuttle protein" overexpressed on the endothelial cells of glioma blood vessels and glioma cells), while the second one can interact with heparan sulphate proteoglycan (HSPG, an important component of the extracellular matrix).

4. Zhao Y. and co-workers [112] synthesised a liposome which could penetrate the BBB and target ischemic lesions in individuals affected from ischemic stroke by conjugating the DDS with T7 peptide (able to interact with transferrin receptors) and stroke homing peptide (SHp, able to accumulate in ischemic brain tissues tissues). [113]
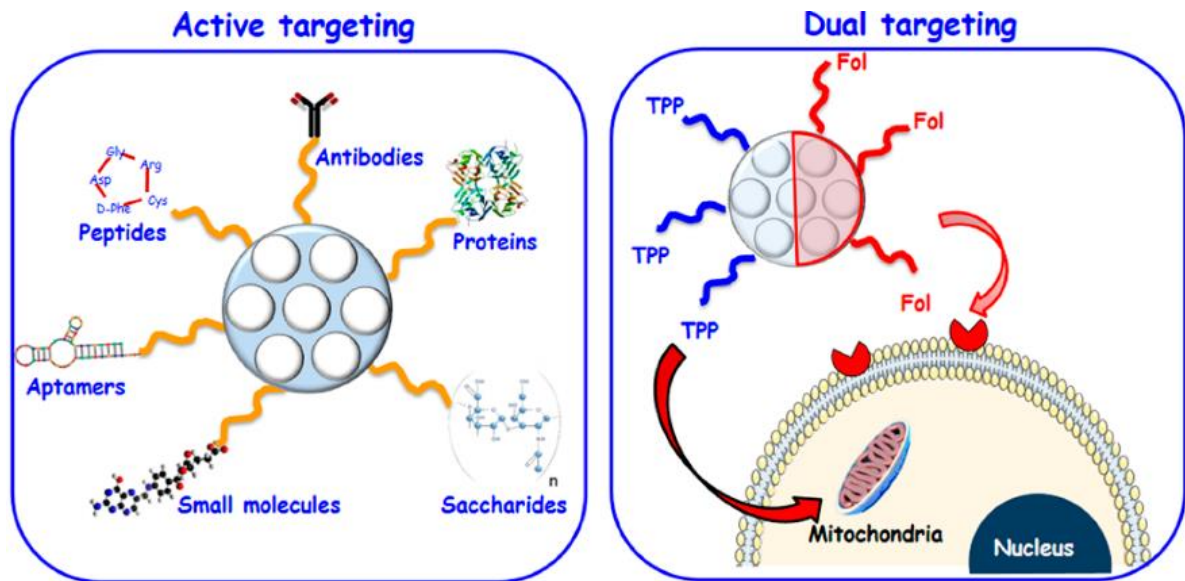
**Figure 1.4:** Schematic representation of active and dual targeting. [113]

## 1.3.1.3 Triggered release (stimuli-responsive systems)

Anti-cancer drugs are extremely hazardous to normal cells. Therefore, it is undesirable for those medications to be released from the DDS before they have reached the disease foci. The so-called "zero premature release" method can reduce toxicity and maximize effective medication accumulation by reducing drug distribution to off-target areas and providing as well a safe dose-escalation. [114] In this regard, internal or external stimuli can be used to trigger the release of the cargo by inducing a change in the DDS. Using this approach, drug(s) and/or molecules release from the delivery systems can be blocked using capping agents and/or gatekeepers, so no release takes place until the systems are exposed to a given stimuli, in order to achieve a better targeting and eliminate off target toxicity. [76, 93, 97, 108, 113-117]

Examples of internal stimuli are:

- pH: the pH around and inside the tumour cells (organelles) and the blood differ [118], this characteristic offers the possibility for developing nanocarriers that will release their drugs preferentially when they reach the tumour tissue and are exposed to a certain pH. In order to develop these systems researchers have used pH-responsive linkers or capping molecules (like

lipids, cyclodextrin, chitosan and gelatine) or pH-responsive interactions between drug molecules and DDSs. As the pH of endosome/lysosome in cancer cells is around 5.0-5.5, this method has been extensively employed in research for delivering anticancer medications that display a triggered release in an acidic environment. [119-127]

- Redox: tumours normally present a hypoxic microenvironment with low oxygen and nutrient levels, resulting in high levels of reductive agents like glutathione. [128-135]

- Enzymes: enzyme-based biochemical stimuli can be utilized to trigger specific responses. These systems advantage of the unique biochemical environment of the disease site, providing targeted and controlled release of therapeutic agents. [136-143]

External stimuli include:

- Temperature: the permeability of blood vessels may be increased by hyperthermia. In fact, temperature changes between 37 and 42°C, can improve the delivery of nanocarriers that are sensitive to changes in temperature. [144-149]

- Light: light-based stimuli-responsive DDSs offer a promising approach for achieving controlled drug release with non-invasive (it can be externally applied) and spatiotemporal control (based on the wavelength used, the release can be precisely controlled allowing a targeted delivery to specific tissues or cells: light penetrates deeper into the body as the wavelength increases). By incorporating light-responsive linkers, able to undergo physicochemical changes, into the DDSs, the release of the cargo can be triggered by illumination with a specific wavelength, such as ultraviolet (UV), visible (Vis), or near-infrared (NIR) light. [150-156]

- Ultrasound (US): another effective approach for achieving spatiotemporal control of medication administration at the target site while avoiding damaging healthy tissues. The depth of tissue penetration can be controlled by adjusting various ultrasound parameters, such as frequency, duty cycle, and exposure times. [157-162]

- Magnetic force and electric field: magnetic NPs (iron oxide) embedded within the DDSs respond to the applied external magnetic/electric field and facilitate the targeted delivery and localization of the NPs to specific sites within the body. [163-167] Another advantage is that the integration of superparamagnetic iron oxide NPs within the DDSs enables the generation of heat upon exposure to an alternating magnetic field (conversion of magnetic energy into thermal energy): the heat generated can induce hyperthermia in specific areas, selectively damaging cancer cells or facilitating the controlled release of encapsulated drugs. [168, 169]

1.3.1.3.1 Glutathione

Glutathione (GSH) is a tripeptide composed of glutamate, cysteine, and glycine that is abundant in almost all mammalian tissues. It can be found in the range 1-10 mM (in most cells the concentration is ~ 1-2 mM) in the cytosol of almost all cells, where the synthesis takes place by the two enzymes glutamate cysteine ligase (GCL) and glutathione synthetase (GS). It can exist in both reduced (GSH) and disulphide/oxidized (GSSG) forms (free reduced GSH being predominant inside the cells). The dynamic equilibrium between the rate of GSH synthesis and the total rate of GSH consumption within the cell and loss through efflux is reflected in the intracellular GSH concentration. [170-173]

The role of GSH in numerous cellular processes is now widely acknowledged: it functions as a reducing agent and antioxidant; participates in the metabolism of xenobiotics and multiple cell molecules; scavenges free-radicals; plays a role in cell-cycle regulation and microtubular-related mechanisms; acts as a physiological reservoir of Cys; controls $Ca^{2+}$ homeostasis; regulates protein function and gene expression via thiol-disulphide exchange reactions; modulates lymphocyte functions and immune responses and it is involved in mitochondrial mechanisms. The sulfhydryl (-SH) group of the cysteinyl moiety, a potent reducing agent, and a potent nucleophile, is responsible for GSH's functionality. [170, 174]

Changes in GSH levels and its metabolism have been linked to a variety of human diseases, including cancer, neurodegenerative diseases, AIDS, aging,

cystic fibrosis, liver diseases, heart attack, stroke, seizure, diabetes, sickle cell anaemia, and kwashiorkor malnutrition. [170]

It has been shown that the levels of GSH are higher in malignant tissues (including breast, ovarian, lung, as well as head and neck cancers), when compared to healthy tissues. [175] In blood plasma, where levels are within the micromolar range, GSH levels sometimes go up to two times higher, and in certain drug-resistant tumours can be even ten times higher. In fact, GSH plays an important role in tumours, with a number of studies demonstrating that increased cellular GSH levels are required for malignancy initiation and proliferation, and that also play a role in drug resistance. [176-183] It is well known that changes in GSH metabolism frequently occur alongside the growth of tumours, possibly as a defence mechanism used by cancer cells to lessen the effects of increased oxidative stress brought on by their extraordinarily high metabolic rates. In addition to the increased levels of ROS production in most tumour cells, the observed rise in GSH levels is also connected to the fact that several of the traditional tumour promoters also stimulate GSH synthesis and turnover pathways. [115, 173, 184]

For these reasons, the reductive environment of cancer cells at the tumour site can be used to trigger the release of the cargo from DDSs, avoiding an early release in the bloodstream and/or healthy tissues.

1.3.1.3.2  Matrix Metalloproteinases (MMPs)

MMPs are a family of zinc- and calcium-dependent proteolytic enzymes with different substrates but similar structural characteristics, which are well known to be overexpressed in all invasive malignant tumours in both cancer cells (including lung cancer cell lines) and in the surrounding stroma (macrophages, fibroblasts, dendritic cells, mast cells, endothelial cells, and lymphocytes (**Fig. 1.5**)). MMPs are found at low quantities in normal adult tissues, but when the system is disrupted during cellular repair, wound healing, or tissue remodelling in pathological circumstances, MMPs are overexpressed. It has been reported that MMPs can be increased in body fluids of cancer patients. In fact, MMPs have undergone extensive research as a biomarker for the detection of cancer, as well as target enzymes during the development of DDSs. [143, 185-187]

**Figure 1.5:** Proteinases expression and their physiological inhibitors in non-malignant stromal cells (*Adapted and reprinted with permission from Elsevier*). [10]

There are 24 MMPs that are known to exist in humans (23 MMPs plus one duplicated MMP-23 protein sequence).Their architectural characteristics can be used to categorize them: as either membrane-anchored (MMP -14, -15, -16, -17, -23, -24, -25) or secreted (MMP -1, -2, -3, -7, -8, -9, -10, -11, -12, -13, -19, -20, -21, -22, -27, -28).

MMPs can be also categorized into groups based on their domain organization, sequence similarity, and substrate specificity:

- Collagenases (cleave some extracellular matrix (ECM) proteins, particularly fibrillar collagen, and other soluble proteins).

- Gelatinases (play a crucial part in numerous physiological processes, such as ECM breakdown and remodelling, osteogenesis, and wound healing; they also play a role in pathological conditions including tumour progression,

angiogenesis, vascular illnesses, inflammatory and infectious diseases, and degenerative diseases of the brain).

- Stromelysins (despite sharing a domain structure with collagenases, stromelysins do not cleave interstitial collagen).

- Matrilysins.

- Membrane-type metalloproteinases (MT-MMP).

- Other MMPs.

MMP expression is controlled by the activation of hormonal and inflammatory agents, as well as by intercellular and matrix interactions. MMPs can degrade the majority of ECM proteins while also regulating the activity of other proteinases, growth factors, cytokines, chemokines, and cell receptors. MMPs can alter signalling pathways by cleaving ECM proteins and other molecules, which makes them central regulators of cell function in both physiological and pathological conditions. Because the majority of MMPs are synthesised in a dormant state, they must be activated after being secreted from cells. Proteolytic removal of the pro-domain or autoactivation mediated by binding to chemicals such as reactive oxygen species, chaotropic agents, or organomercurials are common methods of activation. MMP activity is also regulated by physiological inhibitors found in the ECM and circulation, such as the four tissue inhibitors of MMPs (TIMP-1-4) and $\alpha_2$-macroglobulin. [10, 185-187]

Extensive evidence suggests that MMPs promote many of the alterations in the tumour microenvironment that occur during tumour growth, and they play an important role in the molecular communication between tumour cells and stroma. Cell migration, differentiation, proliferation, apoptosis, inflammatory responses, angiogenesis, and platelet aggregation are some of the biological activities mediated by MMPs in tumorigenesis and cancer progression. The same MMPs may be implicated in many of these activities, with opposing effects depending on which substrates they operate on (**Fig. 1.6**). One example is MMP-9 participation in angiogenesis, a critical process in cancer growth. The enzyme can promote angiogenesis by releasing and activating angiogenesis-promoting molecules and can also increase endothelial cell migration and pericyte recruitment, required for

blood vessel stability. On the other hand, and by producing anti-angiogenic factors, usually fragments of bigger ECM molecules created by proteolysis of the ECM or the basement membrane of vessels, MMP-9 can also perform anti-angiogenic actions. [10, 185-190]
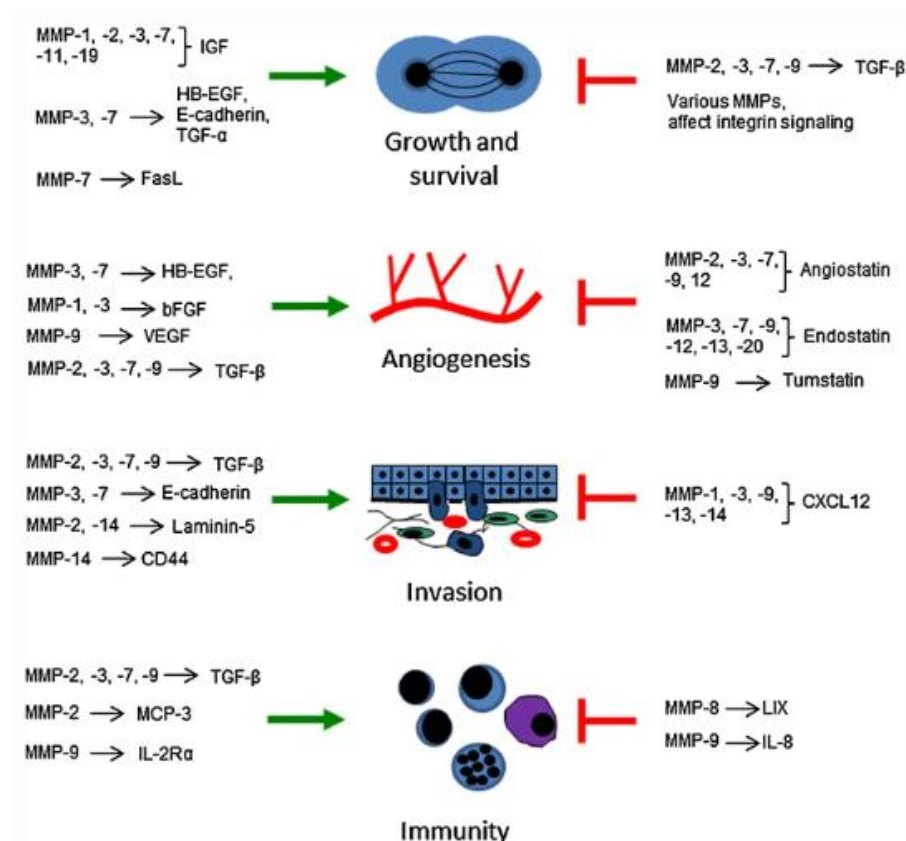


**Figure 1.6:** Roles of MMPs in cancer progression *(Reproduced with permission from Springer Nature).* [185]

Despite the large amount of research in this field, it is difficult to draw solid conclusions about the significance of certain MMPs or their inhibitors in various cancer types since the data are frequently inconsistent. There are several facts that might explain those differences. MMPs are multifunctional enzymes and each enzyme's activity depends on the substrates it works on in a particular biological milieu. Therefore, this may vary across individuals, between organs, and between various stages of cancer onset and progression. It is also challenging to compare findings due to variations in study design. For example, while some studies examine MMP or TIMP expression in tissue samples or tissue extracts, other investigations evaluate the amount of MMPs or TIMPs in blood or urine. While

some estimate overall expression at the transcriptional or protein level, others measure enzyme activity. [185]

MMP-1, MMP-2, MMP-7, MMP-12, MMP-13, and MMP-26 levels have been observed to be elevated in lung cancer patients' tissues. [191-194] A higher risk of metastases and lower survival rates have been linked to high levels of MMP-1 in blood or cancer tissue. Strong immunohistochemical staining for MMP-2 in tumour tissue was found to be a strong predictor of poorer patient survival, according to a systematic meta-analysis of published articles about the relationship between MMP-2 and overall survival in 1,439 patients with NSCLC. [195] There are conflicting reports about the predictive significance of MMP-9 in cancer tissue or blood. Whereas high MMP-9 expression has been linked to a bad prognosis in certain studies, others claim that it has little predictive significance. Nevertheless, a published meta-analysis of ~ 2000 NSCLC cases from 17 different studies [196] reported that patients with positive immunohistochemistry staining for MMP-9 had lower survival rates than patients with negative staining for MMP-9 in the tumours. Strong MMP-7 immunohistochemistry staining in the tumour was strongly linked to a poorer overall survival in NSCLC patients, [197, 198] in contrast to prior research that showed no correlation. [199] With regards to TIMP levels, two different studies from a group at the University of Oulu in Finland revealed contradictory findings; a first study found that high levels of the MMP inhibitor TIMP-1 in the serum of cancer patients were connected to a poor survival, [200] whether in a second study it was found that strong immunohistochemical TIMP-1 staining in tumour tissue was associated with a good prognosis albeit not statistically significant. [185, 201]

The MMPs implicated in lung cancer development and progression are summarised below and in **table 1.4**: [186]

- **MMP-1** is an interstitial collagenase that breaks down collagen types I, II, and III. It is frequently associated to the metastatic tendencies of malignant cell lines in lung cancer, and it is modulated by a variety of factors in lung tissue. There is one study that demonstrates that its elevated expression in pulmonary epithelial cells and skin fibroblasts is associated to tobacco smoking [202] and its expression is frequently increased in tumour metastasis related to lung cancer. [203, 204]

34

- **MMP-2** is crucial for the progression of cancer since it cleaves a number of ECM and basement membrane components. [205] MMP-2 is also involved in tumour growth and angiogenesis. [206] Its activation in metastatic areas stimulates secondary growth and cell preservation. [207] A study by Nawrocki B. *et al.*, [208] demonstrated that MMP-2 expression is predominantly restricted to fibroblasts in NSCLC, specifically in the cytoplasm. It is understood from past studies that specific receptors interact with MMP-2 on the surface of cancer cells, and this shows that cancer cells and fibroblasts work together to degrade the ECM through MMP-2.

- **MMP-7** is the smallest known member of the MMP family, sometimes referred to as matrilysin. It is highly specific for ECM components such as proteoglycans, aggrecan, vitronectin, fibronectin, type IV collagen, and elastin. Although initial research indicated that MMP-7-expressing cancers were invading and metastasizing by proteolytically destroying the ECM, most recent studies showed that this MMP also modifies other members of the family as well as non-ECM molecules involved in growth, invasion, apoptosis, and angiogenesis, suggesting that MMP-7 is implicated in many additional biological processes connected to tumour behaviour. [209] MMP-7 expression and tumour growth are significantly correlated in NSCLCs; their expression is critical in the regulation of tumour proliferation. [186]

- **MMP-9** is a gelatinase which breaks down gelatine and different ECM molecules like aggrecan core protein, collagens, laminin, etc. It is closely connected to lung cancer's ability to metastasize. Its expression levels had a strong correlation with NSCLC metastases and a lower 5-year survival rate, as highlighted by Zheng S. *et al.,* [210] In a 2014 study [211] it was discovered that MMP-9 levels were higher in the tissues and serum of patients with NSCLC than SCLC, and these enzymes also promote tumour growth. Another finding from the same study was that MMP-9 expression levels were greater in advanced lung carcinoma stages III and IV compared to primary stages I and II.

- **MMP-12** is an elastolytic enzyme secreted by inflammatory macrophages. The data available in the literature in relation to MMP-12 are contradictory.

In fact, although MMP-12 has been strongly associated with NSCLC recurrence and metastatic disease, there are studies that suggest that MMP-12 may have a protective role. For example, the study by Houghton A.M. *et al.*, [212] demonstrated that MMP-12-deficient mice had more Lewis lung cancer pulmonary metastases than their wild-type counterparts in both spontaneous and experimental metastasis models, indicating that MMP-12 has tumour-suppressing properties. MMP-12 has also been related to a decrease in the density of tumour-associated micro-vessels *in vivo* and to an inhibition of blood vessel development in the tumour microenvironment preventing the development of lung tumours regardless of angiostatin synthesis. Furthermore, MMP-12 deficiency has been also associated to tumour growth. Therefore, the results from these studies show that MMP-12 actively prevents the development of lung metastases. [212, 213] On the other hand, greater MMP-12 levels have been associated with a more advanced pathological stage and lymph node metastases in individuals with lung adenocarcinoma (LAC). [214] Various findings indicate that MMP-12 is an oncogenic molecule that facilitates LAC development through inflammation. [215] MMP-12 overexpression in NSCLC has also been observed, providing more evidence to its role in the formation and advancement of the disease. Indeed, it has been reported that there is a strong association between MMP-12 expression, local recurrence, and metastatic illnesses in NSCLC patients. [214, 216] Most likely the tumour type is probably a determining factor in whether MMP-12 expression has a favourable or negative impact.

- **MMP-13** exerts its proteolytic activity on a wide variety of substrates increasing the potential for cancer cells to invade nearby tissues and cause metastatic illness. [217] MMP-13 upregulation has been linked to invasion and metastasis in lung cancer. [218] In a study of NSCLC patients, MMP-13 was present in more than 60% of tumour tissue samples and the metastatic status of patients was found to be linked with MMP-13 expression level. [219]

- **MMP-26** is widely expressed in cancer cells derived from epithelial tissue. It is well recognized to aid in tissue growth and restoration following injury. MMP-26 promotes A549 cell invasion and migration *in vitro* in part by

coordinating with MMP-9. [220] MMP-26 has been associated with NSCLC prognosis, clinical stage, lymph node metastasis, and carcinogenesis.

**Table 1.4:** MMPs involved in lung cancer development and progression *(Adapted with permission from "Oxford University Press").* [186]

| MMPs | Biological functions | Signalling pathway/substrates | Stromal cell expression |
|---|---|---|---|
| MMP-1 | Induces cell migration and invasion and reduces proliferation | ECM (collagen) regulates polarization of Th1/ Th2 inflammatory response | Macrophages, fibroblast, dendritic cells |
| MMP-2 | ECM disassembly, increases cell proliferation, invasion/migration, and angiogenesis | Springolipid and Ephrin receptor-signalling pathway (ET-1) | Macrophages, mast cells, endothelial cells, fibroblast, dendritic cells, HPCs |
| MMP-7 | Apoptosis, tumour invasion and metastasis | N-cadherin | Macrophages, endothelial cells, and tumour cells |
| MMP-9 | ECM remodelling, increases cell proliferation, invasion/migration, and angiogenesis | N-cadherin, VSMC-ECM attachment | Neutrophils, HPCs, macrophages, lymphocytes, mast cells, fibroblast, dendritic cells, |
| MMP-12 | Tumour suppressor, ECM remodelling, increases epithelial cell proliferation involved in wound healing | IGF-2, VEGF-B and VEGF-D-signalling pathways | Macrophages |
| MMP-13 | Promotes tumour angiogenesis, ECM disassembly, bone mineralization and morphogenesis | p38, JNK and NF-κB pathways | Fibroblast |
| MMP-26 | Collagen catabolic process, decreases inflammatory response and proteolysis | — | — |

## 1.3.2 Types of nanocarriers

Nanotherapeutics have received a lot of attention in recent years due to their capacity to be employed as effective drug delivery systems with fewer undesired side effects. As previously mentioned, and unlike conventional medicines, nanomaterials may be specifically engineered to target affected areas (tumours) and release their load in a controlled manner. Different materials (**Fig. 1.7**) have been developed in order to achieve both spatial and temporal effective release of the cargo at the therapeutic target. Many DDSs have revolutionized therapies for conditions like cancer and infections and have been approved and are already commercially available (**Table 1.5**). [221-225]
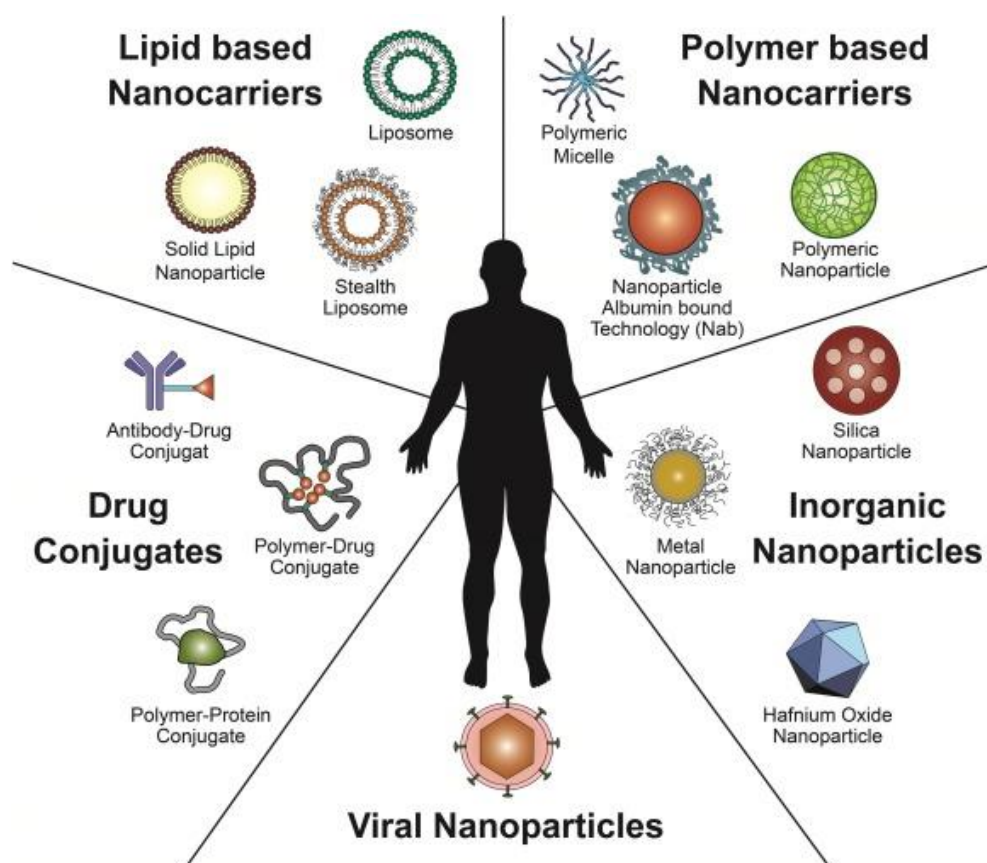


**Figure 1.7:** Different types of nanocarriers. *(Reprinted with permission from Elsevier)* [97]

Nanocarriers can be classified into three major types: [92, 102, 226-231]

- Organic (i.e., liposomes, micelles, polymeric NPs, solid lipid nanocarriers, dendrimers, virus-based NPs, vesicles).

  * <u>Liposomes</u> are vesicles composed of phospholipids, similar to the composition of cell membranes, the first to have been investigated as drug carriers. Phospholipids consist of a hydrophilic head group and a hydrophobic tail group. Liposomes are formed when phospholipids self-assemble into closed, spherical structures with an aqueous core. The liposome structure consists of a lipid bilayer, with the hydrophilic heads facing the aqueous environment both inside and outside the vesicle, while the hydrophobic tails are in the middle. In the presence of a monolayer structures, we talk about <u>micelles</u>. The advantages of liposomes include their ability to encapsulate a wide range of both hydrophilic and hydrophobic agents and a relatively large internal volume, allowing for a higher drug payload per particle compared to other drug delivery systems. The main drawbacks from using liposomes are the relatively high production cost, the premature release of encapsulated drugs or molecules due lower stability causing leakage or fusion, degradation of the liposomal structure and compromised drug encapsulation caused by lipid oxidation and hydrolysis, and rapid clearance from the blood. [232, 233]

  * First generation <u>solid lipid nanoparticles</u> (SLNs) are made from solid lipids. They offer a number of advantages as drug delivery systems such as their ability to protect drugs from harsh environmental conditions, their biocompatibility, good stability, and biodegradability. In addition, their production can be easily scaled up, making them suitable for large-scale manufacturing. However, they present drawbacks such as a low drug loading efficiency and an increased risk of drug release due to possible crystallization under storage conditions. On top of that, an initial burst release, which frequently happens with these formulations, is another possible disadvantage. These issues were avoided or mitigated by the development of a new generation of lipid NPs known as <u>nanostructured</u>

lipid carriers (NLCs), which combine a solid lipid with a liquid lipid. [234, 235]

* Polymeric nanoparticles are solid colloidal particles composed of polymers derived from natural, synthetic, or semi-synthetic sources, and these polymers can be either biodegradable or non-biodegradable. The advantages presented by these DDSs include their higher surface area than other organic nanocarriers, which allows for a better functionalization, the smaller size (diameter ranging from 10 to 100 nm) which allows them to easily navigate through smaller capillaries and reach target cells or tissues, the possibility to control over their size and size distribution, an extended circulation time, and a high drug loading capacity. On the other hand, the disadvantages presented by these nanocarriers include the toxicity of residuals preparation agents and the scaling up their production can be challenging and costly. [236, 237]

* Dendrimers are a type of synthetic polymers known for their unique branched structure. They are characterized by repeating units (dendrons, or dendrimer arms consisting in layers of monomer molecules) that extend from a central focal point (a single atom or molecule called the core), giving them a tree-like or dendritic appearance. One of the distinguishing features of dendrimers is the presence of a large number of terminal functionalities on their surface. Surface functional groups influence dendrimer biocompatibility and physicochemical characteristics. Dendrimers' molecular diameter of 10 nm and less, plus their globular structure allows them to be used for biomimics since they can closely resemble the size and shape of specific proteins and biomolecules. The functional groups at their periphery offer opportunities for the attachment of various molecules, enhancing their interactions with biological targets. The hydrophobic or hydrophilic cavities within their interior can serve as host environments for encapsulating guest molecules. Dendrimers exhibit low polydispersity, which assures consistency and reproducibility in their properties. Despite their potential benefits, dendrimers as drug delivery carriers still face certain challenges that need to be addressed. Two critical factors

influencing their properties are size and surface chemistry, which are closely related to their toxicity and biodistribution: the main issue is size restriction, since smaller dendrimers (generation 5 and below) can be eliminated by glomerular filtration in the renal excretion pathway, while bigger ones (generation 6 and above) go through hepatic clearance pathways; dendrimers with diameter between 4 and 10 nm can interact better with nanometric cellular components and bypass the cellular endocytosis barrier, however their production is very costly and extremely toxic, which limit their usage. The internalization in cells is facilitated by the strong binding ability of cationic dendrimers, but non-specific plasma protein adsorptions and reticuloendothelial system-accelerated elimination are frequent problems for these types of dendrimers. Moreover, cationic dendrimers typically display increased toxicity, especially when they interact with negatively charged cell membranes, which can promote biological membrane instability and ultimately cause cell lysis. [238-240]

- Inorganic (i.e., carbon nanotubes, MSNs (MSNs), gold, iron oxide, silver, graphene).

  * Carbon nanomaterials employed as DDSs are classified in nanotubes (CNTs) and nanohorns (CNHs). Carbon nanoparticles (CNPs) possess a variety of remarkable properties: they exhibit high stability which allows them to withstand harsh environments and maintain their structural integrity, they possess excellent electrical conductivity, they exhibit exceptional mechanical properties, including extreme stiffness, strength, and toughness. CNPs are widely used in a wide range of sectors, including electronics, agriculture, food, pharmaceuticals, cosmetics, and medicine. The disadvantages of these type of DDSs include their potential cytotoxicity and genotoxicity towards different tissues and systems. Contaminants such as residual metal and amorphous carbon, used during the synthetic process, can result in the rise of the amount of reactive oxygen species (ROS), generating oxidative stress in cells. [241] It has been reported that both asbestos and

CNTs have a comparable propensity to cause cancer. [242, 243] CNTs have been demonstrated to alter cell shape and induce necrosis or apoptosis in macrophage cell lines. [244] In another study, [245] which examined platelets aggregation, platelets aggregation was reported after incubation with CNPs. [246, 247]

* Magnetic nanoparticles (MNPs) possess a wide range of characteristics that make them incredibly attractive drug delivery vehicles. These include the possibility to be manipulated and guided to specific locations within the body using an external magnetic field, the potential for passive and active drug delivery strategies, the possibility to be used in Magnetic Resonance Imaging (MRI), and they can be designed to have optimal size, surface properties, and functionalization to enhance their uptake by the target tissue. However, MNPs present two important limitations as DDSs: they have the tendency to aggregate, especially in physiological environments, which can lead to the formation of larger clusters, resulting in a loss of the unique properties associated with their small dimensions. Moreover, while an external magnetic field can guide MNPs towards the target site, the magnetic force may not always be strong enough to overcome the forces exerted by blood flow or other physiological factors, resulting in limited accumulation at the desired target site. [92]

Both organic and inorganic NPs have been widely studied for their application in biomedicine. [224]

• Hybrid materials combine the advantages of organic and inorganic materials, and for example the coating of inorganic NPs with organic functionalities has been used to enhance the selectivity and efficiency of antitumor agents (i.e., surface coating of NPs with polymers).

**Table 1.5:** List of some marketed products containing NPs. [224]

| Marketed Product | Formulation | Drug | Use | Reference |
|---|---|---|---|---|
| **AmiBisome®** | Liposome | Amphotericin B | Antifungal | [248] |
| **DaunoXome®** | Liposome | Daunorubicin | Kaposi's sarcoma associated with HIV | [249] |
| **Doxil®** | Liposome | Doxorubicin | Kaposi's sarcoma associated with HIV, breast cancer, ovarian cancer | [250] |
| **Myocet®** | Liposome | Doxorubicin | Kaposi's sarcoma associated with HIV, breast cancer, ovarian cancer | [251] |
| **Emend®** | Nanocrystals | Aprepitant | Antiemetic | [252] |
| **Megace ES®** | Nanocrystals | Megestrol acetate | Anorexia | [252] |
| **Tricor®** | Nanocrystals | Fenofibrate | In hypercholesterolemia | [252] |

Despite the efforts invested in the design of chemotherapeutic agents and their formulation in NPs, hardly any improvement has been translated into benefit for patients' survival. The nanomedicines that are currently approved for clinical

use are mainly successful in terms of improved bioavailability and tolerability. However, there is an urgent need for DDSs with a better targeting ability in order to treat cancer and prevent relapse and to suppress adverse/toxic side effects of chemotherapeutic agents. The optimal design and application of DDSs have become more important in the past few years due to the increased awareness of the importance of biodistribution and pharmacokinetics of drugs already available for cancer treatment. [75, 253, 254]

### 1.3.3  Mesoporous Silica Nanoparticles (MSNs)

The synthesis of MSNs constitutes an attractive approach for the creation of novel nanocarriers for the delivery of therapeutic agents aiming to cure many pathologies, like cancer. This is mainly due to its extensive multi-functionality, based on its high specific surface area, homogeneous and tuneable pore size, large pore volume, and easy functionalization. [225, 255]

**Fig. 1.8** shows the pore size distribution of some porous materials. The International Union of Pure and Applied Chemistry (IUPAC) has adopted the Greek prefix μέσο ("meso" which means in between) to define the porous materials with pore size between 2 and 50 nm. [256, 257]
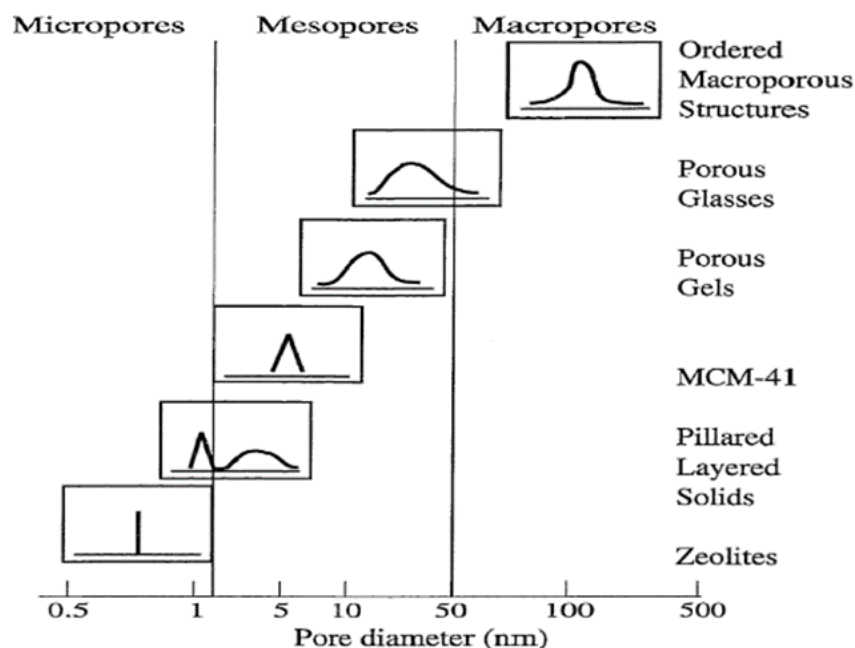
**Figure 1.8:** The pore size distribution of some porous materials. *(Reprinted from an open access article)* [256]

Researchers at Mobil Research and Development Corporation were the first to synthesize mesoporous solids, highly ordered, pure inorganic, porous silica phases (referred to as the M41S family, the generic term for the various types of mobile composition of matter (MCM) materials) from alumina-silicate gels using a liquid crystal template mechanism in 1992. The templating process consisted in the use of a self-assembled molecular array (usually organic), which acted as a structure directing agent (SDA), for the inorganic silica precursor to condense around it building the network via formation of siloxane bonds in a skin-tight manner, so that when removing the templating structure its geometric characteristics were replicated by the inorganic materials. [224, 256, 258, 259]

As shown in **Fig. 1.9** MSNs can be classified in three groups [260, 261]:

- M41S type MSNs family: the first reported ordered porous materials with a regular arrangement of pores that exhibit a high degree of uniformity, in the size range 2nm < dp < 50nm (as per IUPAC). [224, 256, 262-264] The application of MSNs in drug delivery systems started with the discovery of these materials. [265]

- Organically modified silica (ORMOSIL) nanoparticles: organic/inorganic hybrid materials created by incorporating organic functional groups into the

45

silica matrix, which allows for the combination of the unique properties of both organic and inorganic materials. Their average diameter can vary from as small as 15 nm to as large as 80 nm; this size modulation can be achieved by adjusting the composition of the microemulsion during the synthesis process. Furthermore, these NPs exhibit a high degree of mono-dispersity. [266, 267]

- Hollow type MSNs (HMSN): MSNs which present a hollow (empty space/hole) core and a mesoporous shell, and a higher drug loading capacity (>1g drug / g silica). HMSNs are further categorised in hard-template MSNs, soft-template MSNs, and self-template MSNs based on the manufacturing methods used. [268, 269]
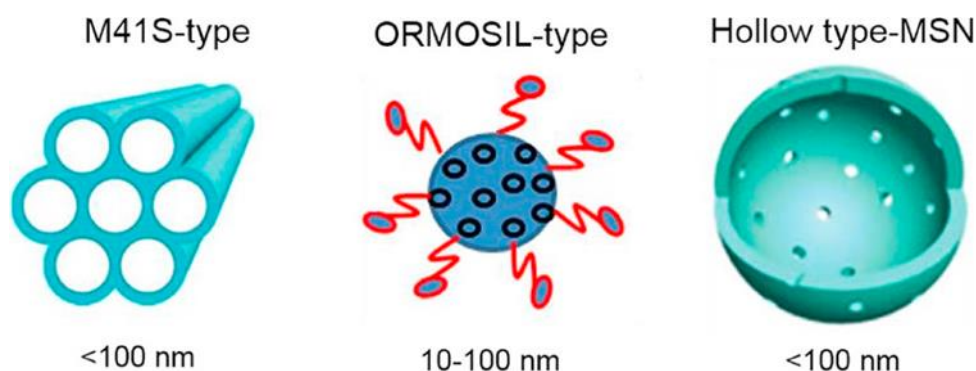


**Figure 1.9:** Three groups of MSNs with their mean particle size range *(Reprinted with permission from Elsevier).* [260]

The three most important and known MCM (**Fig. 1.10**) are [260, 270]:

- MCM-41, with hexagonal pore arrangement (the pores are uniform, unidirectional, and arranged in a honeycomb structure).

- MCM-48, with cubic pore arrangement (this type of MSNs present a very high surface area up to 1600 $m^2$/g and it features an interlaced and branching pore structure, which improves heat stability).

- MCM-50, with lamellar pore arrangement (made up of layers of silicate or porous aluminosilicate that are separated by layers of surfactant. In the production of various mesoporous solids like silica galleries, which have a

variety of biological uses, MCM-50 NPs are utilized as catalysts and sorbents).

These different types of structures can be obtained by modifying the synthesis conditions such as the templates, the silica sources, the use of auxiliary chemicals like swelling agents, or by the modification of the reaction conditions such as the pH of the medium, the solvent used and/or the reactants mole ratio. [256]



**Figure 1.10:** Various types of MCM. [256]

After the introduction of the M41S family of ordered mesoporous silicas, there has been a considerable growth in the synthesis of advanced mesoporous materials, and in the research interest of the biomedical applications of MSNs. These DDSs feature a unique mesoporous structure and a large surface area, which contributes to their diverse uses in bio-catalysis, biosensors, and disease diagnosis and therapy. [114, 261, 271-273]

The many advantages offered by MSNs are:

- Their large surface area (700-1000 m²/g) and pore volume (0.6-1 cm³/g), that allows efficient encapsulation and high loading capacity of therapeutic agents.

- Their tuneable particle size (50-300 nm) and morphology (spheres, rods), both important features for achieving passive targeting as they can allow MSNs to escape renal clearance and to diffuse through the tumour interstitium, and which gives them versatility for different medical applications.

- The presence of two tuneable functional surfaces: the inner one in the pore channels and the outer one on the particles surface, allowing selective

functionalisation to enhance adsorption, targeting, controlled release and bioavailability while minimizing adverse effects, attaining the goal of precision therapy and increased effectiveness.

- Their uniform porous structure and tuneable pore size (2-6 nm), allowing the loading of different therapeutic agents (both hydrophobic and hydrophilic), highly precise drug release kinetics, and preventing a premature release even when the pores are not fully capped.

- That they are quickly endocytosed by numerous mammalian cells, which allows their use as delivery tools of bioactive compounds.

- That they are biocompatible (up to 200 mg/kg) and hemocompatible. [93, 114, 231, 260, 273-277]

MSNs have been investigated as efficient drug delivery systems for a number of therapeutic agents to battle many types of illnesses, such as cancer, diabetes, inflammation, and bone/tendon tissue engineering. Compared to traditional drug delivery technologies like polymer NPs and liposomes, they are more versatile, robust, and flexible. The uneven distribution of the drug throughout the matrix, a limited drug loading capacity, a low yield, and a high cost of manufacture are believed to be significant drawbacks of typical organic nanocarriers.

MSNs, however, are excellent guest molecule reservoirs due to their unique mesoporous structure and high specific surface area, which also allows them to release the loaded molecules under physiological conditions and in a sustained way when functionalised. Their long-range organized pore structure with adjustable pore size and geometry makes also possible to incorporate guest molecules of all shapes and sizes uniformly. [114, 231, 274, 278]

MSNs fabrication is also straightforward, scalable, cost-effective, and controlled. Because it is common in nature, silica is highly compatible and considered "Generally Recognized As Safe" (GRAS) by the FDA. They are used in cosmetics, as FDA-approved food additives, and as excipients in drug tablet formulations. [114, 115]

48

Precise control over particle size, shape, pore size, and pore geometry are crucial for biomedical applications. The type of surfactant templates has a major role in determining the pore size and its orientation; by adjusting the molar ratio of silica precursors and surfactants, controlling the pH with base catalysts, adding co-solvents or organic swelling agents, and adding organo-alkoxysilane precursors during the co-condensation reaction, the particle size and morphology can be tailored to have sphere-, rod-, or wormlike structures. [114]

MCM-41 is the most studied material due to its stability, compared to the rest of the mesophases in the family, and to its easy synthetic route. Today, monodispersed silica NPs are produced using the Stöber method [261, 279], also known as the sol-gel approach, which allows for highly controllable MCM-41 synthesis. It is possible to create multiple structures using different solution compositions (i.e., templates used, the addition of auxiliary organic compounds), concentrations, and temperatures since these NPs' physical configurations are quite controllable. Changes in the synthesis parameters affect the structure of the material at several levels, including changes in the material's size, surface area (up to 1200 $m^2$/g), and pore size. [260]

## 1.3.3.1  Applications of MSNs

As mentioned before, Mobil Company achieved the first surfactant-assisted synthesis of MCM-41 mesoporous silica (Mobil Composition of Matter No. 41) back in 1992, but it wasn't until 2001 when MCM-41 was investigated for its use in biological applications as a drug release matrix. Vallet-Regi M. *et al.,* [272] demonstrated that MCM-41 could host the anti-inflammatory drug ibuprofen, and that its molecules could diffuse out of the pores when the particles were immersed into a simulated body fluid. Numerous investigations and approaches involving the use of MSNs have been carried out since these initial reports, including enhanced MSNs' synthesis, the introduction of multifunctionality, and *in vitro/in vivo* studies (**Fig. 1.11**). [225, 280]
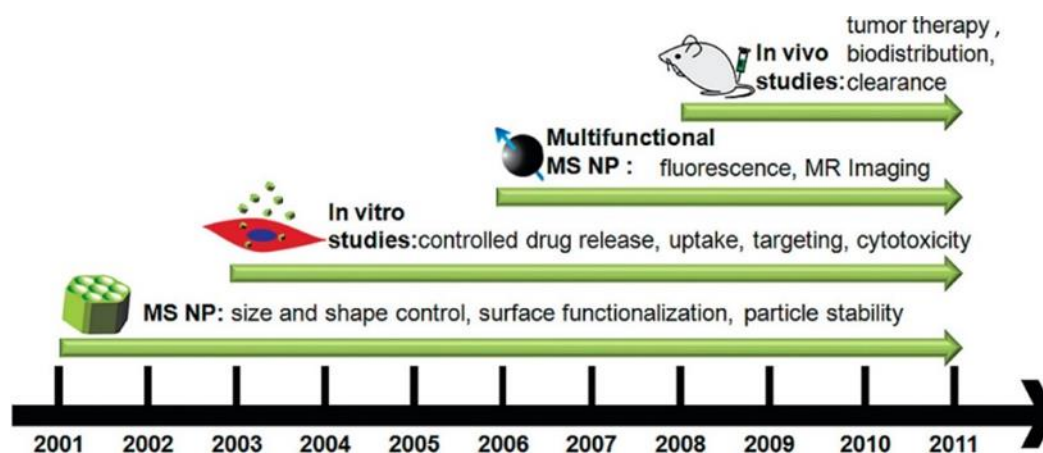
**Figure 1.11:** Temporal MSN NPs development towards bio applications (*Reprinted with permission from J. Phys. Chem. Lett. 2012, 3, 3, 364-374. Copyright 2012 American Chemical Society*). [280]

MSNs have been employed to deliver several pharmaceutical agents, like ibuprofen, doxorubicin, camptothecin, cisplatin, and alendronate, to mention some, which present different hydrophobic/hydrophilic features, molecular weights, and biomedical effects. Mellaerts R. and colleagues in their work [281] assessed the effectiveness of MSNs as a drug carrier for compounds with low water solubility *in vivo*, choosing the drug itraconazole (a drug with known poor intestinal solubility which is the cause of its poor bioavailability) as the model compound assessing its bioavailability as compared with the free crystalline drug and the marketed product Sporanox®. They showed that no systemic itraconazole could be found in dogs after receiving 20 mg of crystalline itraconazole; on the other hand, MSNs increased the $AUC_{0-8}$ to 681±566 nM h. When 8 mg of crystalline itraconazole was loaded into MSNs, the $AUC_{0-24}$ in rabbits considerably rose from 521±159 nM h to 1069±278 nM h following oral administration. In both, rabbits and dogs, the oral bioavailability of itraconazole loaded in MSNs compared to that of Sporanox®. In light of these results, the group concluded that MSNs could be seen as a viable carrier to increase oral bioavailability for medications with poor water solubility. [114]

MSNs have been shown to be also optimal carriers for peptide and protein drugs as powerful therapeutic agents for the treatment of cancer, for immunization, and regenerative medicine, by protecting them from premature degradation. One example comes from the work of Slowing I.I. and co-workers [282] where they

demonstrated the ability of MSNs to deliver the membrane impermeable protein cytochrome C into HeLa cells (immortalized human cervical cancer cells), and also that the enzymes released from MSNs were still able to exert its function. [114]

Non-viral gene delivery techniques are significantly safer and less immunogenic than viral carriers, and MSNs are thought to be attractive candidates for very effective gene delivery. Nucleic acids that are firmly concealed in the mesopores can avoid nuclease destruction during delivery. The well-established surface chemistry makes it simple to modify the surface of MSNs with polycations in order to increase the loading capacity of negatively charged nuclei acids. In their work Xia T. *et al.*, [227] modified the surface of MSNs by the noncovalent attachment of polyethyleneimine (PEI) polymers generating a positively charged surface which allowed the attachment of DNA and siRNA constructs, as well as increasing the cellular uptake. Another example was brought by Li X. *et al.*, [283] who were able to load DNA directly into the structure of MSNs without modifying the surface of the NPs. They synthesised magnetic MSNs (M-MSNs) which presented the typical mesoporous silica shell, but with an inner core of $Fe_3O_4$. The authors hypothesize that intermolecular hydrogen bonds rather than electrostatic interactions served as the primary driving factors for DNA adsorption inside mesopores. In another work from the same group [284] it was demonstrated that siRNA could also be loaded into the mesopores of magnetic silica NPs. PEI was then combined with the siRNA-loaded M-MSNs to create a polymer coating on their outside and protect the siRNA from enzymatic degradation. The encapsulated siRNA molecules were efficiently released from the mesopores and effectively knocked down target genes after being successfully internalized by cultured cells. Other groups, by optimizing a few parameters during the synthesis of MSNs, were able to obtain NPs with larger pores in order to encapsulate DNA molecules. For instance, Gao F and colleagues [285] obtained MSNs with large pore entrance (17nm) and cavities size (up to 20nm), and after surface modification with aminopropyl groups the DNA encapsulation was higher than other silica based materials reported in literature. Kim M.-H. *et al.*, [286] in their work reported the synthesis of MSNs with pore size of around 15nm able to deliver DNA to human cells. They demonstrated that aminated monodisperse MSN with wider pores had a better plasmid loading capacity than those with

smaller pores (2 nm), and the combination of MSN with plasmid DNA easily entered cells without the need of additional polymers such as cationic dendrimers. [114]

Combination treatment, which consists in combining two or more therapeutic agents in order to provide a complementary or synergistic effect, has been used to treat a wide range of conditions, including cancer. MSNs have been shown to be useful co-delivery systems due to their tuneable pore size, that allows the loading of multiple guest molecules, as they provide both the inner pores as well as the outside particle surface, which is very helpful for managing the release order of various cargos. Zhao Y. with colleagues [287] synthesized a double glucose-responsive MSN-based delivery system to deliver both cAMP and insulin. The cAMP molecules were loaded inside MSNs pores capped with gluconic acid-modified insulin (G-Ins) proteins. They demonstrated that, in the presence of saccharides like glucose, a triggered release of G-Ins and cAMP molecules from MSN was obtained. Another example of co-delivery has been reported by Chen A.M. and colleagues [288] who delivered doxorubicin (DOX) and Bcl-2-targeted siRNA into multidrug resistant A2780/AD human ovarian cancer cells using MSN. They demonstrated that it was possible to effectively silence Bcl-2 mRNA and substantially lower the non-pump resistance, boosting DOX's anticancer activity. [114]

In 2003 Lai *et al.* [134] demonstrated the first modified MSNs to enable stimuli-responsive regulated release of neurotransmitters and pharmaceuticals by using cadmium sulphide (CdS) nanocrystals as chemically removable caps. Since then, scientists have looked at combining different elements to provide a variety of diagnostic or therapeutic effects, such as controlled drug release, cell labelling, and targeting. [225, 280]

In 2006 two different groups developed, and independently reported, multifunctional MSNs with imaging capabilities. Kim J. *et al.,* [289] developed mesoporous silica that were embedded with magnetite nanocrystals and quantum dots and Lin Y.-S. *et al.,* [290] synthesised superparamagnetic nanocrystals which were coated with a silica shell. During the synthesis process they also incorporated organic dyes into the mesoporous silica framework by the co-condensation

method, obtaining magnetic core−shell NPs which exhibited magnetic, luminescent, and porous qualities all at the same time. [225, 280]

In an effort to advance MSNs toward therapeutic applications, researchers began examining their *in vivo* behaviour in 2008, including biodistribution, clearance, toxicity, and tumour treatment. [291-297] Before their potential clinical application, numerous significant challenges must be addressed. For instance, when MSNs are administered intravenously, their effective diameter and surface characteristics will largely determine the biodistribution and blood circulation times: large NPs (> 100 nm in diameter) or aggregated NPs are known to be quickly captured by RES, reducing their *in vivo* effectiveness. The same RES uptake is also possible as a result of non-specific protein adsorption to the NPs outer surface, which can cause an increase in their effective diameter. Additionally, it is possible that the population of adsorbed proteins could affect the NPs cellular absorption and destiny. Consequently, controlling the size and stability of the NPs under pertinent biological settings requires substantial effort. [225, 280]


1.3.3.2 Interaction of Mesoporous Silica Nanocarriers with biological systems


The definition of "biocompatibility" was stated in 1986 as "the capacity of a material to operate with an adequate host response in a specific application" during a consensus conference of the European Society for Biomaterials. The concept of "biocompatibility" has expanded significantly since then with the quick development of biomaterials. [114]

One of the main concerns regarding the use of MSNs, or nanomaterials in general, for human applications is related to how and whether nanoscale materials may affect different biological functions and therefore exert any toxic effects. In fact, particles should effectively fulfil the required function(s) while avoiding non-specific and harmful effects in order to be used for *in vivo* biomedical applications. The interaction of MSNs with biological systems through a variety of complex mechanisms, such as membrane peroxidation, GSH depletion, mitochondrial

malfunction, and/or DNA damage, might indeed result in intracellular damages that have the potential to induce cytotoxic effects. [114, 298]

For more than a century, the toxicity of silicon dioxide, both crystalline and amorphous, has been studied, particularly due to the development of silicosis, a form of pulmonary fibrosis, induced by their inhalation. The mechanism(s) through which silica exposure causes silicosis remains unknown, and literature findings are occasionally conflicting, despite the many investigations on the toxicity of amorphous and crystalline silicas. The toxicity of silica NPs has been therefore thoroughly investigated because the high surface to volume ratio of NPs may result in enhanced cellular interactions and different pathways of toxicity compared to coarse-grained silica. It is worth mentioning that depending on the processing conditions and environmental exposure, the amorphous silica framework and surface chemistry (hydroxyl coverage and the size and distribution of siloxane rings that compose the framework structure) can result in a broad range of configurations. As a result, information on the toxicity of MSNs and amorphous silica in general has been largely inconsistent. However, there is a general agreement that toxicity is associated in part with surface silanol ($\equiv$SiOH) groups, which can hydrogen bond to membrane components or, when dissociated to form SiO$^-$, interact electrostatically with the positively charged phospholipids containing tetraalkylammonium, leading to strong interactions and possibly membranolysis. [299]

It has been demonstrated that the physicochemical characteristics of nanomaterials, such as particle size, shape, surface area, and porous structure, play also crucial roles in the particles' biocompatibility and bio translocation. The establishment of a connection between these features and biocompatibility can be of aid in the rational design of nanomaterials. [114]

In a review from 2010, Fadeel B. and A.E. Garcia-Bennett [300] reported that studies on the toxicology of mesoporous silica materials were scarce and challenging to compare due to differences in the synthesis methods described among the studies. In a detailed review article on the synthesis, biocompatibility, and drug delivery of MSNs, Chen and colleagues [114] discussed the discrepancies in the biocompatibility results of different studies; they identified four potential

54

explanations for these conflicting results, including variations in physicochemical parameters, aggregation of MSNs in the bloodstream, ranges of particle size, shape, and dose chosen for evaluations did not coincide among studies. [115]

The discrepancies in the findings of different research might be due to a number of factors:

- it is critical to fix the physicochemical parameters in order to get a meaningful conclusion; this was not adequately examined in several studies.

- Blood serum proteins adsorbed on the surface of the NPs may cause them to agglomerate once they have entered the body. Another factor that can cause agglomeration of the NPs is surfactant template removal by either solvent extraction or heat calcination. Therefore, the primary particle size and shape may no longer be useful tuning features for NPs biocompatibility.

- There is a chance that separate studies will not match in the range of particle size, shape, and dosage chosen for examination.

- The *in vivo* bio translocation process of NPs is so complex that the existing assessment level and technique are incapable of identifying all of the alterations triggered by nanomaterials. [114]

### 1.3.3.2.1 Effect of size

The size of the particles might have an impact on the biological parameters such as distribution, duration in blood circulation, or elimination rate. However, the precise relation between particle size and possible toxicological consequences of nanomaterials, particularly MSNs, is still not fully understood. [225]

Two different ideas concerning the size influence on biocompatibility have emerged as a result of growing knowledge: one school of thought holds that one of the most crucial factors affecting nanomaterial's biocompatibility is its particle size, whereas other school of thought believes that size has little significance. [114, 301]

Lu F. *et al.*, [302] investigated how particle size affected the uptake of MSNs by HeLa cells. They concluded that the degree of cellular uptake is size-dependent

in the following order: 50 nm > 30 nm > 110 nm > 280 nm > 170 nm, with the cellular uptake of 50-nm NPs being approximately 2.5 times higher than that of 30-nm particles. This outcome is in line with the trend from studies with different NPs, [303, 304] which demonstrated that cellular uptake of 50-nm particles was the highest. [114]

A study from He Q. *et al.*, [305] on the cytotoxicity of spherical MSNs with particle sizes of 190, 420, and 1220 nm to human breast-cancer cells (MDA-MB-468 cells) and African green monkey kidney cells (COS-7 cells), discovered a strong correlation between the cytotoxicity and particle sizes. At doses higher than 25 mg/mL, 190-nm and 420-nm MSNs exhibited notable cytotoxicity, but microscale particles with a diameter of 1220 nm exhibited very modest cytotoxicity because of reduced endocytosis. [114]

Lin Y.-S. and C.L. Haynes [306] investigated the effect of both nonporous and porous silica particles' size in red blood cells (RBSs). The findings demonstrated that red blood cell membrane damage is size- and concentration-dependent for both nonporous and porous silica. The size-dependent haemolysis effect in the case of MSNs only appeared when the NPs exhibited long-range ordered porous structure, demonstrating the importance of pore structure in cell-NPs interactions. Overall, MSN showed less haemolytic activity than their nonporous counterparts of comparable size. The explanation to these results is most likely owing to the fact that porous silica NPs present less silanol groups that can interact with cells. It was observed that as the pore structure is impaired by moderate aging in phosphate-buffered solutions, the degree of haemolysis by MSNs rose. These *in vitro* findings have however not been supported by *in vivo* studies. [114, 115]

Zhao Y. and colleagues [307] looked into the size- and surface-dependent hemocompatibility of MCM-41 and SBA-15, and they presented the first evidence of MSN engulfment by RBCs. They concluded that the only MSN materials that may be evaluated as possibly safe candidates for intravascular drug administration are small MCM-41-type MSN materials (100–200 nm). They found that the surface derivatization of MSN materials to reduce their contact with RBCs is a key element

in their biocompatibility. Reduced interactions have a significant impact on maintaining RBCs' deformability, which is essential for proper blood circulation. [115]

The biocompatibility of three different MSN types (MCM-41, SBA-15 and MCF) was examined in a research carried by Hudson S.P. *et al.*, in 2008 [308], where it was described that although MSNs exerted some *in vivo* toxicity this was not dependent on their size but on the route of administration. NPs with different sizes were administered to male Sprague-Dawley rats and male SV129 mice. Following subcutaneous (s.c.) injection into rats, the amount of material gradually decreased at the site of injection over the course of three months, did not cause harm to the animals and did not induce significant histological damage. In contrast, mice that received intra-peritoneal (i.p.) or intra-venous (i.v.) injections died or had to be euthanised during the course of the study. Microscopic examination of the mice's lung tissue revealed that thrombosis may had been the cause of death. The authors concluded that MSNs may have a higher systemic toxicity than other more commonly used polymeric delivery systems at even higher concentration but that this toxicity could be minimized by modifying the materials. [114, 115]

Two years later Lu J. *et al.*, [309] treated two separate groups of mice with MSNs in a size range 100-130 nm: one group received the NPs intravenously at a concentration of 0.06-1 mg/mouse/day twice weekly for a total of two weeks treatment and the second group received 1 mg/mouse/day intraperitoneally twice weekly for a total of two months treatment. By examining animal condition (body weight, grooming, food intake and mobility), and by conducting serological, haematological, and histological analyses of blood and tissues, the authors concluded that the MSNs were well tolerated in both cases. In addition, it was observed that 94.4% of the silicon administered was cleared 96 h following i.p. injection of 1 mg MSNs. Mice bearing subcutaneous tumours were injected with empty MSNs and high tumour accumulation, as well as accumulation in the kidney and liver, was identified. Moreover, MSNs loaded with the anticancer medication camptothecin reduced tumour volume. [115]

A study from He Q. *et al.*, [294] investigated the effects of the particles size and PEGylation after a single 20 mg/kg intravenous injection. Throughout the one-month monitoring period, every mouse survived, and none of the microscopic

histological investigations revealed any clinical abnormalities. They reported that MSNs of all sizes were largely found in the liver and spleen after intravenous injection, whereas a smaller number were found in the lung and a lesser proportion in the kidney and heart. At 30 minutes after injection, the distribution in the liver and spleen rose as particle sizes grew from 80, 120, to 200 nm. PEGylation generally reduced MSN accumulation in the liver, spleen, and lung. Importantly, smaller particles had a longer blood-circulation lifespan. The excretion rate from urine rose significantly as particle size increased, and the excretion of degradation products from PEGylated MSNs was lower than that of comparable-sized non-PEGylated MSNs. [114, 115]

## 1.3.3.2.2 Effect of surface properties

The general consensus is that cationic NPs cause a greater immune response and cytotoxicity than their neutral and anionic counterparts, but they are better suited for trans vascular transport in tumours. In contrast, neutrally charged particles favourably exhibit long circulation times and interstitial transport in tumours. [310, 311] Although it is believed that no more than 6% of the total MSNs surface silanol groups are exposed to the surrounding environment, these can still interact with biological components such as cellular membrane lipids and proteins and disrupt their structure. [312] Proteins, lipids, enzymes, and other macromolecules can coat the NPs surfaces after their interaction with biological fluids and form a "biomolecular corona" surrounding the particles. This can hinder the ability of the NPs to be absorbed by the targeted tissue or increase their clearance from the circulation through immune system recognition. [313-315] Bare MSNs, which present a negative zeta potential, would quickly bind to serum opsonin in the absence of surface modification and, after entering the bloodstream, be quickly eliminated from circulation by macrophages in the RES. MSNs surface modification is critical for changing surface reactivity, enhancing biocompatibility, and extending *in vivo* circulation time. [114]

PEGylation is the most effective surface modification method. The FDA-approved polyethylene glycols (PEGs) can create a hydrophilic coating and provide a greater particle dispersion, which significantly lengthens the half-life by delaying

opsonization. It serves as a shield to hide the silanol groups that are reactive on the surface and blocks the access of more silanol groups from collapsed pores. It has been shown that after being administered intravenously, PEGylated MSNs had a reduced distribution in RES-related tissue of the liver and spleen. PEGylation can also reduce the endocytosis of MSNs and improve their cytotoxicity and haemolytic activity. [114]

PEGylation, however, is not the gold standard for RES escape. In fact, the production of specific anti-PEG IgM, which promotes accelerated blood clearance of the NPs following repeated injection, has been proposed by recent investigations, contrary to the broadly accepted idea that PEGylation can avoid immune recognition. It has been outlined that different surface functionalization via amino (-NH$_2$), carboxyl (-COOH), phenyl (-Ph), and methyl phosphonate (-PO$_3$) groups with negative, neutral, and positive zeta potentials can control the uptake and cytotoxicity of MSNs *in vitro* as well as their *in vivo* biodistribution and excretion. [114]

1.3.3.2.3 Effect of shape

Since it was discovered that non-spherical particles had decreased macrophage phagocytosis and a prolonged *in vivo* circulation time, [316, 317] particles shape has attracted increasing amounts of interest. Nevertheless, due to the limited number of fabrication techniques that can be employed to synthesise particles with different shapes using biocompatible materials, it is challenging to consider shape as a single variable and establish the link between particles shape and biocompatibility. However, it is possible to study the shape influence on nanotoxicity, biodistribution, and performance for drug delivery thanks to the possibility of synthesizing MSNs with diverse shapes but comparable composition, structure, diameter, and dispersity. [114]

Trewyn B.G. *et al.*, in their work [318] analysed spherical (size distribution from 80 to 150 nm) and tube-shaped (600 nm in length and 100 nm in breadth) MSNs cellular uptake on Chinese hamster ovary (CHO) cells and human fibroblast cells *in vitro*. It was observed that while both MSNs were rapidly and similarly

endocytosed by CHO cells, spherical MSNs were endocytosed by fibroblast cells much more quickly than rod-like MSNs. [114]

Huang X. *et al.*, [295] investigated the effect of different MSNs shapes (short-rod and long-rod NPs both with and without PEGylation surface modification) on biodistribution, clearance and biocompatibility *in vivo*. In a previous work from the same group, [319] it was demonstrated that particles shape could influence their interaction with cells. In this work it was reported that, after i.v. administration, MSNs were mostly found in the liver, spleen, and lung (>80%), with clear impacts of particles shape on *in vivo* behaviours: while long-rod MSNs distributed mainly in the spleen, short-rod MSNs were retained in the liver. After functionalization with PEG, both MSNs were mainly found in the lungs. It was also found that MSNs were mostly eliminated through urine and faeces, with short-rod MSNs having a faster clearance rate than long-rod MSNs in both excretion routes, although PEGylated MSNs were eliminated more gradually. MSN amounts in the liver, spleen, and lungs were still elevated after 7 days. To conclude, it was reported that MSNs did not cause considerable toxicity *in vivo*, as seen from haematology, serum biochemistry, and histopathology analysis results, where no abnormalities were found. However, both PEGylated and non-PEGylated MSNs impaired glomerular filtration and biliary excretion. [115]

1.3.3.2.4 Effect of porous structure

MSNs are porous, present a low density, and a high surface area; the high specific surface area may be beneficial for encapsulating guest molecules, but it may also bring additional risks and dangers due to higher reactive and oxidative activity. It is widely acknowledged that the toxicity of NPs is strongly associated with their specific surface area. NPs having high surface areas and numerous silanol groups can produce reactive oxygen species (ROS), which play an important role in nanomaterial-induced damage. MSNs have been shown to impair cellular and mitochondrial respiration and produce oxidative stress. However, contradictory experimental results are obtained when the toxicity of porous and non-porous silica NPs are compared. In a study carried by Lee S. and colleagues, [320] spherical MSNs with a diameter of 100 nm demonstrated decreased

cytotoxicity, inflammatory response, and contact hypersensitivity when compared to their colloidal solid counterparts. In line with these findings, two more investigations also reported that MSNs were less cytotoxic and had lower haemolytic activity than their nonporous counterparts. [306, 321] It is believed that the rationale behind this observation is that the "cell-contactable surface area" of NPs controls how they interact with cells and tissues and, although porous silica has a larger surface area than its nonporous counterpart, porous silica NPs have a smaller "cell-contactable surface area", which is the region with which cell membrane, cell-bound proteins, and cell-associated chemicals may interact. [114]

Although particle size and surface modification affect the *in vivo* breakdown rate of MSNs, it has been observed that surfactant-extracted MSNs are degraded more quickly in simulated bodily fluid than calcined MSNs and amorphous solid silica. [114]

In a study carried out by Yu T. and colleagues [322] it was found that surface charge and pore size of MSNs could induce cellular toxicity but that this toxicity was cell-type dependent. Haemolytic activity was also proven to be geometry- and porosity-dependent for unmodified MSNs and surface charge-dependent for amine-modified MSNs. [115]

In another study from 2013, Townson J.L. and colleagues [323] demonstrated that when tested *in vitro* and *in vivo*, two types of MSNs that presented similar primary and hydrodynamic particle size, shape, pore structure, colloidal stability, and zeta potential, but different surface chemistry (the spatial arrangement and relative exposure of surface amines), interacted with cells and tissues in remarkably different ways. These particles were surface-functionalized with PEG derivatives (PEG-PEI and PEG-NMe$_3^+$), had a diameter of around 50 nm and were positively charged. However, while the PEG-PEI MSNs presented exposed polyamines, in the other NP type the amines were obstructed. In the case of PEG-PEI MSNs, the NPs showed non-specific binding to different cell types tested *in vitro*, and to endothelial and white blood cells *in vivo*, while the PEG-NMe$_3^+$ modified MSNs showed minimal nonspecific binding to proteins, cells or tissues and remained in circulation for longer than 6 h after injection because of their protein corona neutrality. [115]

In summary, although MSNs can be considered as excellent candidates for biomedical applications due to their biodegradability and controllable breakdown rate, [114] MSNs' physicochemical characteristics, such as particle size, surface charge, shape, and porous structure, may have a significant impact on their biocompatibility.

## 1.4 Project aims

Data published by the World Health Organization (WHO) in 2019, showed that the first and/or second leading cause of death in 112 of 183 countries was cancer (diagnosed before the age of 70); and it was either the third or fourth cause in other 23 countries.

GLOBOCAN estimates for year 2020 showed that 1 in 5 people will get cancer during their lifetime, and 1 in 10 will die from it. 19.3 million new cancer cases were diagnosed worldwide in 2020 and, in the same year, 10 million cancer deaths were recorded. The highest diagnosis numbers were recorded for female breast cancer, whether the highest deaths numbers were recorded for patients suffering from lung cancer.

One of the main problems of chemotherapeutic drugs is that they are non-selective and for this reason they can also damage other rapidly growing healthy cells, causing severe unintended and undesirable side effects. On top of that, the bioavailability of chemotherapeutics to tumour sites/tissues is poor and higher doses are usually required. All these factors can potentially contribute to cause high toxicity in healthy cells, in addition to an increased incidence of multiple drug resistance. For this reason, and in order to reduce both, side effects and drug resistance, it is of great importance to develop new approaches that will specifically target cancer cells.

The overall aim of this research project is to develop biocompatible NPs based on mesoporous silica for the delivery of contrast agent(s) and/or chemotherapeutic drug(s) for the diagnosis and/or therapy of lung cancer, that can

serve as a starting step to build up libraries of NPs for improving the management of cancer.

For this purpose, MSNs will be designed with the main aim of responding promptly to the presence of (a) known specific biomarker(s). It is expected that the system loaded with the contrast agent(s) and/or with chemotherapeutic agent(s) will provide a stimuli-responsive release triggered by the presence of the tumour biomarker(s).

The specific aims of this research project are:

- Developing and screening a panel of MSNs in terms of particle size, surface area, pore volume and diameter, degradation rate and dispersibility.

- Loading the nanoparticles with contrast agent(s) and/or chemotherapeutic(s).

- Functionalising the outer surface with polymers able to enhance their stability, as well as their delivery/targeting abilities. The resultant particles will be characterised to detect possible changes in structure, morphology, and physicochemical properties as compared to unmodified MSNs.

- Performing release assays at relevant conditions (physiological temperature, high GSH levels and enriched MMP media) to determine kinetic parameters and assess the gating and release behaviour in order to obtain optimal nanoparticles (i.e., no significant release until specific biomarkers are recognised by the ligands on the outer surface).

- *In vitro* testing of the nano-systems including cellular binding and uptake (confocal microscopy/flow cytometry), release and effect of the loaded content on lung cancer cells (A549 and LLC1 cells).

- Assessing the blood compatibility of the nano-systems *ex vivo* using red blood cells and platelets isolated from human blood.

- Investigating the safety and efficacy of the nano-systems *in vivo* in a mice model of lung cancer.

- Evaluating nanoparticles' potential using a 3D cell model of glioblastoma multiforme established by our research group, to have a better understanding of the effect of the nano-systems in a model that mimics the complexity and three-dimensional architecture found *in vivo.*

The thesis will provide a comprehensive and detailed overview of the entire research project, including the rationale, methods, results, and conclusions, with the aim to provide valuable insights into the potential of MSNs as a nanotherapeutic agent for cancer, focusing on lung cancer.

# 2   CHAPTER 2: MATERIALS AND METHODS

## 2.1   Materials

Doxorubicin hydrochloride (DOX) and 3-(mercapto)propyltrimethoxysilane were purchased from Fluorochem Ltd (Hadfield, UK). Cetyltrimethylammonium bromide (CTAB) was purchased from AlfaAesar, Avocado Research Chemicals Ltd (Heysham, UK). Collagen (Chrono-Par®) fibrils (type I) from equine tendons was purchased from Chrono-Log Corporation (Havertown, USA). Tetraethyl orthosilicate (TEOS), sodium acetate anhydrous, dimethyl sulfoxide (DMSO), poly-(ethylene glycol) methyl ether thiol (PEG), Aldrithiol-2™, glutathione (GSH), Dulbecco's modified Eagle's medium (DMEM F12), Minimum Essential Medium Eagle (MEM), Dulbecco's Phosphate Buffered Saline (DPBS), foetal bovine serum (FBS), trypsin-EDTA solution 0.25%, gelatine from porcine skin (~ 175 g Bloom), fibrinogen from bovine plasma type I-S, safranin-O, rhodamine B isothiocyanate, dichloromethane (anhydrous), glutaraldehyde solution (50 wt % in $H_2O$), Brilliant Blue G, sodium citrate tribasic dihydrate, sodium chloride, N, N, N', N'- tetramethyl-ethylenediamine, sodium azide, Tyrode's Salts, calcium chloride dihydrate, sodium dodecyl sulphate, glycine, acrylamide/bis-acrylamide 30% solution  and Triton™ X-100 were purchased from Sigma-Aldrich (Arklow, Ireland). Sodium hydroxide (NaOH) and hydrochloric acid (HCl) were purchased from Lennox, Laboratory Supplies Ltd (Dublin, Ireland). Absolute alcohol (EtOH), acetonitrile (ACN), dichloromethane and acetic acid were purchased from Trinity College Dublin (Dublin, Ireland). Phosphoric acid was purchased from VWR International Ltd (Dublin, Ireland). Phosphate-buffered saline (PBS) tablets, potassium dihydrogen orthophosphate, Tris Base, Ammonium acetate and formaldehyde 4% buffered solution were purchased from Fisher Scientific UK Ltd (Loughborough, UK). Cell Counting Kit-8 (CCK-8) was purchased from Tebu-Bio Ltd (Peterborough, UK). ActinGreen™ 488 ReadyProbes™ reagent, Pierce™ BCA Protein Assay, Albumin Standard, Antibiotic-Antimycotic (100X), Trypan Blue Stain (0.4%) and Pierce™ Unstained Protein MW Marker were purchased from Thermo Fisher Scientific (UK).

Paclitaxel (PTX) was purchased from Tokyo Chemical Industry Co., LTD (Zwijndrecht, Belgium).

## 2.2 Methods

### 2.2.1 MCM-41 MSNs synthesis

MCM-41 type of MSNs was synthesized using a modified Stöber method, based on the sol-gel process in a basic environment, using tetraethyl orthosilicate (TEOS) as the silica precursor and cetyltrimethylammonium bromide (CTAB) as the template. 1 g of CTAB was dissolved in 480 mL of double distilled water in a 1 L beaker and put under magnetic stirring at 100 rpm and at 80 °C on a stirrer hotplate (Stuart™, UK). 3.5 mL of sodium hydroxide (NaOH) 2 M were added and, once the solution reached the temperature of 80 °C, 5 mL of TEOS were rapidly injected using a BD Microlance™ 21G 1½" needle, and the stirring increased to 550 rpm. The mixture was left to react for two h. The stirring was then stopped, and the suspension of newly formed particles let to cool down to room temperature. The suspension was then centrifuged at 10,000 rpm using a 5810 R centrifuge (Eppendorf®, Germany) for ten minutes, in order to recover the NPs, and washed with double distilled water until reaching a neutral pH. The pellet was dried in an oven at 100 °C overnight. To remove the surfactant template, the NPs were ground with a mortar, transferred to a 250 mL round bottom flask, and refluxed into 100 mL of an ethanolic solution (the mixture of 8.33 mL HCl 37 % with 91.67 mL EtOH) at 85 °C and under magnetic stirring at 600 rpm overnight. The suspension of extracted particles was let to cool down once again to room temperature, centrifuged at 10,000 rpm for ten minutes, washed several times with double distilled water, until reaching a neutral pH, and washed one last time with absolute alcohol to help the drying process. In the final step the NPs were dried in an oven at 100 °C overnight.

### 2.2.1.1 MCM-41 functionalized with rhodamine B isothiocyanate

For the rhodamine B isothiocyanate (RhBITC) functionalised MSNs, the initial step consisted in activating RhBITC by reaction with APTES: 1 mg of the dye was left to react with 2.2 μL of APTES in 0.1 mL of ethanol at room temperature, under light sealed conditions for 2 h. Afterwards, RhBITC-APTES was added to the 5mL of TEOS, and the reaction was carried out as described above.

### 2.2.2 Dynamic Light Scattering (DLS) and zeta (ζ)-potential analysis

Zeta (ζ)-potential, hydrodynamic particle size distribution and polydispersity index (PDI) of MCM-41 NPs were measured using a Zetasizer Nano series Nano-ZS ZEN3600 (Malvern Instruments, UK) equipped with a 633 nm red laser. The particle size and PDI were analysed using Dynamic Light Scattering (DLS) technique, which measures the diffusion of particles moving under Brownian motion. The particle size was measured at a scattering angle of 173º and calculated based on the diffusion coefficient, and the zeta (ζ)-potential was determined calculating the electrophoretic mobility using Laser Doppler Micro-electrophoresis technique. The NPs were resuspended in deionized water at a concentration of 1 mg/mL, ultrasonically dispersed using a FB11207 Ultrasonic Bath (Fisherbrand™, Thermo Fisher Scientific, USA) in order to obtain homogenization of the sample, and then diluted to 0.1 mg/mL for size and PDI analysis, which were carried in a DTS0012 disposable cuvette. The 1 mg/mL suspension was used for zeta (ζ)-potential analysis, which was carried in a disposable folded capillary cell (DTS1070). The measurements were carried out at 25 ºC, the equilibration time was set to 120 seconds and each parameter was measured three times.

### 2.2.3 Fourier-transform infrared spectroscopy (FTIR)

FTIR spectra of MCM-41 NPs were collected using a FTIR Spectrometer Spectrum 100 (PerkinElmer, USA), ranging from 400 to 5,000 cm$^{-1}$, in order to identify the chemical groups on the surface of the NPs, and to analyse the bonding architecture.

### 2.2.4  Nitrogen adsorption/desorption analysis

The surface areas, pore volumes and pore size distributions of the MCM-41 NPs were analysed by nitrogen adsorption/desorption using a Gemini VI, Surface Area, and Pore Size Analyzer (Micromeritics, USA). Before measurements, the samples were degassed at 120 °C overnight using a SmartPrep, Programmable Degas System (Micrometrics, USA). The data were analysed using MicroActive for TriStar® II Plus software. The Brunauer-Emmett-Teller (BET) method was used to calculate the specific surface area, by determining the monolayer volume of adsorbed gas from the isotherm data. The Barrett-Joyner-Halenda (BJH) model was used to derive the pore volumes and pore size distribution from the adsorption data.

### 2.2.5  Powder X-ray diffraction (PXRD)

Powder X-ray diffraction was performed using a Miniflex II, Desktop X-ray Diffractometer (Rigaku, Japan). The X-ray tube was operated at 30 kV and 15 mA. The dried samples of NPs were scanned over a 2θ range of 2-10 degrees.

### 2.2.6  Thermal Gravimetric Analysis (TGA)

Thermogravimetric analysis was used before and after the template removal process to confirm the removal of the template, the successful load of the dye/drug into the pores of the NPs and surface functionalization. The analysis of the decomposition profiles was conducted using a TGA Q50 (TA Instruments, USA) with a heating rate of 10 °C/min under a nitrogen atmosphere, by placing a

minimum of 5 mg of sample in an alumina pan, which was then placed in a platinum crucible. During the procedure, MCM-41 NPs were first heated from 25 $^{\circ}$C to 100 $^{\circ}$C. At this point, the temperature was then held constant for 5 minutes to make sure all the water would evaporate, and as the final step the particles were heated from 100 $^{\circ}$C to 600 $^{\circ}$C.

## 2.2.7  Electron Microscopy

### 2.2.7.1  Scanning Electron Microscopy (SEM)

The morphology of MCM-41 NPs and the mean particles' size were characterized by SEM analysis. The SEM images were taken with a Zeiss Ultra plus microscope (Carl Zeiss AG, Germany), equipped with both InLens, for high resolution details, and SE2 detectors, for topographical details. The dried NPs were first ultrasonically dispersed in absolute alcohol, and afterwards a few drops were placed on aluminium stubs and let to air dry. In order to improve the imaging contrast, prevent damage to the samples, and reduce image artifacts, the samples were coated with a thin film of gold/palladium under vacuum. The samples were then screened at the SEM.

### 2.2.7.2  Transmission Electron Microscopy (TEM)

The morphology and the pore structure of MCM-41 NPs were characterized by TEM analysis. The TEM images were acquired with a JEOL 2100 microscope at 200 kV. The particles were redispersed in absolute alcohol, and afterwards one drop of the sample was deposited onto a carbon-coated 200 mesh copper grid and left to dry at room temperature before analysis. In order to visualize the organic coating around gelatine-functionalised NPs, a 1% solution of phosphotungstic acid (PTA) (pH 7.0) was employed as staining agent.

## 2.2.8  Dye/drug loading

MCM-41 NPs loaded with safranin-O, doxorubicin hydrochloride (DOX), or paclitaxel (PTX) were obtained using a solution immersion approach. The amounts of safranin-O or DOX and particles used were calculated always considering a ratio of 0.8 mmol of cargo per g of NPs. [324] PTX and NPs amounts were calculated considering a ratio of PTX to MSNs equal to 1:3. [325] The calculated amount of safranin-O, DOX, or PTX was solubilized in dd $H_2O$, acetate buffer (pH 5.4), or dichloromethane (DCM), respectively, and added to the NPs. After ultrasonically dispersing the NPs in the dye/drug solution, the mixture was left under magnetic stirring, under light-sealed conditions and at room temperature for 24 h. The NPs were collected by centrifugation at 5,000 rpm for 20 minutes and dried at 37 °C overnight (or for longer if needed). 200 µL of the feeding solution, and the resultant supernatant from the centrifugation of the NPs' suspension were collected and stored at -20°C (DOX) or 4°C (Safranin-O) for further analysis (PTX samples were usually analysed straight away due to the high volatility of DCM).

## 2.2.8.1  MCM-41 Loading Capacity (LC %) quantification

The feeding solution, and the supernatant collected after the loading were analysed in order to calculate the amount of unloaded cargo, and subsequently calculate the loading content of MCM-41 particles by the following equation (**1**):

$$LC \% \left(\frac{w}{w}\right) = \left(\frac{mass\ of\ cargo\ in\ NPs}{mass\ of\ NPs}\right) x\ 100 \qquad (\mathbf{1})$$

where the mass of cargo in the NPs was calculated by subtracting the amount measured in the collected supernatant, from the initial amount used. The amount of cargo in the supernatant was measured by fluorescence analysis in a FLUOstar OPTIMA microplate reader (BMG Labtech, Germany) for safranin-O and DOX, or by High Performance Liquid Chromatography (HPLC) using an Alliance e2695 Separation Module (Waters, USA), for PTX. In the latter, the column used was a Gemini® 5 µm C18 110 Å, 250 x 4.6 mm (Phenomenex®, USA), equipped with a

guard column. The mobile phase consisted of an aqueous phase containing dd H$_2$O (30%), and an organic phase of acetonitrile (ACN – 70%). The flow rate was set at 1 mL/min and the injected volume was 20 µL. Waters 2487, Dual λ Absorbance Detector (Waters, USA) was used at a detection wavelength of 227 nm. The samples were filtered through a PTFE syringe filter with a pore size of 0.2 µm (Thermo Fisher Scientific, UK) before injection. Safranin-O, DOX, or PTX solutions of known concentrations were used to generate the calibration curves.

### 2.2.9  MSNs functionalization

### 2.2.9.1  Functionalization with PEG (MSNs-PEG)

The external surface of MCM-41 NPs was modified by grafting a layer of poly-(ethylene glycol) methyl ether thiol (PEG) with an average Mn of 800 using disulphide bonds, in order to cap the pores of the particles and control the release. The coating of the particles with PEG is also useful to ensure the dispersion in water and to prevent non-specific interactions with bio-macromolecules like blood proteins and macrophages. The procedure suggested by Giménez C. *et al.*, [324] was followed (**Fig. 2.1**). The first step of this synthesis consisted in ultrasonically dispersing the NPs in ACN (8.5 mL for 250 mg of MSNs), then (3-mercaptopropyl)trimethoxy-silane was added (in the ratio 464 µL per 250 mg of NPs) and the mixture was left under magnetic stirring at room temperature, for 5.5 h. In the second step, Aldrithiol™-2 (2,2'-dipyridyl disulphide) was added to the mixture (in the ratio 550.77 mg per 250 mg of NPs) and stirred at room temperature overnight, always under light-sealed conditions, in order to obtain 2-pyridinyldisulfanylpropyl-functionalized MSNs. The suspension was then centrifuged at 13,000 rpm for 5 minutes and the supernatant collected and stored for further HPLC analysis (for loaded NPs only, in order to quantify the amount of cargo lost during these steps). MSNs were washed once with ACN, and the supernatant collected and stored. For the formation of the disulphide bonds, 2-pyridinyldisulfanylpropyl-functionalized MSNs were re-suspended in fresh ACN (3.33 mL for 120 mg of PEG), and PEG was added (in the ratio 120 mg per 50 mg

of particles). The mixture was left under magnetic stirring at room temperature overnight, under light-sealed conditions. The day after, the suspension was centrifuged at 13,000 rpm for 5 minutes and the supernatant collected and stored for further analysis. MSNs were then washed three times with ACN and several times with double distilled water, always collecting and storing the supernatants as before. The PEGylated NPs were dried at 37 °C overnight (or for longer if needed).
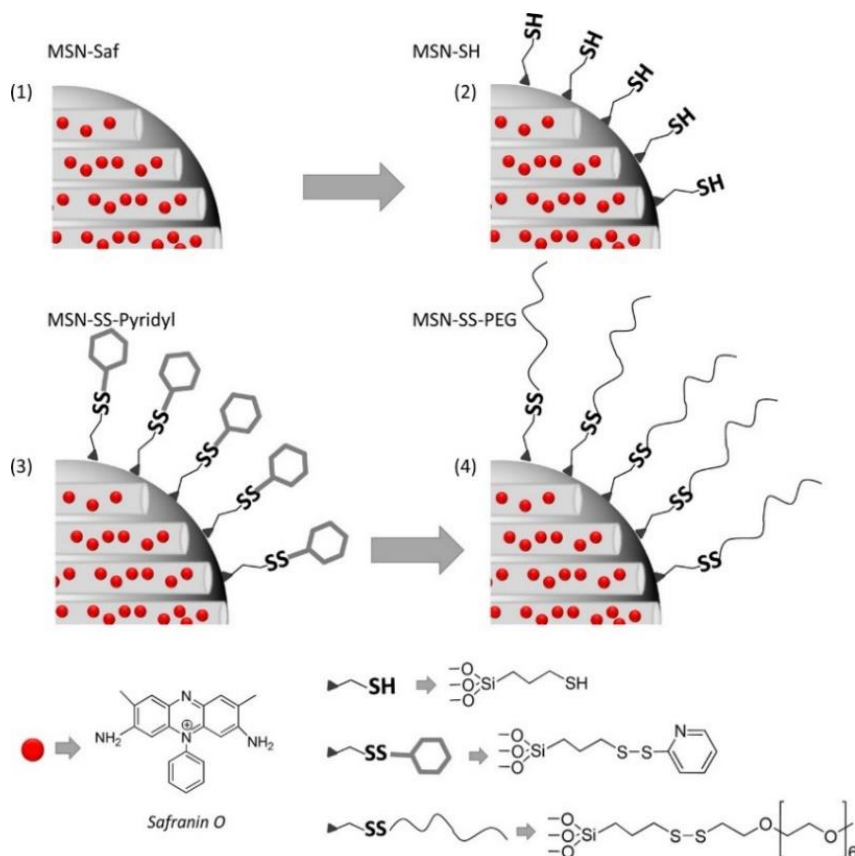


**Figure 2.1:** Schematic representation of MSNs functionalization with PEG: 1-loaded MSNs; 2- addition of thiol groups; 3- formation of disulphide bonds; 4- addition of PEG chains. [324]

## 2.2.9.2 Functionalization with gelatine (MSNs-GEL)

The external surface of MCM-41 NPs was modified by grafting a layer of type A gelatine with an average strength of 175 g Bloom, in order to cap the pores of the particles and control the release of their cargo. The NPs were first functionalised with aldehyde groups following three steps: [143]

1. Neo-synthesised MSNs, with CTAB still present in the pores, where functionalised with amino groups by reacting them with APTES in the ratio 6 mmol APTES per g of NPs. To achieve this, the particles were resuspended in ACN (100 mL for 1 g of MSNs), ultrasonically redispersed for 5 minutes, and the APTES was subsequently added to the suspension. The particles were left to react under magnetic stirring, at room temperature overnight. The particles were then recovered by centrifugation (10,000 rpm for 10 minutes) and the excess APTES removed by three washing cycles with deionized water; the NPs were dried at 70 °C overnight (or for longer if needed).

2. At this point the template was removed from the pores as previously described, which led to obtaining amino functionalised MSNs (MSNs-$NH_2$).

3. As the final step, the particles were functionalised with aldehyde groups by reacting MSN-$NH_2$ with glutaraldehyde (GTA, 50% solution in $H_2O$). The NPs were resuspended in dd $H_2O$ at a concentration of 10 mg/mL, ultrasonically redispersed for 5 minutes, and subsequently GTA was added to the suspension to a final concentration equal to 0.5% (v/v). The particles were left to react under magnetic stirring, at room temperature overnight. They were then recovered by centrifugation (10,000 rpm for 10 minutes) and the excess GTA was removed by three washing cycles with deionized water; the NPs were dried at 70 °C overnight (or for longer if needed).

Following this process, the obtained aldehyde-functionalised (MSNs-CHO) NPs were  functionalised with gelatine, or loaded with the molecule of interest first (as described above) and then functionalised, through the formation of Schiff-base bonds between the aldehyde groups on the surface of the NPs and the amine groups of the gelatine. [143] For this purpose, a solution of 1% gelatine in PBS was left at 37 °C and under magnetic stirring (100 rpm) overnight. Afterwards, the NPs were resuspended in PBS (10 mg/mL), ultrasonically redispersed for 5 minutes and the gelatine solution was added to obtain a final concentration of 0.1%. The reaction was left for 24 h, at room temperature and under magnetic stirring. The

particles were recovered by centrifugation (10,000 rpm for 10 minutes) and the excess gelatine removed by washing with PBS first and deionized water after; the NPs were dried at 37 °C overnight (or for longer if needed). Again, if the particles were loaded, the supernatants were collected and stored for further analysis.

2.2.10 Release studies

The *in vitro* release behaviour of safranin-O from MCM-41 NPs was studied from the two synthesized stimuli-responsive systems, MSNs-PEG, and MSNs-GEL, in order to test their ability to inhibit the release of the cargo when not in the presence of the stimulus and their responsiveness to the latter (GSH for MSNs-PEG, and gelatinases for MSNs-GEL), allowing the opening of the pores and the release of the dye.

2.2.10.1     MSNs-PEG

Both PEG-capped and uncapped particles were tested in duplicate. First, they were ultrasonically dispersed in PBS (pH 7.4) at a concentration of 2 mg/mL, then the NPs dispersion was further diluted in fresh PBS (1:10) in order to obtain a homogenous and well dispersed suspension. At this point the NPs were kept in PBS at 37 ºC, under agitation (500 rpm) and in light sealed conditions in a PHMT thermo-shaker for microtubes (Grant Instruments, UK). The PEGylated NPs stock was divided into two further samples: presence (GSH) and absence (negative control, PBS only) of the stimulus, at a final concentration of 10 mM (intracellular concentration), in order to test the capping efficiency and reactivity. The GSH was added at 30 minutes, and the concentration was kept constant for the whole duration of the assay. At predetermined time intervals (5, 30, 60, 120 minutes, 4, 6 and 24 h), aliquots of 0.5 mL were withdrawn, centrifuged at 13,000 rpm for 5 minutes, the supernatants collected, centrifuged further at 13,000 rpm and 0.4 mL were collected and stored at 4 ºC for further analysis. The pellet of NPs obtained from the first centrifugation cycle was re-suspended in 0.5 mL of fresh media and

added back to the initial suspension. The cumulative safranin-O release was calculated using the following equation (**2**):

$$Cumulative\ Release\ (\%) = \left(\frac{Amount\ released}{Amount\ released\ at\ 24h\ timepoint}\right) \times 100 \quad (2)$$

and the amount of dye released by the NPs was calculated considering the dilutions made each time 0.5 mL of fresh media was added back to the initial suspension.

### 2.2.10.2     MSNs-GEL

Both GEL-capped and uncapped particles were tested in duplicate. First, they were ultrasonically dispersed in PBS (pH 7.4) at a concentration of 2 mg/mL, then the NP dispersion was further diluted in fresh PBS (1:10) in order to obtain a homogenous and well dispersed suspension. At this point, the NPs were kept in PBS at 37 °C, under agitation (500 rpm) and in light sealed conditions in the thermo-shaker. The GEL-functionalised NPs were divided into two further samples: presence (MMP-9) and absence (negative control, PBS only) of the metalloproteinase (MMP-9) enzyme, at two different concentrations of 10 and 30 nM, in order to test the capping efficiency. The MMPs were added at 30 minutes, and the concentration was kept constant for the whole duration of the assay. At predetermined time intervals (5, 30, 60, 120 minutes, 4, 6 and 24 h), aliquots of 0.5 mL were withdrawn, centrifuged at 13,000 rpm for 5 minutes, the supernatants collected, centrifuged further at 13,000 rpm and 0.4 mL were collected and stored at 4 °C for further analysis. The pellet was re-suspended in 0.5 mL of fresh media and added back to the initial suspension. The cumulative safranin-O release was calculated using Eq. (**2**) as described above.

### 2.2.10.2.1    Release profiles in the conditioned cell culture media

The responsiveness of MSNs-GEL to MMPs was also tested using serum-free conditioned cell media harvested from human (A549) and murine (LLC1) lung

cancer cells. This assay was performed not only to assess the particles' reactivity to gelatinases, but also to validate the release of MMPs by lung cancer cells and the potential of obtaining sufficient enzyme levels to perform release assays without the use of commercial MMPs and under experimental conditions closer to the physiological ones.

The steps were identical to those described above, with the exception of the media used for the assay: the functionalised NPs were first resuspended in fresh media before being diluted (1:10) in conditioned cell medium at timepoint "0". The negative and positive controls were kept in fresh media.

## 2.2.11 *In vitro* 2D cell assays

### 2.2.11.1 Cell culture

Human NSCLC cells (A549) were obtained from the European Collection of Authenticated Cell Cultures (ECACC - 86012804). Lewis lung carcinoma cells (LLC1) were a gift from Professor Seamas Donnelly's group in Trinity College Dublin. Cells were cultured in Dulbecco's modified Eagle's medium (DMEM F12) with L-glutamine, supplemented with 10% (v/v) foetal bovine serum (FBS), and incubated in a 170L silver $CO_2$ cell culture incubator (GS Biotech, UK) at 37 ºC in 5% $CO_2$ atmosphere. When cells were cultured in the presence of NPs, the media were also supplemented with penicillin (100 U/mL), streptomycin (100 µg/mL) and amphotericin B (0.25 µg/mL).

Human fibrosarcoma cells (HT1080) were obtained from the American Type Culture Collection (ATCC - CCL-121). Those cells were cultured in Minimum Essential Eagle's medium (MEM), supplemented with 10% (v/v) FBS and 1% L-glutamine, and incubated in a 170L silver $CO_2$ cell culture incubator (GS Biotech, UK) at 37 ºC in 5% $CO_2$ atmosphere.

## 2.2.11.2    *In vitro* cytotoxicity assay

The effect of free DOX, free PTX, empty and PTX-loaded bare (MSNs), aldehyde-functionalised (MSNs-CHO), PEG-functionalised (MSNs-PEG) and gelatine-functionalised (MSNs-GEL) NPs on A549 and LLC1 cell viability was evaluated using the CCK-8 assay (Dojindo Laboratories, Japan) following the manufacturer instructions. Briefly, the product uses a tetrazolium salt, WST-8, which is reduced by the activity of the dehydrogenase enzyme in the cells and gives a formazan dye which is yellow in colour. The amount of the formazan dye, generated by the activities of dehydrogenases in cells, and measured as absorbance at 450 nm, is directly proportional to the number of living cells.

A549 and LLC1 cells were seeded in 96-well plates (Corning™ Costar™ Flat Bottom Cell Culture Plates, Thermo Fisher Scientific, UK) at a density of 5 x $10^3$ cells per well in 0.2 mL of DMEM supplemented with 10% FBS and incubated at 37 $^{\circ}$C for 24 and 48 h respectively. Afterwards, the growth medium was removed, the cells washed once with 0.2 mL of serum-free DMEM, and 0.2 mL of serum-free DMEM containing different concentrations of either free DOX (0.2, 0.9, 1.7, 9, 17, and 43 µM), free PTX (0.06, 0.12, 0.6, 1.2, 3.5, and 7.2 µM), empty NPs (5, 10, 25, 50, 100, 200, and 400 µg/mL), or loaded NPs (with the corresponding PTX concentrations of 0.06, 0.12, 0.6, 1.2, 3.5, 7.2, 10, 12, 20, 50, and 60 µM) were added in triplicate. The cells were then incubated at 37 $^{\circ}$C for 24 h, 48 h and 72 h. At each time point the media was removed, the cells washed with 0.2 mL of PBS 2 or 3 times, and 0.15 mL of serum-free DMEM containing 10 µL of CCK-8 reagent were added to each well, and the cells incubated for one additional h. As final step the absorbance of the formazan product was measured at 450 nm in a FLUOstar OPTIMA microplate reader (BMG Labtech, Germany).

Cell viability was calculated as percentage of the control (non-treated cells, taken as 100% of viability). The $IC_{50}$ was calculated by plotting log[drug] x viability (%) and fitting the curve with a non-linear regression function on GraphPad Prism 9 (GraphPad Software, San Diego, California USA).

## 2.2.11.3     Flow Cytometry

NP's cell internalization was analysed by flow cytometry using fluorescently labelled NPs (rhodamine B isothiocyanate, RhBITC) before and after the addition of 20 μL of trypan blue, as a RhBITC quenching agent. Data were acquired on the LSRFortessa flow cytometer (BD Biosciences, San Jose USA). Rhodamine was detected via the 561 nm laser, through the 582/15 band pass filter. Cell debris was excluded with a gate on Forward Scatter Channel (FSC) vs Side Scatter Channel (SSC), with doublets subsequently excluded via FSC-A vs FSC-W (see **Appendix 2**, **Fig. A2. 1**).

For the analysis, cells were seeded in 6-well plates (Corning™ Costar™ Flat Bottom Cell Culture Plates, Thermo Fisher Scientific, UK) at a density of $300 \times 10^3$ (A549) and $150 \times 10^3$ (LLC1) cells per well, in 2 mL of DMEM supplemented with 10% FBS and incubated at 37 ℃ for 24 and 48 h, respectively. Afterwards, the growth medium was removed, the cells washed with 2 mL of serum-free media, and 2 mL of serum-free media containing either MSNs-RhBITC, MSNs-CHO-RhBITC, MSNs-PEG-RhBITC or MSNs-GEL-RhBITC, at a concentration of 50 μg/mL, were added to the cells at different time points (1, 4 and 24 h), and incubated at 37 ℃. At the pre-determined time points, cells were washed with 0.5 mL of PBS and detached with 0.5 mL of trypsin-EDTA 0.25%, and 0.5 mL of DMEM (10% FBS) were added to neutralise the trypsin. Cells were then transferred to a 15 mL falcon and centrifuged at 1,500 rpm for 10 minutes. The supernatant was discarded, and 0.5 mL of formaldehyde 4% buffered solution added to the falcons for 20 minutes in order to fix the cells. They were subsequently centrifuged one more time, the supernatant was discarded, and the cells resuspended in 0.3 mL of PBS and stored at 4 ℃ until further analysis.

## 2.2.11.4     Confocal Laser Scanning Fluorescence Microscopy

The cellular internalization of RhBITC labelled NPs was also analysed by confocal laser scanning fluorescence microscopy. The images were obtained with

a Leica TCS SP8 inverted microscope (Leica Microsystems, Germany) and micrographs captured by a digital camera.

A549 and LLC1 cells were seeded in a μ–Slide 8 Well (Ibidi, Germany) at a density of 30 x 10³ and 15 x 10³ cells per well respectively, in 0.2 mL of DMEM supplemented with 10% FBS and incubated at 37 ºC for 24 and 48 h respectively. Afterwards, the growth medium was removed, the cells washed with 0.2 mL of serum-free media, and 0.2 mL of serum-free media containing either MSNs-RhBITC, MSNs-CHO-RhBITC, MSNs-PEG-RhBITC or MSNs-GEL-RhBITC, at a concentration of 50 μg/mL, added to the cells and incubated at 37 ºC. At different time points (1, 4 and 24 h), the cells were washed with 200 μL of PBS, fixed in 200 μL formaldehyde 4% buffered solution for 20 minutes, washed with 200 μL of PBS twice and stored in the fridge in 0.2 mL of PBS until further analysis.

Before performing the confocal analysis, the cells cytoskeleton was stained with ActinGreen™ 488 ReadyProbes™ Reagent (AlexaFluor™ 488 phalloidin, Invitrogen, Thermo Scientific, UK) by adding 2 drops of the reagent per mL of PBS and incubating the cells for 30 minutes at room temperature. Afterwards, the media were removed, and the cells nuclei were stained with DAPI (1 μg/mL in PBS) incubating the cells for 2 to 3 h at room temperature. The cells were then washed with PBS twice and kept in 0.1 mL of PBS for the analysis. The NPs cellular internalization was investigated as compared to control cells (non-treated cells).


2.2.11.5    Concentration of MMPs in conditioned media from cancer cells


2.2.11.5.1    HT1080 cells

Phorbol 12-myristate 13-acetate (PMA) is known to promote MMPs upregulation in HT1080. [326] Human fibrosarcoma cells were cultured in T75 flasks. Once the cells had reached their logarithmic growth phase, and 70-80% confluency, the cells were washed with 5 mL of serum-free MEM, and fresh 10mL of serum-free MEM containing 10 μM PMA was added to the flask. After 24 h of incubation, the media were collected and centrifuged at 900 rpm for 5 minutes in

order to remove any debris and stored at -20 °C until further use for protein quantification and gel zymography.

Cell media were collected from 4 different flasks and from cells at different passage numbers.

### 2.2.11.5.2    A549 and LLC1 cells

Both, A549 and LLC1 cells were cultured in T75 flasks. Once they reached the logarithmic growth phase, and 70-80% confluency, the culture media were removed from the flask, the cells washed with 5 mL of serum-free DMEM, and either 10mL of serum-free DMEM containing 10µM PMA, or 10mL of serum free DMEM, were added to the flasks and cells incubated for 24 and 48 h, respectively, before the media was collected. The cell media were centrifuged at 900 rpm for 5 minutes in order to remove any debris and a small aliquot (0.100 mL) was collected and stored at -80 °C for further analysis. The rest of the supernatant was then concentrated using Pierce™ Protein Concentrators PES (Thermo Fisher Scientific, USA), 3K MWCO, in order to concentrate the media and retain MMP-2 and -9. The cell media were centrifuged at 4000g three times: the first time for 15 minutes, the second time for 1 h, and the third and last time for another 60 minutes. Each time a small aliquot was taken and  stored at -20°C for further analysis.

Cell media were collected from 3 different flasks and from cells at different passage numbers.

### 2.2.11.6      Total protein quantification

The total protein concentration in the cell media before and after the different centrifugation steps with the protein concentrators was quantified using Bicinchoninic acid (BCA) or Bradford protein assays.

The BCA protein assay is a widely used colorimetric assay for the quantification of proteins in a sample. The assay is based on the ability of proteins to reduce $Cu^{2+}$ to $Cu^{1+}$ in an alkaline environment, which leads to the formation of a light blue complex. The BCA is then added and reacts with the reduced (cuprous)

cation to form an intense, purple-coloured complex. The intensity of the purple colour is directly proportional to the amount of protein in the sample and can be measured using a spectrophotometer at a wavelength of 562 nm. (Pierce™ BCA Protein Assay, Thermo Fisher Scientific, UK)

The Coomassie dye-based (Bradford) protein assay is also a widely used method for the detection and quantitation of total protein in biological samples. It is a colorimetric assay based on the binding of Coomassie dye to basic amino acids in the protein in an acidic environment. This binding results in a shift in the absorbance spectrum of the dye from the reddish/brown form to the blue form, which can be measured at an optimal wavelength of 595 nm. The amount of blue colour formed by the Coomassie dye-protein complex is proportional to the amount of protein present in the sample. (Bio-Rad protein assay kit II, Bio-Rad Laboratories, USA)

## 2.2.11.7     Gelatine zymography assay

Gelatine zymography was used for detecting pro and active forms of MMP-2 and MMP-9, as previously described, [327] in order to evaluate the activity of MMPs in the cell culture media collected from the cancer cells incubated in the presence or absence of PMA (gelatine zymography was performed by the MSc student Anushka Kulkarni). For the list of buffers and solutions prepared prior to performing the zymography assay please refer to **Appendix 2**, **Tab A2. 4**.

### 2.2.11.7.1    Gels preparation

Solutions of 8% sodium dodecyl sulphate (SDS)-polyacrylamide gel containing 2% of gelatine were carefully pipetted into 0.75 mm assembled glass plates and overlayed with dd $H_2O$, in order to allow the polymerization process.

After the resolving gels had solidified, the water was decanted and the stacking solution added, 10 wells combs inserted and left to solidify. Once the gels had solidified, the combs were removed for loading the samples (otherwise gels

were stored at 4°C, wrapped around wet paper and cling film, without removing the combs, for further use).

### 2.2.11.7.2 Samples preparation

Samples were allowed to thaw in ice, mixed with zymography loading buffer and loaded into the gels. Recombinant MMP-9 was run concurrently in order to identify gelatinase activity and quantify the MMP concentration in the samples.

### 2.2.11.7.3 Run zymography

Zymography was run following the steps bellow:

1) First, the glass plates were assembled into a Bio-Rad Mini-PROTEAN cell, the inner chambers filled with tank buffer and the samples, already prepared as described in the previous section, loaded into the gel lanes carefully using gel loading tips.

2) The Mini-PROTEAN cells were then placed in the electrophoresis boxes, and the outer chambers filled with tank buffer. The lid was placed on top, and the power pack connected. The zymography was run at 150 V for 1 h and 20 minutes.

3) After the electrophoresis was completed, the gels were removed from the glass plates and the stacking gels discarded. Gels were first washed three times with 2.5% Triton buffer and then twice with zymography buffer (for 20 minutes each time), under continuous agitation.

4) Then, the gels were transferred to a tray containing fresh zymography buffer, covered with cling film and incubated in a water bath at 37°C overnight. During this step, the MMPs, if present in the samples, start digesting the gelatine in the gels, resulting in the appearance of bands.

5) The final steps involved the staining (with 0.05% Coomassie brilliant blue G-250 in a solution of methanol-acetic acid-water) and distaining (in a solution of methanol-acetic acid) of the gels under agitation in order to visualize the transparent bands (gelatinolytic activity) against the background of the blue-stained gelatine.

2.2.11.7.4    Gelatinase activity quantification

The gels were visualised using a gel documentation system ChemiDoc™ MP Imaging system (BioRad, USA), and the intensity of the bands analysed using the software Biorad Image Lab version 6.1. The unknown gelatinase activity in the samples was then quantified correlating their intensity with the intensity of the bands for the known concentrations of MMP-9 loaded in the gel.

2.2.12  Blood compatibility

This study was approved by the School of Pharmacy and Pharmaceutical Sciences Trinity College Dublin Research Ethics Committee (2020-06-01-MS).

2.2.12.1    Blood collection and preparation

Blood was donated by healthy donors (**Fig. 2.2**) who had not taken any drugs known to affect platelet's function within the previous 14 days. Informed consent was first obtained, and blood (36 mL) withdrawn carefully, gently mixed with 4 mL of 3.15% sodium citrate in a 50 mL falcon and centrifuged at 250 x g for 20 min at room temperature (RT).

The uppermost fraction, platelet rich plasma (PRP), was gently collected and the platelets' count adjusted to 250,000 platelets/µL with Tyrode's solution. Platelets were counted using a Coulter counter (Beckman Coulter Inc. Brea, CA, USA).

For haemolysis assays, the buffy coat in the falcon was discarded and red blood cells (RBC) retained. RBC were washed three times with sodium chloride 0.9%, and then 1 mL diluted with 49 mL of PBS.

Platelets poor plasma (PPP) was obtained by further centrifugation of PRP at 13,000 rpm for 5 min at RT.
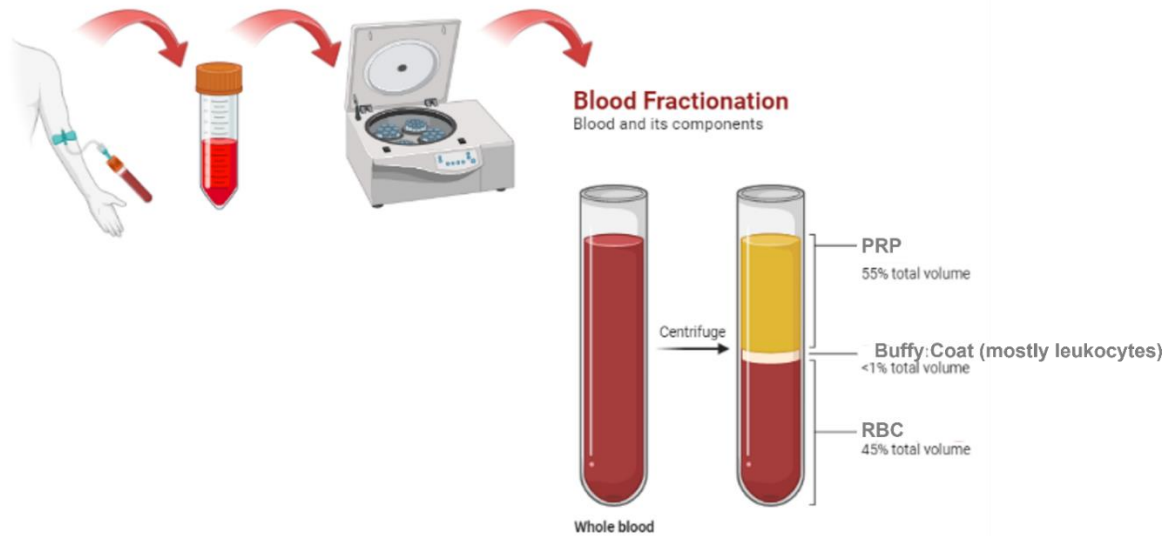
**Figure 2.2:** Schematic representation of blood collection from a healthy donor, and its separation by differential centrifugation. PRP: platelet rich plasma; RBC: red blood cells. *(Created in BioRender.com)*

### 2.2.12.2    Light transmission aggregometry (LTA)

Platelet aggregation was measured as a change in the amount of light passing through the platelet suspension under stirring over time, using an eight-channel Platelet Aggregation Profiler® (PAP-8E, Bio/Data Corporation, USA) linked to the Start PAP-8E v1.08 software.

In LTA, platelets are exposed to various stimuli or agonists in a controlled *in vitro* environment, which initiate platelet activation and induce the process of platelet aggregation. Traditional light transmission aggregometers measure changes in light transmission of platelet suspensions under stirring. The photodetector captures the changes in light intensity and converts them into a signal that can be recorded and analysed.

The calibration of the device is performed taken a cuvette containing PPP (plasma in the absence of platelets), which equates to 100% light transmission, and a cuvette containing PRP under stirring that equates to 0% light transmission

(absence of aggregation). When platelets aggregate, the light transmission through the cuvette increases and the software correlates the amount of light with the percentage of platelets aggregated in the cuvette. Collagen (platelet agonist) at a final concentration of 10 µg/mL was added to the platelets under stirring to confirm the preservation of their function following blood preparation and used as the positive control. Platelets under stirring co-incubated with vehicle (PBS) were used as control for analysing the potential effect of the NPs on platelets' aggregation. The results are presented as a percentage of the maximum aggregation (where the light transmission for platelets in the presence of collagen was considered 100%).

The particles were left under magnetic stirring in PBS at a concentration of 1.25 mg/mL overnight. They were then diluted in PBS to the required concentrations and ultrasonically redispersed for 10 minutes before the experiment was run. Platelets were incubated for 2 minutes at 37°C prior to the addition of the NPs, or collagen. Platelets were incubated in the presence of vehicle, MSNs, MSNs-PEG, or MSNs-GEL at concentrations of 1, 3, 5, 10, 20, 50, 75 and 100 µg/mL and their effects recorded by the software for 30 minutes.

## 2.2.12.3    Quartz crystal microbalance with dissipation (QCM-D)

A Quartz Crystal Microbalance with Dissipation (QCM-D) was used to further investigate the interactions between platelets and NPs. The principle of analysis of this technology is based on the vibration of a quartz crystal when an alternating electric field is applied across the crystal. The device measures two parameters: frequency of vibration and energy dissipation. Deposition on the surface of the crystal induces a decrease in the frequency of vibration (that correlates with deposition of mass), while an increase in the thickness/viscoelasticity of the layer deposited on the sensor induces an increase in the dissipation factor.

The Q-Sense® E4 QCM-D system (Q-Sense AB, Vastra Frolunda, Sweden) was used for measuring the potential interaction of plasma proteins and platelets

with NPs under flow conditions. For this purpose, four temperature and flow-controlled modules were set up in parallel configuration and attached to a peristaltic microflow system (ISM 935; Ismatec SA, Glattbrugg, Switzerland) for sample perfusion. Polystyrene-coated quartz crystals with a fundamental frequency of 4.95 MHz and coated with fibrinogen (100 µg/mL, 15 min) were used as sensors as previously described. [328, 329]

The particles samples were prepared as described in the previous section, and PRP (210,000 platelets/µL), PPP (used as the control for protein plasma deposition) and PRP/PPP +/- MSNs, MSNs-PEG, or MSNs-GEL (at a final concentration of 100 µg/mL) were perfused at a flow rate of 100 µL/min for 30 min at 37 °C. Changes in frequency and energy dissipation in response to the adhesion of platelets/plasma proteins under flow conditions were recorded in real time with the Q-Sense software (QSoft401).

The results are presented as a percentage of frequency and dissipation from the third overtone, where 100% corresponds to the highest change in frequency (negative shift) and dissipation (positive shift) at 20 and 30 minutes of perfusion for the control (PPP and PRP respectively).

### 2.2.12.4 Haemolysis assay

The haemolysis assay was performed in order to assess erythrocyte integrity, by measuring haemoglobin release, when RBCs were incubated with the NPs.

For this purpose, MSNs, MSNs-PEG, or MSNs-GEL in PBS, were added at 1, 3, 5, 10, 20, 50, 75 and 100 µg/mL to RBCs in triplicate, and incubated in a 96 well plate, at 37 °C. Positive and negative control samples were prepared by adding Triton X and PBS to RBCs, respectively. Following 60 minutes of incubation, the plate was centrifuged (500 x g for 5 minutes at RT) and 100 µL of the supernatant collected. The haemolytic activity of the NPs was determined in a FLUOstar OPTIMA microplate reader (BMG Labtech, Germany) at 540 nm by

measuring the absorption peak of haemoglobin, which was released to the solution from haemolyzed cells.

### 2.2.13 *In vitro* 3D cell model assays

The NPs were also tested *in vitro* on a well-established 3D cell model of glioblastoma multiforme, in order to have a better understanding of the effect of the nano-systems in a model that mimics the complexity and three-dimensional architecture found *in vivo*.

The protocol for optimal spheroids growth is well-established in our group and described elsewhere. [330]

(The experiments with U-87 3D spheroids were carried out by Dr Amelia Ultimo, together with Ph.D. students Mila Djisalov and Teodora Knezic).

### 2.2.13.1    U-87 3D spheroids growth and viability assay

U-87 human glioblastoma multiforme cells were cultured in Minimum Essential Medium Eagle (MEM) supplemented with 10% (v/v) foetal bovine serum (FBS) and with 1% (v/v) L-glutamine and incubated in a 170L silver $CO_2$ cell culture incubator (GS Biotech, UK) at 37 ºC in 5% $CO_2$ atmosphere.

Nunclon Sphera low-attachment surface 96-well plates (Thermo Fisher Scientific, UK) were used for U-87 spheroids growth *in vitro*. U-87 cells were seeded at a density of 1,000 cells/well in 200 µL of media, centrifuged at 1,500 rpm for 10 minutes and spheroids left to grow for 4 days after incubation at 37 ºC in 5% $CO_2$ atmosphere. Subsequently, they were treated in triplicate with increasing concentrations of MSNs+DOX-PEG, or MSN-CHO+DOX-GEL (0.01, 0.1, 1, 10, 25, 50 and 100 µg /mL) for 24, 48 and 72 h. The viability of the spheroids was measured at each time point with CellTiter-Glo® 3D Cell Viability Assay (Promega Corporation, USA) and plotted as percentage (%) of luminescence normalised to the control (spheroids growing without treatment that were considered as 100%

viable). Briefly, in this assay, the amount of ATP present is quantified, which indicates the presence of metabolically active cells, and it is directly proportional to the number of viable cells present in culture. The reagent is added to the wells, mixed by shaking for 5 minutes in order to induce cell lysis and incubated at room temperature for 25 minutes. The luminescence signal is then recorded (**Fig. 2.3**) using a FLUOstar OPTIMA microplate reader (BMG Labtech, Germany).
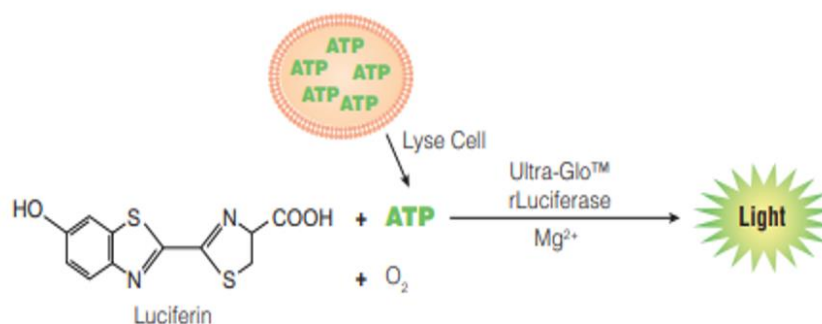


**Figure 2.3:** Principle of the CellTiter-Glo® 3D Cell Viability Assay. (https://worldwide.promega.com/products/cell-health-assays/cell-viability-and-cytotoxicity-assays/celltiter-glo-3d-cell-viability-assay/#protocols)

The spheroids were imaged using an AxioCamERc5s coupled to Nikon Diaphot 300 Inverted Phase Contrast Microscope and using the Zeiss Zen 3.1 software. The spheroid growth (diameter) was monitored before, during and after treatment at the various NPs concentration and measured using ImageJ software.

2.2.13.2    Nanoparticles internalization by spheroids

The cellular internalization of RhBITC labelled NPs by spheroids was analysed by Confocal Laser Scanning Fluorescence Microscopy. The images were obtained with a Leica TCS SP8 inverted microscope (Leica Microsystems, Germany).

MSNs-PEG-RhBITC or MSNs-GEL-RhBITC were prepared at a concentration of 100 µg/mL in MEM, added to the wells and the spheroids incubated at 37 °C. At different time points (4, 6 and 24 h), media were removed,

and the spheroids washed with PBS twice. At this point they were fixed with formaldehyde 4% buffered solution for one h, then washed twice with PBS and kept in PBS in the fridge until ready to be stained before confocal analysis. Cells cytoskeleton and cells nuclei were stained by ActinGreen™ 488 ReadyProbes™ Reagent (AlexaFluor™ 488 phalloidin, 3 drops/mL of PBS) and methyl green (5 µg/mL of PBS), respectively, followed by incubation for further 24 h at room temperature. The spheroids were then washed with PBS once and transferred in PBS to a µ–Slide 18 Well (Ibidi, Germany) and immersion oil added to each well. The NPs cellular internalization was investigated and compared to control spheroids (non-treated spheroids).

### 2.2.14 *In vivo* studies

The animal studies were performed by Dr Maria Manuela de Jesus Guilherme Gaspar, Faculty of Pharmacy, Universidade de Lisboa.

### 2.2.14.1    Animals

All animal experiments were conducted according to the Animal Welfare Organ, ORBEA, of the Faculty of Pharmacy, Universidade de Lisboa, and approved by the competent national authority Direção-Geral de Alimentação e Veterinária (DGAV) in accordance with the EU Directive (2010/63/EU) and Portuguese laws (DR 113/2013, 2880/2015, and 260/2016) for the use and care of animals in research.

Male 6-8 weeks old C57/BL6 mice were purchased from Charles River, Barcelona, Spain.

The animals (23 ± 2 g) were kept under standard hygiene conditions, in ventilated cages, at a constant temperature of 20-24 °C and 50-60% humidity, and on standard lighting conditions (12 h light / 12 dark cycle). They were fed with commercial chow and given acidified drinking water *ad libitum.*

## 2.2.14.2    *In vivo* safety assessment of MSNs-PEG and MSNs-GEL

The effect of empty PEG- and GEL-functionalised MSNs was evaluated in C57/BL6 male mice.

The particles were exposed for 1 h to UV light and resuspended under sterile conditions in glucose 5%. They were ultrasonically dispersed using an Ultrasonic Bath (Bandelin, GmbH & Co. KG, Berlin, Germany) for 1 h in order to obtain homogenization of the sample, making sure the temperature of the bath did not go above 40 °C.

The animals were divided into 5 groups of six mice each and were injected retro-orbitally with the MSNs formulations at two different doses, or with just the vehicle:

- 4.4 mg/kg (total daily dose) of body weight of MSNs-PEG.
- 13.9 mg/kg (total daily dose) of body weight of MSNs-PEG.
- 5.64 mg/kg (total daily dose) of body weight of MSNs-GEL.
- 17.8 mg/kg (total daily dose) of body weight of MSNs-GEL.
- 5% glucose only.

Two injections (150 µL each) were performed daily, for five consecutive days, for a total of 2 weeks (for a detailed description of the calculations for MSNs formulations preparation see **Appendix 4**, **Table A4. 1**).

Body weight and animal behaviour (signs of pain and/or distress) were monitored every day. Three days after the last injection, mice were anesthetized, following exposure to isoflurane, blood samples were collected by cardiac puncture and then euthanized by cervical dislocation. Vital organs under study namely liver, spleen, lung, and kidney were collected, weighed (for tissue index determination) and subsequently sent for histological analysis. Serum of all animals was tested for aspartate aminotransferase (AST), alanine transaminase (ALT), γ-glutamyl transpeptidase (GGT) and urea.

The tissue index was calculated according to the following equation (**3**) [331]:

$$Tissue\ index = \sqrt{\frac{organ\ weight}{animal\ weight}} \times 10 \qquad (3)$$

## 2.2.14.3    Lung cancer model

The lung cancer model was established by carrying out three separate assays, injecting the mice with different LLC1 concentrations in order to decide which was the most suitable one. For each assay the groups comprised 5 mice in total, 4 animals received the cancer cells, and the 5th was the naïve animal:

1) In the first assay, the mice received 100,000 LLC1 cancer cells retro-orbitally and animals were sacrificed 15 days after injection. During the experimental protocol, the animal weight was recorded. Histological analysis of selected organs was performed after the mice had been sacrificed.

2) In the second assay, the mice received 500,000 LLC1 cancer cells retro-orbitally and animals were sacrificed 15 days after injection. During the experimental protocol, the animal weight was recorded. Histological analysis of selected organs was performed after the mice had been sacrificed. The tissue index values for lung, liver, kidney, and spleen were determined.

3) In the third assay, three groups of mice received 100,000 LLC1 cancer cells retro-orbitally, and animals were sacrificed 15, 30 and 35 days after the injection. During the experimental protocol, the animal weight was recorded. Histological analysis of selected organs was performed after the mice had been sacrificed. The tissue index values for lung, liver, kidney, and spleen were determined.

## 2.2.14.4    *In vivo* efficacy assessment

For tumour induction, a total of 200,000 LLC1 cancer cells, suspended in PBS (150 µL), were injected retro-orbitally. After two weeks the animals were randomly divided into 6 groups of five mice each:

- Group 1 received MSNs+PTX-PEG at the highest concentration (corresponding to a total of 8 mg/kg of PTX weekly).
- Group 2 received MSNs-CHO+PTX-GEL at the highest concentration (corresponding to a total of 8 mg/kg of PTX weekly).
- Group 3 received empty MSNs-PEG.
- Group 4 received empty MSNs-GEL.
- The positive control group received free PTX in CrEL at a dose of 8 mg/kg
- The negative control group received glucose 5% only.

Two injections (150 µL each) were performed daily, for five consecutive days.

Body weight and animal behaviour for any sign of pain and/or distress were monitored every day.

Three days after the last injection, mice were anesthetized, following exposure to isoflurane, blood samples were collected by cardiac puncture and then euthanized by cervical dislocation. Blood and vital organs were collected for analysis as stated above. Tissue index was calculated according to Eq. (**3**).

2.2.15 Statistical analysis

All data presented in this thesis were plotted as mean ± Standard Error of the Mean (SEM) from at least 3 independent experiments (in some instances only 2 experiments were carried out and, in that case, appropriately indicated) and were analysed using GraphPad Prism 9 (GraphPad Software, San Diego, California USA). Analyses of variance (ANOVA) followed by Tukey's or Bonferroni's post-test (comparing all treatment groups), or Dunnett's post-test (comparing treatment

groups against the control), were performed where relevant. Data were considered significant when p ≤ 0.05 (*), p ≤ 0.01 (**), p ≤ 0.001 (***), or p ≤ 0.0001 (****).

# 3 CHAPTER 3: MESOPOROUS SILICA NANOPARTICLES AS TRIGGERED DRUG DELIVERY SYSTEM

## 3.1 Synthesis and characterization of MCM-41

MCM-41 type of MSNs was synthesised using a modified Stöber method (**Fig. 3.1**), based on the sol-gel process, which consists in using a cationic surfactant as the template around which the inorganic silica precursor can condense and build the network via formation of siloxane bonds, in a base-catalysed environment. The Rhodamine B Isothiocyanate functionalised MSNs were synthesized by co-condensation methods, which consists in employing functional silanes in conjunction with TEOS allowing the *in-situ* insertion of various functional groups to the silica surface during the synthesis process.
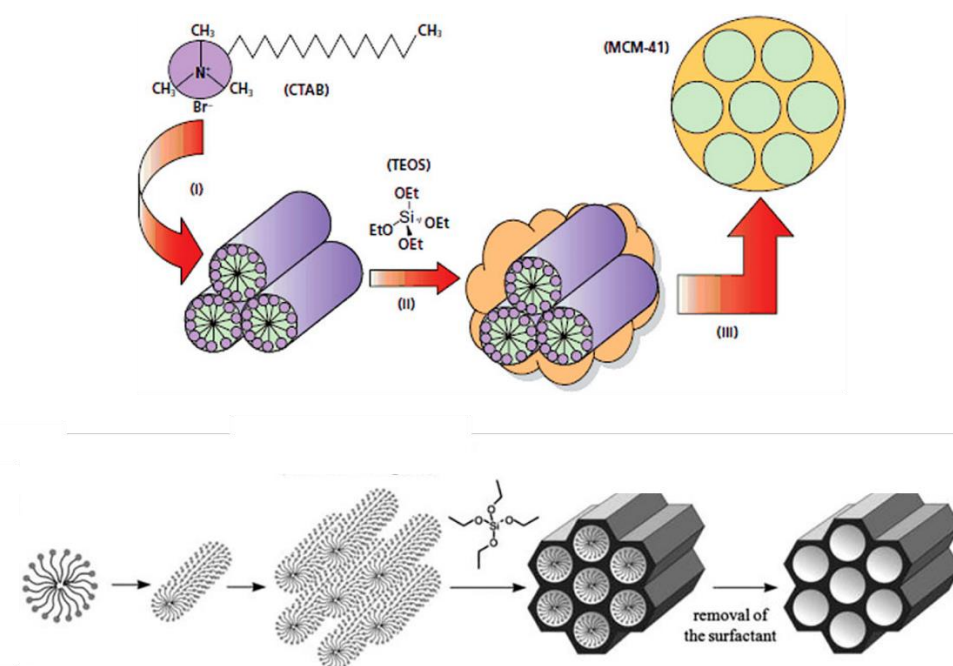


**Figure 3.1:** MCM-41 type of MSNs synthesis. [332]

In literature, different MSNs synthesis methods have been reported (**Table 3.1**), which yield to particles with different diameter and pore sizes. [333]

**Table 3.1:** MSNs synthesis methods. (*Adapted with permission of Royal Society of Chemistry, from Nanoscale, 2010. 2(10): p. 1870-1883.*) [333]

| MAIN PRECURSOR | STRUCTURE DIRECTING AGENT | PARTICLE SIZE (nm) | PORE DIAMETER (nm) | pH CONDITIONS |
|---|---|---|---|---|
| **TEOS (tetraethyl orthosilicate)** | CTAB (cetyltrimethylammonium bromide) | 15 | 3 | Alkaline |
| **TEOS** | CTAC (cetyltrimethylammonium chloride) | 20–50 | 3 | Alkaline |
| **TEOS/APTS (tetraethyl orthosilicate / (3-Aminopropyl)triethoxysilane)** | Fatty acid | 270 | 3 | Alkaline |
| **TEOS** | CTAB, dodecyl amine | 65–740 | 3 | Alkaline |
| **TEOS/organo silanes** | CTAB | 50–200 | 3 | Alkaline |
| **TEOS/APTS** | CTAB | 70–100 | 3 | Alkaline |
| **Waterglass** | P123 (Pluronic P123) | 50–300 | 5–7 | Acidic |
| **TEOS/APTMS (tetraethyl orthosilicate / (3-Aminopropyl)trimethoxysilane)** | CTAB | 30–280 | 3 | Alkaline |
| **TEOS** | CTAB | 40–550 | 3 | Neutral |

| | | | | |
|---|---|---|---|---|
| **TMOS (tetramethyl orthosilicate)** | CTAB | <20 | 3 | Alkaline |
| **TEOS** | F127 (Pluronic F127) | 50–300 | 17–20 | Acidic |
| **TEOS/thiol-silane** | CTAB | 200–250 | 2.3–2.7 | Alkaline |
| **TEOS** | $C_n$TAB ($n$ = 14, 16 and 18), $C_n$TAC ($n$ = 10, 16) | 70–150 | 1.6–3 | Close to neutral |
| **TMOS** | $C_n$TAC ($n$ = 14, 16 and 18) | 150–870 | 2–2.3 | Alkaline |
| **TEOS** | F127 | 120 | about 6 nm | Acidic |

After the particles were synthesised, the template was removed from the pores of the NPs by solvent extraction method. For well-dispersed, uniform NPs, the template removal procedure is crucial. Solvent extraction techniques are commonly used to remove the template, as calcination can cause issues with particle re-dispersibility and inter-particle condensation. Moreover, since CTAB, which is one of the most used structure directing agents, is cytotoxic, an insufficient template removal could restrict the application of the particles in biological systems. [333]

The NPs were dried and recovered after the template removal process, and were subsequently characterised by different techniques, in order to analyse and confirm the morphology and size of the particles, the pore volume and surface area, the ordered pore structure, the successful removal of the template, the chemical composition, and the hydrodynamic diameter and zeta potential of the NP dispersion.

### 3.1.1 Removal of the template: Thermogravimetric Analysis (TGA) and Fourier transform infrared (FTIR)

Thermogravimetric Analysis (TGA) and Fourier transform infrared (FTIR) analysis were carried out in order to confirm the effective removal of the template from the pores of the synthesised MCM-41 NPs.

The presence of residual surfactant can be toxic to cells, and it is important to ensure that the extraction method removes as much surfactant as possible. CTAB is known to degrade between 100 and 300 °C. [334, 335] The TGA analysis (**Fig. 3.2 A**) showed that the total amount of CTAB present in the pores of the as-synthesized MCM-41 particles was around 35%. After completion of the extraction process, the total amount of residual surfactant left was calculated to be 4%. It is worth noting that it is not possible to completely remove the surfactant with the extraction method, unlike calcination, and multiple extraction cycles may be required to remove as much surfactant as possible. [308] It is critical to keep the residual surfactant content below 5%: CTAB is known to be toxic to cells. [336-341] The released molecules and the double-layer structure of CTAB are responsible for its toxicity. [337, 339, 342-344] The positively charged surfactant interacts with the negatively charged cell membrane, disrupting it, and eventually leading to the cells' death. [339, 343, 345] Therefore, minimizing the residual surfactant content is important to ensure the biocompatibility of the synthesized NPs.

The presence or absence of specific bands in the FTIR spectra can provide information about the chemical composition of the sample being analysed. Before the extraction of the surfactant (**Fig. 3.2 B**), the FTIR spectrum of the NPs showed bands corresponding to the symmetric and asymmetric stretching of methyl (-CH$_3$) and methylene (-CH$_2$) groups, as well as the bending of methylene (-CH$_2$) groups, at 2900 and 1400 cm$^{-1}$, respectively. These bands are characteristic of the CTAB template molecule. After the extraction of the template (**Fig. 3.2 B**), the FTIR spectrum of the NPs did not show these bands, indicating the successful removal of the template from the NPs' pores. Additionally, the FTIR spectra also showed typical bands from MSNs: the Si-O-Si stretching band at 800 cm$^{-1}$, the Si-OH stretching vibration band at 960 cm$^{-1}$, and the Si-O-Si asymmetric stretching band

at 1050 cm$^{-1}$. These bands indicate that the NPs maintained their structure and properties even after the extraction of the surfactant template.
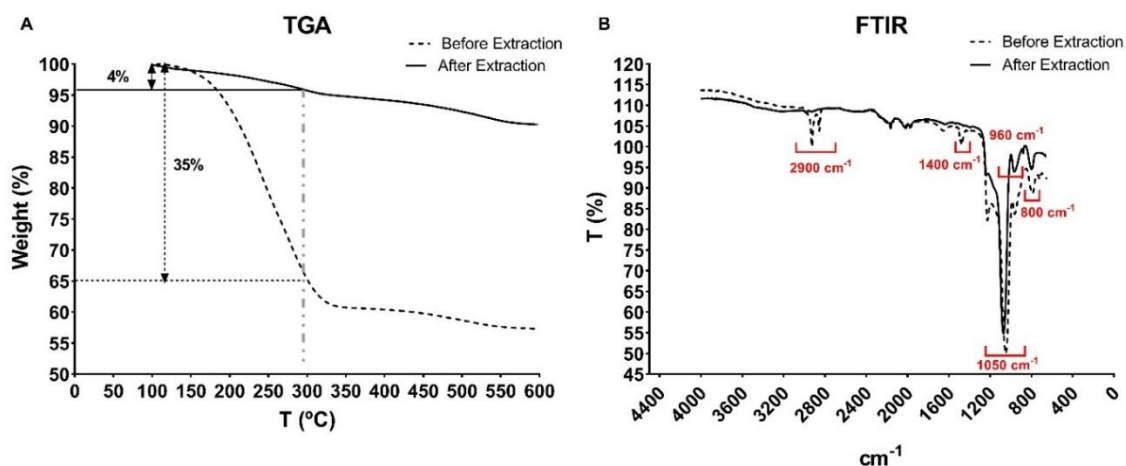


**Figure 3.2: A-** TGA curve of MCM-41 type of MSNs before and after extraction of the template. **B-** FTIR spectra of MCM-41 type of MSNs before and after extraction of the template.

### 3.1.2 Size and morphology: Scanning Electron Microscopy (SEM)

The synthesised MCM-41 NPs were characterized in the dry state by scanning electron microscopy (SEM). The images of the synthesised MSNs were taken with an InLens (**Fig. 3.3 A**) and a SE2 detector (**Fig. 3.3 B**), at two different magnifications. From the SEM images, it can be confirmed that the synthesised particles have a near spherical morphology, and a uniform size distribution around 100 nm. Additionally, the images showed that the MSNs tend to form aggregates. Overall, scanning electron microscopy is a strong tool for evaluating the shape and size distribution of NPs. It is important to keep in mind, however, that SEM only offers information on the particles in their dry state and may not represent their behaviour in solution. Additional characterization techniques, such as dynamic light scattering (DLS), are required to completely understand the NPs' characteristics.
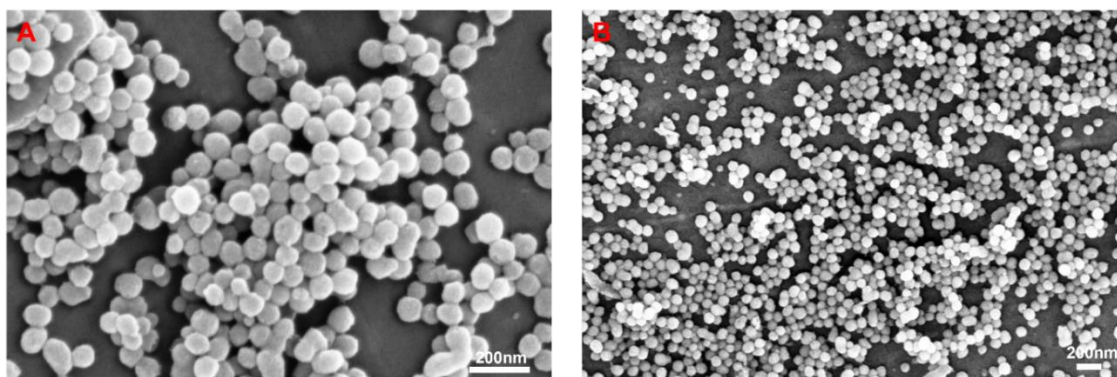
**Figure 3.3:** Scanning electron microscope images of the synthesised MCM-41 NPs with **A-** InLens and **B-** SE2 detectors.

### 3.1.3 Hydrodynamic diameter and surface charge

The synthesised NPs were further characterised in the wet state by Dynamic Light Scattering (DLS) and zeta (ζ)-potential measurements. The DLS analysis revealed that the mean hydrodynamic diameter for two separate batches (MSNs$_1$ and MSNs$_2$) of the particles was 215±18 nm (**Fig. 3.4 A**) with a PdI of 0.2, which is consistent with the uniform size distribution observed with SEM. However, the diameter measured with DLS was slightly larger than the one observed with SEM because of the formation of a layer of counterions (hydrate layer) on the surface of the particles in the wet state, due to the presence of a surface charge. [346] ζ-potential measurements showed that the synthesized NPs had a negative charge on their surface, with values around -21 mV (**Fig. 3.4 B**). This is indicative of the presence of negatively charged silanol groups on the particle surface. The ζ-potential values can also explain why the MSNs tend to aggregate in suspension: in fact, when the zeta potential of NPs falls between ±10 and ±30, the suspensions become less stable, leading to particle aggregation. [347]
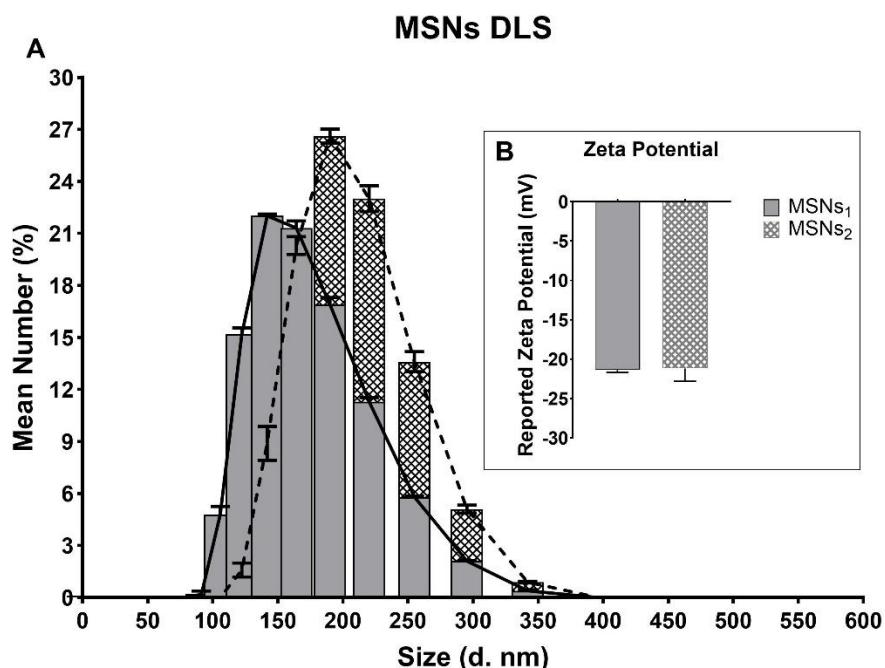
**Figure 3.4: A-** Size distribution (3 measurements) by number (%), measured by dynamic light scattering of the synthesised MCM-41 type of MSNs (mean±SEM). For size distribution by intensity, and correlograms see **Appendix 1**. **B-** Zeta *(ζ)*-potential distribution of the synthesised MCM-41 MSNs. (mean±SEM).

### 3.1.4 Low-angle X-Ray Diffraction (XRD) and Nitrogen Adsorption-Desorption Analysis

X-ray diffraction is used to obtain information about the crystalline structure of materials, while low-angle XRD provides information about the long-range microstructure. Before and after extraction of the template, the typical low-angle patterns of MCM-41 were observed (**Fig. 3.5 A**), confirming the porous order of the MSNs. There is no crystallinity at the atomic level and for this reason no peaks were seen at higher degrees. The synthesized particles showed the typical hexagonal mesopore order of MCM-41 NPs, which is characterized by the four main reflection lines d100, d110, d200, and d210 at low angles ($2\theta \leq 10°$). The sharp peak centred at $2.2°$ and three smaller peaks between $3.5°$ and $5.5°$ are indicative of the hexagonal structure of MCM-41 and demonstrate that this was not damaged by the extraction of the template.

100
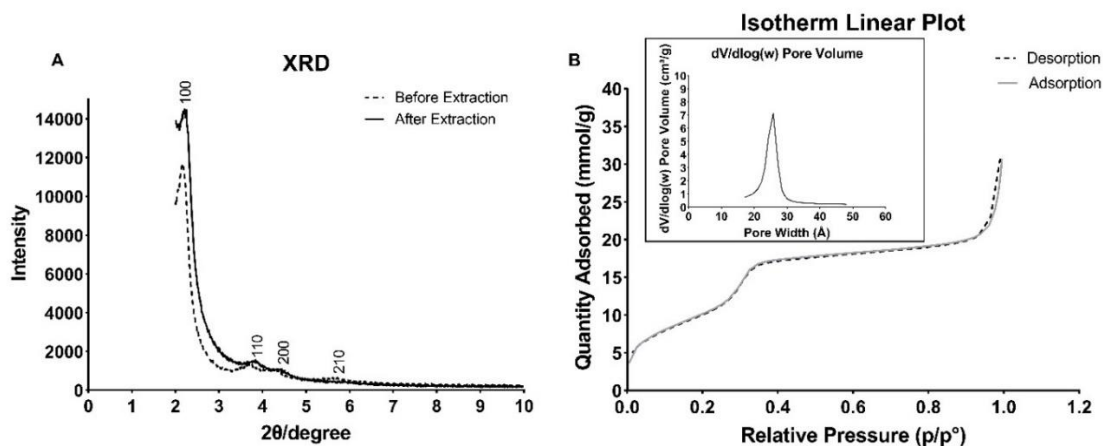
**Figure 3.5: A-** XRD patterns of the synthesised MCM-41 type of MSNs before and after extraction of the template. **B-** N$_2$ adsorption-desorption isotherm of the synthesised MCM-41 type of MSNs. **B inset-** BJH Adsorption dV/dlog(w) Pore Volume of the synthesised MCM-41 type of MSNs.

The particles showed a characteristic type IV(b) N$_2$ adsorption-desorption isotherm (**Fig. 3.5 B** and **3.6 A**) of MCM-41 type of MSNs with well-defined adsorption of nitrogen at relative pressure (p/p$^o$) of 0.2 - 0.4, confirming the presence of the meso-channels.

The graph (**Fig. 3.5 B**) shows the N$_2$ amount adsorbed, plotted against the equilibrium relative pressure. When analysing the gas adsorption of mesoporous materials, what is observed is a multilayer adsorption followed by capillary condensation. A first adsorption process is observed between p/p$^0$ 0.2 - 0.4, which corresponds to the nitrogen condensation inside the mesopores by capillarity; a second adsorption process can be observed at relative pressure > 0.9, which corresponds to the filling of the voids among the particles.

Type IV isotherms (**Fig. 3.6 A**) can present hysteresis loops (**Fig. 3.6 B**) because capillary condensation and capillary evaporation often do not take place at the same pressure, or, in other terms, the desorption isotherm branch does not coincide with the adsorption isotherm branch. The H1 hysteresis loop is one of the most common types of hysteresis observed in Type IV isotherms. This type of hysteresis loop is symmetrical, and the adsorption and desorption branches are similar, indicating the presence of mesoporous materials that have uniform

cylindrical pores, with open ends and with a narrow pore size distribution, typical of mesoporous materials such as MCM-41, MCM-48, and SBA-15. [348-350] However, in our case the isotherms of the analysed MSNs batches did not present any hysteresis.

A BET surface area between 700 and 1000 m²/g was calculated for different batches. This high surface area is the reason for the tendency of MSNs to form aggregates. The BJH average pore diameter was 2.5 nm (**Fig. 3.5 C**) and the calculated pore volume was between 0.6 and 0.9 cm³/g.
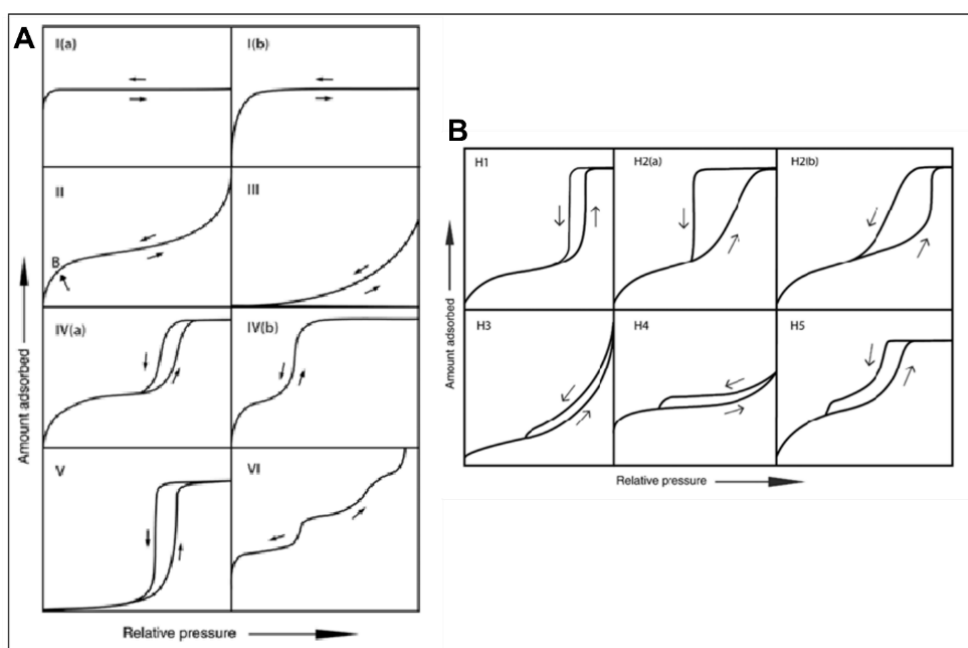


**Figure 3.6: A-** Updated classification of physisorption isotherms. **B-** hysteresis loops of the original IUPAC classification from 1985. [348]

## 3.1.5 Transmission Electron Microscopy (TEM)

The morphology and the pores structure of the NPs were also analysed by Transmission Electron Microscopy (TEM). With this technique it was possible to confirm the presence of uniform, unidirectional pores, arranged in a honeycomb structure (**Fig. 3.7 A, B, C** and **D**), and the spherical shape of MSNs, with an average size of 100 nm.
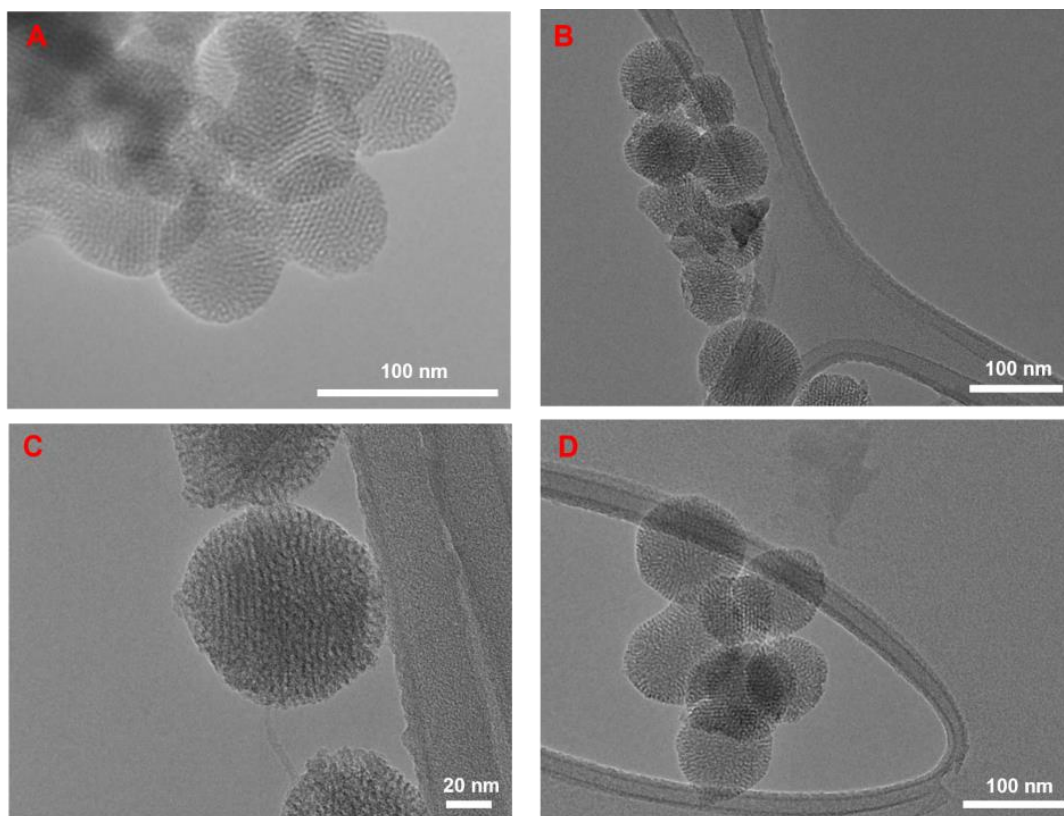
**Figure 3.7: A-, B-, C-** and **D-** TEM images of the synthesised MSNs.

## 3.1.6  MSNs functionalization

The presence of highly reactive silanol groups in high density on the surface of MSNs allows their functionalization, enabling the mesoporous material's surface to be tailored to specific applications like the stabilization of biomolecules such as enzymes or antibodies. Mesoporous nanomaterials can also be functionalized to improve their properties: for instance, the addition of hydrophilic groups can improve their water stability. [332]

### 3.1.6.1  Functionalization with Polyethylene glycol (PEG)

MSNs are known to have a high tendency to aggregate, due to their high surface area, and also due to the presence of silanol groups which can form siloxane bridges when the particles are dried, making re-dispersibility difficult.

PEGylation is a commonly used technique for improving the colloidal stability and dispersibility, and for reducing protein adsorption on the NPs surface prolonging their circulation time in biological environments. PEG is a hydrophilic polymer that forms a layer around the surface of the NPs, creating a steric barrier that reduces the interaction between the NPs and blood serum proteins. This steric barrier is often referred to as "molecular cushion". [333, 351]

The successful functionalization of MSNs with PEG was confirmed by DLS, ζ-potential, TGA and FTIR analyses.

DLS analysis (**Fig. 3.8 A** and **B**) indicates that functionalization with PEG improved the dispersion of the NPs. It can be seen that for one of the two batches of MSNs analysed (**Fig. 3.8 A**), the functionalization did not cause significant changes in the NPs' size, with an average hydrodynamic diameter of 223±3 nm (before functionalization the average size recorded was 239±4 nm). However, the PdI improved, decreasing from 0.242±0.052 for the unfunctionalized NPs, to 0.160±0.010 for MSNs-PEG, indicating a more uniform distribution of the particles. For the second batch (**Fig. 3.8 B**), it can be seen that PEGylation not only improved the PdI (from 0.266±0.012 for the unfunctionalized MSNs, to 0.161±0.021 for MSNs-PEG), but the hydrodynamic size also decreased, with particles' hydrodynamic diameter decreasing from around 206±5 nm to around 168±2 nm. The better re-dispersibility of MSNs following functionalization with PEG was confirmed.
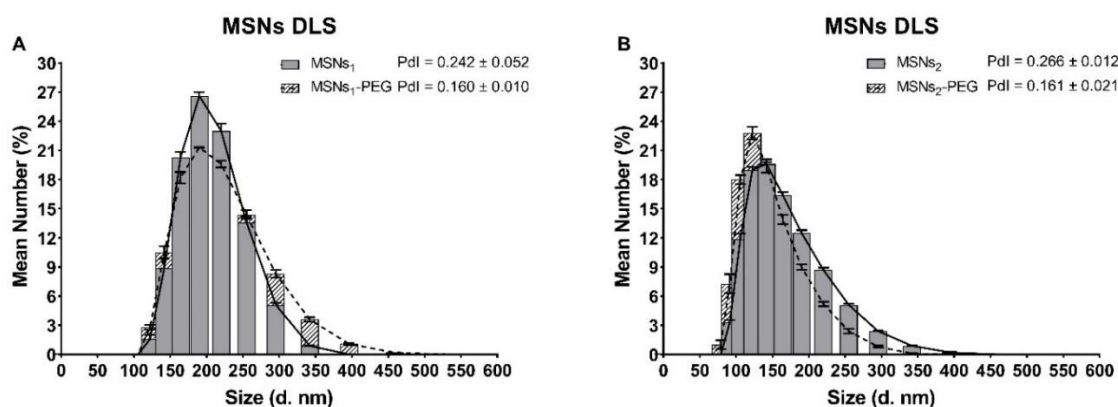


**Figure 3.8: A-** and **B-** Size distribution (3 measurements) by number (%), measured by dynamic light scattering of the synthesised MCM-41 type of MSNs before

(MSNs) and after (MSNs-PEG) PEGylation (mean±SEM). For size distribution by intensity (%) see **Appendix 1**.

Zeta ($\zeta$)-potential analysis results also confirmed the successful functionalisation, as it can be observed how the surface charge of the NPs (**Fig. 3.9**) changed from -21±2 to -23±0 mV (MSN$_1$) and from -16±1 to -25±0 mV (MSN$_2$) after grafting a layer of PEG on their surface via disulphide bonds, improving their colloidal stability.
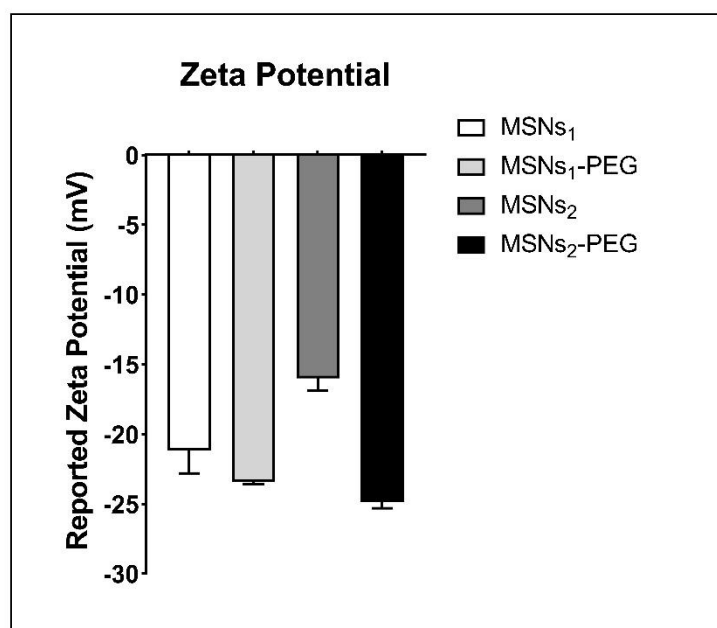


**Figure 3.9:** Zeta potential values of the synthesised MCM-41 type of MSNs after template extraction (MSNs), and functionalization with PEG (MSNs-PEG).

By FTIR analysis, it was also possible to confirm the presence of a layer of PEG on the particles' surface. In **Fig. 3.10 A** and **B** we can see the FTIR spectra of two different MSNs batches before and after PEG functionalization: before poly-(ethylene glycol) addition, the particles spectra showed the typical MSNs' bands as previously described, whereas after PEG addition, we could additionally observe the polymer's C-H bending bands between 1420 and 1538 cm$^{-1}$, and one C-H stretching band at 2980 cm$^{-1}$. The introduction of PEG onto the particles' surface was therefore confirmed once again. [352]
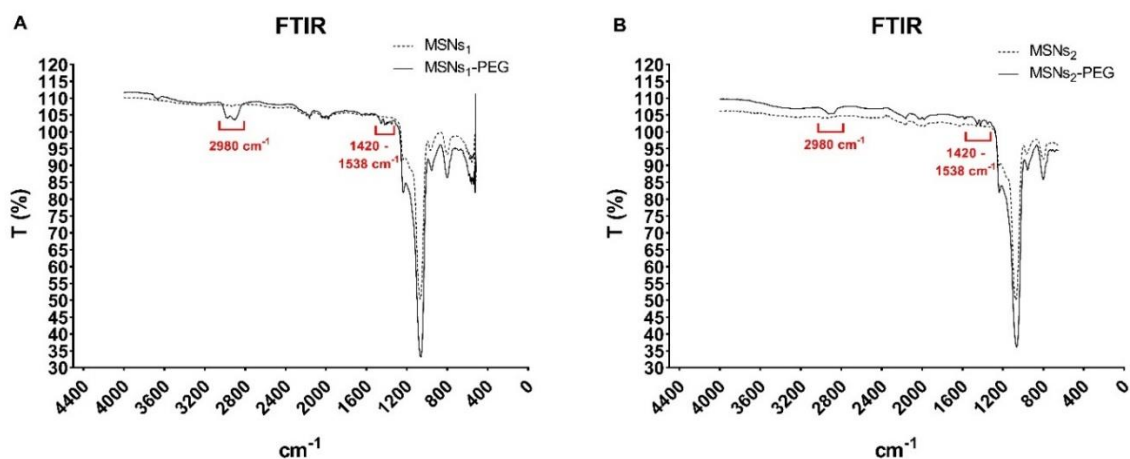
**Figure 3.10: A-** and **B-** FTIR spectra of MCM-41 type of MSNs before (MSNs) after (MSNs-PEG) functionalization with PEG.

Thermogravimetric analysis confirmed the presence of a layer of PEG on the surface of the NPs too. The results of the TGA analysis (**Fig. 3.11 A** and **B**) showed that both batches of the functionalized MSNs had a higher percentage of organic material loss when compared to the unfunctionalized NPs.
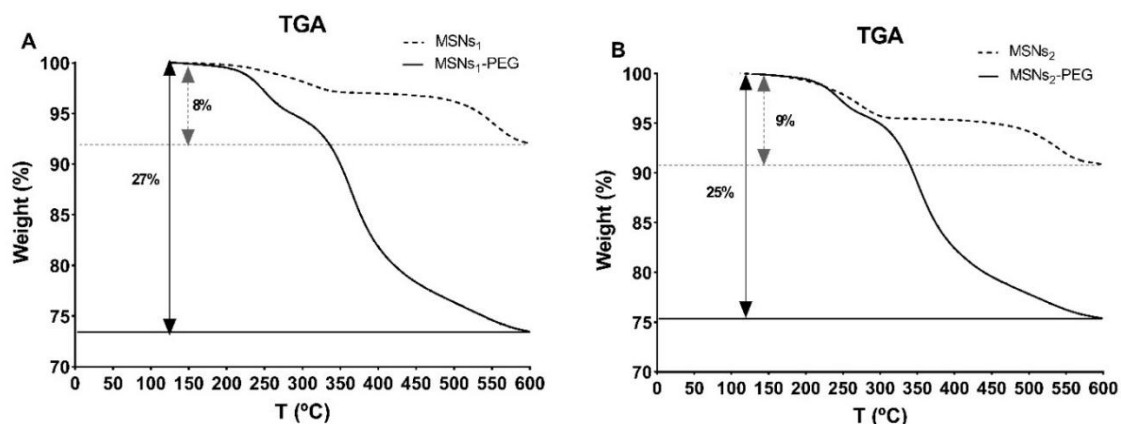


**Figure 3.11: A-** and **B-** Thermogravimetric analysis of MCM-41 type of MSNs before (MSNs) and after (MSNs-PEG) PEG functionalization.

3.1.6.2 Functionalization with gelatine (GEL)

The gelatine (GEL) functionalization was used as a capping system in order to avoid a premature leakage of the loaded cargo from MSNs, and in order to respond to the overexpression of MMPs in the tumour microenvironment.

Gelatine is a collagen derivative, which is produced through partially acidic or alkaline hydrolysis of animal collagen (i.e., from the skin or bones of bovines or pigs). The intra- and inter-molecular covalent bonds that stabilize collagen are hydrolysed by an acid (type A GEL) or a base (type B GEL) and it is considered a GRAS (Generally Recognized As Safe) substance by the FDA, with a long history of usage in pharmaceutical, cosmetic, and food products. Gelatine has a natural origin and is biodegradable, with low toxicity and non-immunogenic properties due to its partial denaturation, while collagen can produce an immune response. Moreover, gelatine possesses Arg-Gly-Asp sequences that regulate cell adhesion, improving its final biological behaviour as opposed to polymers that do not have these cell-recognition sites. [143, 353-356]

The successful functionalization of MSNs with GEL was confirmed by DLS, ζ-potential, TGA and FTIR analyses.

DLS analysis (**Fig. 3.12 A and C**) of two different batches of unfunctionalized (MSNs-CHO) and functionalised (MSNs-GEL) NPs, showed that the hydrodynamic size of the particles increased upon grafting of gelatine on their surface (from 220±2 to 253±5 nm for batch No 1, and from 207±5 to 442±6 nm for batch No 2), with an increase in the PdI values too, which can be explained by the formation of a thicker hydration layer on functionalised NPs due to the presence the hydrophilic polymer coating. These findings are consistent with previously published works. [353, 357] The PdI values of the particles after GEL functionalization, despite being higher, remained in the range 0-0.5, indicating that the suspension was homogenous and monodisperse. [358]
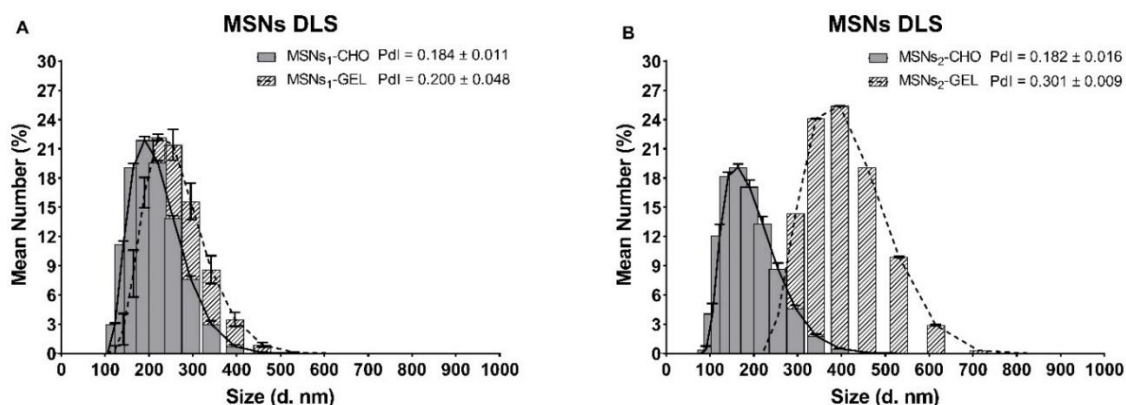
**Figure 3.12: A-** and **B-** Size distribution by number (%), measured by dynamic light scattering of the synthesised MCM-41 type of MSNs before (MSNs-CHO) (3 measurements) and after (MSNs-GEL) (5 measurements) functionalization with GEL (mean±SEM). For size distribution by intensity (%) see **Appendix 1**.

The effective functionalization was further supported by ζ-potential analysis, which showed that the positive charge of MSNs functionalized with amino groups and GTA (23±4 mV) had reduced following gelatine functionalization (2±2 mV) (**Fig. 3.13**). Gelatine type A has an isoelectric point (pI) in the range of 7-9, which explains why values very close to zero were recorded when analysing MSNs-GEL ζ-potential in water. [359] As reported by Liao Y.-T. and colleagues, [360] the lower surface charge of gelatine would neutralize the particles' ζ-potential and make it less positive in our case, as it was observed.
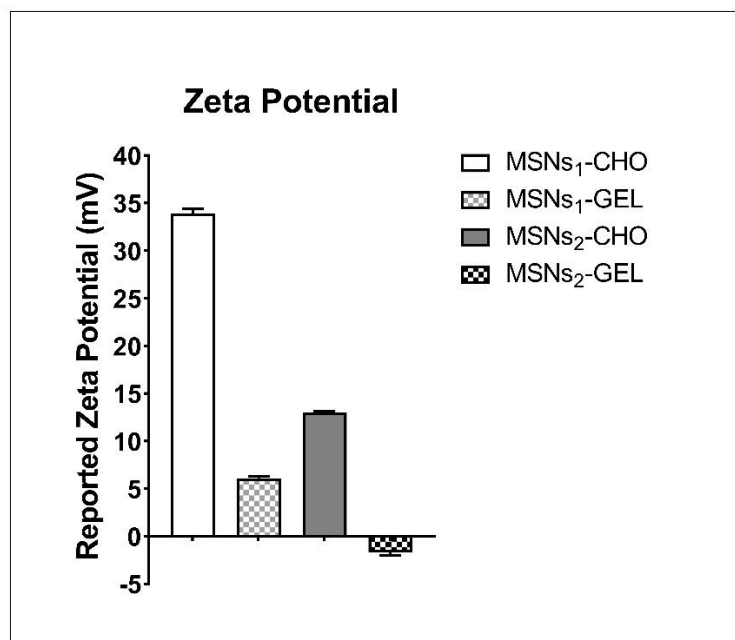
**Figure 3.13:** Zeta potential values of unfunctionalized (MSNs-CHO) and gelatine functionalised (MSNs-GEL) NPs.

The successful functionalization with GEL was confirmed by FTIR analysis (**Fig. 3.14 A** and **B**). MSNs-GEL spectra showed bands around 1650 cm$^{-1}$ and 1545 cm$^{-1}$, corresponding respectively to C=O stretching and C-H stretching / N-H bending from the gelatine's amide vibrations, indicating the presence of gelatine in the sample. Additional bands around 1440 cm$^{-1}$ can be attributed to aldimine (RCH=NR) stretching vibration, which confirms the crosslinking of gelatine (**Fig. 3.14 C**) with GTA. [355, 357]

Thermogravimetric analysis also confirmed the presence of gelatine on the surface of the NPs. The TGA curves shown in **Fig. 3.15 A,** and **B** demonstrate the difference in weight loss as the temperature increases for two different batches of functionalized and unfunctionalized MSNs. The higher percentage of organic material loss observed in the functionalized MSNs can be attributed to the presence of the gelatine layer. These results suggest that the gelatine layer was successfully grafted onto the surface of the MSNs, providing evidence of a successful functionalization. Moreover, the differences observed between the two batches could be due to the presence of a smaller or larger layer of gelatine on the

particles' surface, which could also explain the differences observed between the two batches' DLS and ζ-potential results.
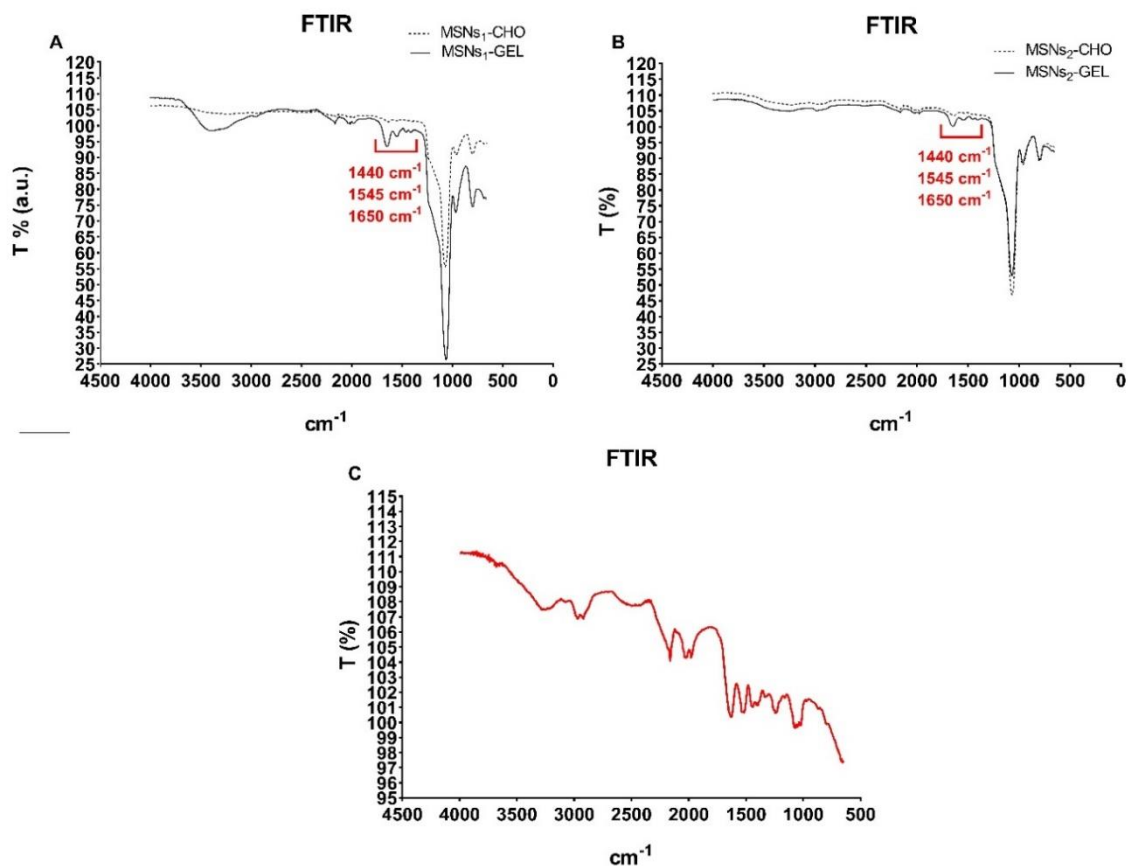


**Figure 3.14: A-** and **B-** FTIR spectra of MCM-41 type of MSNs before (MSNs-CHO) and after (MSNs-GEL) functionalization with GEL. **C-** FTIR spectra of gelatine (type A) from porcine skin.
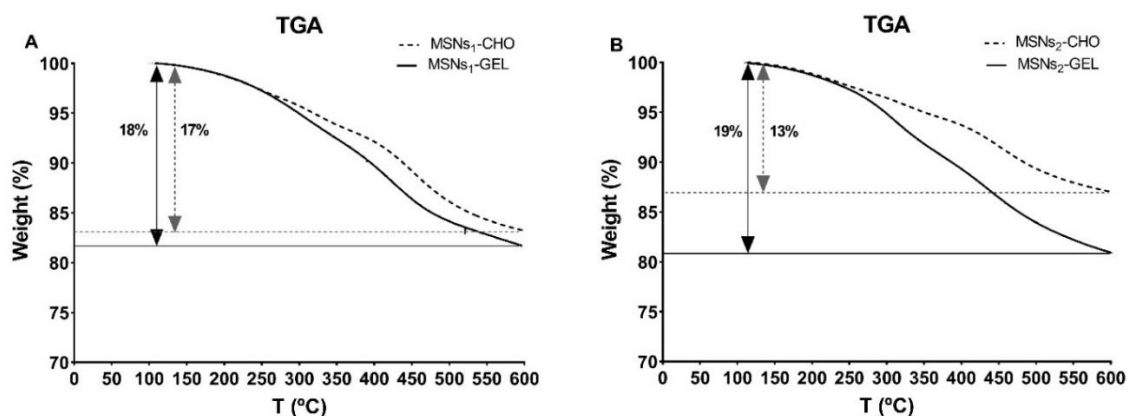


**Figure 3.15: A-** and **B-** Thermogravimetric analysis of MCM-41 type of MSNs before (MSNs-CHO) and after (MSNs-GEL) GEL functionalization.

The successful functionalization with gelatine was further confirmed by TEM analysis after the staining of the organic layer with 1% phosphotungstic acid (PTA). The organic coating could be seen in TEM images as areas of high contrast (**Fig. 3.16**), while the inorganic silica matrix could be seen as brighter zones. [357]
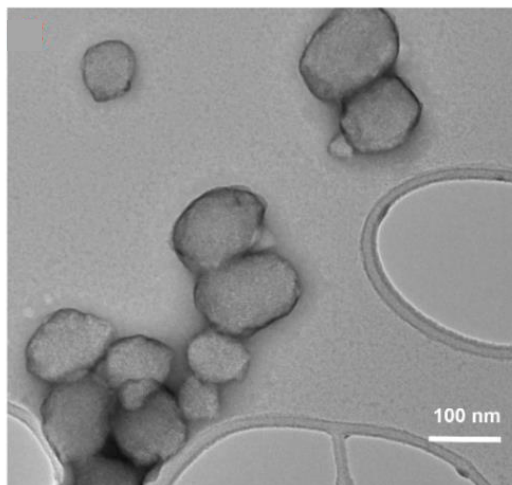


**Figure 3.16:** TEM image of MSNs functionalised with gelatine. Samples were stained with 1% of phosphotungstic acid (PTA).

### 3.1.7 MSNs loading, functionalization and *in vitro* release studies

After confirming all of the MCM-41 NPs' characteristic features, the particles were loaded with Paclitaxel (PTX), the model drug chosen for our studies, while other MSNs batches were loaded with Doxorubicin Hydrochloride (DOX), in order to conduct *in vitro* studies on a 3D model of glioblastoma multiforme.

As a proof of concept for the PEG and GEL gating systems during release studies, safranin-O was also loaded into the NPs.

Significant amounts of drug can be introduced into the porous matrix by adsorption on the pore walls since MSNs have high specific areas and pore volumes. This makes MSNs an ideal carrier for hydrophobic drugs, as they can be loaded in non-aqueous media where repulsive forces between the carrier and drug are minimized; on top of that MSNs' structural integrity is preserved in organic solvents. [333]

### 3.1.7.1 Paclitaxel (PTX)

Paclitaxel (PTX) is a very potent chemotherapeutic drug which is used for a variety of cancers, including NSCLC, but its poor water solubility limits its usage. [361-364] Many studies have been carried out in order to improve the solubility of poorly water-soluble drugs, and consequently their bioavailability, in the past recent years. [365-374] Since Cremophor EL® (the most commonly used vehicle for PTX) can cause a series of side effects, [375-380] and impact the pharmacokinetics of PTX, researchers have been working in order to find less toxic alternatives to deliver this hydrophobic drug. One of these is Abraxane®, a protein-based nanoscale DDS PTX formulation for infusion where PTX is bound to albumin, a human blood protein which aids in the solubilization of the drug, enabling its administration without the use of toxic solvents, and enabling the drug to circulate in the body for a longer period of time. [381-386] However, the cost of using human albumin in large quantities can be a limiting factor and therefore there is ongoing research to develop alternative Cremophor EL®-free formulations of PTX that are more cost-effective while maintaining the safety and efficacy of Abraxane®. [387-390]

MSNs have been reported in the literature as suitable carriers for hydrophobic drugs like PTX, and others. [325, 388, 391, 392]
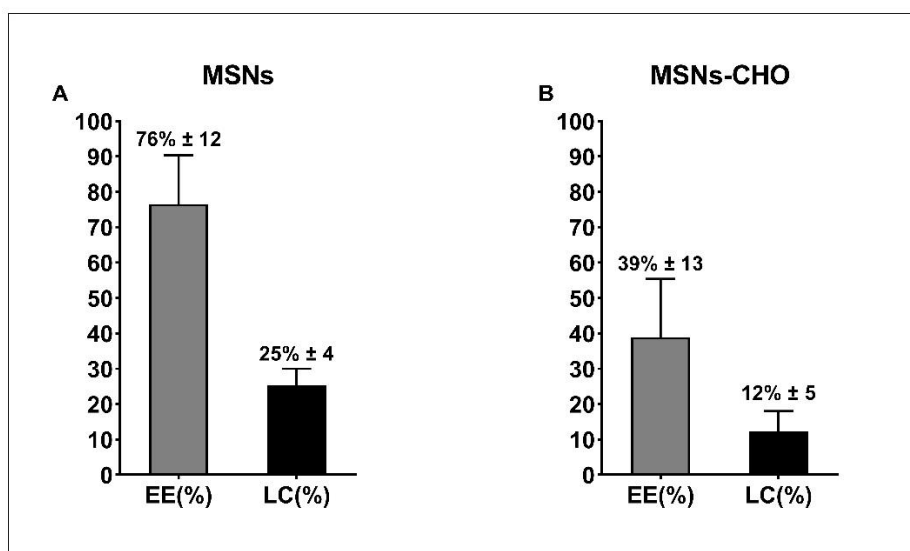
**Figure 3.17:** Paclitaxel encapsulation efficiency (EE%) and loading capacity (LC%) for **A-** MSNs and **B-** aldehyde-functionalised MSNs. (mean±SEM)

Dichloromethane (DCM) was used as the loading medium to adsorb PTX into the mesopores via a solution immersion method. Due to its low polarity, DCM has been shown to be more effective in encapsulating larger amounts of PTX than other solvents such as ethanol and DMSO. [388] Our findings demonstrate that MSNs (**Fig. 3.17 A**) have a good loading capacity, with an average amount of drug loaded equal to 250 µg per mg of NPs, which is consistent with what is reported in the literature. [388] The observed variability across MSNs batches might be attributed to experimental errors induced by the high volatility of DCM. Variability in particle pore diameters may potentially explain the observed discrepancies across batches, since MSNs with bigger pore sizes may facilitate the entrance of molecules into the pores. The study by Jia L. *et al.*, [325] showed how the loading capacity of MSNs with pores with a size around 10 nm was almost two times higher than the one from MSNs with pores of 3 nm. In a later study, [393] it was reported that MSNs with bigger pores could load higher amounts of DOX. The diameters of the pores in our study did not vary that much across batches (**Fig. 3.18 A**) as in the cited works, but we cannot rule out the possibility that the changes in pore sizes and volumes might have had an effect on the loading capacity, explaining the observed variability. It is also known that the high surface area of MSNs contributes to a higher drug loading capacity. The availability of a higher number of adsorption

113

sites in some MSNs batches leads to an increase in the amount of drug that can be loaded into the NPs. [394-398]
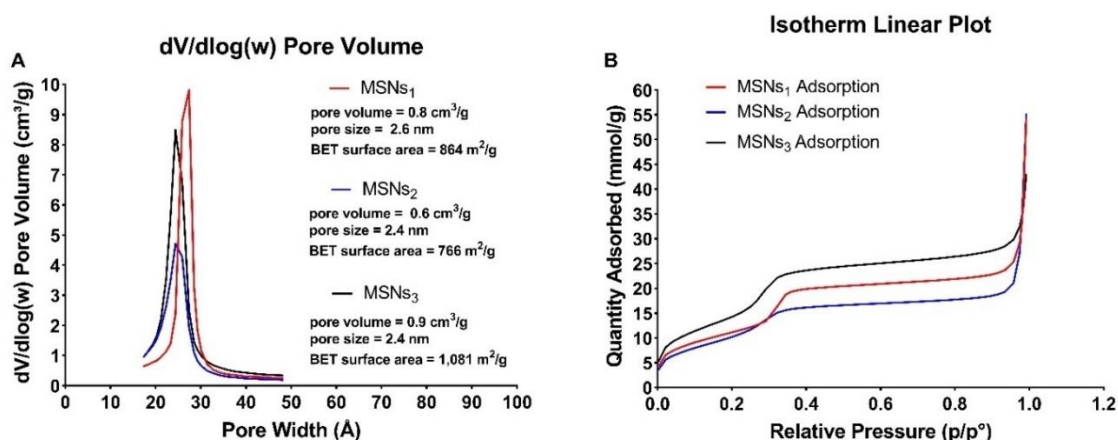


**Figure 3.18: A-** BJH Adsorption dV/dlog(w) Pore Volume of 3 different batches of synthesised MCM-41 type of MSNs. **B-** $N_2$ adsorption-desorption isotherm of 3 different batches of synthesised MCM-41 type of MSNs.

The aldehyde functionalized MSNs' encapsulation efficiency and loading capacity were both lower than those of MSNs (**Fig. 3.17 B**). This was likely owing to the functional groups' presence on the NPs' surfaces, which may have created steric hindrance. It is well known that when additional functional groups penetrate into the silica walls, they can reduce the size of the pores and the surface area of the particles (**Table 3.2**), limiting the amount of drug that can be loaded into the particles. [332] The nitrogen adsorption/desorption analysis (**Fig. 3.19**) showed that the particles pore volumes and surface area decreased after aldehyde functionalization, confirming the grafting of aldehyde groups on the pores surface, and also that the structure of the mesopores was altered by the newly inserted functional groups: specifically, the isotherms did not present the typical well-defined step at relative pressure (p/p°) of 0.2 - 0.4. [399]
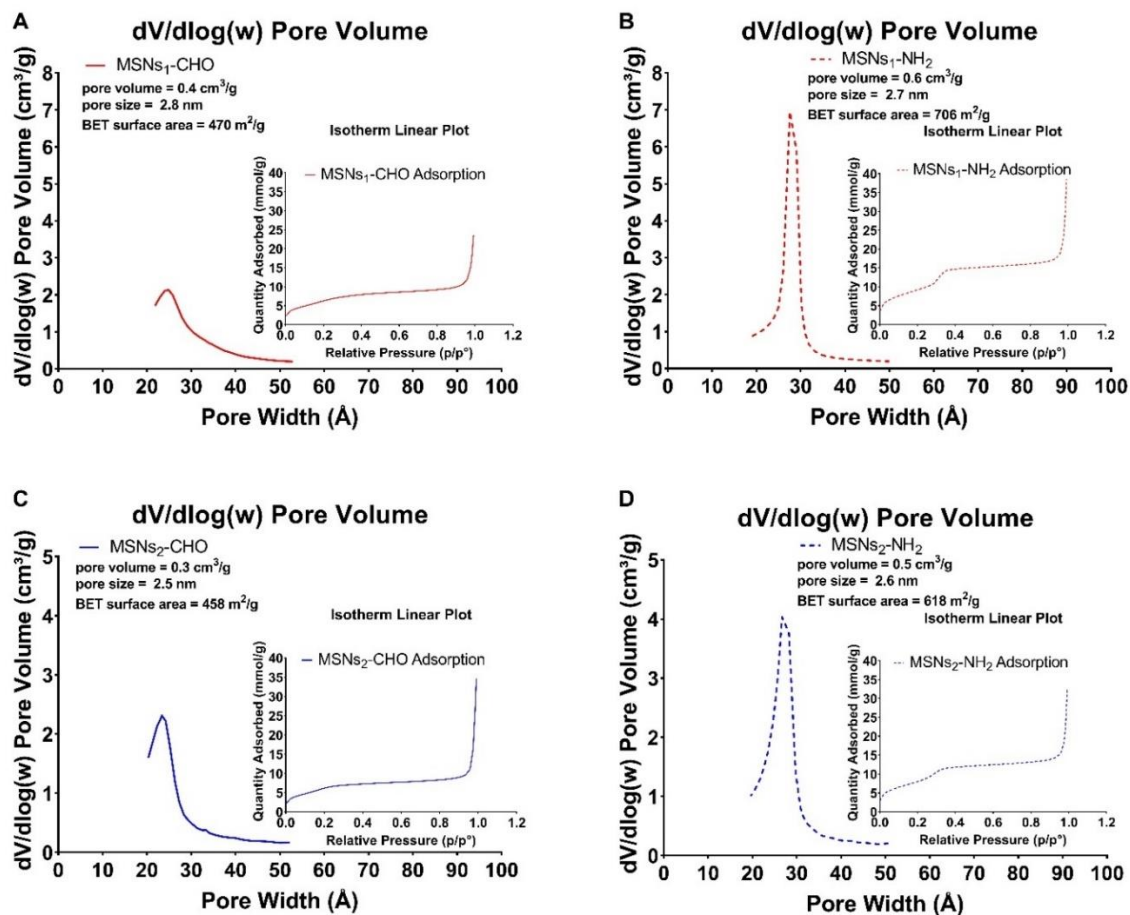
**Figure 3.19: A-** and **C-** BJH Adsorption dV/dlog(w) Pore Volume of MSNs functionalised with aldehyde groups. **B- and D-** BJH Adsorption dV/dlog(w) Pore Volume of MSNs before functionalization with aldehyde groups. **A, B, C** and **D inset-** $N_2$ adsorption-desorption isotherm of MCM-41 type of MSNs before (MSNs-$NH_2$) and after (MSNs-CHO) functionalization with aldehyde groups.

**Table 3.2:** Porous characteristics of MSNs before and after functionalization with glutaraldehyde.

| SAMPLE | BET SURFACE AREA ($m^2/g$) | PORE VOLUME ($cm^3/g$) | PORE SIZE (nm) |
|---|---|---|---|
| MSNs$_1$-NH$_2$ | 714 | 0.6 | 2.7 |
| MSNs$_1$-CHO | 540 | 0.4 | 2.8 |
| MSNs$_2$-NH$_2$ | 620 | 0.5 | 2.6 |
| MSNs$_2$-CHO | 460 | 0.3 | 2.5 |

As done previously for the empty NPs, TGA and FTIR analysis were carried out in order to confirm the successful loading of PTX and, subsequently, the functionalization with PEG and GEL. FTIR spectra of PTX loaded MSNs (**Fig. 3.20 A**) showed bands at 1716 and 1635 cm$^{-1}$ which most likely correspond to PTX (**Fig. 3.20 B**). PTX absorption peaks would normally be present at 1736, 1709 and 1647 cm$^{-1}$ (respectively the ester carbonyl, ketone, and amide groups) for pure PTX, but the observed switch is probably due to the hydrogen bonds formation between the PTX carbonyl groups and the MSNs' silanol groups. [388] In the spectra of the aldehyde functionalised MSNs loaded with PTX (**Fig. 3.20 C**), the occurrence of two bands at 1718 and 1640 cm$^{-1}$ are again most likely a shift of PTX bands, confirming the presence of the drug in the pores. After PEG functionalization (**Fig.**

**3.20 A**) we can observe the typical PEG bands as described before, and the same after grafting of GEL on the surface of the particles (**Fig. 3.20 C**).
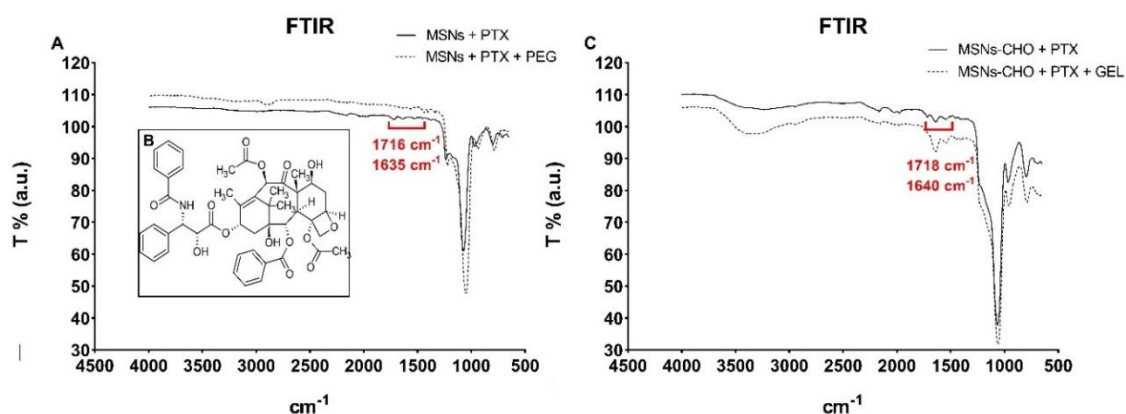


**Figure 3.20: A-** FTIR spectra of MCM-41 type of MSNs after PTX loading (MSNs+PTX) and PEG functionalization (MSNs+PTX+PEG). **B-** PTX chemical structure. **C-** FTIR spectra of MCM-41 type of MSNs aldehyde-functionalised after PTX loading (MSNs-CHO+PTX) and GEL functionalization (MSNs-CHO+PTX+GEL).

TGA results (**Fig. 3.21**) of PEG- and GEL-functionalised NPs showed, in both cases, higher values of % weight loss in the following order: empty NPs < loaded NPs < loaded-functionalised NPs. This order suggests that the presence of drugs and/or functional groups within the NPs leads to higher weight loss compared to the empty ones. **Table 3.3** summarizes the % of organic loss for the different batches of NPs. The results show that the two batches of bare MSNs exhibited lower organic loss compared to MSNs-CHO, indicating that the functionalization process with aldehyde groups introduced additional organic material, leading to higher weight loss during TGA analysis. Furthermore, both types of empty NPs had a lower % weight loss compared to the loaded NPs, indicating that the loaded NPs contained further organic material (the drug) within their pores, resulting in higher weight loss during TGA analysis, and therefore confirming the successful loading. Lastly, the functionalization with PEG and GEL was verified by the largest % weight loss reported in the TGA data of the functionalized loaded NPs.
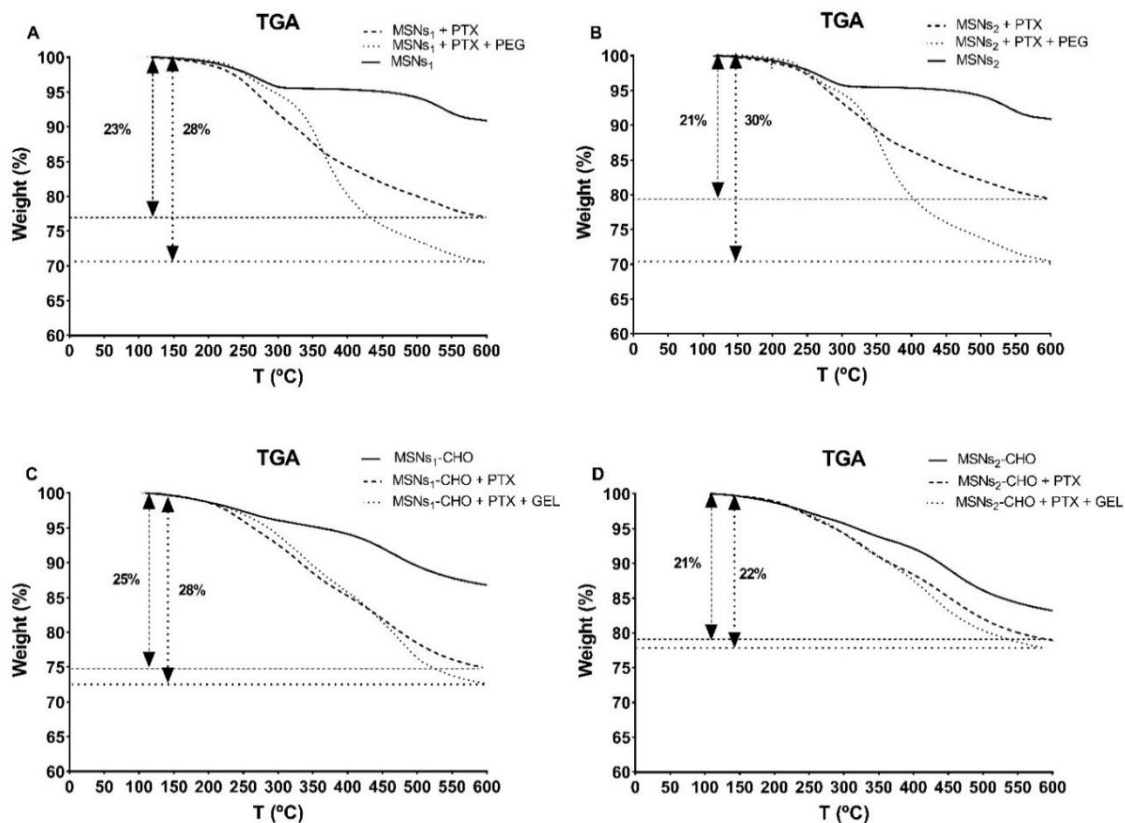
**Figure 3.21: A- B-** Thermogravimetric analysis of MCM-41 type of MSNs before (MSNs) and after PTX loading (MSNs+PTX), and after PEG functionalization (MSNs+PTX+PEG). **C- D-** Thermogravimetric analysis of MCM-41 type of MSNs, aldehyde-functionalised, before (MSNs-CHO) and after PTX loading (MSNs-CHO+PTX), and after GEL functionalization (MSNs-CHO+PTX+GEL).

**Table 3.3:** Total organic material loss (%) analysed by thermogravimetric analysis (excluding water molecules) of different MSNs batches before loading (MSNs/MSNs-CHO), after PTX loading (MSNs+PTX/MSNs-CHO+PTX), and after functionalization (MSNs+PTX+PEG/MSNs-CHO+PTX+GEL).

| SAMPLE | $MSNs_1$ | $MSNs_2$ | $MSNs_1$+PTX | $MSNs_2$+PTX | $MSNs_1$+PTX +PEG | $MSNs_2$+PTX +PEG |
|---|---|---|---|---|---|---|
| ORGANIC LOSS (%) | 9% | 9% | 23% | 21% | 28% | 30% |

| SAMPLE | MSNs-$CHO_1$ | MSNs-$CHO_2$ | MSNs-$CHO_1$+PTX | MSNs-$CHO_2$+PTX | MSNs-$CHO_1$+PTX+ GEL | MSNs-$CHO_2$+PTX+ GEL |
|---|---|---|---|---|---|---|
| ORGANIC LOSS (%) | 13% | 17% | 25% | 21% | 28% | 22% |

### 3.1.7.2 Doxorubicin (DOX)

DOX is an anthracycline antitumor drug, with a broad spectrum of antitumoral activity, which can interfere with DNA inhibiting the topoisomerase II-DNA complex by intercalation into the DNA double helix, inducing DNA damage and subsequently cancer cell apoptosis. DOX has been approved for the treatment of different solid tumours, but the clinical use of DOX is limited due to its low target selectivity, the rapid clearance from the body and its toxicity, including fatigue, nausea, myelosuppression, and especially fatal cardiotoxicity. In recent years, a substantial degree of effort has been paid in developing delivery methods that would increase the therapeutic effectiveness and lessen the negative effects of many drugs. Many nanocarriers have been proposed as drug delivery systems for DOX, including MSNs. [400-402]

In order to improve the water solubility of DOX, the amino sugar connected to the anthraquinone nucleus is protonated forming DOX hydrochloride (DOX) (**Fig. 3.22**). [403]
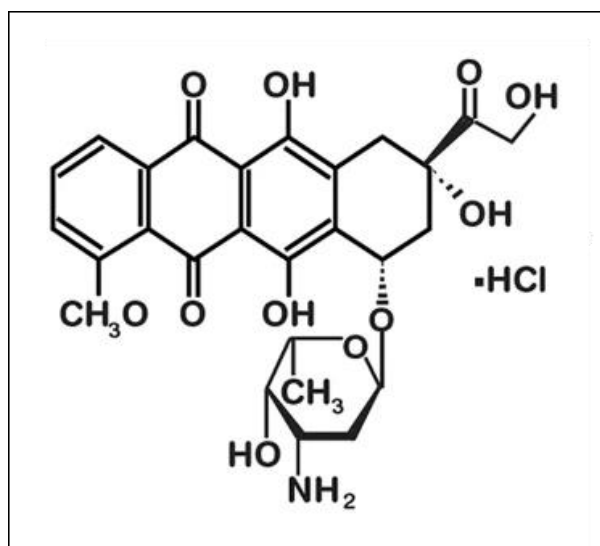
**Figure 3.22:** Doxorubicin Hydrochloride structure.
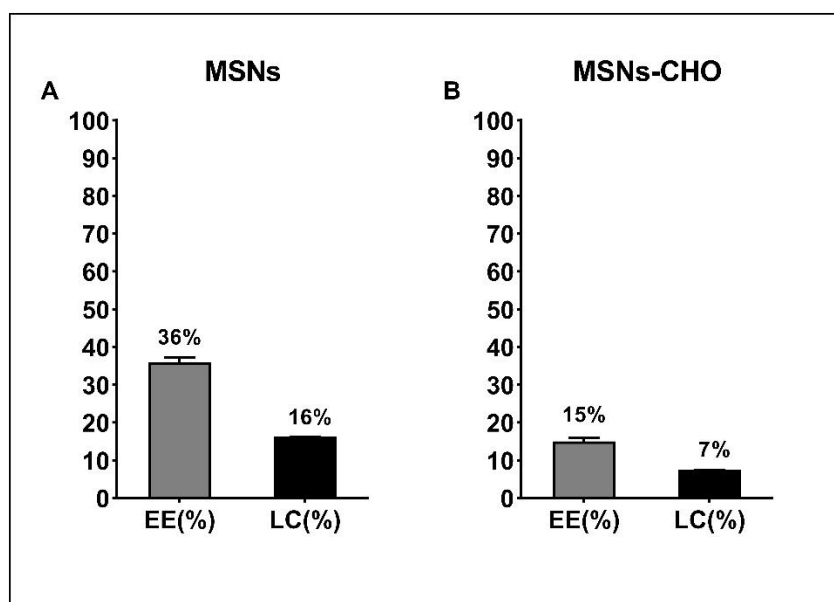


**Figure 3.23:** DOX encapsulation efficiency (EE%) and loading capacity (LC%) for **A-** MSNs and **B-** aldehyde-functionalised MSNs. (Results are presented as mean±SEM of 2 independent loading experiments).

Acetate buffer (pH 5.4) was used as the loading medium to adsorb DOX into the mesopores via a solution immersion method, as previous experiments in which dd $H_2O$ had been used did not produce satisfactory results. In fact, DOX has a pKa equal to 8, which makes the molecule protonated on the amino group at acidic pH, so positively charged, more soluble and stable. [404] At acidic pH the silanol groups

on the surface of the MSNs are present mainly in the non-ionized form, whereas at a higher pH of 8-9 they are present in the ionized form. [404] The pH of the water in our laboratory resulted to be slightly basic, and we speculated that this might have affected the loading since the DOX molecules were present in the non-protonated form, probably impacting its interaction with MSNs. On the contrary, being the pH of the loading media equal to 5.4, we expect DOX to interact with some of the silanol groups present in the ionized form (**Fig. 3.24 b**). In their work Roik N.V. *et al.*, [404] refer to the possibility of neutral drug molecules forming hydrogen bonds with non-ionized silanol groups and therefore contributing to the adsorption process. Further investigations are necessary to gain a better understanding of the interaction between DOX and the MSNs' surface and therefore the absorption mechanism.
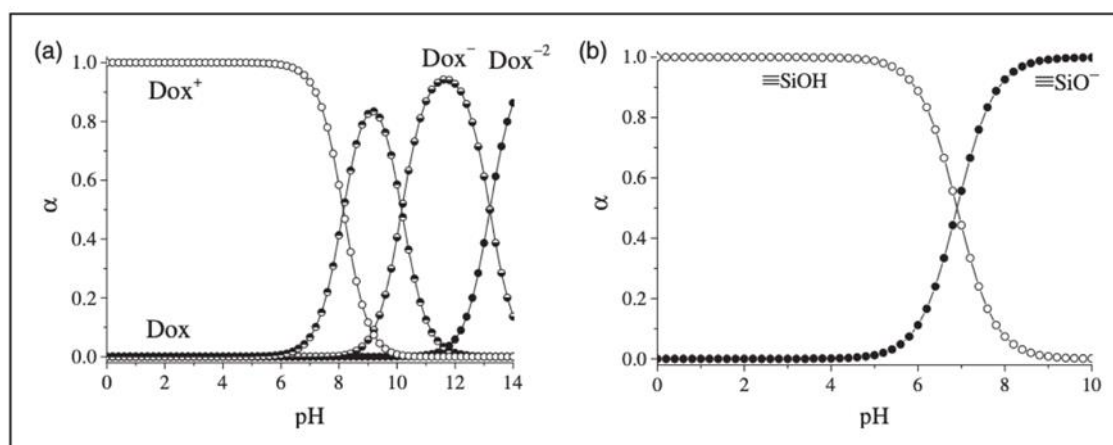


**Figure 3.24:** Diagrams showing **a)-** the protolytic forms of Dox and **b)-** the distribution of surface silanol groups and as a function of pH. [404]

Our findings (**Fig. 3.23 A** and **B**) showed that the particles' loading capacity for DOX resulted to be lower than the one for PTX, with an average amount of drug loaded equal to 160 µg per mg of NPs for MSNs, and 70 µg per mg for aldehyde-functionalised NPs. Similar results were reported previously in the literature. [143, 393, 402] Nevertheless, both in the literature and in previous experiments, higher loading capacities were obtained (25%±4) demonstrating that the variability between batches could be due to intrinsic NPs characteristics and/or the media used for the loading. The lower loading capacity of aldehyde-functionalised

particles can be again explained by the presence of the functional groups on the NPs' surfaces which may have created steric hindrance.

FTIR spectra of the loaded NPs (**Fig. 3.25 A** and **B**) showed bands at around 1410/1417 cm$^{-1}$ probably from the vibrations of the C–H bonds in the CH, CH$_2$, and CH$_3$ groups, 1550 and 1613/1630 cm$^{-1}$ belonging to the stretching vibrations of the C=O bonds from the anthracene ring, indicating the presence of DOX molecules. [404] PEG and GEL functionalization were also confirmed by the appearance of their typical bands as previously discussed.
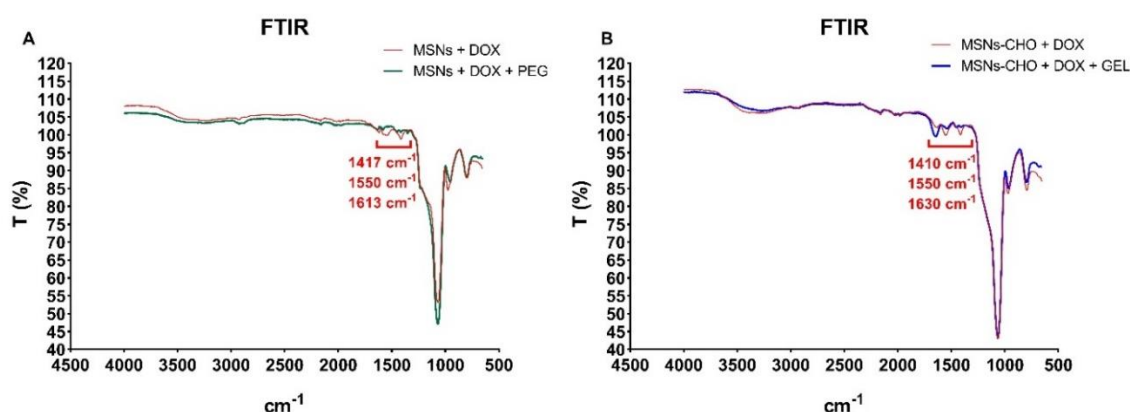


**Figure 3.25: A-** FTIR spectra of MCM-41 type of MSNs after DOX loading (MSNs+DOX) and PEG functionalization (MSNs+DOX+PEG). **B-** FTIR spectra of MCM-41 type of MSNs aldehyde-functionalised after DOX loading (MSNs-CHO+DOX) and GEL functionalization (MSNs-CHO+DOX+GEL).

According to the TGA results presented in **Fig. 3.26 A** and **B**, varying degrees of weight loss for the different types of NPs were observed as follow: empty NPs < loaded NPs < loaded-functionalised NPs. Once again, this order suggests that the presence of drugs and/or functional groups within the NPs leads to higher weight loss compared to the empty ones. The graphs indicate that the bare-empty NPs (MSNs and MSNs-CHO) exhibited a weight loss of 10% or less. This low weight loss can be attributed to the presence of residual CTAB molecules inside the mesopores. The loading of DOX resulted in an increase in weight loss of 15 and 18% for MSNs and MSNs-CHO, respectively. This indicates that DOX was successfully loaded into the NPs. Furthermore, after functionalization with PEG and GEL, the organic material loss increased to 31 and 19%, respectively.

This higher weight loss confirms the successful functionalization of the NPs with PEG and GEL.
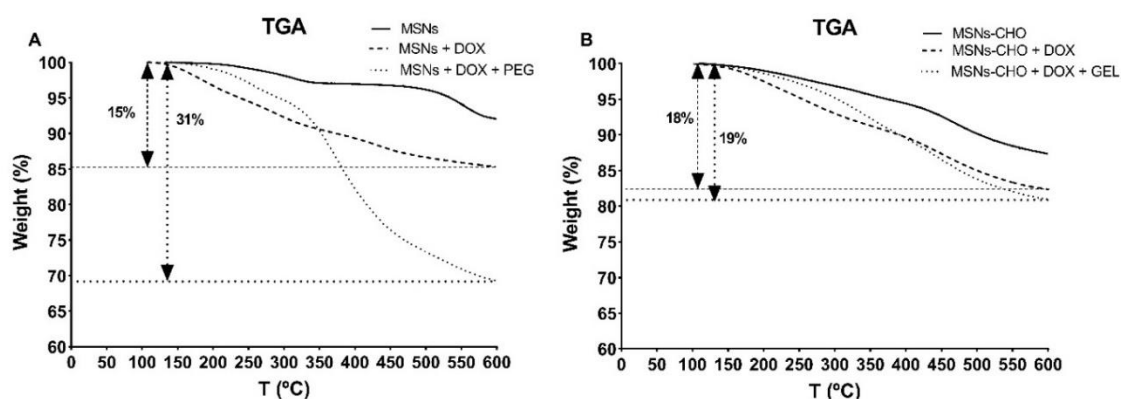


**Figure 3.26: A-** Thermogravimetric analysis of MCM-41 type of MSNs before (MSNs) and after DOX loading (MSNs+DOX), and after PEG functionalization (MSNs+DOX+PEG). **B-** Thermogravimetric analysis of MCM-41 type of MSNs, aldehyde-functionalised, before (MSNs-CHO) and after DOX loading (MSNs-CHO+DOX), and after GEL functionalization (MSNs-CHO+DOX+GEL).

3.1.7.3  Safranin-O release studies: proof of concept

Stimuli-responsive NPs are designed to remain stable and inactive under physiological conditions, and upon exposure to a stimulus they undergo a physicochemical change, resulting in the release of the cargo.

Using organic polymers as capping systems to trigger the release of cargo molecules   allows to achieve prolonged release. PEGylation involves the covalent attachment of PEG chains to the surface of the carrier, which can simultaneously improve the stability, solubility, and half-life of the payload in the body, and protect it from a premature release before the activation by a specific stimulus. [324] Similarly, the GEL-capping system is used to protect the cargo from premature release and involves the use of a gel-like coating, which can respond to specific stimuli, such as temperature, pH, and enzyme activity, to trigger the release of the cargo. [143, 355, 357, 360, 405]

The redox-responsive PEG-system was designed in order to respond to the differences in concentration levels of glutathione (GSH), achieving a targeted and

prolonged drug release in reducing conditions (as the tumour microenvironment). The disulphide bonds connecting the PEG to the surface of the NPs would be cleaved in the presence of high GSH concentrations and allow the release of the cargo from the pores. Other groups have previously worked with similar systems. [324, 406] Cui Y. *et al.*, [352] in their work functionalised MSNs loaded with fluorescein dye with a detachable PEG shell connected to the MSNs via a disulphide bond. They demonstrated that the presence of the disulphide bond between the PEG shell and MSNs allowed for a controlled drug release, since the bond was cleaved when in the presence of high GSH concentrations, resulting in the detachment of the PEG shell from the MSNs. Iyer R. *et al.*, [407] developed a biodegradable polyurethane with disulphide links in the backbone, designed to be responsive to GSH. The group's study demonstrated how MSNs functionalised with the latter polymer, exhibited minimal release of the encapsulated drug in the absence of GSH. However, the released of cisplatin form the MSNs' pores was triggered by increasing GSH concentrations. The work conducted by Wang K. and co-workers, [408] involved the design of a triblock copolymer capable of self-assembling into micelles in an aqueous solution. The copolymer consisted of three distinct blocks. The outer layer of the micelles was formed by a PEG segment, which was attached to the middle block through a disulphide linkage. When exposed to GSH, its reaction with the disulphide bonds present in the copolymer led to the cleavage of these bonds, the detachment of the PEG corona and, consequently, the collapse of the micelles due to the loss of their stabilizing layers, and the release of the encapsulated drug.

The GEL-system was designed in order to respond to the presence of metalloproteinase enzymes (MMPs), especially MMP-9 and -2 (also called gelatinases), in the tumour microenvironment as they could digest the layer of gelatine covering the surface of the NPs allowing the release of the cargo in situ. This system was also previously investigated by other groups. Liao Y.-T. *et al.*, in their work, [360] functionalised MSNs with a GEL layer in order the test the ability of these nanocarriers (using different levels of thickness of GEL) to control the release of pilocarpine. The group observed that in the presence of MMP-2, the GEL layer was effectively digested by the enzymes. This enzymatic degradation led to the

release of pilocarpine from the MSNs, resulting in a long-lasting release profile that extended over a period of 36 days. Xu J.-H. *et al.*, [143] reported the development of a system based on MSNs loaded with DOX and functionalised with GEL able to protect the loaded drug molecules until coming in contact with MMP-9. The researchers demonstrated that the developed system effectively prevented the leakage of the drug molecules under normal conditions. The GEL functionalization served as a protective barrier, preventing the premature release of the cargo. However, when the MSNs came into contact with MMP-9, the enzyme selectively degraded the GEL polymer. This enzymatic degradation triggered the release of the loaded drug molecules, enabling targeted drug delivery. Zou Z. and co-workers [355] exploited the benefits of both PEG and GEL functionalization. The incorporation of PEG on the surface of the MSNs aimed to enhance the circulation time of the nanocarrier in the bloodstream. Upon reaching the tumour site, the system was designed to release the encapsulated drug by taking advantage of the presence of MMPs, which would degrade the layer of GEL enabling the release of the drug molecules.

The PEG- and GEL-capping systems' ability to protect the cargo from an early release before the activation by a stimulus was tested using particles loaded with the dye safranin-O.

According to the findings from the release studies (**Fig. 3.27**), the PEG-functionalised NPs (**Fig. 3.27 A**) showed a lower release when not in contact with GSH. The addition of GSH (red arrow) caused a burst release of the cargo from the pores due to their opening following the cleavage of the disulphide bonds, confirming the responsiveness of the nano-system to the specific stimulus. After GSH addition, the release curve of MSNs-PEG became very similar to the one of the uncapped NPs, where the safranin-O molecules were able to leave the pores freely and $22 \pm 5\%$ of the total amount released was in solution after only 5 minutes, as opposed to the capped MSNs which had released only $5 \pm 1\%$ at the same time point. Moreover, after the addition of the stimulus, the amount of safranin-O present in solution increased from 5 to $29 \pm 1\%$ and kept increasing over time. However, after 24 h, the capped NPs in a non-reductive environment had released $46 \pm 11\%$. This leakage could be due to several factors, such as the presence of not fully

capped pores, molecules of Safranin-O still present on the surface of the NPs after functionalization, or the degradation of the polymer over time. Further studies might be necessary to investigate this issue. Overall, the results showed the ability of the PEG capping system to form a barrier and inhibit a burst release of the cargo, as well as to respond to GSH, confirming its potential to promptly release the payload once in the proximity of a tumour.

The GEL capping system was investigated using both commercial MMPs (**Fig. 3.27 B**), that were added to the NPs suspension after 30 minutes (red arrow), and conditioned media (**Fig. 3.27 C**) from human (A549) and murine (LLC1) lung cancer cells.

When using commercial enzymes (MMP-9), two different MMPs concentration were used: 10 and 30 nM (corresponding to 800 and 2,400 ng/mL, respectively). It is known that MMP-2 and –9 are enzymes that play a role in extracellular matrix degradation, and their overexpression has been associated with tumour invasion and metastasis in various types of cancer. [143, 185-187] It has been reported that in some malignant tumour tissues, such as those from breast cancer, colon cancer, brain tumours, and others, MMP-2 and -9 expression is increased. Furthermore, it has been shown that MMP-9 is expressed in NSCLC tumour cells and also in the stromal cells around them. [409]

In the literature, mainly concentrations of circulating MMPs in cancer patients are reported, rather than concentrations in the tumour microenvironment. In their work, Iizasa T. and colleagues [409] reported higher plasma concentrations in NSLC patients (71.0 ± 60.2 ng/mL mean ± SD), when compared to healthy patients; and positive immunohistochemical staining for MMP-9 and 2 in the cytoplasm of the tumour cells. The group discussed the work from Zucker S. and co-workers [410], where no elevated MMPs levels in NSLC patients were detected and explained that these discrepancies could be due to differences in the avidity and affinity of the different antibodies used. However, in a later work from Zhang Y. *et al.*, [411] the serum levels of MMP-9 in patients with NSCLC were found to be 1,092.5 ng/mL (range, 660.5–1,825 ng/mL), which was higher than what was previously reported. These discrepancies could be due to differences in numbers of patients enrolled in the studies (73 [409] vs. 332 [411]), the histological type, the

cancer staging and especially the techniques used for MMPs detection. In other two studies, [412, 413] the serum levels of MMP-9 in patients with lung malignancies were 673 ± 182 and 887 ± 553 ng/mL, respectively. Many other studies have investigated the expression of MMPs in lung cancer tissue samples by immunohistochemistry, [199, 210, 412, 414, 415] and reported the presence of higher levels when compared to healthy tissues. Those results, however, were mainly reported as picograms per milligram of wet sample weight, and/or percentages of tumours expressing different MMPs. As a result, the concentrations of commercial MMPs used in our release studies were chosen according to the circulating levels of MMPs reported in the literature with the assumption that those concentrations would be similar and/or lower than those in tumour tissues, where we expect our system to be digested by the enzymes and deliver the drug.

According to the findings of the release studies with GEL-functionalised MSNs using commercial MMP-9 (**Fig. 3.27 B**), it can be seen how the addition of MMPs (red arrow) caused a burst release of safranin-O, with the percentage of dye in solution increasing from 14 ± 0.3% to 36 ± 5% and 46 ± 6% at MMPs concentration of 10 (800 ng/mL) and 30 (2,400 ng/mL) nM, respectively. On the contrary, capped MSNs which had not been in contact with the enzymes, did not show a burst release, with safranin-O increasing from 14 ± 2% to 21 ± 3% at the same time points. The positive control (uncapped MSNs) showed a burst release after only 5 minutes, due to the absence of a coating of gelatine inhibiting safranin-O molecules release, with 33 ± 3% of the total cargo release escaping into solution (as opposed to capped MSNs, which released only 10 ± 0.9% after 5 minutes). The total amount of dye released by the functionalised MSNs in the absence of the stimulus reached 55 ± 11% after 24 h, whereas the uncapped NPs had released almost the same amount (59 ± 6%) after only one h. These results confirmed the presence of the gelatine layer on the surface of the NPs, and its ability to delay the release of the content from the pores. Che E. *et al.*, in their work [353] demonstrated how the level of crosslinking of gelatine could affect the release patterns, reporting that a higher crosslinking density results in a more compact gelatine layer and restricts the gelatine network's mobility, preventing the liquid from penetrating deeper and wetting the drug molecules and eroding the gelatine shell. Our results

for the cumulative safranin-O release from capped MSNs in PBS are similar to the authors' findings, where NPs with GTA % (v/v) of 0.4 exhibited relatively low burst-release effect and relatively high cumulative release percentages. These results indicate that further studies should be carried out in the future, testing different GTA percentages for gelatine crosslinking, in order to assess if a lower basal leakage can be achieved.

The gelatine-functionalized MSNs were also tested for their ability to respond to MMPs present in conditioned media collected from A549 and LLC1 cancer cells. The results (**Fig. 3.27 C**) indicated that the particles were selective towards MMPs, with an amount of safranin-O released in the presence of MMPs higher than the one released in fresh media: $79 \pm 6\%$ (LLC1) and $69 \pm 8\%$ (A549) after 6 h, compared to fresh media (DMEM 0% (v/v) foetal bovine serum) in which the particles had released only $18 \pm 2\%$ at the same time point. It is worth noting that the presence of gelatinases in the conditioned cell media had been previously confirmed, as well as the potential of obtaining sufficient enzyme levels to perform those release assays without the need of using commercial MMPs. As reported in **Chapter 4**, the human lung cancer cells (A549) showed a lower production of MMPs (1,400 ng/mL) when compared to the murine cancer cells (LLC1) (2,000 ng/mL), which was reflected in a lower safranin-O cumulative release. It can be also observed that in this instance, the negative control did not release more than half the amount of safranin-O that had been released previously in PBS (pH 7.4). These discrepancies could be due to several factors, such as variability between batches, with varying thickness of gelatine layers allowing different levels of basal leakage of dye molecules, various aldehyde groups densities on the particles surface leading to different degrees of crosslinking, or to the varying stability of gelatine in the different media. It has been reported by Rosellini E. and colleagues [416] that blends based on alginate and gelatine, especially the ones with higher gelatine contents, showed lesser stability in PBS compared to cell culture medium, suggesting a hydrolytic degradation process.

Overall, those results successfully demonstrated that both stimuli-responsive systems responded to the presence of the specific stimulus and

protected the release of the cargo in its absence. The basal leaking of the cargo from the capped nano system needs to be further investigated.
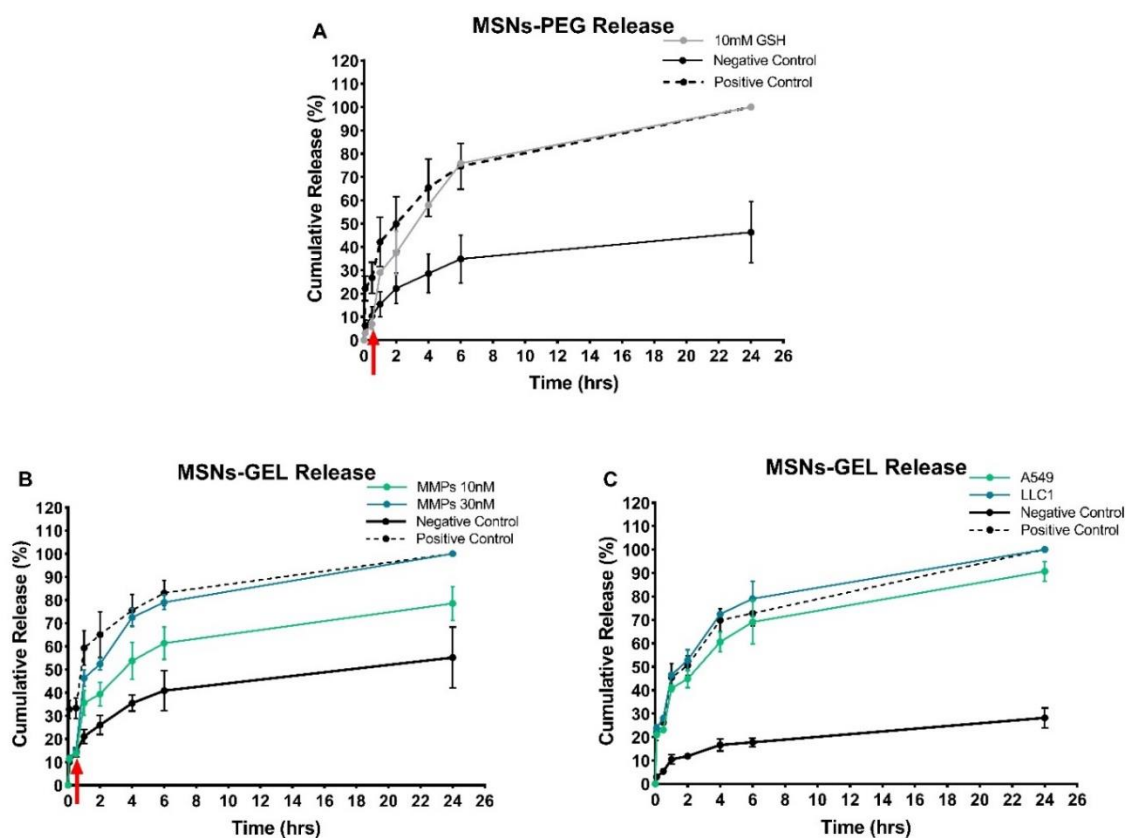


**Figure 3.27:** Time course of safranin-O release from **A-** MSNs-PEG with (red arrow) and without the addition of 10mM GSH and uncapped MSNs (positive control) (Mean±SEM). **B-** MSNs-GEL with (red arrow) and without the addition of 10 and 30 nM commercial MMP-9 and uncapped MSNs (positive control) (media±SEM). **C-** MSNs-GEL in conditioned and unconditioned (negative control) cell media and uncapped MSNs (positive control) (media±SEM). The results were normalized for the highest amount released.

### 3.1.8  Conclusions

Since their discovery, there has been a significant interest in the synthesis and characterization of MSNs because of their potential applications in biomedicine and other fields.

MCM-41 type of MSNs was successfully synthesised and characterised, confirming the typical physical-chemical properties of this type of nanomaterial. MSNs exhibited a near-spherical morphology with a uniform size distribution of approximately 100 nm. They displayed a typical hexagonal mesopore structure, a high pore volume ranging between 0.6 and 0.9 cm³/g, indicating a substantial capacity for molecular encapsulation, and a surface area ranged between 700 and 1000 m²/g. The MSNs were successfully functionalized by grafting a layer of either poly(ethylene glycol) or gelatine onto their surface. This functionalization enhanced their re-dispersibility.

Paclitaxel or doxorubicin hydrochloride were both effectively loaded into the MSNs' pores, confirming the efficient encapsulation, and loading capacity of both hydrophobic and hydrophilic molecules by this nanocarrier.

The PEG- and GEL-capping systems demonstrated their effectiveness in protecting the encapsulated cargo against premature release. Additionally, the systems exhibited responsiveness to specific stimuli. Safranin-O, used as a model cargo molecule, confirmed these properties, suggesting the potential for controlled drug release in response to specific triggers.

# 4 CHAPTER 4: *In vitro* cell studies

## 4.1 Cytotoxicity assays

One of the major challenges with drug delivery systems is owed to their potential intrinsic cytotoxicity. Therefore, it is very important not only to test the *in vitro* effect of the drug after encapsulation in the DDS, but the cytotoxicity of the DDS itself.

When nanomaterials are introduced into living organisms, they come into contact with various biomolecules, especially proteins, but also lipids, and other macromolecules. [417-429] These biomolecules compete for binding to the surface of the nanomaterials, leading to the formation of a layer called the "biomolecular corona" that can be schematically represented as a double layer coating the NPs: a first layer usually referred to as "hard" corona (proteins with strong affinity to the NPs surface), and a second layer, the outer one, called "soft" corona (loose proteins reflecting the abundance of serum proteins). This layer can boost the clearance from the circulation via immune system detection or interfere with the ability of the NPs to be internalized by the targeted tissue. In fact, the formation of this layer determines the ultimate surface characteristics, aggregation rate, hydrodynamic size, and cellular interactions of the NPs, as well as their potential toxic effect. [430-433]

NPs must be able to avoid the immune system's fast clearance and endure prolonged blood circulation in order to target specific organs. One of the well-known "biological barriers" which can affect the delivery of nanomaterials is the mononuclear phagocyte system (MPS) also known as the reticuloendothelial system (RES) (constituted of both cellular and noncellular elements). RES, particularly liver and spleen, is responsible for the clearance of foreign particles from the bloodstream. Phagocytic cells may adhere to NPs triggering the release of cytokines, such as tumour necrosis factor (TNF), interleukins, and interferons, causing an immune response and, subsequently, increase the removal of the NPs from the circulation which can lead to a localized tissue inflammation that can cause tissue damage. [434-436] NPs can be engineered to minimize their interaction

131

with the RES, for example, by utilizing stealth strategies, such as the use of PEGylation that can prevent opsonization (binding of opsonins that mark particles for clearance) and subsequent recognition by immune cells. [437] PEGylation creates a hydrophilic layer around the NPs, reducing interactions with plasma proteins and immune components, and improving the bioavailability. [433]

For these reasons, when conducting biological assays involving nanomaterials, it is important to consider that the properties of the NPs may change from their initial characterization. Controlling the interactions between nanomaterials and biological systems is a significant challenge in the field of nanomedicine, and therefore, researchers in nanomedicine devote great efforts to studying the relationships between the design of drug nanocarriers, their interactions with biomolecules, and the resulting physiological responses. [438] By understanding these relationships, scientists can design nanomaterials with improved properties for targeted drug delivery and minimize undesired interactions that may affect their efficacy and safety. [76, 439-441]

Cell viability of human non-small-cell lung cancer (A549) and Lewis Lung Carcinoma (LLC1) cell lines after incubation with free drug, empty and loaded NPs in serum free media at different time points was investigated.

## 4.1.1  Human non-small-cell lung cancer (A549) cells

### 4.1.1.1  Empty MSNs

*In vitro* testing of empty MSNs' potential cytotoxic effect on the human non-small-cell lung cancer (A549) cell line was carried out using a CCK-8 assay as detailed in **section 2.2.11.2** in **Chapter 2**.

To aid in the interpretation of the data, a line was added on the graphs to indicate 80% cell viability. According to the standard ISO 10993-5, [442] any percentage of cell viability above 80% would suggest that the treatment or substance being tested is not cytotoxic. The exposure of A549 cells to the NPs revealed a lack of cytotoxicity for the aldehyde (**Fig. 4.1 A**) and gelatine (**Fig. 4.1**

**B**) functionalized NPs at any of the three time points studied. Furthermore, the data show that even at the highest concentration tested (400 µg/mL), the aldehyde functionalized MSNs did not exhibit significant toxicity towards the cells after 72 h of exposure, with cell viability stable at around 80% of the control. Despite the fact that GTA is known to be toxic to cells, [443-445] in the study conducted by Azami M. and colleagues, [446] which involved culturing L929 fibroblast cells with scaffolds crosslinked using different concentrations of GTA, cellular toxicity was observed in cells treated with scaffolds crosslinked with GTA solutions at a concentration of 2.5%, but not with lower ones (from 0.5 to 2%, with 0.5 and 1% showing the lowest toxicity). The researchers concluded that the selection of GTA concentration within the range of 0.5% to 2% for crosslinking would depend on optimizing characteristics such as the mechanical properties of the scaffolds, and they considered concentrations within this range to be safe in terms of cellular toxicity. Nevertheless, bare MSNs (**Fig. 4.2 A**) demonstrated considerable cytotoxicity against A549 cells after just 24 h of treatment at doses as low as 25 µg/mL, with cell viability decreasing to 71% of the control. Even at lower doses (10 µg/mL), unfunctionalized MSNs showed harmful effects with cell viability decreasing to around 50% of the control after three days of treatment. PEGylated MSNs (**Fig. 4.2 B**) were less toxic, with the highest concentration tested (400 µg/mL) decreasing cell viability to 58% of the control after 2 days treatment, while, at the same time point, unfunctionalized NPs had the cells viability dropping to 52% of the control at a concentration as low as 25 µg/mL. However, after 72 h, the cell viability decreased to around 40% of the control for NPs concentrations of 100, 200, and 400 µg/mL, showing a similar pattern to that of bare MSNs, where the drop in cell viability was a function of both concentration and time. These results may be attributed to the cleavage of the disulphide bonds and removal of PEG from the NPs' surface due to the presence of GSH in the cellular microenvironment [170, 175] which lead to the exposure of the silanol groups on the surface of the MSNs.
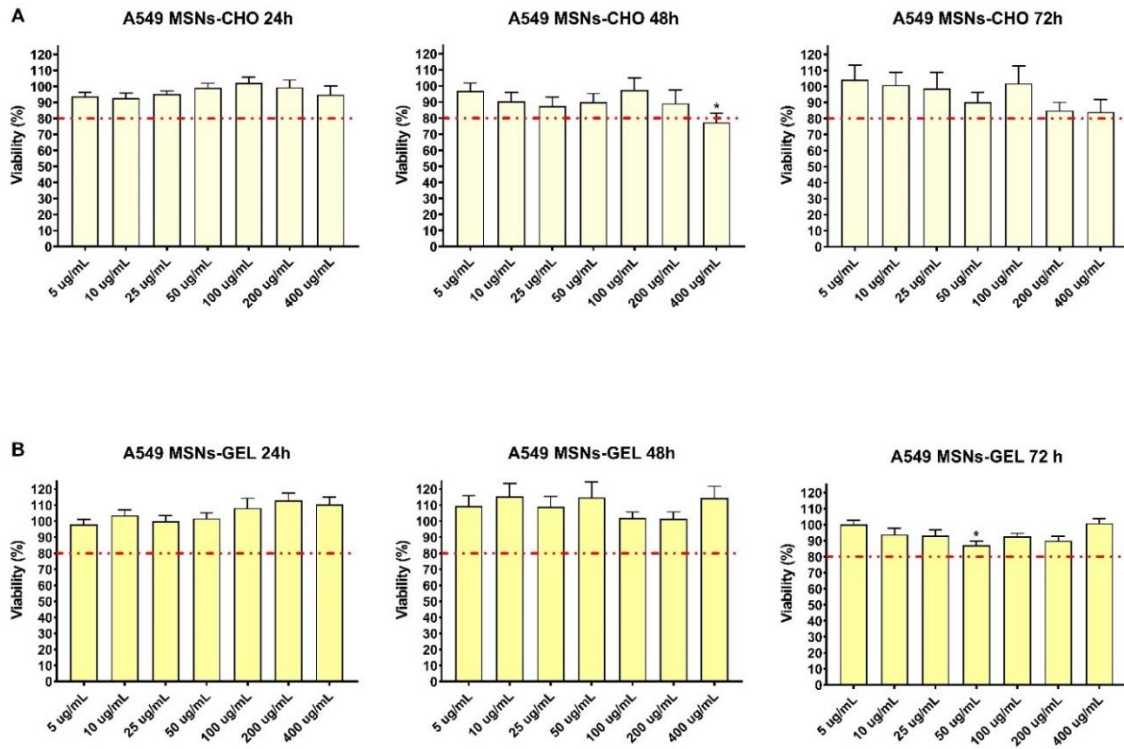
**Figure 4.1:** A549 cell viability assay upon incubation with empty **A-** MSNs-CHO and **B-** MSNs-GEL, for 24, 48 and 72 h (mean ± SEM). The x-axis corresponds to MSNs concentration. Statistical test: One-way ANOVA with Dunnett's post-test comparing all treatments versus the control (non-treated cells, taken as 100% of viability) n=6, p ≤ 0.05 (*)
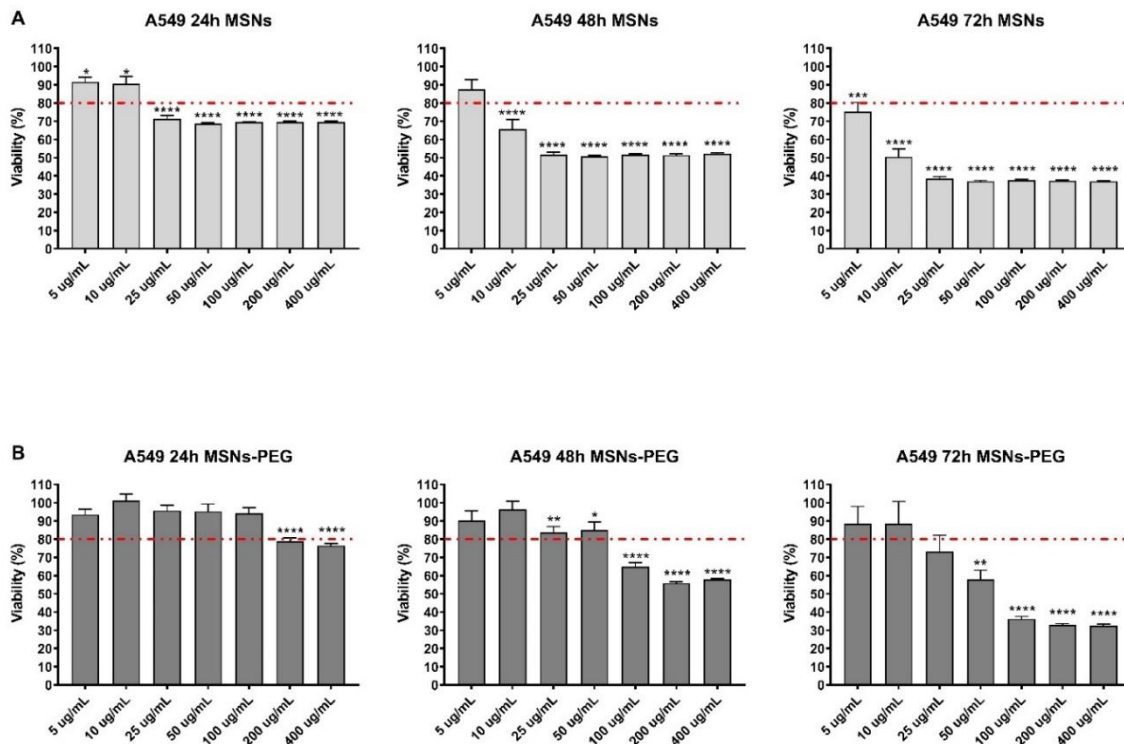
**Figure 4.2:** A549 cell viability assay upon incubation with empty **A-** MSNs and **B-** MSNs-PEG, for 24, 48 and 72 h (mean ± SEM). The x-axis corresponds to MSN concentration. Statistical test: One-way ANOVA with Dunnett's post-test comparing all treatments versus the control (non-treated cells, taken as 100% of viability) n=3, p ≤ 0.05 (*), p ≤ 0.01 (**), p ≤ 0.001 (***), p ≤ 0.0001 (****)

The toxicity of bare MSN towards lung cancer cells is in agreement with the work from other groups available in the literature. Lesniak A. and colleagues, in their work, [441] observed that the A549 cells exposed to silica NPs in the absence of serum altered their phenotype and became spherical, indicating loss of cell adhesion and damage. They also conducted ATP analyses of the cells exposed to various doses of silica NPs and found a dose-dependent reduction in cell viability when cells where exposed to them in serum-free media. The researchers concluded that despite the fact that all the concentrations used were rather large, the nature of interactions of the same substance in the presence or absence of proteins was highly different. This suggests that the presence of serum or proteins can influence the toxicity of silica NPs on cells.

It is well established that silica causes pulmonary toxicity [447, 448] and since MSNs present surface sites equivalent to crystalline silica, it is believed that the

NPs could facilitate ROS production via their exposed surface sites, causing cellular apoptosis. [449] Lin W. *et al.*, in their work from 2006 [450] tested two different sizes of silica NPs (15 and 46 nm) and compared their toxicity to crystalline silica (Min-U-Sil 5), which was used as a positive control towards A549 cells. The results showed that the silica NPs, irrespective of size, caused a reduction in cell viability at concentrations ranging from 10 to 100 µg/mL in a dose-dependent manner. Interestingly, the silica NPs were even more toxic than the positive control, suggesting a high level of cytotoxicity. The researchers also observed an increase in oxidative stress, as evidenced by raised levels of reactive oxygen species (ROS). This increase in oxidative stress was correlated with a reduction in GSH levels and an increased lipid peroxidation, which was highlighted by an increased release of malondialdehyde and lactate dehydrogenase from the cells. These findings suggest that the silica NPs induced oxidative stress, resulting in damage to the cell membrane and ultimately cell death, something that would be worth to explore further in the case of the NPs developed during this work in the future.

Tao Z. and colleagues [451] observed distinct cytotoxicity patterns for two types of MSNs, SBA-15 and MCM-41, in a T lymphocyte cell line (Jurkat cells). Interestingly, when aminated MSNs were used, no substantial cell death was observed. In contrast, MCM-41 NPs showed significant toxicity after only 24 h of treatment at concentrations of 50, 100, and 200 µg/mL. The same researchers also found that human neuroblastoma cells (SK–N–SH) were more tolerant to the treatment of MSNs, whether aminated or not, which demonstrates that different cell lines can react differently to the same material. By investigating the uptake of the particles, the group discovered that non-functionalized MSNs were engulfed by the cells' membrane, whereas endocytosis was substantially less efficient in cells treated with amino-functionalized particles. It was hypothesized that instead of allowing the materials to enter the cytoplasm, the positively charged groups on the mesoporous NPs' surface tended to bind the negatively charged cell membrane. Despite the possibility of lipid membrane disruption, the cells were actually shielded from severe harm by this endocytosis failure. They concluded that silica NPs toxicity is particle-dependant as well as cell-type-dependant.

The study by Gehrke H. *et al.*, [452] suggests that the cytotoxicity caused by $SiO_2$ particles is dependent on the concentration of serum in the surrounding medium. When serum levels are low (1%), the $SiO_2$ particles disrupt the structural integrity of membrane proteins, leading to increased leakage of lactate dehydrogenase (LDH) from the cells (indicator of cell membrane damage and cell death). However, when the serum levels are high (10%), the surface of the $SiO_2$ particles becomes saturated with serum proteins, resulting in the formation of a protein corona around the particles. This protein corona prevents the particles from directly interacting with the cell membrane proteins, reducing their cytotoxicity, and resulting in no significant LDH leakage from the cells.

Di Pasqua A.J. with co-workers [449] investigated the toxicity of MSNs, including MCM-41, towards SK-N-SH cells. Interestingly, the researchers used a different approach and quantified the toxicity of the particles in terms of the number of particles applied to the cells, rather than their concentration (mass/mL). The results showed that the MCM-41 were the most toxic of the MSNs tested, causing the highest toxicity at the lowest number of particles. The researchers concluded that the toxicity of the MSNs was dependent on their BET surface area, with higher surface area resulting in higher toxicity. However, the study did not rule out the possibility that other factors, such as the type of functional groups attached to the particle surface, size and shape could also affect cytotoxicity.

It is important to note that while bare MSNs may exhibit cytotoxic effects on certain cell lines, as reported in the literature and shown in our studies, they do not necessarily represent the final product that would be used in practical applications. In fact, different studies have demonstrated that functionalized MSNs can have lower toxicity than their bare counterparts. One widely used molecule for this purpose is PEG. In the study conducted by Kostiv U. *et al.*, [453] in 2017, they investigated the effects of PEGylation on the biocompatibility of $SiO_2$ coated $Fe_3O_4$ NPs using murine neural stem cells. They found that the addition of PEG on the NPs surface significantly improved their biocompatibility, particularly at high concentrations (200 μg/mL). In contrast, the bare NPs caused a reduction in cell viability of approximately 50% even at a lower dose of 20 μg/mL after a 24 h incubation period. The results from this study are similar to the ones obtained in

our study. We observed a higher cytotoxicity of bare MSNs towards A549 cells, with viability decreasing to around 40% of the control for concentrations as low as 25 μg/mL after 72 h treatment. On the contrary, the PEGylated counterpart was better tolerated, with cellular viability decreasing to only 73% of the control at the same concentration and time point. This demonstrates the advantageous properties of PEG in increasing the biocompatibility of NPs.

Additionally, in real-world scenarios, NPs are often exposed to biological fluids before interacting with cells. This exposure can result in the formation of a protein corona around the particle surface, which can, as outlined previously, modify the interactions between the particles, the cellular membrane and cellular machinery, thereby mitigating acute cellular toxicity. Therefore, not only the lack of a protective coating on the surface of bare MSNs may have led to the exposure of the NPs' silanol groups, causing damage to the cells, but also the absence of serum in the cell media could have contributed to the observed cytotoxicity of the un-functionalized MSNs. In fact, the previously cited study by Lesniak A. and colleagues [441] highlights the importance of considering the influence of serum in *in vitro* studies of NPs and their biological interactions with cells. The presence of serum can significantly affect the uptake of NPs by cells, as well as their impact on cell function and viability. In this work, the researchers observed that silica NPs were more easily taken up by cells and caused cellular damage when exposed to cells in a serum-free media setting. In contrast, when serum was present, there were no indications of cell toxicity or the presence of loose NPs in the cytoplasm. This suggests that serum may prevent NPs from adhering to the cell membrane and from entering the cells. Additionally, the authors suggest that the biological effects of nanomaterials cannot be directly linked to the nature of the particles themselves but must also be correlated with the nature of the corona complexes that form on their surfaces. In a study from Stayton I. and co-workers, [454] the internalization of silica NPs in human lung cancer cells (A549) at a single cell level was investigated. The researchers coated the particles with different proteins such as histone, haemoglobin, and bovine serum albumin (BSA) and observed their internalization over time. The most relevant findings reported included: first, a competitive process of particle agglomeration/protein adsorption occurred after the

proteins quickly saturated the particle surface upon exposure; second, the rate of uptake was influenced by the surface charge of the particles after protein coating, especially when the charge difference was significant, and finally, the particles without any protein adsorbed on their surface were taken up by cells almost three times faster than those with protein coating and the same surface charge. The authors hypothesized that silica NPs can be rapidly adsorbed onto proteins present in the cell membrane and their subsequent internalization facilitated by the continuous recycling of the lipid bilayer during exocytosis and endocytosis or by the recycling of membrane protein structures that had undergone damage or modification. Another interesting observation was that while particles leave the cells over time, this exocytosis process was slower than internalization and did not reach completion during the 24-hour analysis period. However, the pace of exocytosis was greater with the highest amount of internalized particles.

Therefore, as previously mentioned, the toxicity observed with PEG-functionalised NPs could have been caused by removal of the PEG shell, which resulted in the exposure of the NPs' silanol groups, and in an increase of oxidative stress and membrane damage due to the absence of serum in the cell media. On the other hand, even after the removal of the gelatine shell due to the presence of MMPs, the presence of the aldehyde groups on the surface of MSNs-CHO protected the cells from interaction with silanol groups.

### 4.1.1.2 Free drug – Comparison between Doxorubicin Hydrochloride and Paclitaxel

Next, the effect of Doxorubicin Hydrochloride (DOX) and Paclitaxel (PTX) on the A549 cell line was examined *in vitro*, in order to determine which of the two drugs was the most effective, so that it could be utilized as the model cargo for the developed DDS.

Doxorubicin is a chemotherapy medication that belongs to the anthracycline class of drugs. It is one of the first anthracyclines that was identified together with daunorubicin (DNR) from the pigment-producing *Streptomyces peucetius* in the early 1960s. It is one of the most effective antineoplastic medications with the

broadest spectrum of activity in its class, and it is commonly used in the treatment of various types of cancer, including breast cancer, lung cancer, ovarian cancer, and leukaemia, often in combination with other chemotherapy drugs. Doxorubicin Hydrochloride is a hydroxy derivative of the cytotoxic anthracycline antibiotic. DOX works by interfering with the DNA of cancer cells, preventing their replication, and causing them to die, it intercalates into the DNA helix, within the base pairs, and/or bind covalently to proteins involved in DNA replication and transcription. In addition to its intercalation into the DNA helix, DOX also generates free radicals that can cause cellular damage, leading to cell death. [455, 456]

Paclitaxel (PTX) was discovered in the 1960s (**Fig. 4.3**) as part of the US National Cancer Institute's new cancer medication screening and discovery program, where over 30,000 plant extracts were tested looking for anticancer activity, including a crude extract from the bark of *Taxus brevifolia* (Pacific Yew), which showed an anticancer effect against many cancers cell lines. The chemical structure of the extract's active component was identified as PTX. PTX is an "antimicrotubular drug", specifically a microtubule-stabilizing agent as it promotes tubulin dimer polymerization to form microtubules [364, 457] even in the absence of components ordinarily necessary for microtubule assembly like guanine triphosphate (GTP), and subsequently stabilizes the microtubules by inhibiting depolymerization. In addition to being extremely stable, the microtubules created as a result of PTX activity are also defective, which causes cell death. PTX stops cells in the late G2 and M phases of the cell cycle, reducing cell reproduction.

| | |
|---|---|
| 1962-68 | NCI screening of cytotoxic agents from natural products |
| 1967 | Antitumor activity detected |
| 1969 | Pure paclitaxel isolated |
| 1971 | Structure elucidated |
| 1983 | Phase I studies initiated |
| 1986 | Hypersensitive reactions observed |
| 1988 | NCI suggests premedication regimen |
| 1989 | Proved effective against ovarian cancer |
| 1991 | Proved effective against breast cancer |
| 1992 | Proved effective against non-small cell lung cancer |
| 1992 | Approved by US FDA for ovarian cancer |
| 1994 | Approved by US FDA for breast cancer |
| | Total synthesis by Nicolaou and Holton, Independently |
| 1994 | Approved in India for ovarian cancer |
| 1995 | Approved in India for breast cancer |

**Figure 4.3:** The development of paclitaxel as an anticancer drug through the years since its discovery (*Reprinted from Panchagnula, R., Pharmaceutical aspects of paclitaxel. International Journal of Pharmaceutics, 1998. 172(1): p. 1-15, Copyright © 1998, with permission from Elsevier).* [364]

For testing the cytotoxic effect of DOX and PTX on A549 and LLC1, cells were exposed to the drugs at various concentrations up to 72 h and their $IC_{50}$ calculated. As shown in **Fig. 4.4 A**, DOX had a larger $IC_{50}$ (139 nM) than PTX (**Fig. 4.5 A**), which had a considerably more toxic effect against lung cancer cells, with an $IC_{50}$ around 5 nM after 72 h treatment. Jiménez-López J. *et al.*, [458] and Mo Y. and L.-Y. Lim [459] reported an $IC_{50}$ of 10.5 ± 0.9 and 3.04 ± 0.24 nM, respectively, for PTX on the same cell line. The differences observed could be due to the different experimental conditions and time of incubation (96 and 72 h, respectively). Nevertheless, both groups reported values close to the one obtained in our study.

**Fig. 4.4 B** shows how the viability of A549 cells decreases with time and with increasing DOX concentrations. The same pattern is observed with PTX (**Fig. 4.5 B**). It is worth noting how PTX decreases cell viability to 76% at the lowest concentration tested after just 24 h, and how DOX on the other hand seems to not have a significant effect on cells viability after 24 h treatment at the lowest dose tested, proving PTX as a more potent cytotoxic drug for this specific cell line. After

24 h, the viability of A549 cells did not fall below 80% of the control for any of the DOX amounts investigated, with higher toxic effects appearing after 48 h.
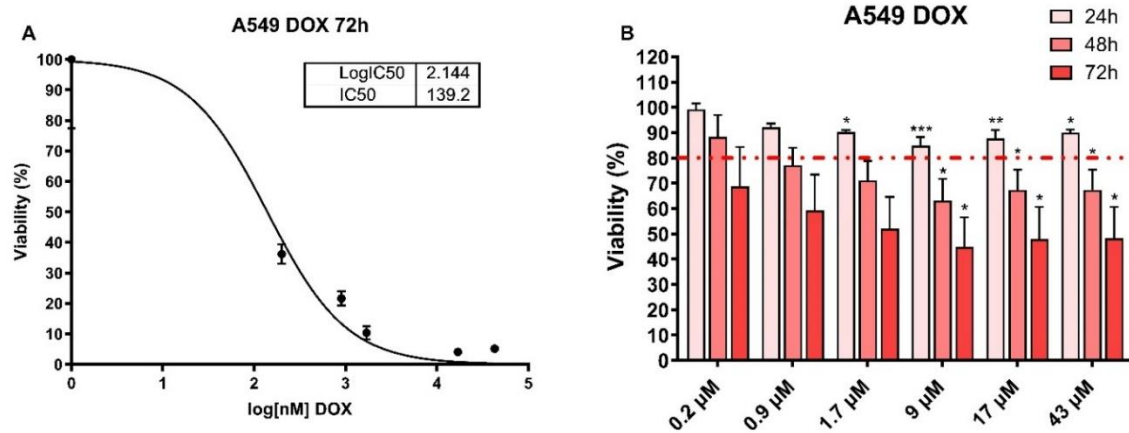


**Figure 4.4: A-** DOX $IC_{50}$ (nM) in A549 cells after 72 h treatment. **B-** A549 cell viability upon treatment with free DOX for 24, 48 and 72 h (mean±SEM). The x-axis corresponds to DOX concentration. For the corresponding amount in µg/mL see **Appendix 2, Table A2.1** Statistical test: One-way ANOVA with Dunnett's multiple comparison post-test comparing the different drug concentrations to the control (non-treated cells, taken as 100% of viability) at the same time point. n=4, $p \leq 0.05$ (*), $p \leq 0.01$ (**), $p \leq 0.001$ (***)
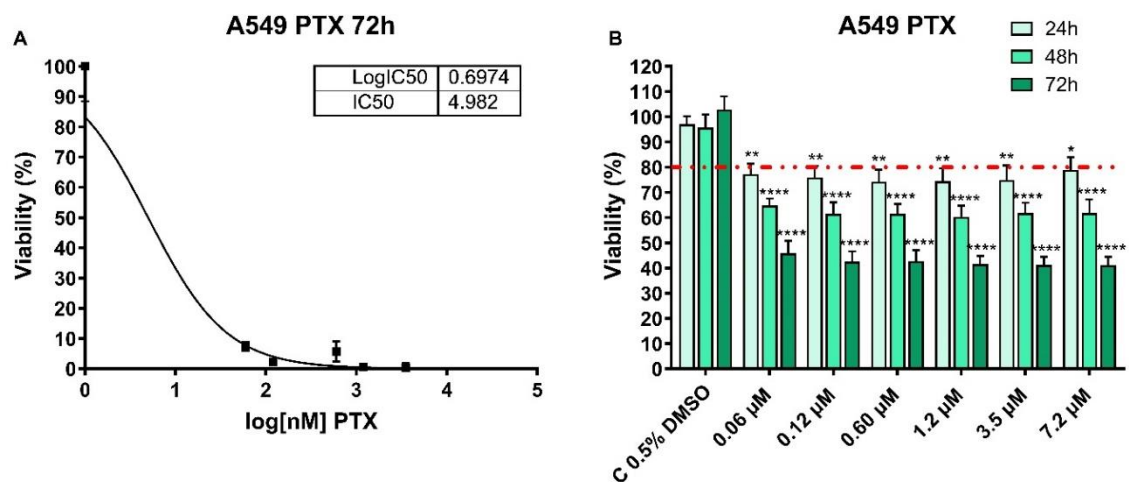


**Figure 4.5: A-** PTX $IC_{50}$ (nM) in A549 cells after 72 h treatment. **B-** A549 cell viability upon treatment with free PTX for 24, 48 and 72 h (mean±SEM). The x-axis corresponds to PTX concentration. For the corresponding amount in µg/mL  see **Appendix 2, Table A2.1** Statistical test: One-way ANOVA with Dunnett's multiple comparison post-test comparing the different drug concentrations to the control (non-treated cells, taken as 100% of viability) at the same time point. n=4, $p \leq 0.05$ (*), $p \leq 0.01$ (**), $p \leq 0.0001$ (****)

It has been reported that PTX-induced cell death may be attributed to an array of pathways depending on the drug dose. High doses of PTX cause the formation of stable microtubule bundles and an increase in polymer mass in cells, disrupting the normal polymerization/depolymerization cycle of microtubules and causing cell cycle arrest in the G2/M phase, which is essential for preventing DNA-damaged cells from going through mitosis. The G2/M checkpoint can cause apoptosis if the DNA damage is too great to be repaired, killing the damaged cell before it divides and possibly creates daughter cells with mutations that might cause cancer or other disorders. Contrarily, it has been found that lower drug concentrations do not affect the polymer mass or cause the creation of bundles. In a work published in 1998 by Torres K. and S.B. Horwitz, [460] the authors observed that cell death was triggered by irregular mitosis at low PT concentrations (< 9 nM), which lead to the formation of multinucleated cells. At higher concentrations (≥ 9 nM) the drug induced apoptosis through a process that is dependent on the Raf-1 kinase enzyme.

### 4.1.1.3  Paclitaxel loaded MSNs

PTX is generally administered using a combination of solubilizing agents, such as Cremophor/ethanol (CrEL), due to its hydrophobicity. [375-380] In fact, PTX's insolubility in aqueous solvents is related with poor pharmacokinetics, elevated protein binding, and distribution volumes that much surpass total body water. In addition, CrEL can also alter the pharmacokinetic profile of the drug, and according to several investigations, PTX micellar confinement by CrEL in plasma reduces its availability for distribution in tumour tissues, increases the systemic exposure of the drug and decreases its systemic clearance, affecting the drug's pharmacodynamics and raising the risk of systemic toxicities. PTX side effects include hypersensitivity responses, myelosuppression, bradycardia, hypotension, peripheral neuropathy, myalgias, arthralgias, nausea, diarrhoea, mucositis, and alopecia and it is believed that CrEL might also contribute to some of these unwanted effects. Overall, there are a number of factors that have a significant detrimental effect on the therapeutic index of the drug and only a small fraction of

the injected dosage reaches the desired location of therapy. For this reason, several delivery techniques have been investigated in order to enhance intratumorally PTX concentrations and lessen the adverse side effects. [461] Fonseca C. *at al.,* [462] synthesised PLGA NPs which showed excellent incorporation efficiencies of PTX and were able to enhance its anti-tumoral efficacy *in vitro* (on a human small cell lung cancer cell line, NCI-H69 SCLC) when compared to the free drug, thanks to the sustained release from the nano system. Lu H. *et al.,* [463] demonstrated that the use of PTX NPs (PTX-incorporating micellar nanoparticle formulation) could effectively inhibit the progression of ovarian carcinoma in the peritoneal cavity of female F344 rats. They significantly reduced the tumour weight and ascites volume, indicating a higher antitumor effect compared to the free drug. Furthermore, the study highlighted the lymphatic targeting property of PTX NPs. The concentration of the drug in the tumour site and pelvic lymph nodes was found to be significantly higher in animals treated with PTX NPs compared to those treated with free PTX, suggesting that the NPs have an enhanced ability to accumulate in the lymphatic system, potentially improving their efficacy in targeting metastatic cells in the lymph nodes.

Upon loading and functionalization, the NPs were tested in order to assess and compare their toxicity effect towards A549 cells with the free drug.

**Fig. 4.6** shows a similar response between the effect of free PTX and MSNs+PTX. The drug is delivered, affecting cell viability, demonstrating a successful loading and release from the NPs. After 24 h of treatment cells viabilities decreased to around 80% of the control and continued to decline with increasing treatment duration. According to previous studies, [464] when cells are exposed to PTX for extended incubation times, more cells enter G2 and M phases, increasing the drug's ability to limit cell growth and cause cell death.

Since previous cell viability assays with empty MSNs (**Fig. 4.2**) evidenced a harmful effect of the silica NPs on lung cancer cells which was concentration and time dependent, the possible contribution of the silica itself to the *in vitro* cytotoxicity observed when A549 cells were exposed to MSNs-PTX was also investigated. **Fig. 4.7** provides a comparison between empty and loaded NPs in terms of the concentrations of silica NPs used. This comparison helps visualize

144

which concentration of empty MSNs resulted safe in the previous cytotoxicity assays (**Fig. 4.2**), and it allows to determine which of the observed toxic effects (**Fig. 4.6**) can be attributed solely to the release of PTX.
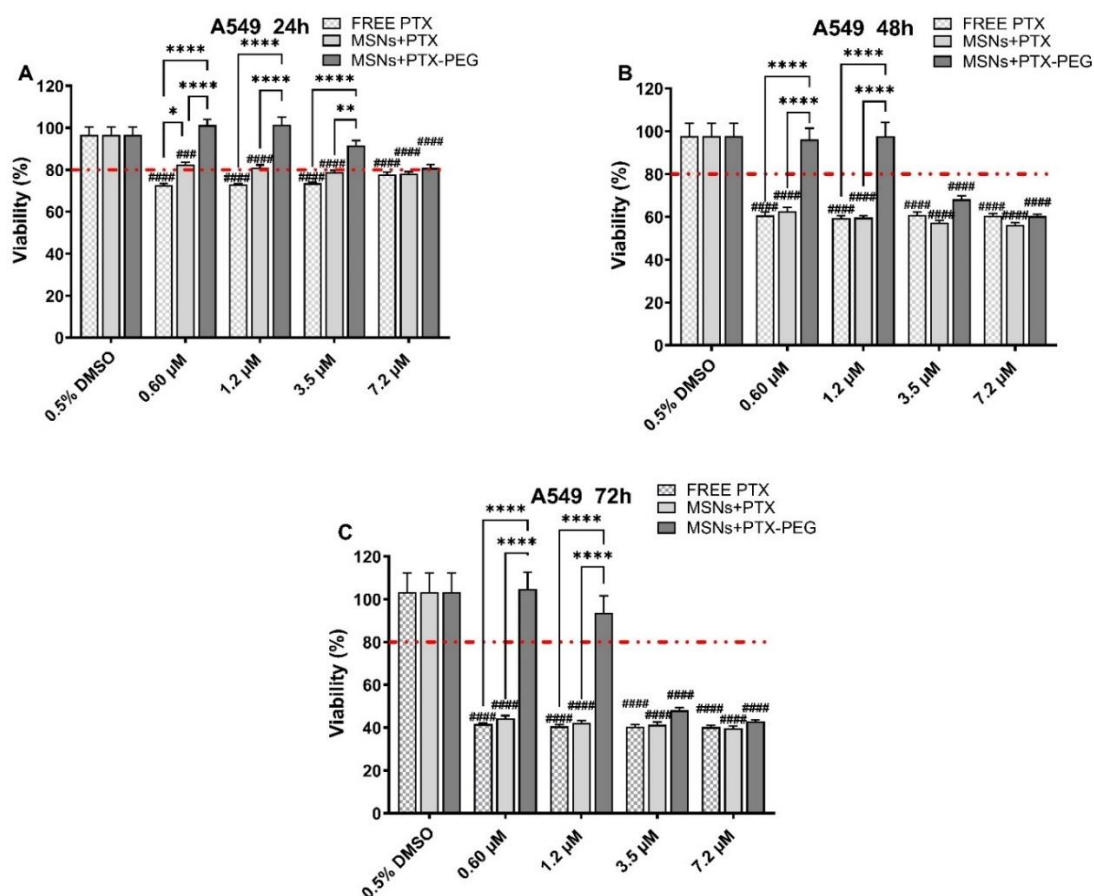


**Figure 4.6:** Comparison of A549 cell viability upon treatment with free PTX, MSNs+PTX and MSNs+PTX-PEG at the corresponding drug concentrations after **A-** 24, **B-** 48, and **C-** 72 h. (mean ± SEM) For the corresponding NPs concentrations see **Appendix 2, Table A2.2** or **Fig. 4.7** and **4.8**. Statistical test: Two-way ANOVA with Tukey's multiple comparison post-test comparing all treatments showing the differences between the same drug concentration. Non-treated cells taken as 100% of viability n=4 free PTX, n=3 loaded NPs, p ≤ 0.05 (*), p ≤ 0.01 (**), p ≤ 0.0001 (****). Two-way ANOVA with Dunnett's multiple comparison post-test comparing all treatments to the control (0.5% DMSO). Non-treated cells taken as 100% of viability. p ≤ 0.001 (###), p ≤ 0.0001 (####)
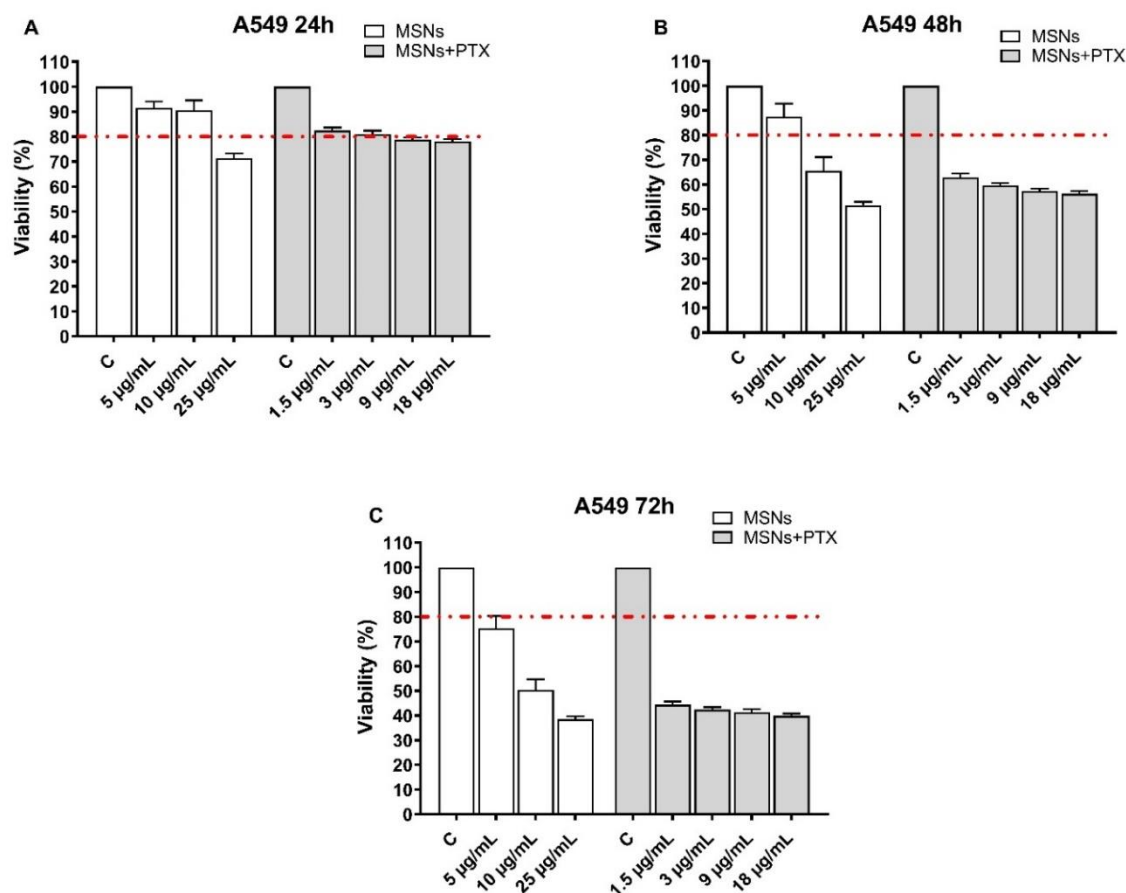
**Figure 4.7:** Graphical representation of A549 cell viability assay upon treatment with MSNs and MSNs+PTX after **A-** 24 h, **B-** 48 h and **C-** 72 h. (mean ± SEM) n=3 The x-axis corresponds to NPs concentration. For the corresponding amount of drug loaded see **Appendix 2**, **Table A2.2** or **Fig. 4.6**.

At the concentrations studied, the toxic effect on A549 cells can be attributed to the PTX released from the DDS after 24 h (**Fig. 4.7 A**). On the other hand, after 48 and 72 h (**Fig. 4.6 B** and **C**) we have to consider that the silica itself may be playing a role in the observed toxicity towards A549 cells, and the results should be analysed together with those observed for the empty MSNs (**Fig. 4.7**). In fact, after 2 days of treatment (**Fig. 4.7 B**), concentrations of MSNs as low as 10 and 25 µg/mL began to produce a toxic effect on the cells, suggesting that the cytotoxic effect of PTX cannot be regarded as the sole variable for similar MSNs+PTX concentrations of 9 and 18 µg/mL (corresponding to 3.5 and 7.2 µM loaded PTX). Contrarily, we may see a rising harmful impact over time at the lowest concentrations (1.5 and 3 µg/mL) presumably as a result of a prolonged drug

release, with an increasing cumulative drug released and/or an increasing contact time with the cells, in contrast to similar empty MSNs concentrations which did not exhibit any toxic effect (5 µg/mL).

In the case of MSNs-PEG, the presence of a PEG capping system on the surface of the NPs may prevent the drug from being released immediately (burst release), enhancing the PTX effect over 48 h (**Fig. 4.8 B**). At 72 h (**Fig. 4.8 C**), the toxic impact from the empty NPs is noticed for concentrations of MSNs-PEG equal to 25 and 50 µg/mL, with cell viability dropping to 73 and 58%, respectively. This could be explained by the delayed opening of the pores, with NPs becoming hazardous after 3 days when the polymer coating is gradually removed, and silica comes into contact with the cells. Nevertheless, cellular viability of cells treated with MSNs+PTX-PEG at concentrations equal to 25 and 50 µg/mL (**Fig. 4.8 C**) decreased to 48 and 43% of the control, respectively, after 72 h, indicating that PTX is being released increasing the NPs' toxicity. When we look at the effect of the lowest MSNs+PTX-PEG concentrations (4.5 and 9 µg/mL) (**Fig. 4.8**), no toxic effect is noted on the cells for both empty (corresponding concentrations of 5 and 10 µg/mL) and loaded NPs. We may explain these findings by assuming that the quantity loaded in the pores is not entirely released and/or that the cumulative drug released is too little to have a discernible effect.

Another possibility might be drug resistance in the cells: failure of a chemotherapeutic treatment may be due to the tumour being intrinsically resistant to the treatment or to resistance developing during therapy. Chemotherapy can fail in part because of substantial intertumoral heterogeneity, which is the cause of the presence of cancer cells with varying responsiveness to anticancer medications inside a tumour, one of these being lung cancer. [465] Several mechanisms have been hypothesized as the reason for cancer cells' resistance to PTX, including changes in microtubule dynamics and altered binding to its biological target, the microtubule. [466] As previously mentioned, PTX exerts its activity by attaching to the microtubule polymer and promoting tubulin polymerization, resulting in mitotic and postmitotic arrest and cell death. By doing so, the drug reduces the threshold concentration of microtubule protein required for microtubule assembly (by a factor of twenty with a drug concentration of 5 µM), leading to increased microtubule

polymer mass and reduced microtubule dynamics. It has been shown that microtubule-stabilizing agents like PTX can generate aneuploid cell populations (with an abnormal, or non-euploid, number of chromosomes) in the absence of a prolonged mitotic block when lower concentrations are used and consequently only a specific fraction of the binding sites are occupied. [466] Replogle J.M. with colleagues [467] assessed PTX effect (20 nM for 72 h) against the pseudodiploid colon cancer cell line HCT116 (with paired chromosomes), and in four aneuploid cancer cell lines derivatives of HCT116. They observed that three of the four cell lines with an abnormal number of chromosomes survived PTX treatment when compared to HCT116. They hypothesized and confirmed that the common feature causing this resistance was the slowed progression through G1 and S phase of the cell cycle, concluding that aneuploidy-induced delayed proliferation and drug resistance are directly connected. In fact, by delaying the cells in G1 they do not reach the point in the cycle where the drug can exert its toxic effect. S.B. Horwitz reported in their work [468] that aneuploid populations in A549 cells were the result of defective mitosis induced by low PTX concentrations. It has been hypothesized that aneuploidy increases the malignancy resistance to treatments and therefore the need of higher doses for obtaining the same effect. These findings could also explain why at the lowest concentrations (4.5 and 9 µg/mL, corresponding to 0.6 and 1.2 µM of PTX, respectively) MSNs+PTX-PEG did not exhibit a toxic effect. The amount of drug released might not have been enough to kill the cells, and/or might have caused the cells to become resistant following the formation of aneuploid populations due to defective mitosis.
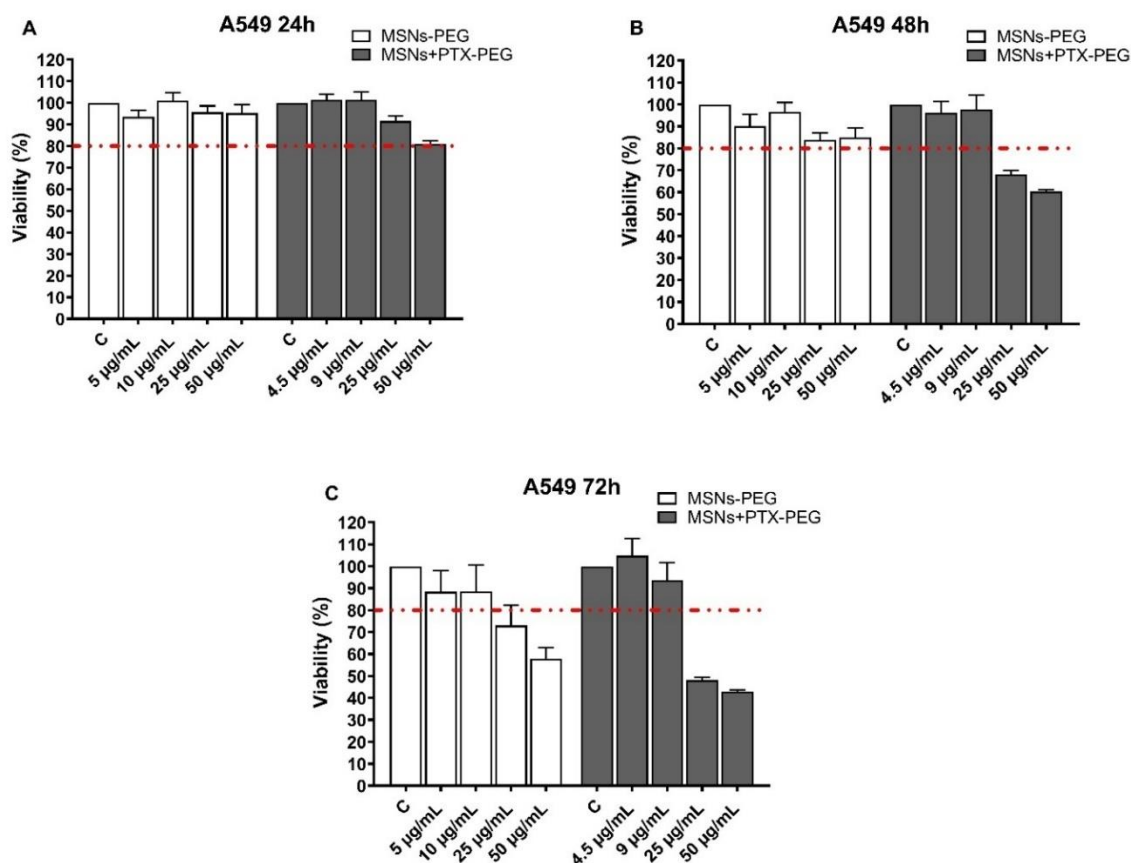
**Figure 4.8:** Graphical representation of A549 cell viability assay upon treatment with MSNs-PEG and MSNs+PTX-PEG for **A-** 24 h, **B-** 48 h, and **C-** 72 h. (mean ± SEM) n=3 The x-axis corresponds to NPs concentration. For the corresponding amount of drug loaded see **Appendix 2**, **Table A2.2** or **Fig. 4.6**.

As previously shown in **Fig. 4.1**, MSNs functionalized with both aldehyde groups (MSNs-CHO) and gelatine (MSNs-GEL) did not exert any detrimental effect towards A549 cells at the concentrations tested. By comparing the concentrations of silica NPs used, of unloaded (MSNs-CHO) and loaded (MSNs-CHO+PTX) aldehyde functionalised NPs (**Fig. 4.9**) and unloaded (MSNs-GEL) and loaded (MSNs-CHO+PTX-GEL) gelatine functionalised NPs (**Fig. 4.10)**, it seems reasonable to assume that the toxic effect on cancer cells is caused by the release of the drug from the pores.
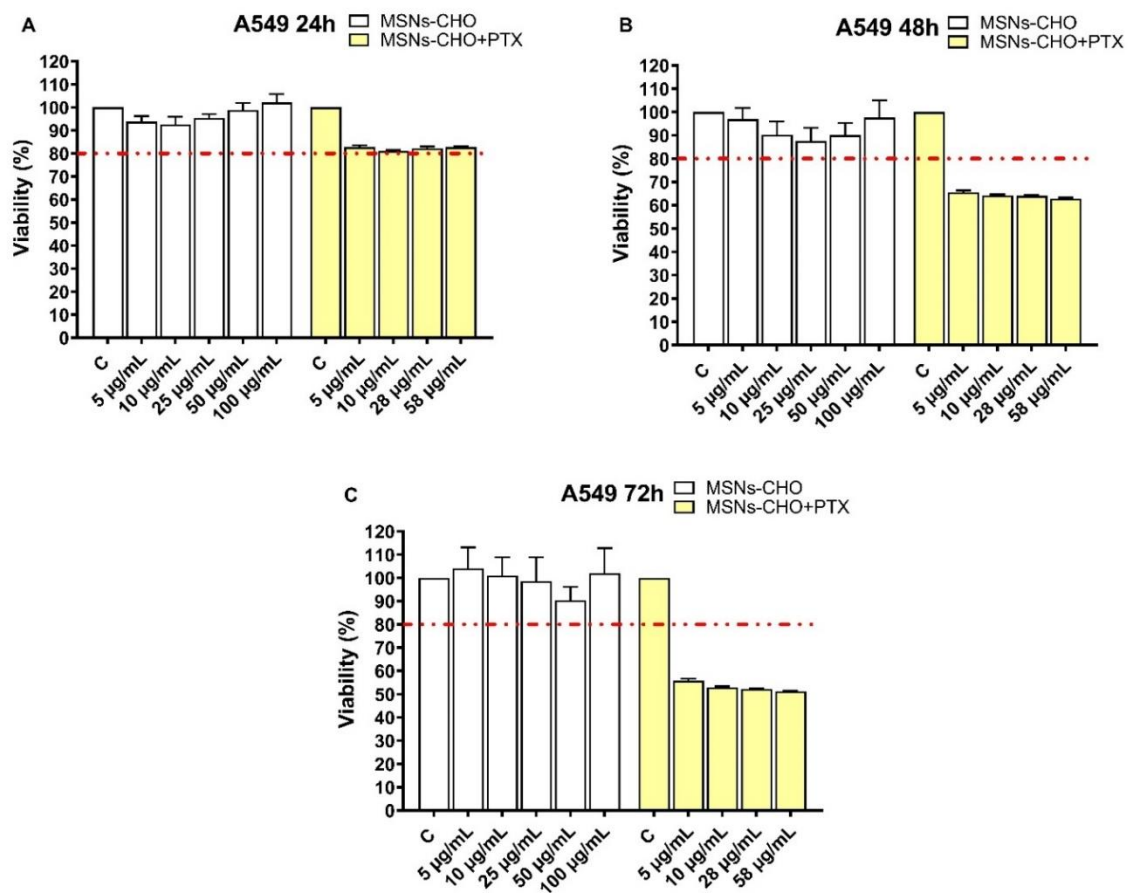
**Figure 4.9:** Graphical representation of A549 cell viability assay upon treatment with MSNs-CHO and MSNs-CHO+PTX for **A-** 24 h, **B-** 48 h, and **C-** 72 h. (mean ± SEM) n=6 empty NPs, n=3 loaded NPs. The x-axis corresponds to NPs concentration. For the corresponding amount of drug loaded see **Appendix 2**, **Table A2.3** or **Fig. 4.11**.
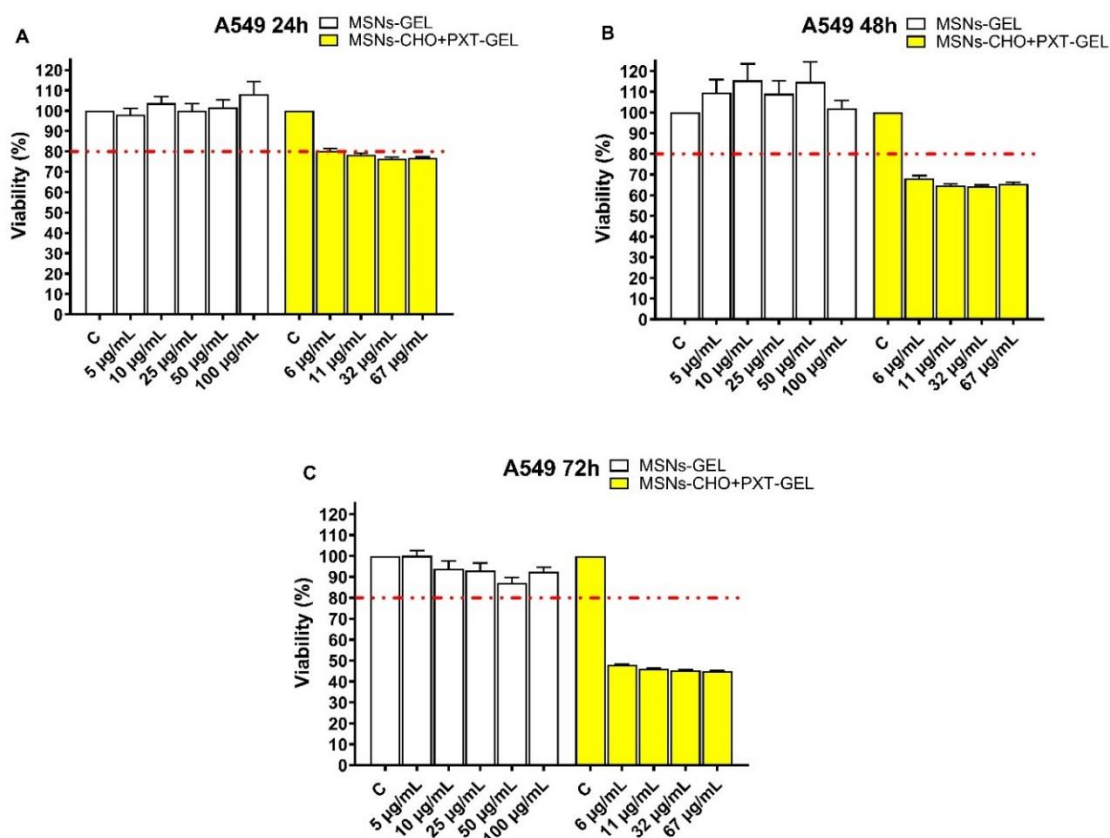
**Figure 4.10:** Graphical representation of A549 cell viability assay upon treatment with MSNs-GEL and MSNs-CHO+PTX-GEL for **A-** 24 h, **B-** 48 h, and **C-** 72 h. (mean ± SEM) n=6 empty NPs, n=3 loaded NPs. The x-axis corresponds to NPs concentration. For the corresponding amount of drug loaded see **Appendix 2**, **Table A2.3** or **Fig. 4.11**.

PTX seems to be released in a similar fashion from both NPs over time, since their toxic effects are similar to those of the free drug (**Fig. 4.11**). We could hypothesize that the capping system is removed faster than PEG once in contact with MMPs, allowing PTX to exert its effect immediately, as with uncapped MSNs. The degree of crosslinking of the polymer might explain these results; in fact, Che E. and colleagues [353] demonstrated how the degree of crosslinking of gelatine covering magnetic MSNs could control drug release (with increasing quantities of crosslinker, burst release was reduced). After 72 h incubation, gelatine NPs were more toxic than the unfunctionalized ones (**Fig. 4.11**), most likely due to the drug's delayed release caused by the capping effect of the polymer remaining even after the fast initial MMPs-mediated degradation.

**Figure 4.11:** Comparison of A549 cell viability upon treatment with free PTX, MSNs-CHO+PTX and MSNs-CHO+PTX-GEL at the corresponding drug concentrations after **A-** 24, **B-** 48, and **C-** 72 h. (mean ± SEM) For the corresponding NPs concentrations see **Appendix 2, Table A2.3** or **Fig. 4.9** and **4.10**. Statistical test: Two-way ANOVA with Tukey's multiple comparison post-test comparing all treatments showing the differences between the same drug concentration. Non-treated cells taken as 100% of viability. n=4 free PTX, n=3 loaded NPs, $p \leq 0.05$ (*), $p \leq 0.01$ (**). Two-way ANOVA with Dunnett's multiple comparison post-test comparing all treatments to the control (0.5% DMSO). Non-treated cells taken as 100% of viability. $p \leq 0.0001$ (####)

## 4.1.2  Lewis Lung Carcinoma (LLC1) cells

Lewis Lung Carcinoma (LLC1) cell line was used to establish the *in vivo* model. Therefore, the experimental procedures carried out in A549 were conducted on this cell line as well.

## 4.1.2.1 Empty MSNs

*In vitro* investigation of unloaded MSNs' cytotoxic effect on LLC1 cells revealed that aldehyde- (**Fig. 4.12 A**) and gelatine-functionalised (**Fig. 4.12 B**) NPs did not exert any cytotoxic effect at the concentrations tested. Surprisingly, aldehyde-MSNs enhanced LLC1 growth. It is worth noting that there are a number of publications were the authors reported cancer cell lines becoming resistant when cultured under stressful conditions, like serum starvation, or in the presence of cytotoxic drugs. For example, in the study by White E.Z. *et al.,* [469] the authors reported that prostate cancer cells may become more resistant to oxidative stress (in this case induced by $H_2O_2$) when they are cultured under conditions of starvation. This implies that cancer cells may be able to adapt to stressful conditions and become more aggressive. The researchers observed that the prostate cancer cells did not display a cell death morphology, but instead developed a flatter morphology and increased in size and number. This suggests that the cells were adapting to the stressful conditions by changing their morphology and increasing their proliferation rate. Park E.-J. and K. Park [470] observed a growth in the viability of splenocytes of mice (to about 180% of the control group) treated with silica NPs (50mg/kg i.p.). The authors hypothesized that this response might have been connected to macrophages activation, cytokines production, and nitric oxide (NO) generation, that could have stimulated splenocyte growth. As the doses administered were increased (100 mg/kg and 250 mg/kg), a cytotoxic effect was noticed. In a different study, Sydlik U. and colleagues [471] demonstrated that ultrafine particles (including amorphous silica NPs) can induce proliferation of rat lung epithelial cells (RLE-6TN) by increasing DNA synthesis. The group also reported increased levels of the apoptotic marker caspase-3 activity, but they noticed that amorphous silica induced a higher proliferation rate than ultrafine carbon particles, which, on the other hand resulted being a stronger inducer of apoptosis.

153

Although to our knowledge there are no studies with LLC1, Lewis lung carcinoma is a highly aggressive and metastatic murine cancer, that is known for spontaneously metastasizing to other organs in immunocompetent mice. It is possible that LLC1 cells developed resistance during the three days they were incubated without FBS. In the absence of FBS, the cells may have adapted to the stress by altering their gene expression profile and cellular physiology, which could have contributed to the observed increase in viability. However, this explanation alone does not account for the differences observed with gelatine-functionalized NPs. For example, the particles may be taken up by the cells more efficiently, or they may not be as toxic against the LLC1 cells as they are against other types of cancer cells, due to differences in their surface receptors or internalization mechanisms.
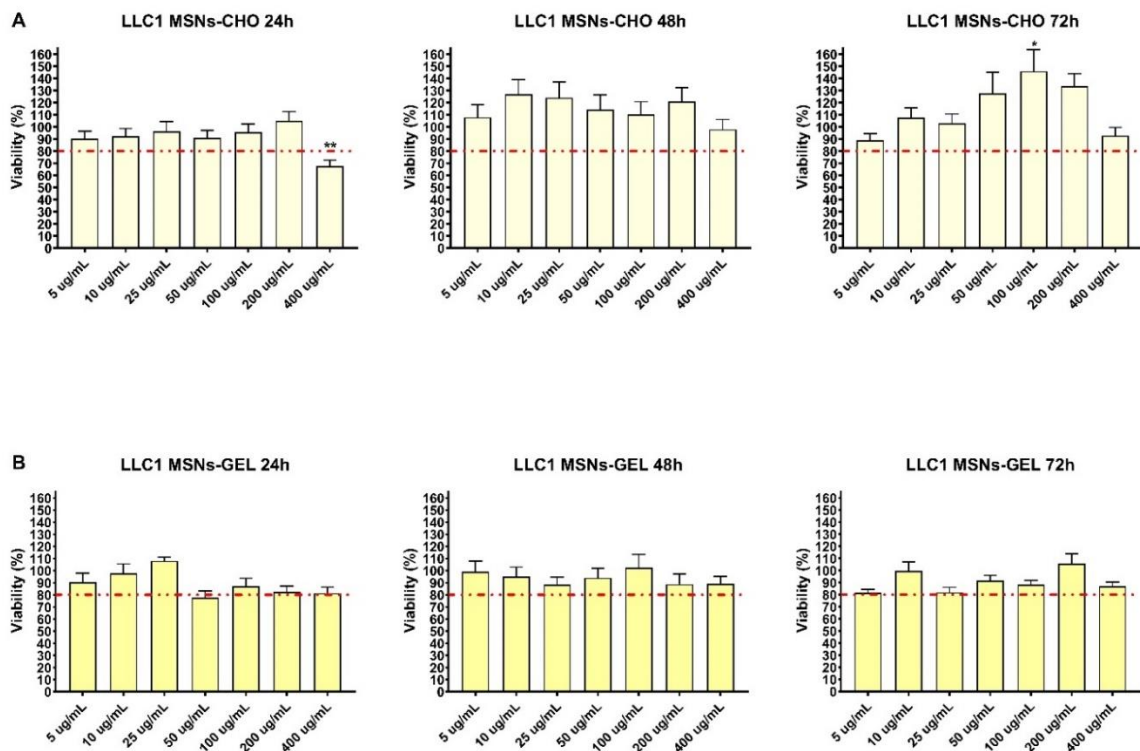


**Figure 4.12:** LLC1 cell viability assay upon incubation with empty **A-** MSNs-CHO and **B-** MSNs-GEL, for 24, 48 and 72 h (mean ± SEM). The x-axis corresponds to MSN concentration. Statistical test: One-way ANOVA with Dunnett's post-test comparing all treatments versus the control (non-treated cells, taken as 100% of viability) n=4, p ≤ 0.05 (*), p ≤ 0.01 (**)

Overall, the results obtained after exposure to bare MSNs and MSNs-PEG NPs (**Fig. 4.13**) suggest that both NPs have relatively lower toxicity to LLC1 than to A549 cells (**Fig. 4.2**). However, there are some notable differences between the effects of silica NPs on murine and human lung cancer cells, which may be due to a range of factors including intrinsic differences in the cell lines used. Gehrke H. and co-workers [452] for example, did not observe reactive oxygen species formation in HT29 cells over 24 h, even though other studies have shown that silica NPs induce oxidative stress through ROS formation in different cell lines. This suggests that the effects of silica NPs may vary depending on the specific cell type being tested.
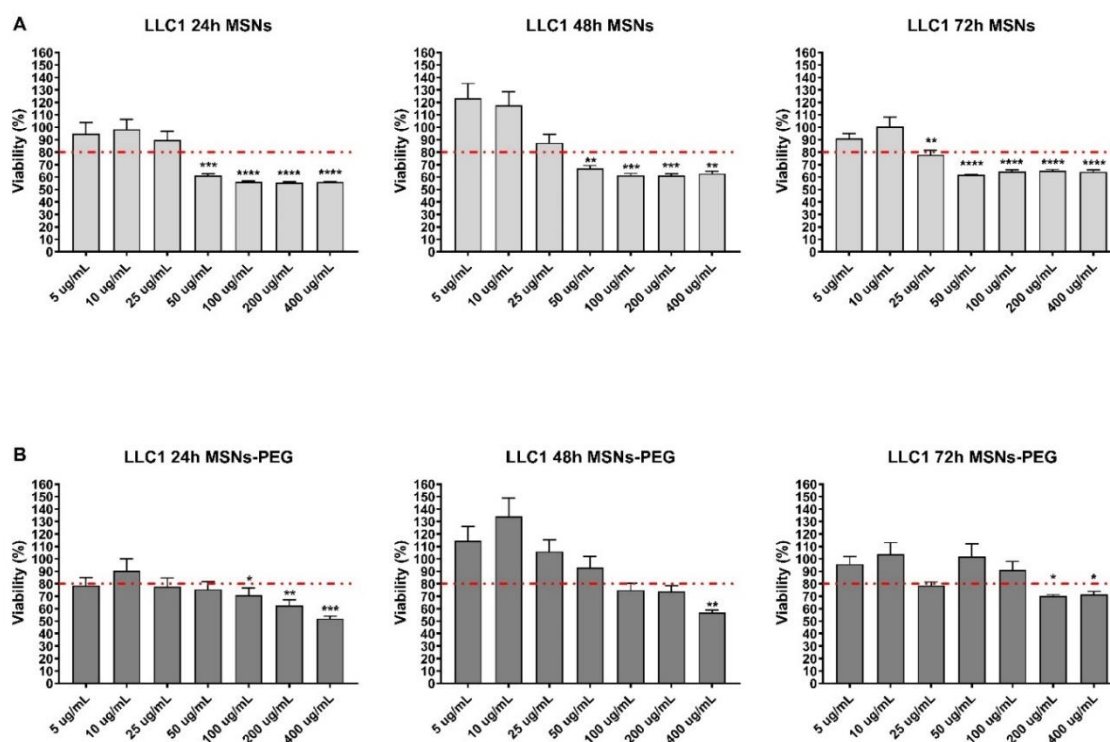


**Figure 4.13:** LLC1 cell viability assay upon incubation with empty **A-** MSNs and **B-** MSNs-PEG, for 24, 48 and 72 h (mean ± SEM). The x-axis corresponds to MSN concentration. Statistical test: One-way ANOVA with Dunnett's post-test comparing all treatments versus the control (non-treated cells, taken as 100% of viability) n=4, p ≤ 0.05 (*), p ≤ 0.01 (**), p ≤ 0.001 (***), p ≤ 0.0001 (****)

### 4.1.2.2 Free drug – Comparison between Doxorubicin Hydrochloride and Paclitaxel

LLC1 cells, like A549 cells, appeared to be more sensitive to PTX (**Fig. 4.14 A** and **B**) than to DOX (**Fig. 4.15 A** and **B**). However, when comparing their $IC_{50}$ values, LLC1 cells were found to be more resistant to PTX than A549 cells (**Fig. 4.5**). Specifically, LLC1 cells required almost twice the concentration of PTX (9 nM) to achieve the same level of inhibition than A549 cells (5 nM) after 72 h of treatment with the free drugs. These results are in line with the ones reported by Jiménez-López J. *et al.*, in their work. [458] The $IC_{50}$ for PTX reported from the group was in fact higher for LLC1 cells ($27.65 \pm 0.8$ nM) than for A549 cells ($10.5 \pm 0.9$ nM). Irrespective of the reported values for LLC1 being 3 times higher than the ones we reported, their results confirm the murine lung cancer cell line as more resistant than the human one. Yakisich J.S. with colleagues [465] demonstrated how lung cancer cells (NCI-H460) become more resistant to various cytotoxic drugs, including PTX, when cultivated under prolonged periods of serum starvation. They found the same behaviour in the MCF-7 breast cancer cell line, suggesting that this tolerance is not unique to one cell line, but a more general feature of all cancer cells. By microscopy analysis, the authors noted that malignant cells could divide in starving conditions, with the number of cells growing over time. As mentioned above, being LLC1 a very aggressive cell line, it could have developed resistance to PTX, which resulted in a higher $IC_{50}$.

As it happened with the A549, the viability of LLC1 cells declines with time and increasing PTX and DOX concentrations (**Fig. 4.14 B** and **4.15 B)**.
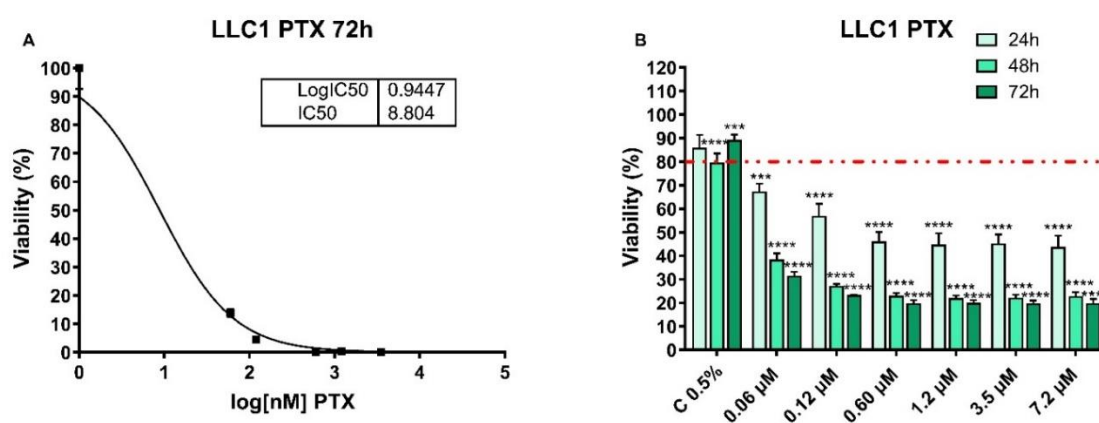


**Figure 4.14: A-** PTX $IC_{50}$ (nM) in LLC1 cells after 72 h treatment. **B-** LLC1 cell viability upon treatment with free PTX for 24, 48 and 72 h (mean±SEM). The x-axis corresponds to PTX concentration. For the corresponding amount in µg/mL see **Appendix**
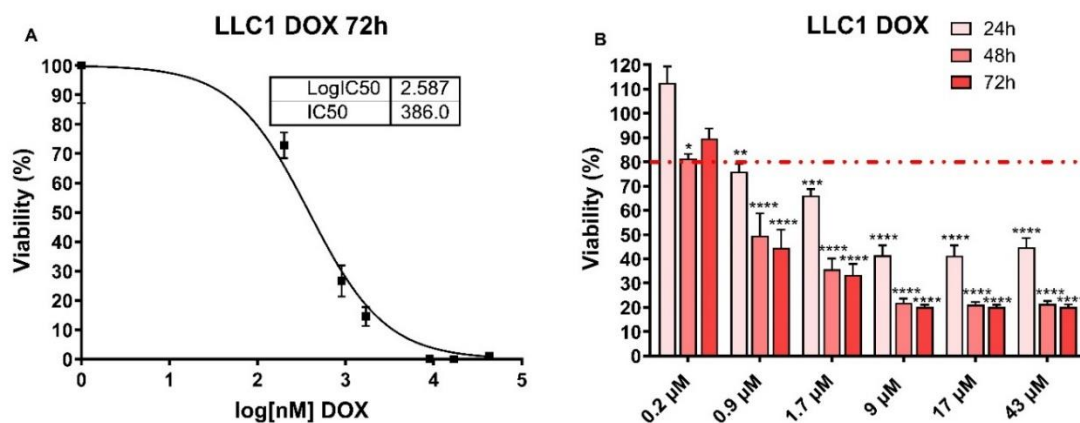
**Figure 4.15: A-** DOX $IC_{50}$ (nM) in LLC1 cells after 72 h treatment. **B-** LLC1 cell viability upon treatment with free PTX for 24, 48 and 72 h (mean±SEM). The x-axis corresponds to DOX concentration. For the corresponding amount in µg/mL see **Appendix 2, Table A2**.**1** Statistical test: One-way ANOVA with Dunnett's multiple comparison post-test comparing the different drug concentrations to the control (non-treated cells, taken as 100% of viability) at the same time point. n=3, p ≤ 0.05 (*), p ≤ 0.01 (**), p ≤ 0.001 (***), p ≤ 0.0001 (****)

### 4.1.2.3  PTX loaded MSNs

After assessing the *in vitro* toxicity of the free drugs towards LLC1 cells, PTX-loaded MSNs were also tested on the murine lung cancer cells.

Based on the results shown in **Fig. 4.16**, it appears that the free drug is more toxic towards LLC1 cells than the loaded NPs (MSNs and MSNs-PEG) after 24, 48 and 72 h of exposure. As already suggested, murine lung cancer cells may have some degree of resistance towards both the empty NPs and the free drug. This resistance may have an impact on the cytotoxicity results obtained. One possible explanation for these findings is that the dose of the drug released by the NPs may not be sufficient to produce a toxic effect on LLC1, or that the NPs might be taken up in lower amount by the cells. We expect bare MSNs to release PTX quicker than the PEG-functionalized NPs (as seen for the *in vitro* release assays with safranin-O), which may account for their greater toxic impact on LLC1 cells.

157

In contrast, PEG-functionalized NPs would have a delayed drug release, which may result in a lower dose of the drug released at the same time points and, therefore, insufficient to produce a toxic effect. This will need to be confirmed with *in vitro* release studies, but the faster release due to the absence of a capping system could explain why higher doses or prolonged exposures to the drug may be required to achieve the desired therapeutic effect in the case of functionalised NPs. Interestingly, in a study by Allalunis-Turner M.J., F.Y.F. Lee, and D.W. Siemann, [472] it was found that the levels of GSH were greater in human tumour cell lines than in rodent lines. The authors reported two further works where similar results had been found. [473, 474] These outcomes may also contribute to explain our results, as the A549 cell line, which was found to be more sensitive to MSNs+PTX-PEG than LLC1 cells (**Fig. 4.6**), is known to have high levels of GSH. [475] Therefore, it is possible that the sensitivity of cancer cells to MSNs+PTX-PEG may be influenced by cellular antioxidant levels, and this may be an avenue for further investigation in future studies.
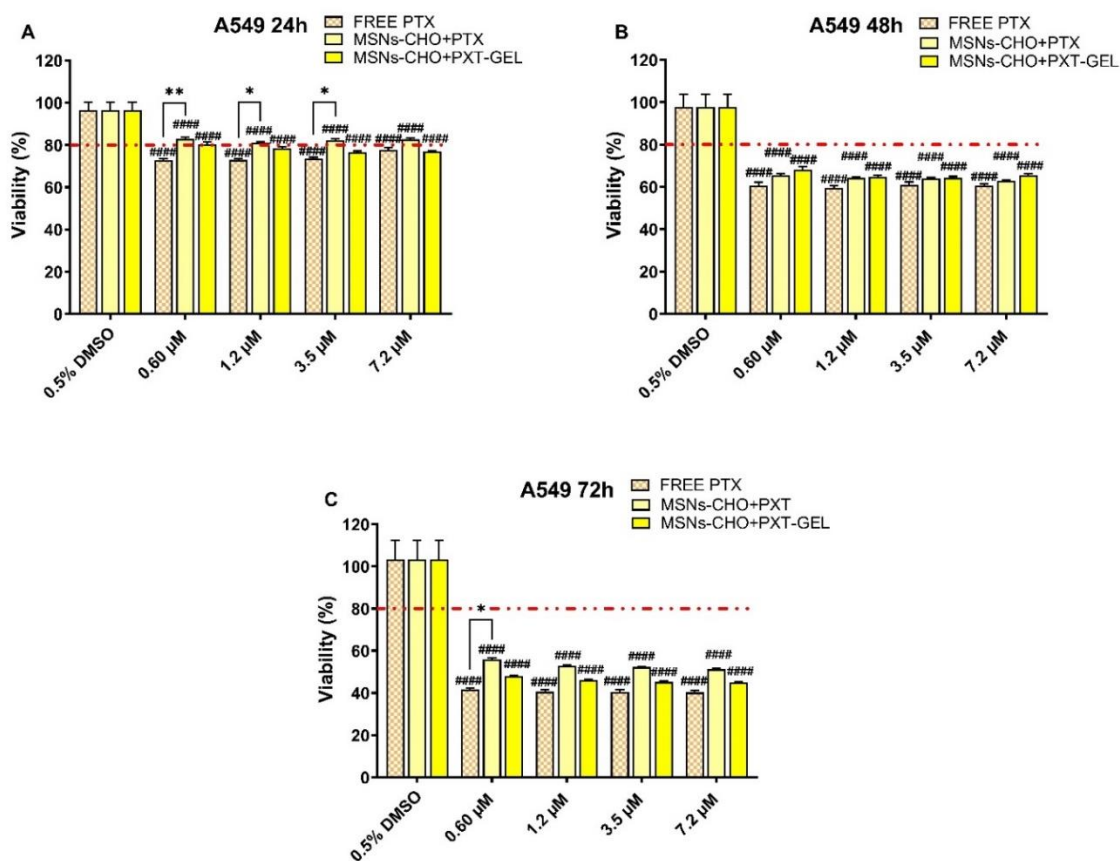
.
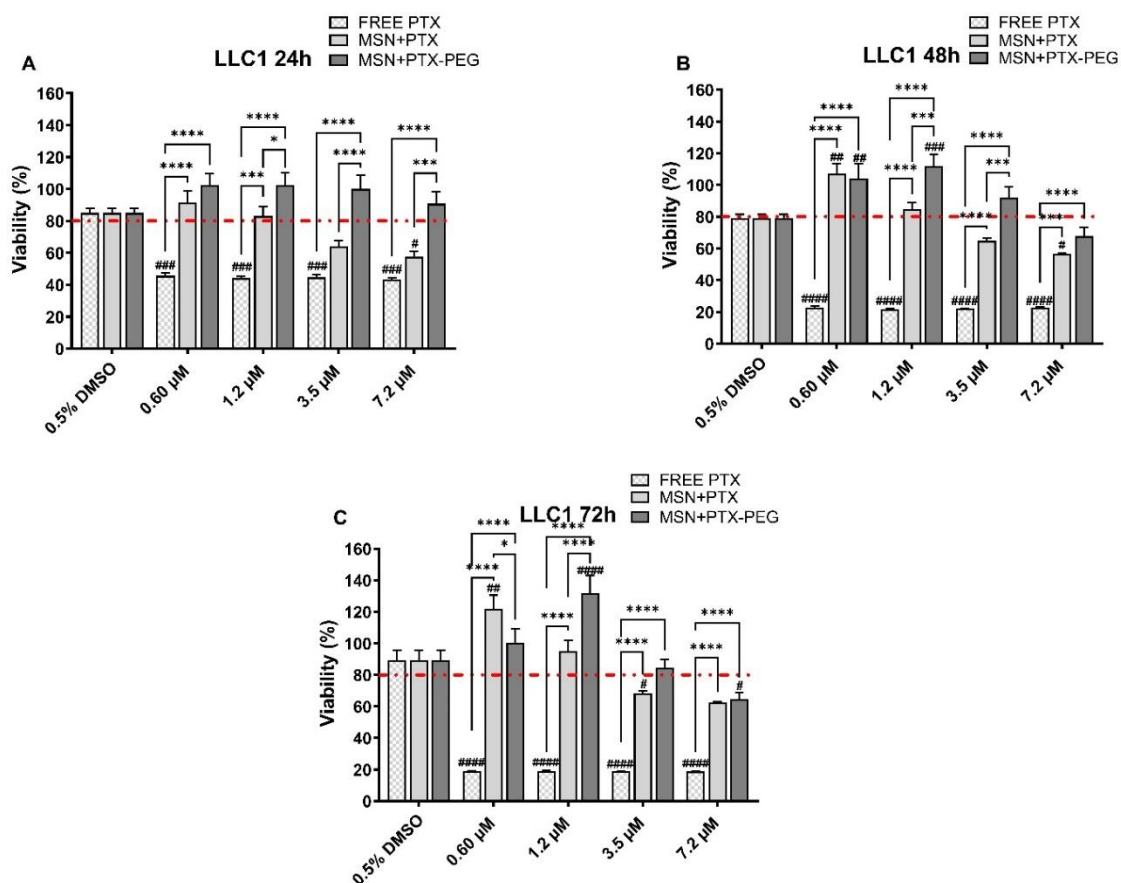
**Figure 4.16:** Comparison of LLC1 cell viability upon treatment with free PTX, MSNs+PTX and MSNs+PTX-PEG at the corresponding drug concentrations after **A-** 24, **B-** 48, and **C-** 72 h. (mean ± SEM) For the corresponding NPs concentrations see **Appendix 2, Table A2.2** or **Fig. 4.17** and **4.18**. Statistical test: Two-way ANOVA with Tukey's multiple comparison post-test comparing all treatments showing the differences between the same drug concentration. Non-treated cells taken as 100% of viability. n=3 free PTX, n=5 loaded NPs, p ≤ 0.05 (*), p ≤ 0.01 (**), p ≤ 0.001 (***), p ≤ 0.0001 (****). Two-way ANOVA with Dunnett's multiple comparison post-test comparing all treatments to the control (0.5% DMSO). Non-treated cells taken as 100% of viability. p ≤ 0.05 (#), p ≤ 0.05 (#), p ≤ 0.01 (##), p ≤ 0.001 (###), p ≤ 0.0001 (####)

Based on the data shown in **Fig. 4.17** and **Fig. 4.18**, it seems that the toxicity observed in LLC1 cells is primarily due to drug release from the NPs rather than the inherent cytotoxicity of the NPs themselves. Empty MSNs at concentrations of 10 and 25 µg/mL did not show any toxic effect towards LLC1 cells at any of the analysed time points, with cellular viability never dropping below 80% of the control. On the other hand, loaded MSNs at concentrations of 9 and 18 µg/mL reduced the

viability of the cells to 64 and 58%, respectively, at 24 h; 65 and 56%, respectively, at 48 h; and 68 and 62%, respectively, at 72 h.
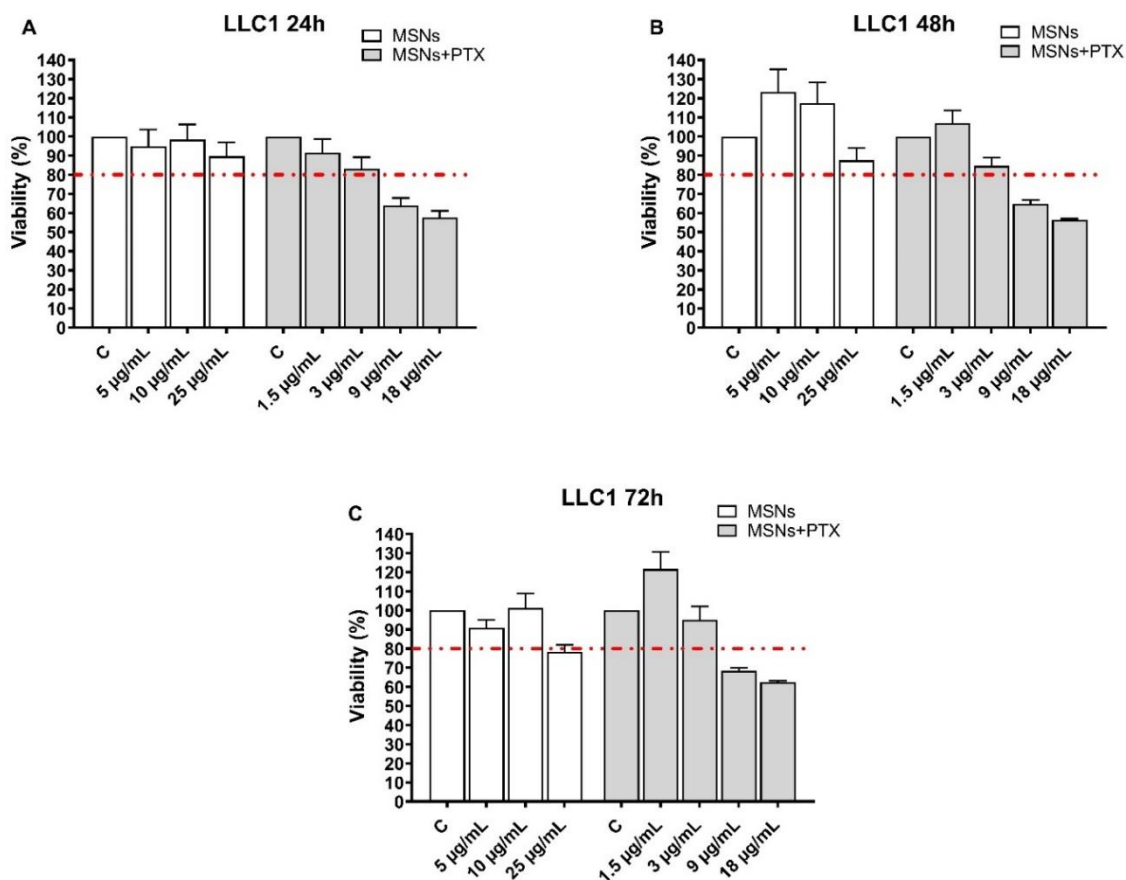


**Figure 4.17:** Graphical representation of LLC1 cell viability assay upon treatment with MSNs and MSNs+PTX after **A-** 24 h, **B-** 48 h and **C-** 72 h. (mean ± SEM) n=4 unloaded NPs, n=5 loaded NPs The x-axis corresponds to NPs concentration. For the corresponding amount of drug loaded see **Appendix 2**, **Table A2.2** or **Fig. 4.16**.
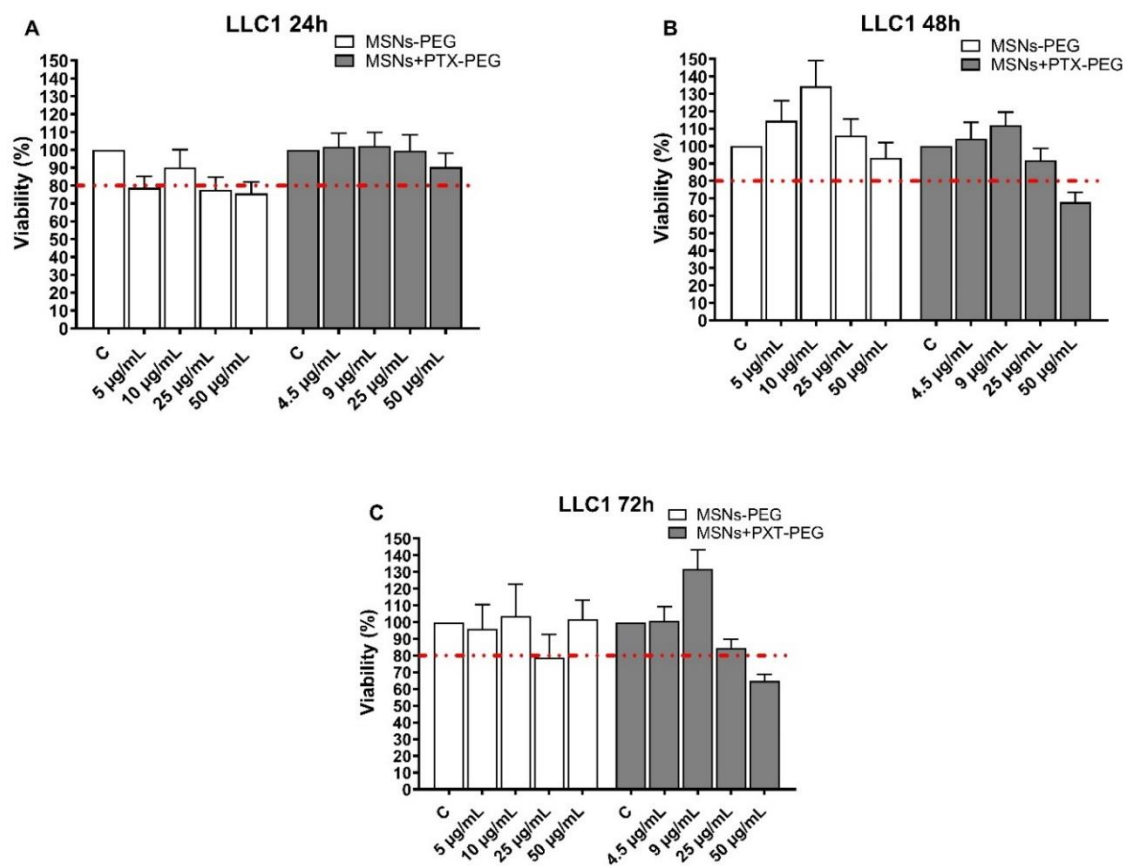
**Figure 4.18:** Graphical representation of LLC1 cell viability assay upon treatment with MSNs-PEG and MSNs+PTX-PEG after **A-** 24 h, **B-** 48 h and **C-** 72 h. (mean ± SEM) n=4 unloaded NPs, n=5 loaded NPs The x-axis corresponds to NPs concentration. For the corresponding amount of drug loaded see **Appendix 2**, **Table A2.2** or **Fig. 4.16**.

The graphs in **Fig. 4.19** and **Fig. 4.20** show that increasing the concentrations of the NPs, and hence the drug in the case of loaded MSNs, seems to lead to a higher toxic effect on murine cancer cells. While the possibility of toxicity from the bare particles cannot be entirely ruled out based on the data represented in **Fig. 4.19**, the data in **Fig. 4.20** suggest that larger amounts of drug are released over time from PEGylated MSNs having a more substantial toxic impact than lower concentrations.
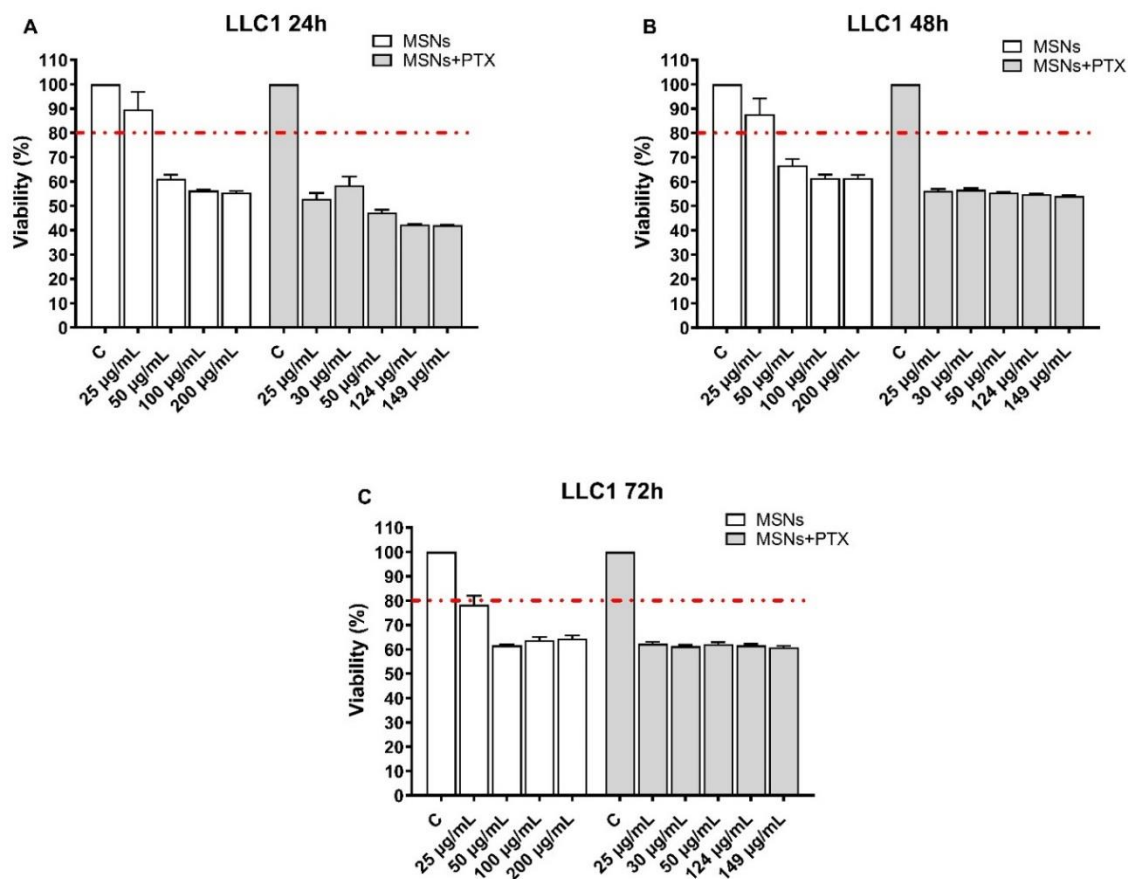
**Figure 4.19:** Graphical representation of LLC1 cell viability assay upon treatment with higher MSNs and MSNs+PTX after **A-** 24 h, **B-** 48 h and **C-** 72 h. (mean ± SEM) n=4 unloaded NPs, n=5 loaded NPs The x-axis corresponds to NPs concentration. For the corresponding amount of drug loaded see **Appendix 2**, **Table A2.2** or **Fig. 4.16**.
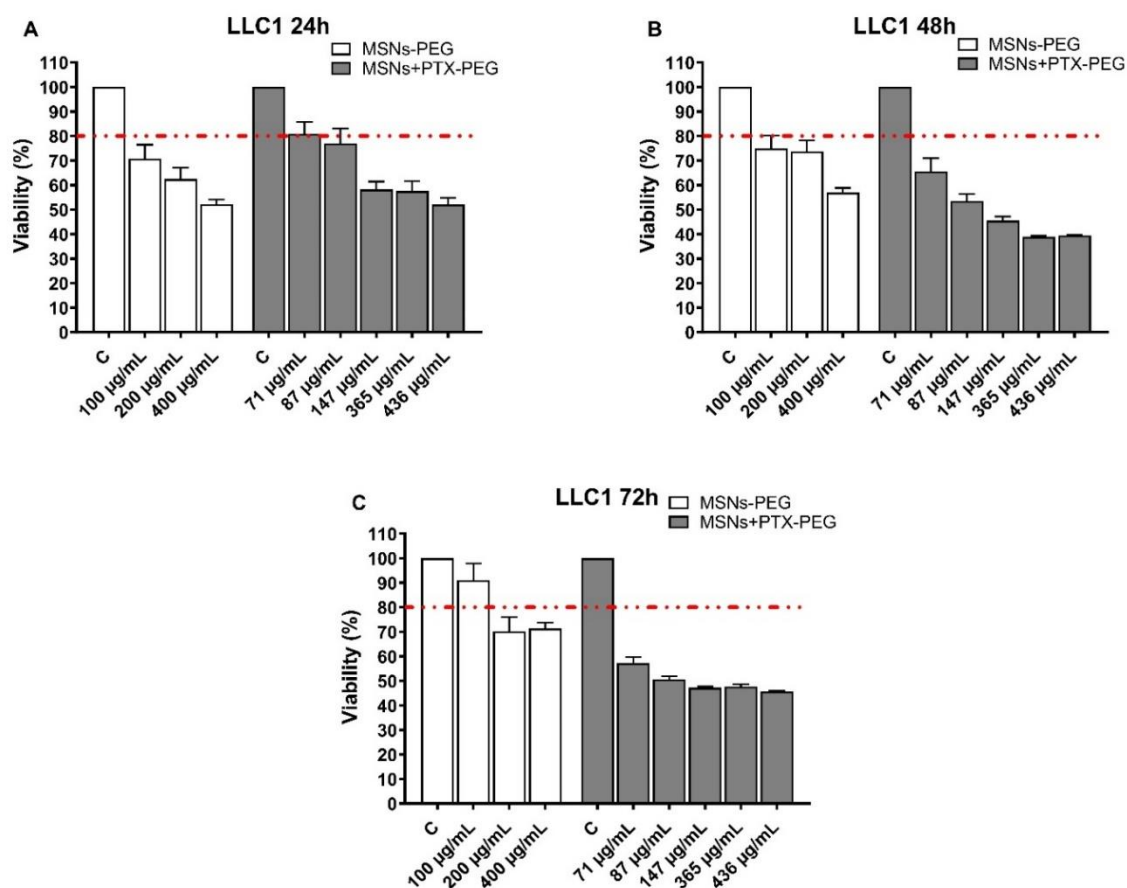
**Figure 4.20:** Graphical representation of LLC1 cell viability assay upon treatment with higher MSNs-PEG and MSNs+PTX-PEG after **A-** 24 h, **B-** 48 h and **C-** 72 h. (mean ± SEM) n=4 unloaded NPs, n=5 loaded NPs The x-axis corresponds to NPs concentration. For the corresponding amount of drug loaded see **Appendix 2**, **Table A2.2** or **Fig. 4.16**.

Gelatine-functionalized MSNs (**Fig. 4.21**) appear to be more effective in killing LLC1 cells than PEGylated ones (**Fig. 4.16**). Similar to the outcomes of A549 cells treated with the same type of NPs at the same concentrations (**Fig. 4.11**), in **Fig. 4.21** it can be observed that there is a greater difference in cell viability over time. For the reasons already mentioned, it appears that the free drug has a more harmful impact than the loaded particles. In addition, gelatine NPs present a higher level of toxicity than the loaded unfunctionalized NPs (MSNs-CHO+PTX), as it has already been shown for human lung cancer cells (**Fig. 4.11**), with cellular viabilities dropping to 42% of the control for MSNs-CHO+PTX-GEL at the highest concentration tested (7.2 µM loaded PTX) and 58% for MSNs-CHO+PTX (7.2 µM loaded PTX) after 72 h. It is interesting to note that even in this instance, the cells

appear to be developing some level of resistance and beginning to grow again; this is more evident at the lowest NPs concentration (equivalent to 0.60 μM PTX loading). The amount of drug which is released is probably insufficient to have a long-lasting toxic effect. However, NPs containing higher amounts may continue to release the drug over time, producing a more consistent toxic effect. When comparing the highest concentrations (equivalent to 3.5 and 7.2 μM PTX loading) to the control (0.5% DMSO), the loaded NPs confirm the ability of the particles to release the drug and exert a toxic effect towards the cancer cells in a similar fashion to the free drug.
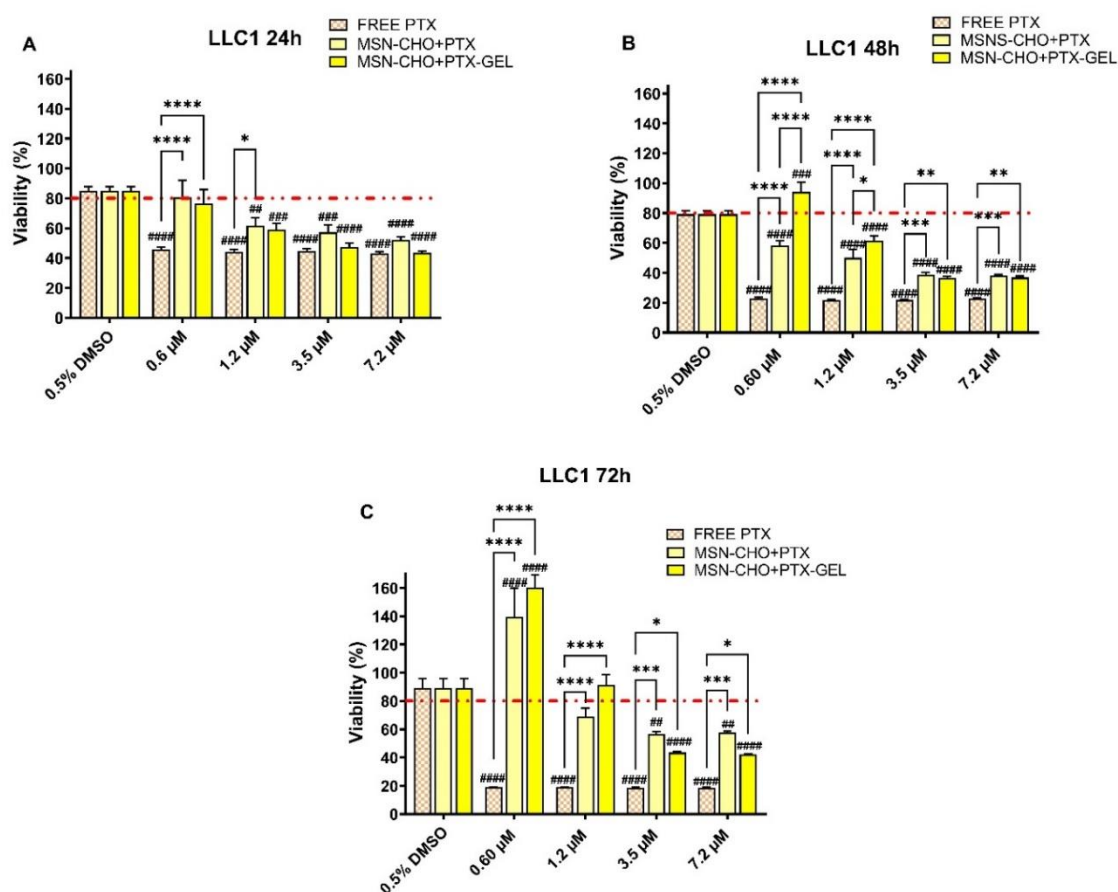


**Figure 4.21:** Comparison of LLC1 cell viability upon treatment with free PTX, MSNs-CHO+PTX and MSNs-CHO+PTX-GEL at the corresponding drug concentrations after **A-** 24, **B-** 48, and **C-** 72 h. (mean ± SEM) For the corresponding NPs concentrations see **Appendix 2, Table A2.3** or **Fig. 4.22** and **4.23**. Statistical test: Two-way ANOVA with Tukey's multiple comparison post-test comparing all treatments showing the differences between the same drug concentration. Non-treated cells taken as 100% of viability. n=3, $p \leq 0.05$ (*), $p \leq 0.01$ (**), $p \leq 0.001$ (***), $p \leq 0.0001$ (****). Two-way ANOVA with Dunnett's

multiple comparison post-test comparing all treatments to the control (0.5% DMSO). Non-treated cells taken as 100% of viability. p ≤ 0.01 (##), p ≤ 0.001 (###), p ≤ 0.0001 (####)

Again, if we compare empty MSNs-CHO and MSNs-CHO loaded with PTX (**Fig. 4.22**), as well as the same for gelatine functionalized NPs (**Fig. 4.23**), we can deduce that the toxic effect is caused by the drug released from the nanocarriers over time, with higher concentrations having a more consistent effect and the lower dosages not releasing enough drug to provide a reliable effect, which may have led the cells to acquire some resistance and keep growing when exposed to the NPs at the lowest concentrations tested.
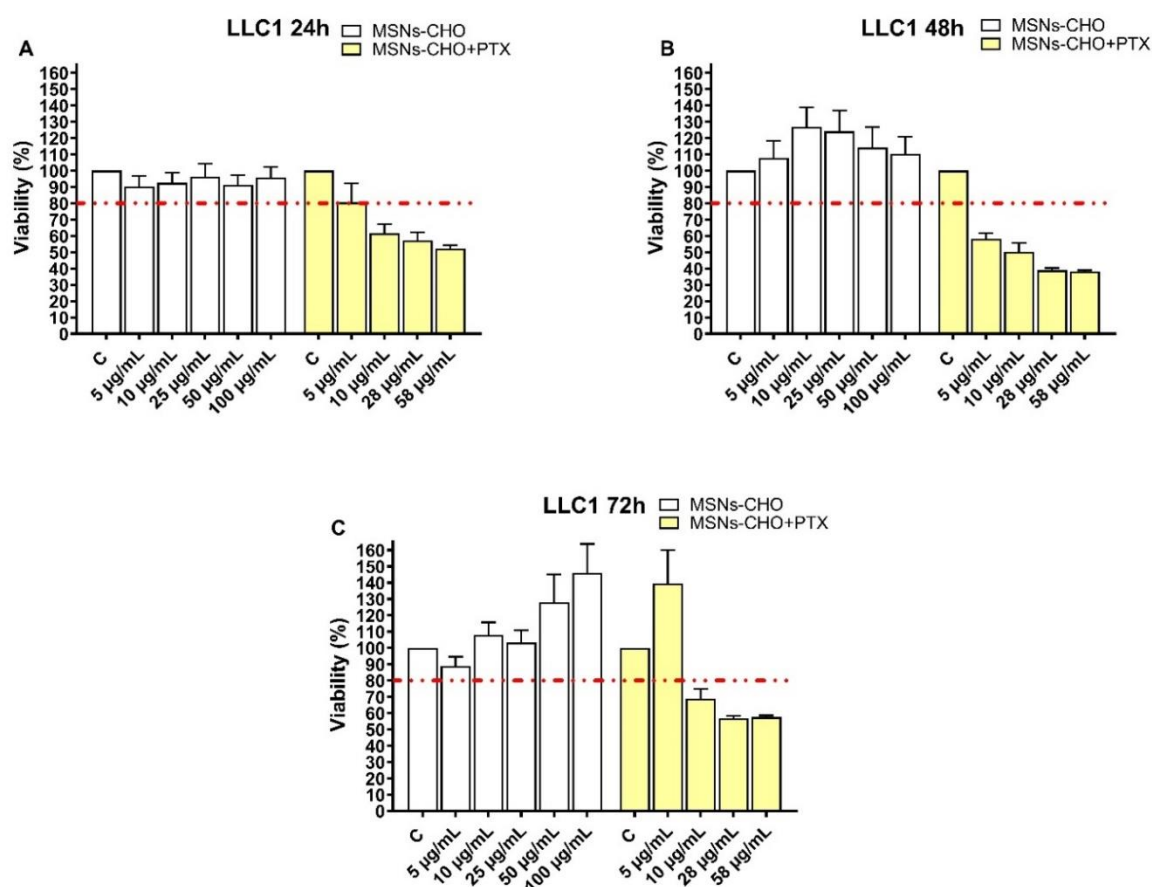


**Figure 4.22:** Graphical representation of LLC1 cell viability assay upon treatment with MSNs-CHO and MSNs-CHO+PTX for **A-** 24 h, **B-** 48 h, and **C-** 72 h. (mean ± SEM) n=6 empty NPs, n=3 loaded NPs. The x-axis corresponds to NPs concentration. For the corresponding amount of drug loaded see **Appendix 2**, **Table A2.3** or **Fig. 4.21**.
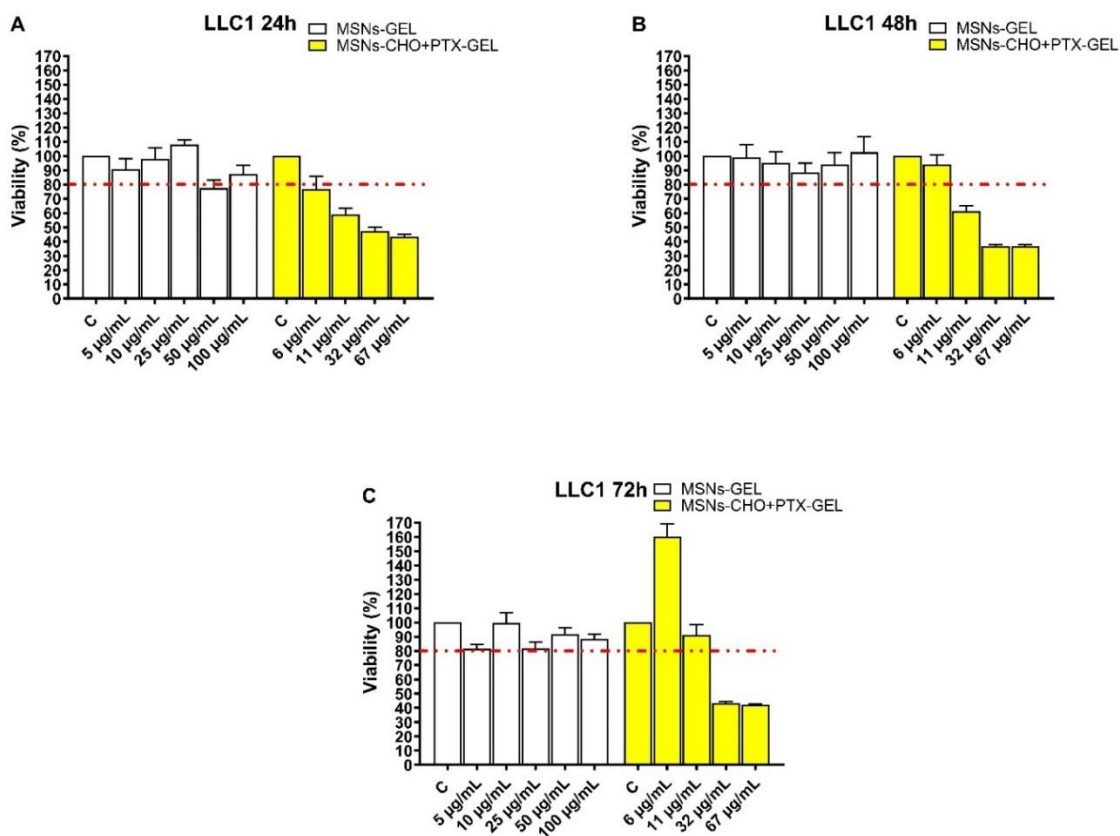
**Figure 4.23:** Graphical representation of LLC1 cell viability assay upon treatment with MSNs-GEL and MSNs-CHO+PTX-GEL for **A-** 24 h, **B-** 48 h, and **C-** 72 h. (mean ± SEM) n=6 empty NPs, n=3 loaded NPs. The x-axis corresponds to NPs concentration. For the corresponding amount of drug loaded see **Appendix 2**, **Table A2.3** or **Fig. 4.21**.

### 4.1.3  MSNs Internalization Studies – A549 cells

The uptake of the NPs by the cells, its quantification and the NPs cellular localization were investigated *in vitro* using flow cytometry and confocal laser scanning fluorescence microscopy.

### 4.1.3.1  Flow Cytometry

For this purpose, NPs were functionalised with Rhodamine B isothiocyanate, RhBITC, cells exposed to 50 µg/mL and images captured after 1, 4 and 24 h of exposure as detailed in **sections 2.2.1.1** and **2.2.11.3** in **Chapter 2**.

From the flow cytometry assay results (**Fig. 4.24**), it is evident that A549 cells take up a considerable amount of NPs after only one hour of treatment, with the functionalized NPs being internalised more efficiently than the bare MSNs. However, it is important to note that the observed variability between experiments was large, indicating the need for further assays to confirm these findings. The variability observed, particularly for MSNs-PEG-RhBITC at 1 and 4 h, was attributed to the inconsistent number of events registered by the flow cytometer. This variability could be a result of cell death caused by the toxicity of the NPs.
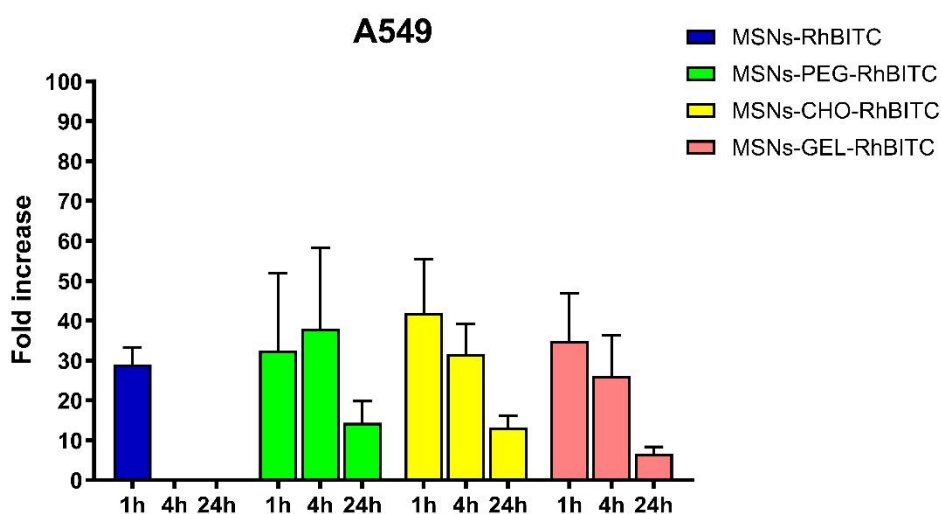


**Figure 4.24:** Fold increase of fluorescent A549 cells in relation to untreated cells, after treatment with 50 µg/mL of MSNs-RhBITC, MSNs-PEG-RhBITC, MSNs-CHO-RhBITC and MSNs-GEL-RhBITC for 1, 4 and 24 h. Statistical test: Two-way ANOVA, n= 3, p= 0.7959

In fact, it was not possible to analyse the cellular internalization of the bare MSNs at 4 and 24 h due to the low number of events detected by the flow cytometer, most likely due to the loss of cell adhesion and damage caused by the NPs. This was confirmed by optical microscope images (**Fig. 4.25**), where it can be observed that cells treated with bare MSNs (**Fig. 4.25 B**) became spherical and detached, explaining the difficulty in collecting enough cells after 1 h of treatment. As previously mentioned, and as demonstrated by other groups, [441, 476] A549 cells exposed to silica NPs in serum-free conditions altered their phenotype and adopted a spherical form, losing cell–cell contact and rolling up rather than spreading out, indicating loss of cell adhesion and cell damage. As reported in the literature, and

observed in the cellular viability assay results, the cytotoxic effect of silica NPs is known to be suppressed by functionalization of the particles' surface. [477, 478] However, a reduction in fluorescence was also observed over time, indicating a possible release of NPs from the cells into the extracellular environment. [454]
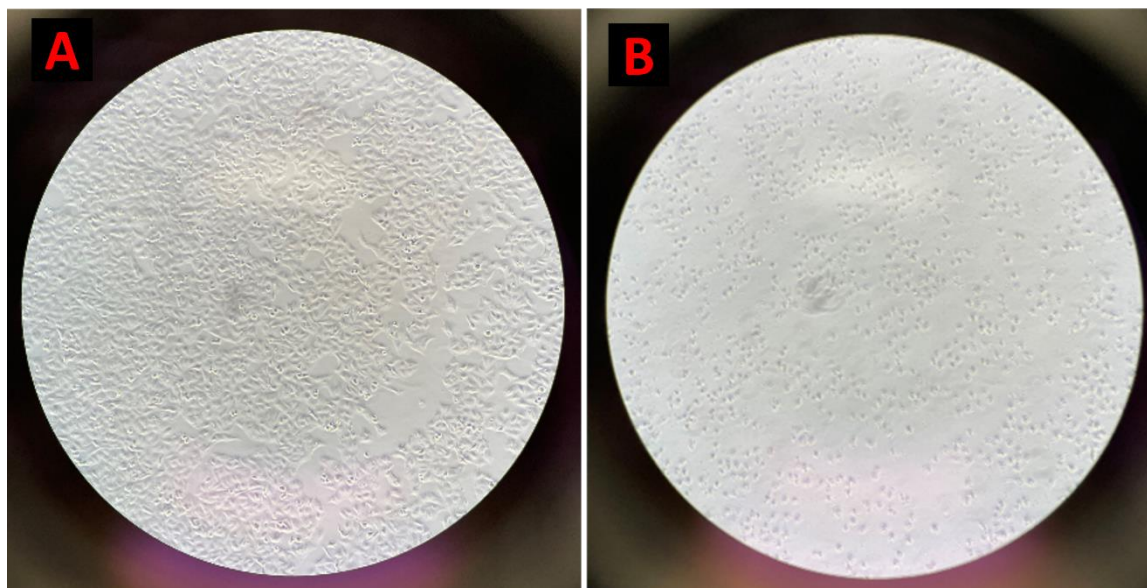


**Figure 4.25: A-** Optical microscopy images of A549 cells without treatment after 24 h. **B-** Optical microscopy images of A549 cells after treatment with bare MSNs for 24 h. Magnification: 5x. In the pictures it can be seen how, after 24 h incubation with MSNs, A549 cells started to become spherical and to detach probably due to damage caused by the silica.

### 4.1.3.2  Confocal Microscopy

Confocal microscopy analysis was used to investigate NPs cellular uptake in human lung cancer cells. For this purpose, cells were exposed to 50 µg/mL of NPs functionalised with Rhodamine B isothiocyanate, RhBITC, and images captured after 1, 4 and 24 h of exposure as detailed in **sections 2.2.1.1** and **2.2.11.4** in **Chapter 2**.

The images obtained using this technique confirmed the results of the flow cytometry analysis. The images available in **Figs. 4.26** and **4.27** demonstrate that the NPs were internalized after 24 h of treatment. Furthermore, the captured images revealed that A549 cells treated with bare MSN had a rounder shape (**indicated by orange arrows in Fig. 4.26**) compared to the control cells and cells

treated with the functionalised MSNs and they lost cell-cell contact, as observed with optical microscope after flow cytometry internalization studies (**Fig. 4.25 B**).
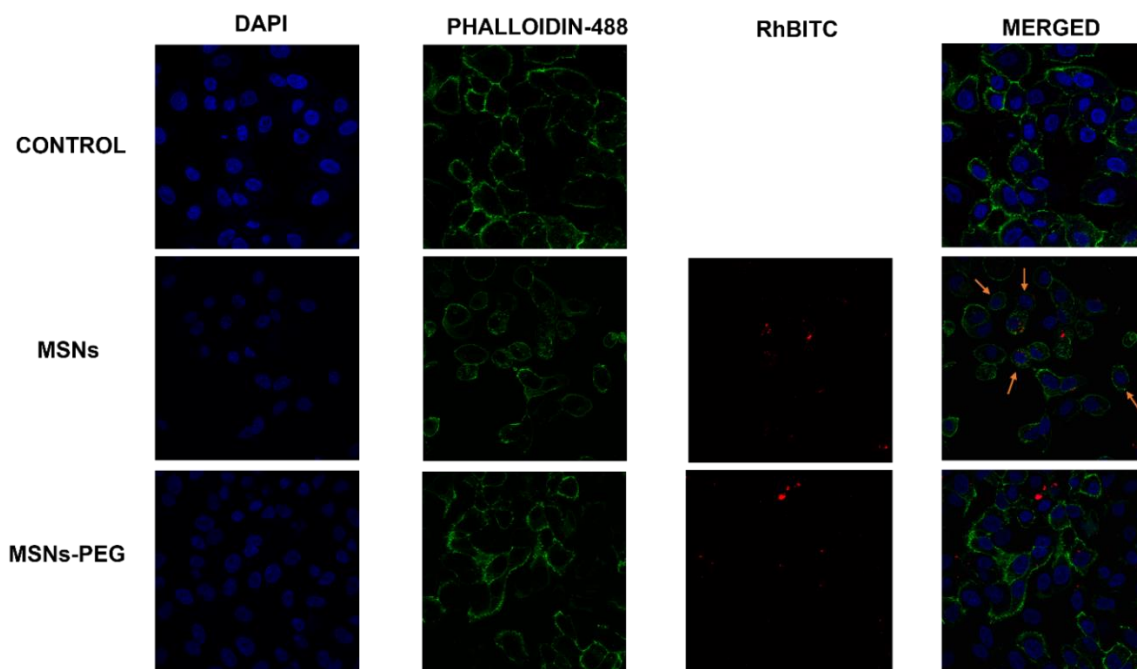


**Figure 4.26:** Representative images from confocal fluorescence microscopy of A549 cells after 24 h treatment with 50µg/ml MSNs-RhBITC and MSNs-PEG-RhBITC, showing internalized NPs (red- RhBITC), cytoskeleton (green- Phalloidin-488), and cell nuclei (blue- DAPI). Magnification: 40x. The orange arrows indicate a change in shape of A549 cells treated with bare MSNs-RhBITC compared to the control (no treatment).
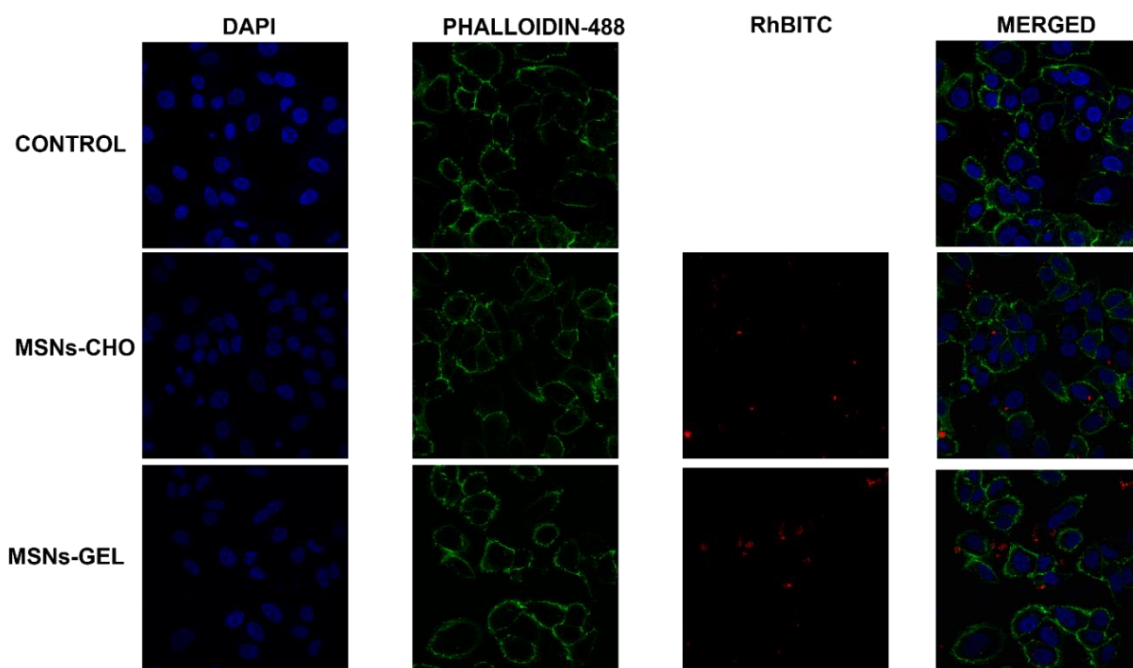
**Figure 4.27:** Representative images from confocal fluorescence microscopy of A549 cells after 24 h treatment with 50μg/ml MSNs-CHO-RhBITC and MSNs-GEL-RhBITC, showing internalized NPs (red- RhBITC), cytoskeleton (green- Phalloidin-488), and cell nuclei (blue- DAPI). Magnification: 40x.

## 4.1.4  MSNs Internalization Studies – LLC1 cells

### 4.1.4.1  Flow Cytometry

From the flow cytometry data investigations of MSNs internalization in LLC1 cells (**Fig. 4.28**), it appears that internalisation of silica NPs by LLC1 murine cells it is not as marked as the cellular uptake by human lung cancer cells (A549, **Fig. 4.24**). It has been reported in the literature that different cell lines, namely HeLa and A549 epithelial cells, 1321N1 astrocytes, HCMEC D3 endothelial cells, and murine RAW 264.7 macrophages showed different uptake kinetics for the same material (polystyrene NPs). [479] Interestingly, despite the lower internalization, the fluorescence of the LLC1 cells seems to be increasing over time, while the fluorescence of A549 cells may reach a saturation point, with particles leaving the cells afterwards. These results suggest that the internalization process of NPs in LLC1 cells may be different from that of A549 cells.
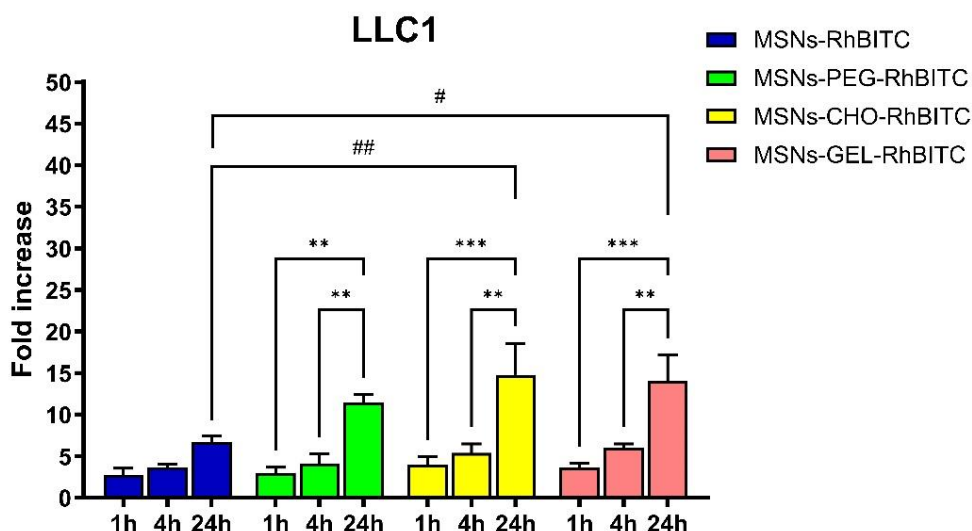
**Figure 4.28:** Fold increase of fluorescent LLC1 cells when compared to untreated cells, after treatment with 50 µg/mL of MSN-RhBITC, MSN-PEG-RhBITC, MSN-CHO-RhBITC and MSN-GEL-RhBITC for 1, 4 and 24h. Statistical test: Two-way ANOVA with Tukey's multiple comparison post-test comparing all treatments, showing the differences between different time points for the same particle type $p \leq 0.01$ (**), $p \leq 0.001$ (***), $p \leq 0.0001$ (****); and the differences between the same time point for different particle types $p \leq 0.05$ (#), $p \leq 0.01$ (##) n=3

## 4.1.4.2  Confocal Microscopy

The internalization of the different MSN types by LLC1 was also qualitatively examined by confocal microscopy (**Fig. 4.29** and **4.30**). NPs were clearly internalised after 24 h of exposure. It is worth noting that the NPs' treated cells present a rounder shape than the control cells, which look flatter and more adherent to the well surface. In the case of the human lung cancer cells (A549**, Fig. 4.26**), a change in shape was only noticed when they were treated with bare silica NPs, suggesting a higher toxicity and cell death. On the contrary, this change in morphology was found in LLC1 regardless of the type of NPs. We speculate that, as previously explained, this may be due to some level of stress induced by the NPs [450, 452, 470, 471] and/or starvation, [469] that may result in cells changing their shape and becoming more resistant.
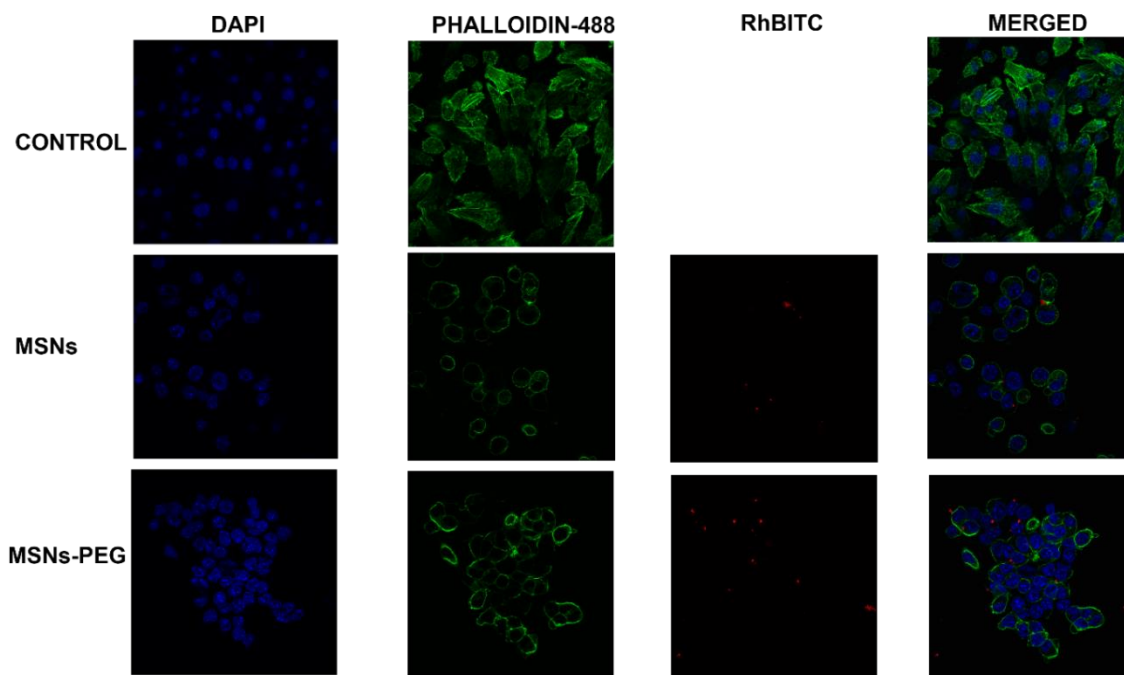
**Figure 4.29:** Representative images from confocal fluorescence microscopy of LLC1 cells after 24 h treatment with 50µg/ml MSNs-RhBITC and MSNs-PEG-RhBITC, showing internalized NPs (red- RhBITC), cytoskeleton (green- Phalloidin-488), and cell nuclei (blue- DAPI). Magnification: 40x.
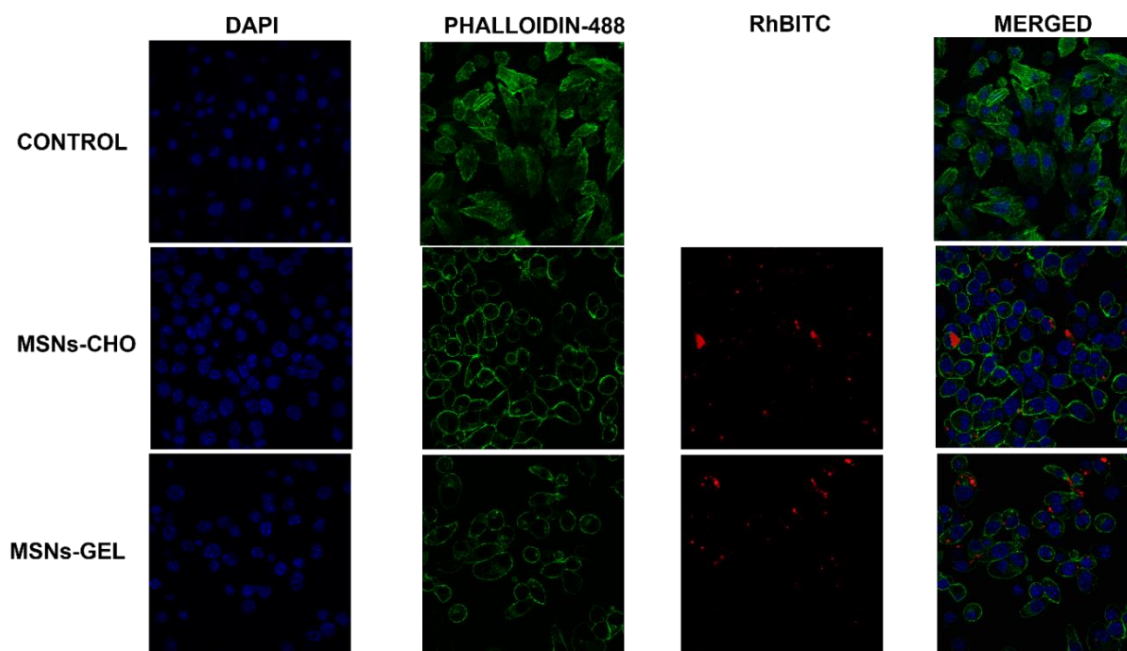


**Figure 4.30:** Representative images from confocal fluorescence microscopy of LLC1 cells after 24 h treatment with 50µg/ml MSNs-CHO-RhBITC and MSNs-GEL-RhBITC, showing internalized NPs (red- RhBITC), cytoskeleton (green- Phalloidin-488), and cell nuclei (blue- DAPI). Magnification: 40x.

172

The results of the flow cytometry and confocal microscopy analyses suggest that both A549 and LLC1 cells internalized the developed NPs, with a higher fold increase in fluorescence observed in A549 compared to LLC1 cells after just 1 h. This indicates a potentially higher level of NPs internalization in A549 cells within that time frame. On the other hand, LLC1 cells exhibited increasing fluorescence over time, suggesting a continuous internalization of the NPs, and indicating that the NPs are being internalized and retained by the LLC1 cells. In contrast, the decrease in fluorescence observed for A549 cells might suggest a possible escape or clearance of the NPs from these cells.

Overall, these findings suggest that while both A549 and LLC1 cells internalized the developed MSNs, there may be differences in the kinetics and mechanisms of internalization between the two cell types. Further studies could help elucidate the underlying factors behind these observations.

## 4.1.5 Identification of MMP activity in the secretome from tumour cells

With the aim to identify the collagenolytic activity of matrix-degrading enzymes from the media of both human (A549) and murine (LLC1) cancer cells lines used in this study, the conditioned and stimulated medium from the different cell cultures was subjected to zymographic analysis. The final goal was the possibility to obtain MMPs using routine laboratory procedures, and to perform release studies with our gelatine-functionalised nano system under conditions close to those encountered in the tumour microenvironment.

Gelatine zymography is a very sensitive technique for identifying and analysing the degree of gelatinase activity (MMP-2 and MMP-9 activity) present in various cell types and tissues at any given time and/or following various treatments. [480]

## 4.1.5.1 Human fibrosarcoma cells (HT1080)

HT1080 were used as a positive control in this study as it is a cancer cell line known to express high levels of MMP-2 and MMP-9. [326, 387] Phorbol 12-myristate 13-acetate (PMA) is a compound that activates protein kinase C, a signalling pathway that is involved in MMPs' regulation. [326] In this study, PMA 10 μM was used to stimulate the production of MMPs by HT1080 cells, and the conditioned medium from the cells collected after 24 h of incubation was subjected to zymographic analysis. **Fig. 4.31** shows the gelatinolytic activity of the MMPs in the media, demonstrated as clear bands against a blue background (stained gelatine) at 72 and 92 kDa, which correspond to the molecular weight of MMP-2 and MMP-9 gelatinases, respectively.
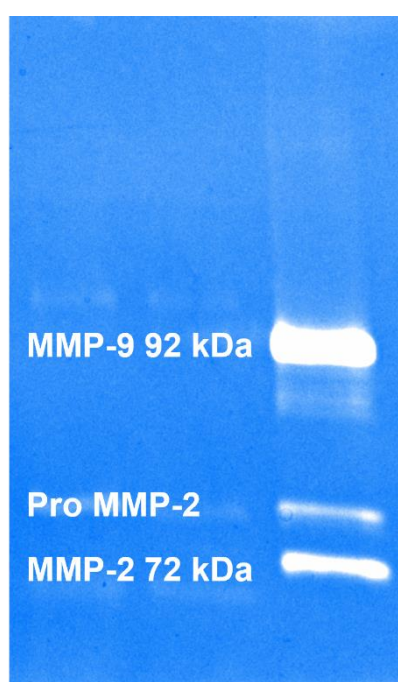


**Figure 4.31:** Zymogram of HT1080 cells showing the presence of MMP-9 and MMP-2 in PMA treated HT1080 conditioned media.

These results are consistent with previous studies that have also shown that PMA can stimulate MMPs' production in cancer cells. Roomi M.W. and co-workers [326] investigated the effect of PMA on the expression of MMPs in 40 cancer cell lines, including HT1080, and compared the secretion of MMPs before and after treatment with PMA. The authors found that, in general, PMA treatment upregulates MMPs in cancer cells and that HT1080 cells in particular, had low

basal levels of MMP-9 before treatment, but significantly increased levels after, indicating that these cells are highly susceptible to PMA induction.

## 4.1.5.2 Human non-small-cell lung cancer cells (A549)

For investigating the production of gelatinases by A549, once they reached the logarithmic growth phase, and 70-80% confluency, cells were incubated with 10mL of serum-free DMEM for 48 h. The conditioned media was then collected and concentrated as detailed in **Chapter 2 section 2.2.11.5.2**. Total protein concentration before and after centrifugation was calculated (**Appendix 2**, **Fig. A2. 1**) and a gelatine zymography carried out (**Fig. 4.32**). As expected, both the total protein concentration (**Appendix 2**, **Fig. A2. 2**) and the intensity of the MMP-2 bands (**Fig. 4.33 A**) increased with the time of centrifugation. Similarly, Roomi M.W. and colleagues [326] describe in their work that although MMP-2 was constitutively expressed in the majority of the cell lines investigated, MMP-9 activity was normally low but could be increased by PMA. As in our case, they found no MMP-9 but only -2 in the conditioned media from A549.
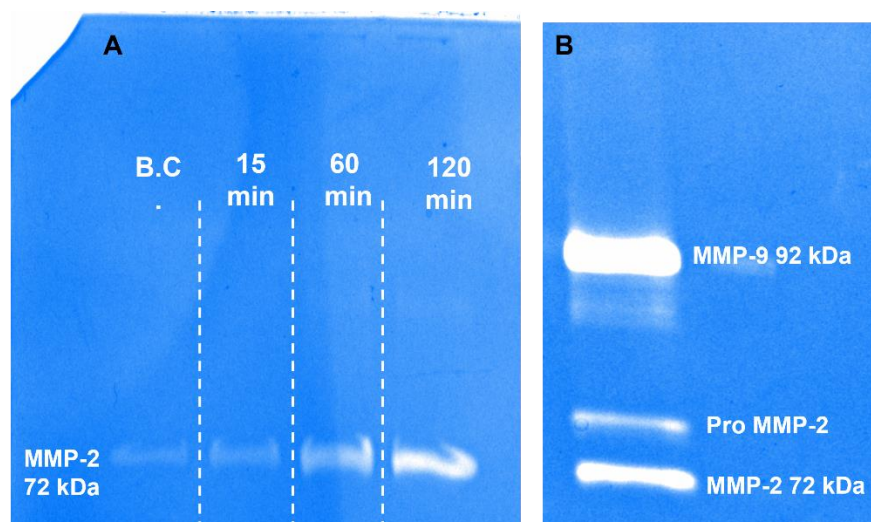


**Figure 4.32: A-** Gelatine zymogram of conditioned media from A549 cells before (**B.C.**) and after (**15**, **60** and **120 min**) media centrifugation. **B-** Conditioned media used as positive control.

For calculating MMPs concentration in the samples (**Fig. 4.33 B**), a gelatine zymography including known concentrations of recombinant MMP was run and the intensity of the bands correlated with the corresponding concentrations of the enzyme (**Appendix 2**, **Fig A2.4**).
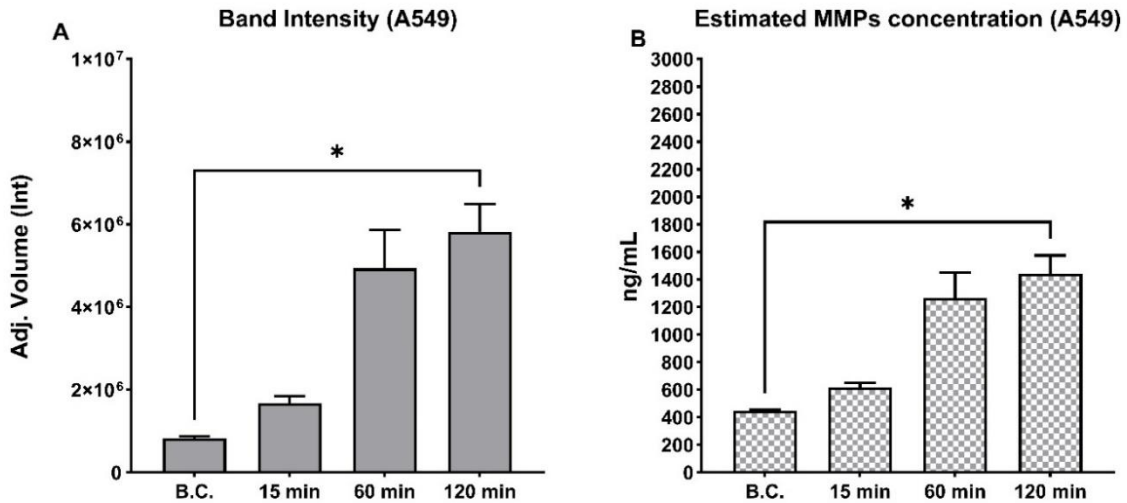


**Figure 4.33: A-** Intensity of the adjusted band volume of A549 cells conditioned media from cells at three different passage numbers, before (**B.C.**) and after (**15**, **60** and **120 min**) centrifugation (mean±SEM), n=3. **B-** MMPs concentration (ng/mL) in A549 cells conditioned media before (**B.C.**) and after (**15**, **60** and **120 min**) centrifugation (mean±SEM). Statistical test: One-way ANOVA with Tukey's multiple comparison post-test comparing all time points. $p \leq 0.05$ (*)

Next, we investigated if the MMP-9 expression from A549 could be induced by PMA, as reported by Roomi M.W. and co-workers, [326] where they found a strong induction of MMP-9 by PMA in various cancer cell lines, including A549. For this purpose, A549 cells were incubated with media containing PMA (10 µM) for 24 h. The zymography of the stimulated media (**Fig. 4.34**) showed bands for both MMP-2 and –9, and once again the intensity of the bands increased over time as the centrifugation times increased (**Fig. 4.35 B**). Kodate M. and colleagues [481] reported the presence of gelatinolytic activity from both MMP-2 and MMP-9 in non-treated and 4-aminophenylmercuric acetate (APMA) treated media from A549 and HT1080 cells. They also found higher activity in poorly differentiated adenocarcinoma cells (110ST) than in moderately differentiated ones (A549).

It has been reported in other studies that patients affected from lung cancer presented elevated levels of MMPs in tumour tissues compared to healthy controls. [482] In a study from 2006 by Leinonen T. and co-workers, [199] the expression of MMP-7 and MMP-9 in tumour cells and stroma was analysed in a cohort of patients with resected NSCLC. The group reported a positive staining for MMP-9 in all the investigated cases of cancer cells, and a high expression of MMP-9 in tumour cells was found in 57% of instances, associated with poor tumour differentiation. MMP-9 (mainly in inflammatory cells and fibroblasts) was found in 32% of cases and associated with higher tumour grade, confirming that this gelatinase is produced also by stromal cells and not only by cancer cells. In a later study, Fiorelli A. *et al.*, [412] reported that MMP-9 levels were significantly higher in patients with lung malignant lesions compared to those with benign lesions, and that no discernible differences in MMP-9 levels were detected between adenocarcinomas, squamous carcinomas, and large-cell carcinomas. Moreover, they suggested that the production of MMP-9 during the metastatic process may not be primarily due to local production by the tumour tissue, but rather to the release of the enzyme by inflammatory and blood cells driven by cancer cells through the creation of regulatory factors such as cytokines. The group examined the expression of MMP-9 in tissue samples of patients with resected cancer, and they found that out of 26 tissue samples examined, 9 (34%) showed positive immunohistochemical staining for MMP-9, indicating the presence of the protein in these samples. The investigators also reported that 7 of the 9 tissue samples were from early-stage cancer, where they were not expecting to find positive staining for MMPs. Upon further investigation, the authors found that MMP-9 expression in these cases was not from the tumour cells themselves, but from infiltrating inflammatory cells, such as macrophages. In a different study, [414] lung specimens were collected from two different regions in patients with NSCLC: the targeted resection region (presumably where the tumour was located) and the remote, normal region (presumably unaffected by the tumour). The specimens were collected from patients with either stage I or II NSCLC, and the malignancies were of either squamous cell or adenocarcinoma subtype. The authors hypothesized that there would be differences in MMPs expression between NSCLC and normal lung tissue, and that these differences would vary based on the specific histologic type of NSCLC

(squamous cell versus adenocarcinoma). The group reported that between the gelatinases, MMP-2 levels were three-fold higher in NSCLC region, and that MMP-9 levels were four times higher in squamous cell carcinoma than adenocarcinoma, where they did not detect any increase in MMP-9.
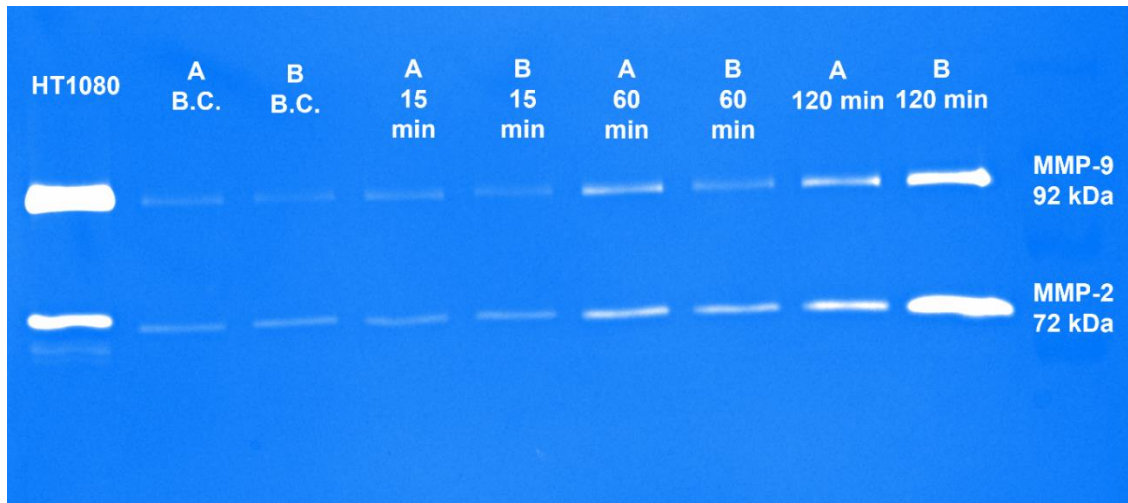


**Figure 4.34:** Gelatine zymogram of media from A549 cells PMA stimulated before (**B.C.**) and after (**15**, **60** and **120 min**) media centrifugation. A and B refer to cells at two different passage numbers.
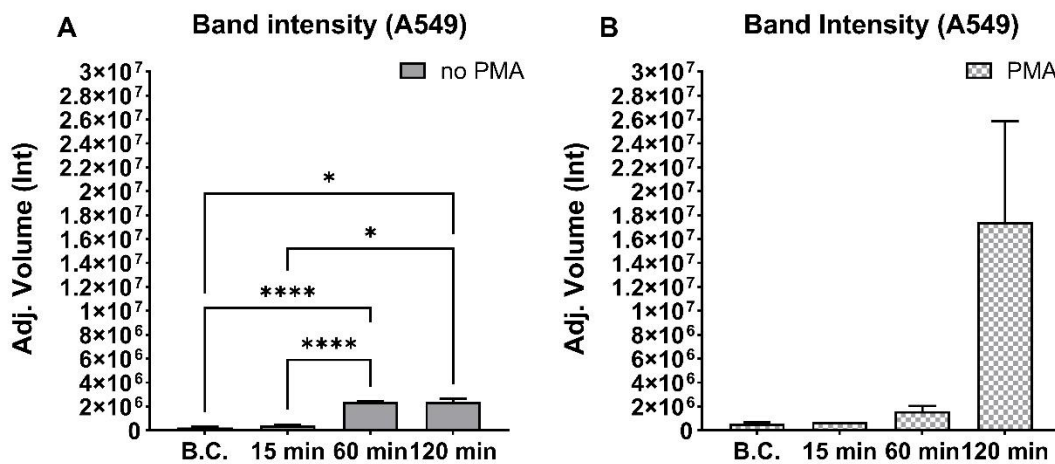


**Figure 4.35: A-** Intensity of the adjusted band volume of A549 cells conditioned media before (**B.C.**) and after (**15**, **60** and **120 min**) centrifugation (mean±SEM). **B-** Intensity of the adjusted band volume of PMA stimulated A549 cells media before (**B.C.**) and after (**15**, **60** and **120 min**) centrifugation (mean±SEM). Statistical test: One-way ANOVA with Tukey's multiple comparison post-test comparing all time points. n=3 **A-** p ≤ 0.05 (*), p ≤ 0.0001 (****). **B-** p=0.1967

178

## 4.1.5.3 Lewis lung carcinoma cells (LLC1)

The zymograms carried out from LLC1 cell medium before and after several centrifugation steps (**Fig. 4.36 A** and **B**) demonstrated the presence of clear bands at 72 and 92 kDa, indicating that this cell line secretes both MMP-2 and -9 to the media. As expected, an increase in the intensity of the bands was also observed with the centrifugation times.
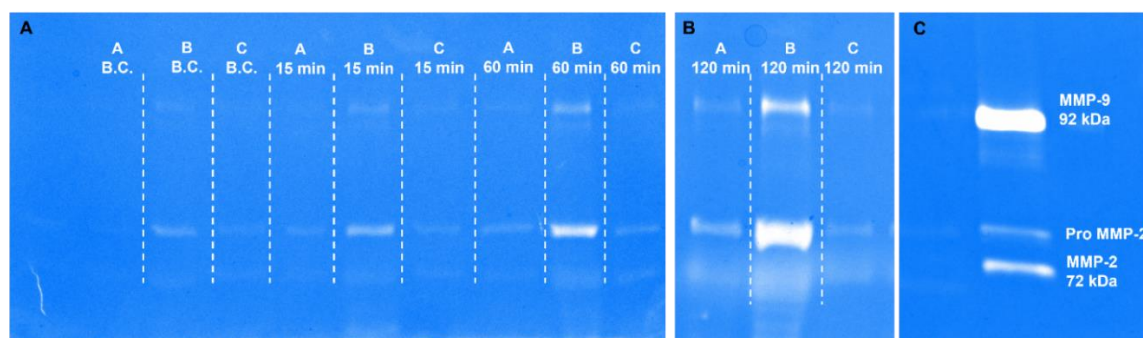


**Figure 4.36: A- and B-** Gelatine zymogram of LLC1 cells conditioned media from cells at three different passage numbers (A, B and C), before (**B.C.**) and after (**15**, **60** and **120 min**) media centrifugation. **C-** positive control.

After analysing and quantifying the intensity of the bands with Image Lab software it was confirmed once again that the bands intensity increased with higher centrifugation times (**Fig. 4.37 A**), hence leading to higher MMPs concentration (**Fig. 4.37 B**).

The total amount of MMPs collected from murine lung cancer cells was higher than the one collected from human ones: with a total concentration of 2 µg/mL after 2 h centrifugation, as opposed to 1.4 µg/mL for A549 at the same time point. These findings might explain why MSNs-CHO+PTX-GEL resulted more toxic towards LLC1 (**Fig. 4.21**) than A549 **(Fig. 4.11**). LLC1 cells viabilities, in fact, decreased to approximately 36% of the control after 48 h of treatment (for concentrations of the loaded drug equal to 3.5 and 7.2 µM). On the other hand, the viabilities of A549 cells decreased to 65% of the control under the same conditions. The higher concentration of MMPs in the LLC1 media likely facilitated the faster removal of the gelatine shell, leading to a higher and quicker accumulation of PTX. This was further supported by *in vitro* release studies, where a higher cumulative

release of safranin-O was observed when MSNs-GEL were resuspended in LLC1 media (**Fig. 3.27**). Again, *in vitro* release studies with PTX will need to be carried out in order to confirm such statement.

The results are in line with what was previously reported by Zheng J. and colleagues [387], where conditioned media from LLC1 cells showed high levels of MMP-2 and –9.
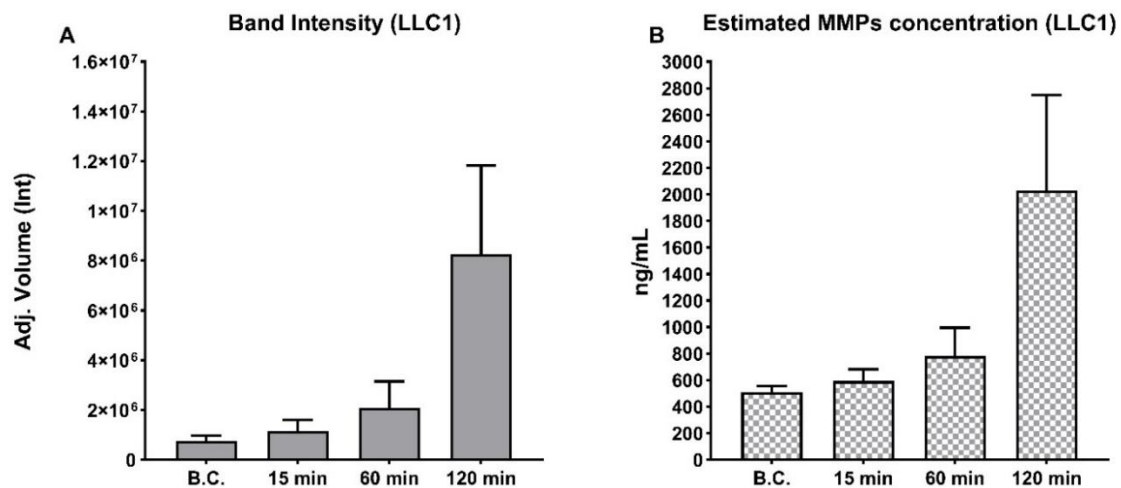


**Figure 4.37: A-** Intensity of the adjusted band volume of LLC1 cells conditioned media from cells at three different passage numbers, before (**B.C.**) and after (**15**, **60** and **120 min**) centrifugation (mean±SEM), n=3. **B-** MMPs concentration (ng/mL) in LLC1 cells conditioned media before (**B.C.**) and after (**15**, **60** and **120 min**) centrifugation (mean±SEM). Statistical test: One-way ANOVA with Tukey's multiple comparison post-test comparing all time points. **A-** and **B-** p= 0.1529

LLC1 cells were also treated with PMA in order to evaluate if the production of MMP-9 could be stimulated and subsequently concentrated by centrifugation. For this purpose, the conditioned media from LLC1 in the presence and absence of PMA before and after centrifugation was analysed again using gelatine zymography media (**Fig. 4.38**). As shown in **Fig. 4.39 A** and **B**, an increase of MMP-9 activity  was demonstrated, which was higher after 60 and 120 minutes of centrifugation.
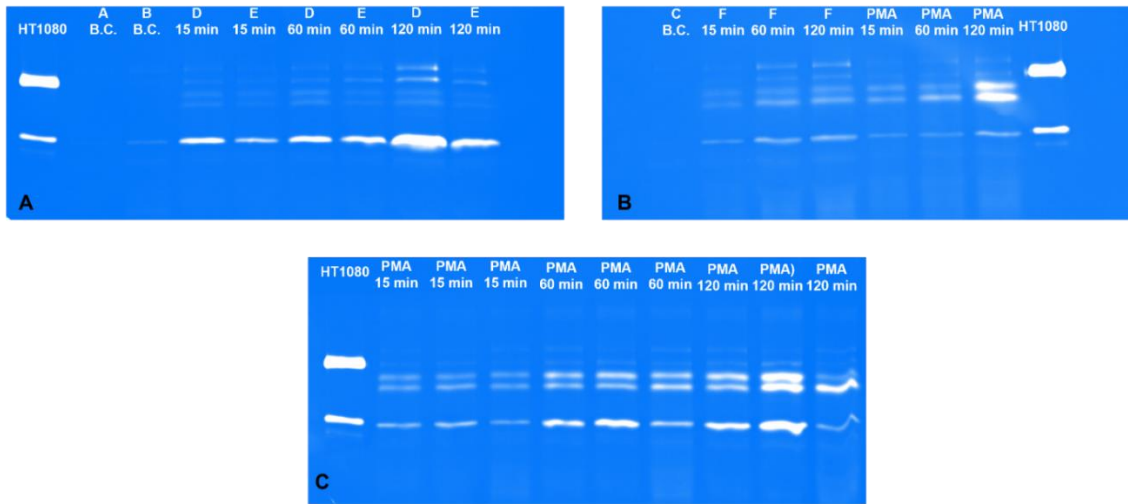
**Figure 4.38: A-** and **B-** Gelatine zymogram of LLC1 cells conditioned media from cells at three different passage numbers, before (**B.C.**, A, B and C) and after (**15**, **60** and **120 min** D, E and F) media centrifugation. **B-** and **C-** Gelatinase zymogram of LLC1 cells PMA stimulated (**PMA**) media from cells at three different passage numbers after media centrifugation.
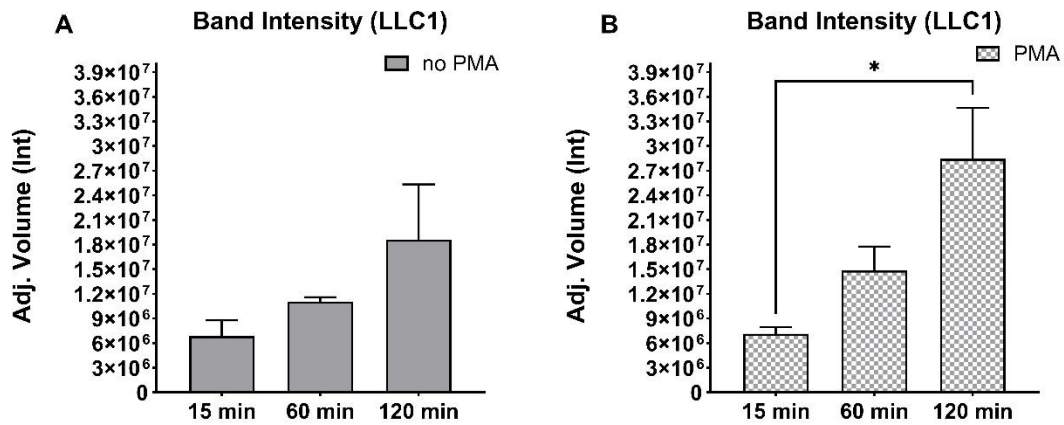


**Figure 4.39: A-** Intensity of the adjusted band volume of LLC1 cells conditioned media after (**15**, **60** and **120 min**) centrifugation (mean±SEM). **B-** Intensity of the adjusted band volume of PMA stimulated LLC1 cells media after (**15**, **60** and **120 min**) centrifugation (mean±SEM). Statistical test: One-way ANOVA with Tukey's multiple comparison post-test comparing all time points. n=3 **A-** p=0.2090; **B-** p ≤ 0.05 (*)

## 4.1.6  Conclusions

Aldehyde- and gelatine-functionalised MSNs did not cause damage to either A549 or LLC1 cells, suggesting that both systems are well tolerated by the cells.

Bare and PEG-functionalized NPs, on the other hand, showed a dose- and time dependent toxicity towards A549 cells. Murine lung cancer cells appeared to be slightly more resistant to silica NPs than human lung cancer cells, suggesting that the cellular response to silica NPs might vary depending on the cell type.

The ability of the stimuli responsive system to respond to specific stimuli (GSH for PEG-functionalised MSNs, and MMPs for GEL-functionalised MSNs) was confirmed by *in vitro* cytotoxicity studies. Both systems demonstrated to be able to release PTX decreasing cell viability over time. However, due to the observed intrinsic toxicity of MSNs and MSNs-PEG, the cytotoxic effect from the loaded NPs could not be solely attributed to the release of the drug from these nano-systems.

The internalization of NPs was demonstrated by flow cytometry analysis and confocal microscopy imaging in both A549 and LLC1 cells.

Zymographic analysis of conditioned and PMA stimulated media from A549 and LLC1 cells helped identify the activity of MMPs in the cellular media. Additionally, it confirmed that sufficient levels of enzyme could be obtained using routine laboratory procedures without the need for commercial sourcing.

# 5 CHAPTER 5: 3D cells culture *in vitro* studies

The two-dimensional (2D) *in vitro* cell culture systems involve cell development in a monolayer on a flat substrate. This approach has been widely employed in research due to its ease of use and low cost. However, 2D culture systems lack the complexity and three-dimensional (3D) architecture found *in vivo*, which can limit their ability to replicate (patho)physiological conditions accurately. 3D cell culture refers to a variety of *in vitro* methods that employ a synthetic microenvironment to grow cells in three dimensions and that offer several advantages over 2D systems. They provide a more realistic environment for cell growth, including interactions between cells and the extracellular matrix (ECM) (**Table 5.1**), mimicking the conditions found *in vivo* in terms of access to oxygen, nutrients, and metabolites, which is important for the growth and survival of cells. [483-485]

The advantages in using 3D models over 2D are:

- The possibility to study cell-cell and cell-matrix interactions.
- The inserts which are used to work with these models can be made of biomaterials with properties similar to the ECM to further enhance the physiological relevance of the microenvironment.
- Differences in physical and physiological properties between 2D and 3D cultures can affect the sensitivity of cells to drugs, with 2D cells being more sensitive due to their inability to maintain normal morphology and to the organization of surface receptors. [483]

For these reasons, 3D culture systems can better replicate the complex cellular behaviour and responses found *in vivo*, which makes them useful for predicting clinical outcomes and testing the efficacy of potential therapies. [483-485]

**Table 5.1:** Main differences between 2D and 3D cell culture systems. (*Adapted from* [483])

| Characteristic | 2D | 3D |
|---|---|---|
| Support for cell growth | Utensils (plastic, polycarbonate) | Extracellular matrix *in vitro* |
| Culturing characteristics | Traditional culture | Imitating the natural microenvironment |
| Interaction and communication | Cell-cell interactions | Cell-cell and cell-matrix 3D interactions |
| Cell morphology | Flat and extensible | Natural cellular structure preserved |
| Media cell interface | Homogeneous exposure of all cells to the media | Heterogeneous exposure (the outer layers are more exposed than the inner layers) |
| Cell junctions | Less common | More common (cell-cell communication) |
| Cell differentiation | Moderately and poorly differentiated | Well-differentiated |
| Cell proliferation | Higher proliferation rate than in the natural environment | Medium or high proliferation rate depending on cell type and 3D culture technique |
| Treatment exposure | Cells homogeneously exposed to treatment | Cells less exposed to treatment |

| | | |
|---|---|---|
| Cost | Less expensive | More expensive |

In 1992, Petersen and Bissell published their work [486] where they first described the development of a 3D cell culture model to mimic breast structures in cancerous and non-cancerous cases. Their study was founded on the concept that it was difficult to explore how normal human epithelial breast cells transition into tumour cells using traditional culture methods since the tumour markers that had previously been identified were also prevalent in normal breast cells. By using cell lines derived from normal and malignant breast tissues, cultured within a reconstituted basement membrane (BM) derived from the Englebreth-Holm-Swarm tumour, the researchers could examine how cells interact with the BM, providing insights into the unique characteristics and behaviours of normal and malignant cells, like the identifications of markers that are specific to different stages of cell differentiation and the investigation of cellular changes associated with the progression from a normal to a malignant state, with the aim to provide a valuable tool for diagnostic and prognostic purposes. [483]

3D models are divided in three categories: [484]

❖ Spheroids (**Fig. 5.1**), cell aggregates grown in suspension on ultra-low attachment plates, or on inert substrates like agar which forces the cells to aggregate and form spheroids. The outer layer of the spheroid is composed of highly proliferative cells that have easy access to oxygen and nutrients. These cells are actively dividing and can be more sensitive to pharmaceuticals that target cell proliferation. The middle layer of the spheroid contains quiescent cells, in a dormant state, that have lower metabolic activity compared to the outer proliferating cells. The inner layer or core of the spheroid consists of necrotic cells. These cells are deprived of oxygen and nutrients due to their location within the spheroid.

❖ Organotypic cultures, where the cells are cultured on various types of extracellular matrices, such as collagen, matrigel, and hyaluronic acid, which provide a scaffold for cells to adhere to and organize into 3D

structures. These 3D models can be composed of one or multiple cell types (coculture).

❖ Organoid models, those are three-dimensional structures that can be grown *ex vivo*, such as patient-derived explants. They are also typically cultured on a matrix.
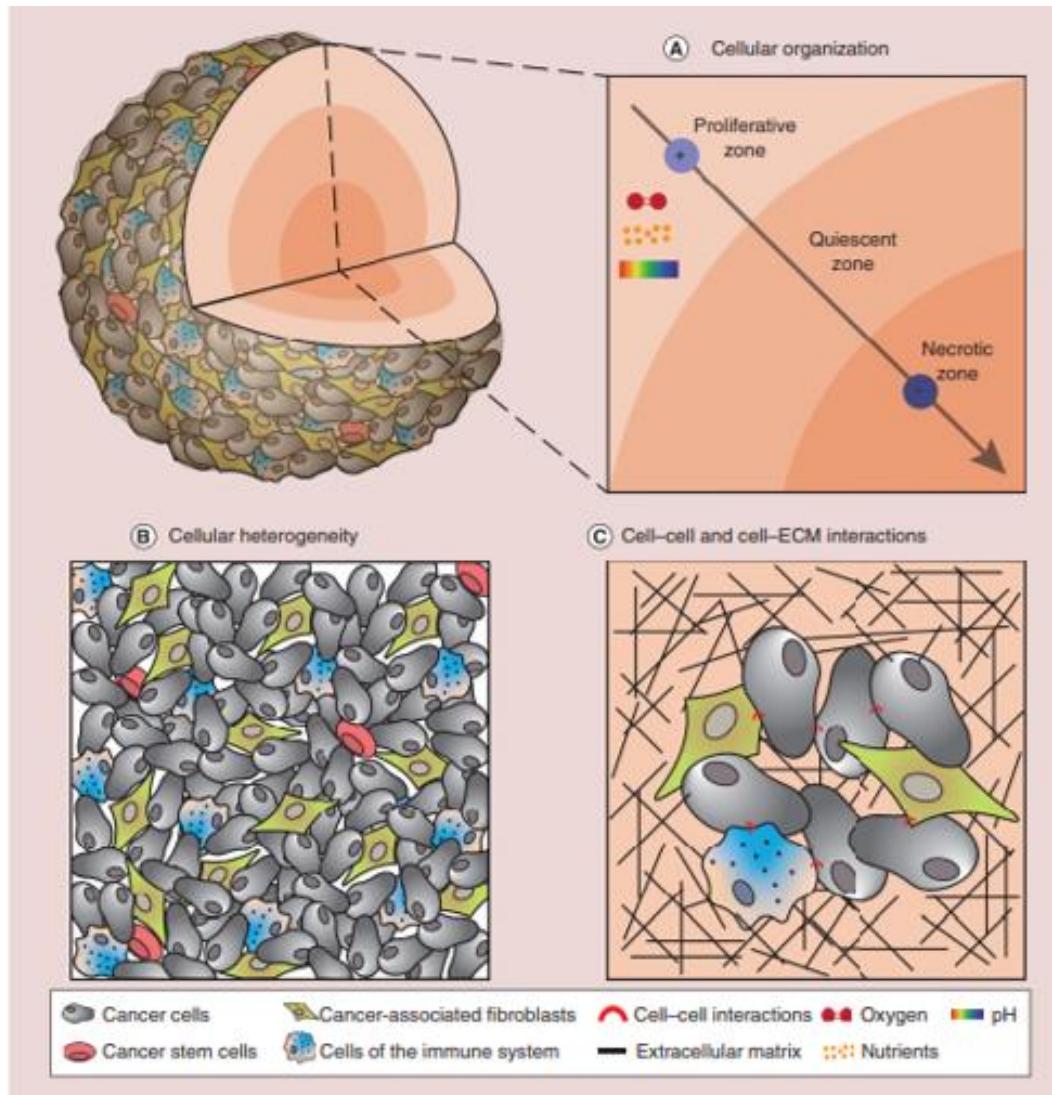


**Figure 5.1:** Spheroids properties. (*Used with permission of Future Medicine Ltd.; permission conveyed through Copyright Clearance Center, Inc.)* [487]

## 5.1  U-87 MG human glioblastoma multiforme cell spheroids

The development of new therapies for GBM, and for cancer in general, is a complex and challenging process. Despite significant investments in research and

development, the majority of the potential therapies fail to show efficacy or safety in clinical trials due to unreliable models that make it difficult to anticipate human efficacy and toxicity. [87, 485, 488]

Spheroids are three-dimensional cell cultures that can mimic the architecture and cellular behaviour of *in vivo* solid tumours to a certain extent. Therefore, they can be used as a model to investigate the ability of nanomedicines to penetrate tumour tissues and to evaluate their efficacy in killing cancer cells. By studying the behaviour of nanomedicines in spheroids, it is possible to predict to some extent their potential behaviour *in vivo* and optimize their physicochemical properties accordingly. This can help to develop more effective and targeted therapies for cancer treatment. [485, 487]

Our group has established a protocol by testing different initial amounts of cell densities and monitoring the growth over the course of a week in order to create a 3D model for GBM. [330, 489] **Figure 5.2** shows the growth of U-87 spheroids over a 4 days period, prior to the start of the treatment.
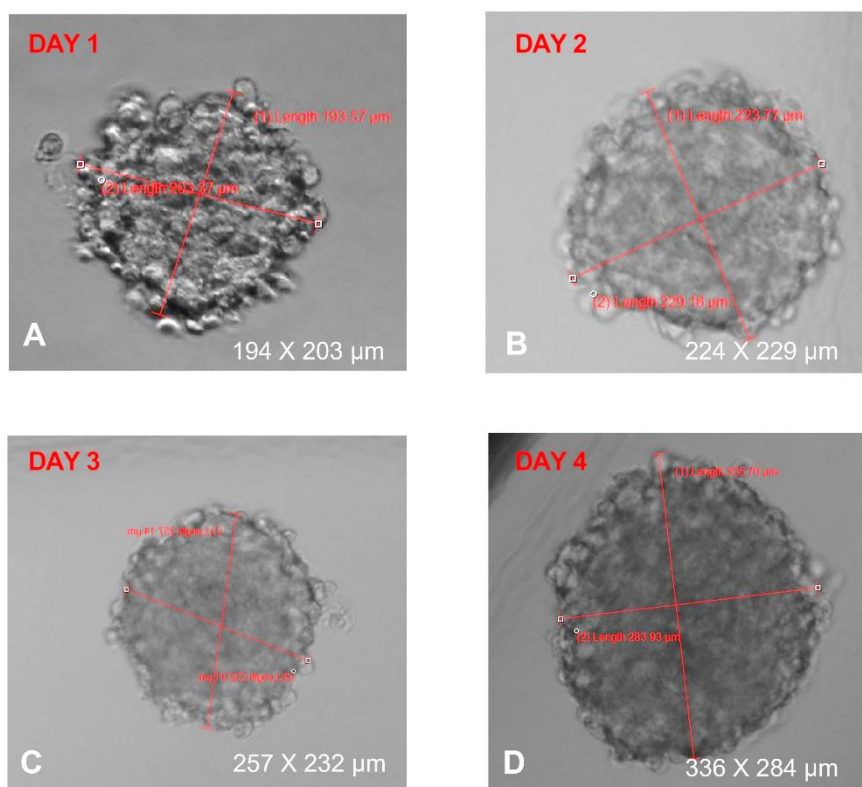


**Figure 5.2:** U-87 spheroids growth at **A-** day 1, **B-** day 2, **C-** day 3, **D-** day 4 before the start of the treatment with respective measurements. Magnification: 10x. (Representative image of U-87 spheroids growth from one of the wells of the Nunclon

Sphera low attachment 96-well plate) The pictures were taken by Dr Amelia Ultimo and Ph.D. students Mila Djisalov and Teodora Knezic; the results were analysed by the candidate.

### 5.1.1  *In vitro* viability assay of free DOX and DOX loaded MSNs

U-87 spheroids were treated with increasing concentrations of DOX, both free and encapsulated in PEG- and GEL-functionalised NPs, with the aim to investigate the ability of the NPs to effectively penetrate the spheroid structure and kill the cancer cells. DOX was chosen as the model drug as it has already been used by our research group for previous 2D *in vitro* cytotoxicity assays with malignant glioma cell lines. [490]

The results from our studies (**Fig. 5.3**) showed that the viability of GBM cancer cells spheroids declined with time and increasing free DOX concentrations. Even at low concentrations, such as 1 µg/mL, the drug exhibited toxicity towards the cancer cell spheroids, causing the percentage of viable cells to drop below 80% within 24 h. With continued exposure to DOX, the cytotoxicity became more pronounced. In fact, 70% of the cell population was killed after 48 h, and only 15% of the total cell population remained viable after the third day of treatment when the spheroids were treated with 1 µg/mL of free DOX. As the concentration of the drug increased, the viability of the spheroids decreased even further. When the concentration reached 100 µg/mL, approximately half of the cell population was killed within just 24 h of treatment and by the end of the 72 h of exposure, the majority of the population had died. These results are in agreement with previous *in vitro* studies reporting that DOX could effectively kill GBM cells. [491]

Furthermore, with increasing concentrations, and with increasing treatment time, both type of NPs showed a higher killing capacity than the free drug alone, indicating that the former was more effective in entering the spheroids structure and in delivering the drug. This is particularly evident after 24 h, when the highest concentration of DOX (100 µg/mL) delivered by the GEL-functionalized NPs resulted in a significant (p=0.0357) decrease in viability when compared to the free drug. The viability of the cells treated with the GEL-functionalized NPs was reduced to 29%, while half of the cellular population was still viable after treatment with the

188

free drug. 10, 25, and 50 µg/mL of DOX delivered by both NPs exhibited a higher killing capacity particularly after 48 h, demonstrating that both capping systems (PEG-functionalized MSNs stimulated by GSH, and GEL-functionalized MSNs stimulated by MMPs) displayed responsiveness to the respective stimulus, allowing for a prolonged release and accumulation of the drug within the cells. Mo J. *et al.*, in their work, [492] demonstrated by confocal microscopy that free DOX had a lower penetration ability than MSNs into the U-87 tumour spheroids, confirming a higher degree of internalization, accumulation and killing abilities of the NPs over the free drug. The group's conclusion was also supported by the observed reduction of the spheroids' diameter after being treated with the loaded MSNs. In our studies we also observed that same effect (**Fig. 5.4**): the spheroids treated with DOX loaded MSN-PEG showed a diameter of 517 ± 18 µm and 425 ± 6 µm after 3 days treatment with DOX concentration equivalent to 0.01 and 10 µg/mL, respectively; while the spheroids treated with DOX loaded MSN-GEL showed a diameter of 434 ± 9 µm and 442 ± 3 µm after 3 days of treatment with the same DOX concentrations as above. On the contrary, the control spheroids (no treatment) showed a diameter of 582 ± 11 µm after seven days (for pictures of spheroids during the tree days treatment refer to **Appendix 3 Fig. A3.1**, **A3.2** and **A3.3**).
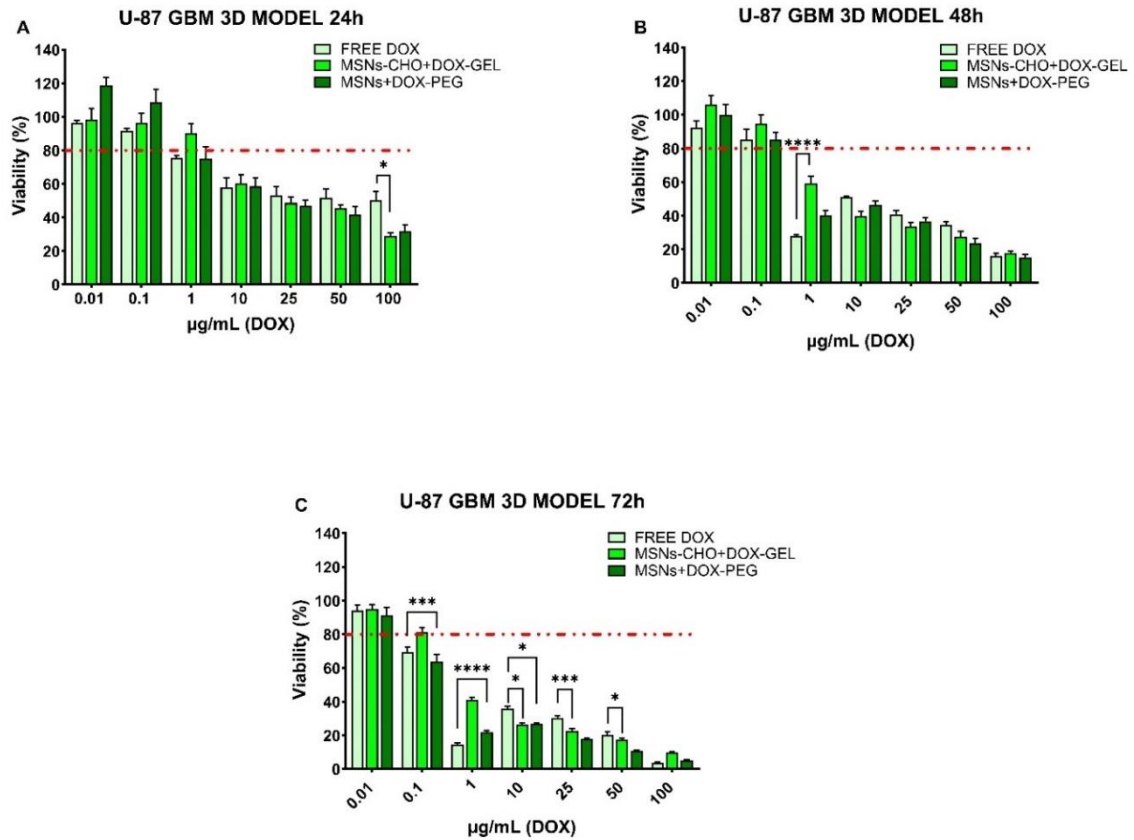
**Figure 5.3: A- B-** and **C-** Comparison of U-87 GBM cell spheroids viability upon treatment with free DOX, MSNs-CHO+DOX-GEL and MSNS+DOX-PEG with corresponding loaded drug concentrations (24, 48 and 72 h). (mean±SEM) The *in vitro* experiments were carried out by Dr Amelia Ultimo and Ph.D. students Mila Djisalov and Teodora Knezic; the results were analysed by the candidate. Statistical test: Two-way ANOVA with Bonferroni's multiple comparison post-test comparing all NPs treatments to the treatment with free drug at the same time point. n=3, $p \leq 0.05$ (*), $p \leq 0.001$ (***), $p \leq 0.0001$ (****)
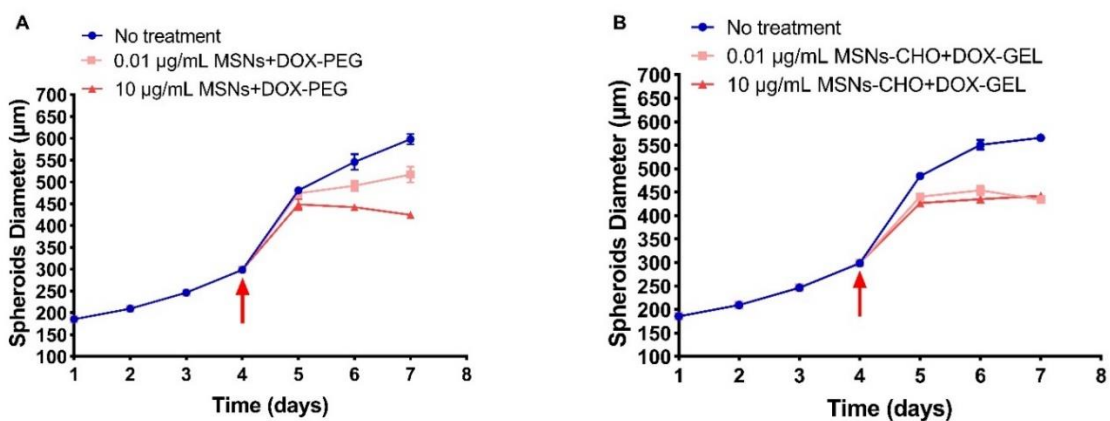
**Figure 5.4:** U-87 spheroids growth in the absence (no treatment) and in the presence of different concentrations of **A-** DOX loaded MSNs-PEG and **B-** DOX loaded MSNs-GEL. (mean±SEM) The *in vitro* experiments were carried out by Dr Amelia Ultimo and Ph.D. students Mila Djisalov and Teodora Knezic; the results were analysed by the candidate. The concentrations refer to the amount of DOX present in the MSNs, and the red arrows indicate when the treatments started.

When comparing the two different formulations, their cytotoxicity levels were similar overall (**Fig. 5.3**). Both formulations resulted in comparable reductions in cellular viability at equivalent drug concentrations, particularly when looking at 10, 25, 50 and 100 µg/mL.

It has been reported in the literature that MMPs are one of the three groups of proteases secreted by GBM, with MMP-2, MMP-9 and the activator MMP-14 being involved in the cancer invasiveness. [493, 494] The levels of the two gelatinases MMP-2 and –9 have been shown to be increased in human gliomas together with tumour progression. [495-497] Studies have shown that MMP-2 activity is significantly increased in GBM tumours compared to normal brain tissue, and the elevated levels of MMP-2 have been associated with the ability of GBM cells to degrade and penetrate the surrounding extracellular matrix, allowing for invasion into adjacent brain tissue. [496-499] It has been suggested that MMP-9 may be involved in mediating angiogenesis since its expression has been detected at the edges of glioblastoma tumours and areas where endothelial cells are proliferating. [496, 500] In fact, it has been shown that MMP-9 [497, 501, 502] or MMP-2 [503-506] inhibition or downregulation, can lead to a reduction in glioblastoma cell invasion.

191

The cytotoxicity results obtained (**Fig. 5.3**) demonstrated a positive responsiveness of the PEG-functionalised NPs to the stimulus GSH, which allowed for a prolonged release and accumulation of the drug within the cells. Even DOX concentrations as low as 1 μg/mL, caused a reduction in cellular viability to 22% of the control after 72 h. The viability reduction after the delivery of concentrations equal to 25 μg/mL was significantly lower than the values observed for the free drug (p=0.0024), indicating a better uptake of the particles over the free drug, and the ability of the former to gradually release DOX and allow its accumulation inside the spheroid structure. As previously mentioned, GSH levels are normally increased in tumour tissues. [175] However, it appears that brain tumours, especially gliomas, [507] present lower GSH levels than the ones found in brain tumour-free tissues, with meningiomas [508] having the highest levels of all the brain cancers, and more aggressive brain malignancies appearing to have the lowest levels. The reported GSH levels for brain tumours are in the range 0.5-3 mM, [508, 509] which are lower that the values reported for other malignancies, as well than the ones used in our release studies. However, accurately measuring GSH concentrations in tissues can be challenging due to various factors. Some brain tumours, such as gliomas, express high levels of γ-Glutamyl transpeptidase (GGT), which can lead to a reduction in GSH levels. This becomes a concern when processing brain tissues for measuring GSH levels because GGT can further degrade GSH and potentially lead to inaccurate measurements, as reported by Gamcsik M.P. *et al.* [174] Nevertheless, despite the possibility that the actual GSH concentration present in our 3D *in vitro* model might be lower than what expected, the PEG system demonstrated a strong sensitivity, resulting in a reduction of GBM spheroids viability due to the successful drug release.

## 5.1.2 Nanoparticles penetration in U-87 GBM cell spheroids

Confocal microscopy was used for visualizing the two different types of NPs and their distribution within the 3D structure of U-87 cell spheroids. The spheroids were grown for 4 days and then treated with RhBITC labelled MSNs: MSNs-GEL-RhBITC and MSNs-PEG-RhBITC at a concentration of 50 μg/mL. The spheroids

were incubated with the labelled MSNs and images were taken after 4-, 6-, and 24-h of MSNs' exposure. The images (**Fig. 5.5**) show that after just 4 h of incubation, the NPs had already begun permeating the cancer cells within the spheroids. By 24 h, MSNs had almost reached the core of the spheroid, indicating successful penetration and distribution throughout it.
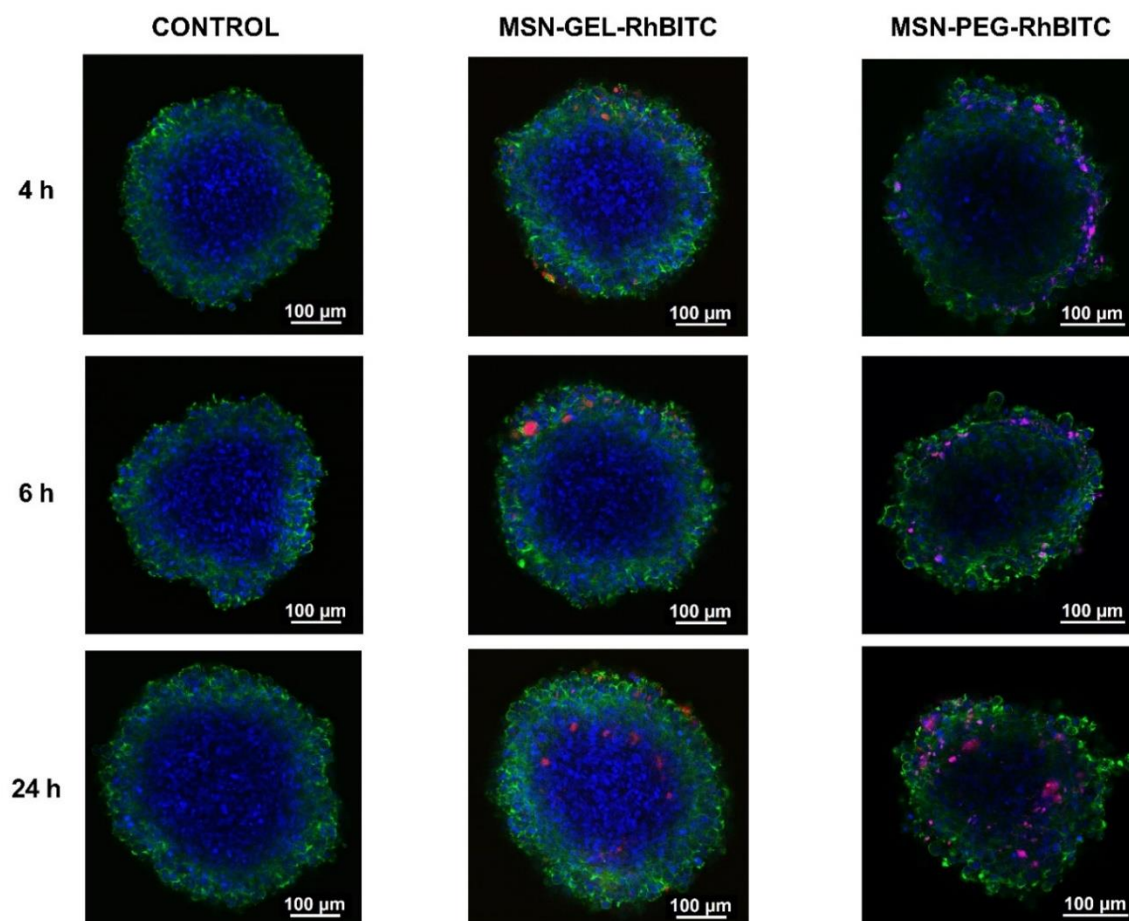


**Figure 5.5:** Confocal fluorescence microscopy of U-87 GBM cell spheroids showing MSNs penetration into spheroids grown for 4 days after **4**, **6** and **24 h** treatment with 50 µg/ml MSNs-GEL-RhBITC and MSNs-PEG-RhBITC. Green- Phalloidin-488 staining cytoskeleton; blue –methyl green staining cell nucleus; red- NPs functionalized with Rhodamine B isothiocyanate (RhBITC). The staining allowed for the observation of MSNS spatial distribution within the spheroids structure. With increasing time of treatment, both MSNs (red/pink cumulus) were observed penetrating deeper into the spheroids, and in higher number. The pictures were taken by Dr Amelia Ultimo and Ph.D. students Mila Djisalov and Teodora Knezic; the results were analysed by the candidate.

### 5.1.3 Conclusions

Overall, the study with a 3D model of glioblastoma multiforme provided evidence of the successful penetration and distribution of the NPs within the spheroids structure, and the effectiveness of both PEG- and GEL-functionalised MSNs in delivering DOX, due to the responsiveness of both systems to the corresponding stimulus and suggesting they may have potential in the treatment options for brain tumours.

# 6   CHAPTER 6: *In vivo* studies

The *in vivo* safety of unloaded PEG- and GEL-functionalised MSNs, and the *in vivo* efficacy of the PTX loaded NPs was evaluated by retro-orbital injection in C57/BL6 mice.

The biodistribution, clearance, and biocompatibility of NPs *in vivo* must be thoroughly studied in order to effectively transfer their use from the bench to the clinic and therefore before it can be employed in human beings (**Fig.6.1**). Unlike soluble molecules or drugs, NPs can interact with biomolecules, cells, and tissues [76, 311, 438-441, 510] depending on their chemical composition, size, shape, and physical properties, which can affect their behaviour in the organism and, as a result, cannot be predicted by only a dose-response correlation determined by routine testing in cellular systems *in vitro* (**Fig. 6.2**):

- The dissolution rates as well as the mechanisms behind it, are important considerations as they can influence NPs' circulation time and consequently their elimination routes.
- Particle components can be released upon dissolution, and this can also have implications on their safety profiles.
- For targeted delivery, it is very important that the surface of the particles remains intact until it reaches the intended target; for this reason, the particles degradation rate, and the mechanisms behind it can be critical factors in determining their efficacy and safety.
- Properties of the target cells can influence how particles are taken up, processed, and eliminated within the cell. Additionally, the culturing conditions of the cells can also impact these processes.
- The route of administration of particles can also have a significant impact on the bioavailability, biodistribution, and pharmacokinetics of the particles. [511-513]
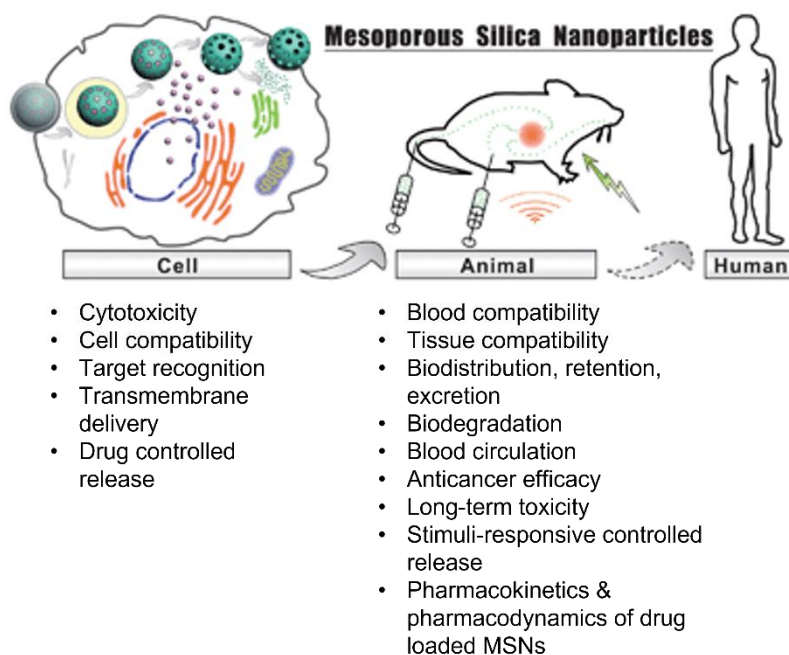
**Figure 6.1:** The research steps for the applications of MSNs in biomedicine. *(Adapted with permission of Royal Society of Chemistry; permission conveyed through Copyright Clearance Center, Inc.)* [514]
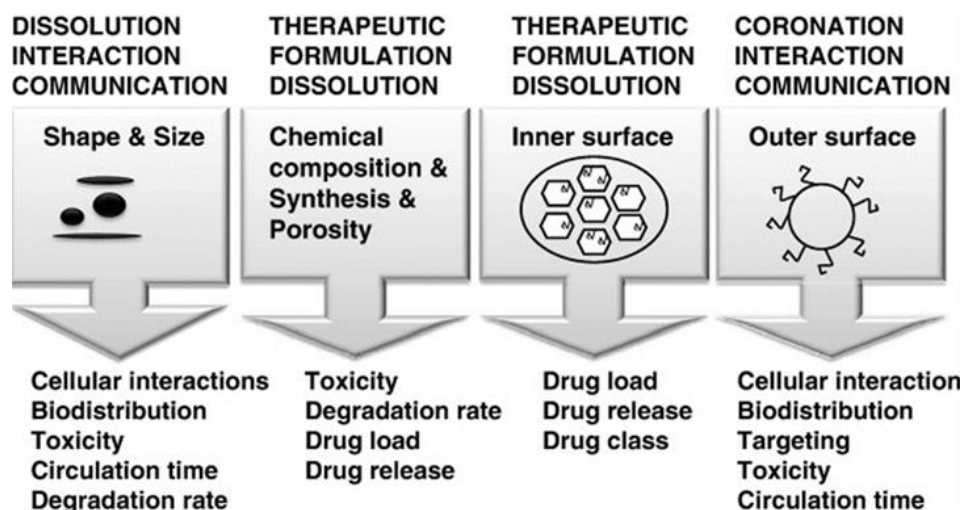


**Figure 6.2**: NPs characteristics which can be tailored to influence their fate *in vivo*. (*Reprinted with permission from Elsevier*) [512]

Many different MSNs formulations have been tested *in vivo* in the recent years (**Table 6.1**). [255] A series of discrepancies between the results of different *in*

196

*vivo* studies has been reported in the literature, making it difficult to reach a general agreement about the biosafety of these nanomaterials. [255, 511, 515]

**Table 6.1:** List of *in vivo* experiments applying different type of MSNs. (*From Chemical Engineering Journal, 2019. 359: p. 684-705. With permission from Elsevier)* [255]

| MSN type | Cargo | Animal model | Reference |
|---|---|---|---|
| QD@MSN-GO-FA | DOX | Hela tumour bearing mice | [516] |
| *Cyc6-FITC-MSN | $Gd_2O_3$ | Bladder tumour bearing mice | [517] |
| XL-MMSNs | IL-4 | Arg-eYFP mice | [518] |
| MUC1-NIR-MSN | NIR-797 | Transgenic murine mouse (mammary gland tumours) | [519] |
| MSN | ICG and WO | B16 subcutaneous tumour model in C57/B6 | [520] |
| ICG/MSNs-RGD | ICG | Mice bearing subcutaneous Hep-G2- (GFP)-fLuc tumours | [521] |
| FA-PEI-PEG-MSN | γ-secretase | 18 FVB/N adult male mice | [522] |
| MSN-AuNC@BSA | Gemcitabine and DOX | Mice with human pancreatic cancer cells | [523] |
| $^{45}$Ti MSNs@PEG | $^{45}$Ti | Breast cancer bearing mice | [524] |
| PEG-MSN | Puerarin | Male Sprague–Dawley rats | [525] |
| PEI-PEG-MSN | Epirubicin hydrochloride and anti BCL-2 siRNA | Tumour bearing Rats | [526] |
| PEG-M−MSN−$NH_2$ | **CpG ODN | Five-week-old male BALB/c mice | [527] |
| MSNs-HP | DOX | H22 mice model and male Sprague-Dawley rats | [528] |
| CTAB- MSN | Curcumin | KM mice | [529] |
| MSNs/CD | Moxifloxacin | Mouse model of lethal pneumonic tularaemia | [530] |
| YMSNs | Doxorubicin | tumour-bearing nude mouse model | [531] |
| MSN/Avidine | Cisplatin | Kras mutant lung cancer mice model | [138] |
| MSN-RGD | NAMI-A | Chick embryo chorioallantoic membrane (CAM model) | [532] |
| PBA-HSA-MSNs | DOX | Tumour model of nude mice | [533] |
| PEG-MSN-CD-PEG-FA | DOX | MDA-MB-231 xenograft model breast cancer | [534] |
| LbL coated MSNs | DOX | BALB/c nude mice | [535] |
| MSN/COOH | DOX | Mice bearing hepatocellular carcinoma | [536] |
| HMSN | DOX | 4T1 murine breast cancer model | [537] |
| (PNIPAM-co-MAA)-MSN | DOX | Mice bearing a murine sarcoma S-180 cell line | [538] |
| $^{64}$Cu-NOTA-MSN-PEG -TRC105 | DOX | 4T1 murine breast tumour-bearing mice | [539] [540] |
| MSNs@Gel | DOX | Tumour xenograft BALB/c nude mice | [143] |
| (PDMAEMA-co-BAC)-MSNs | siRNA | HeLa-Luc xenograft murine model | [541] |
| PEI-PEG-MSN | Pgp-siRNA and DOX | MCF-7/MDR xenograft model nude mice | [542] |

197

| MSN | Paclitaxel | Sprague-Dawley rats | [325] |
|---|---|---|---|
| FA- MSN | CMP | Pancreatic cancer xenografts (PANC-1) nude mice | [543] |
| MSNs | Curcumin | Zebrafish larvae | [544] |
| MSNs and folic acid-MSNs | CMP | Human pancreatic cancer xenografts | [543] |
| HMSNs | Silybin meglumine | Male Beagle dogs | [545] |

QD@MSN-GO-FA: quantum dot core-shell MSN coated graphene oxide targeted FA, * Cyc6, XL; **Cytosine-guanine (CpG) containing oligodeoxynucleotides (ODN) extra-large pores, IL-4; Interleukin 4, MSN-AuNC@BSA: -gold clusters bovine serum albumin capped MSN, $NH_2$-amine, MSNs-HP; Heparinized mesoporous silica nanoparticles (denoted as), YMSNs; Yolk-shell mesoporous silica nanoparticles, PBA-HSA; phenylboronic acid conjugated human serum albumin, BAC; N,N'-(dithiodi-2,1-ethanediyl)bis(acrylamide), LbL; Layer-by-layer.

## 6.1 *In vivo* safety assessment on healthy mice

Before testing the therapeutic efficacy of our PEG and GEL systems loaded with PTX, preliminary toxicity assays were performed by retro-orbitally injecting empty particles in healthy mice and monitoring their body weight and behaviour (signs of pain and/or distress), on a daily basis for a total of 2 weeks.

The maximum tolerated dose (MTD) of PTX in mice has been reported to be 20 mg/kg. [374, 546-548] DLS studies were conducted with empty particles (MSNs-PEG and MSNs-GEL) in order to measure the size distribution of the particles in the vehicle (glucose 5%), and to determine their stability. By performing DLS studies, we aimed to identify the optimal concentration of NPs (considering the particles loading capacity) that could effectively deliver a therapeutic dose of PTX without causing toxicity or adverse effects due to the formation of aggregates. The goal was to find a concentration that would maximize the drug delivery while staying within the safety limits.

Based on the DLS studies (**Fig. 6.3**), we selected two different NPs doses that could be administered considering both safety and efficacy aspects: one that represented the safest dose and allowed for the delivery of a total weekly dose of 2.5 mg/kg of PTX, and another dose that represented the next highest and safest concentration, enabling the delivery of a higher PTX dose of 8 mg/kg weekly. For both MSNs-PEG and MSNs-GEL, the criteria for selecting the lowest safest dose (0.362 and 0.47 mg/mL, respectively) was based on the presence of a proper

dispersion after 1 h of sonication in the vehicle, with the aim to reduce the risk of potential adverse effects related to NPs' aggregation.

Among the different concentrations evaluated (0.3 to 3.7 mg/mL), MSNs-PEG 1.16 mg/mL and MSNs-GEL 1.48 mg/mL were chosen as they exhibited the lowest percentage of aggregates but allowed for the delivery of a higher PTX dose of 8 mg/kg weekly, enabling a more potent therapeutic effect, while still maintaining an acceptable level of stability and safety. GEL-functionalized MSNs (**Fig. 6.3 A**) demonstrated a better PdI of 0.4, indicating a narrower and more uniform size distribution compared to PEG-functionalized MSNs (**Fig. 6.3 B**) (PdI 0.6). The size distribution analysis revealed that the majority of the GEL-functionalized MSNs were present in a size range of 179 ± 50 nm, accounting for 92.4% of the total population, suggesting that MSNs-GEL have a relatively homogeneous size distribution, with most particles falling within a narrow size range. In contrast, the PEG-functionalized MSNs exhibited larger aggregates, with a small population in the size range of 1508 ± 770 nm. However, these aggregates accounted for only 1.2% of the total population. The majority of the particles (98.8%) were in the size range of 191 ± 58 nm. After storing the particles in the fridge for 24 h to test longer-term stability, the PEG-functionalized MSNs (**Fig. 6.3 B**) showed an increase in aggregates size, but these still accounted for the lowest percentage of the total population (2080 ± 767 nm 0.2%, and 4576 ± 837 nm 0.1%). The majority of the sample (99.7%) remained in the size range of 167 ± 72 nm, indicating a slight decrease in mean particle size. On the other hand, the GEL-functionalized MSNs (**Fig. 6.3 A**) exhibited a higher percentage of aggregates and of bigger size (1556 ± 408 nm, as opposed to 700 ± 250 the day before). The rest of the sample (96.3%) also increased in size (211 ± 41 nm), indicating a better stability and resuspension of MSNs-PEG. Based on these results, it was decided that the particles' formulations could be stored for a maximum of 24h before being injected retro-orbitally upon 1 h sonication.
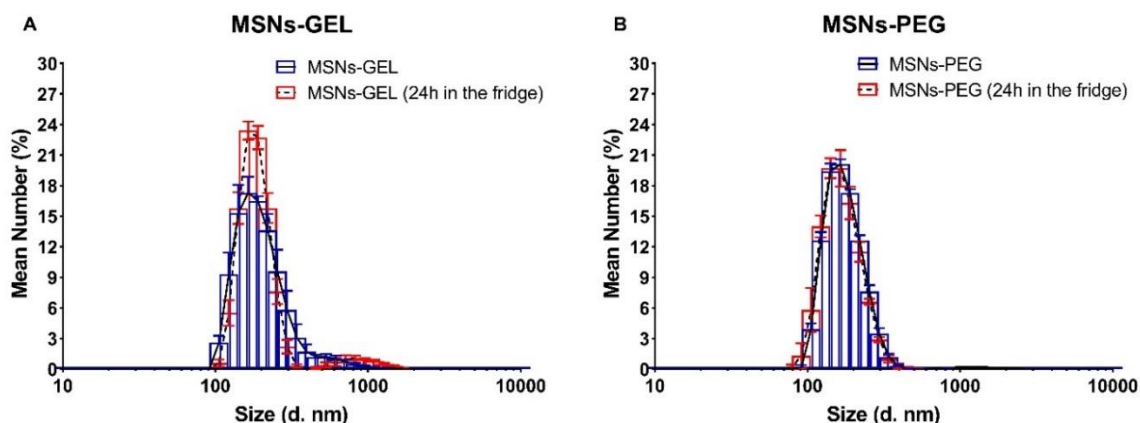
**Figure 6.3:** Size distribution (5 measurements) by number (%), measured by dynamic light scattering of **A-** MSNs-GEL (1.48mg/mL) and **B-** MSNs-PEG (1.16 mg/mL) in glucose 5% after 1 h sonication before and after 24 h storage at 2-8 °C. (mean±SEM)


The mice were randomly divided into five groups of 6 mice each, receiving the vehicle (glucose 5%), or the NPs suspensions at the two selected concentrations in two consecutive retroorbital injections (150 µL each), every day, for five consecutive days (**Fig. 6.4**). The following week, after a two-day break, the mice received the exact same treatments and were euthanised on the third week, three days after the last injection.
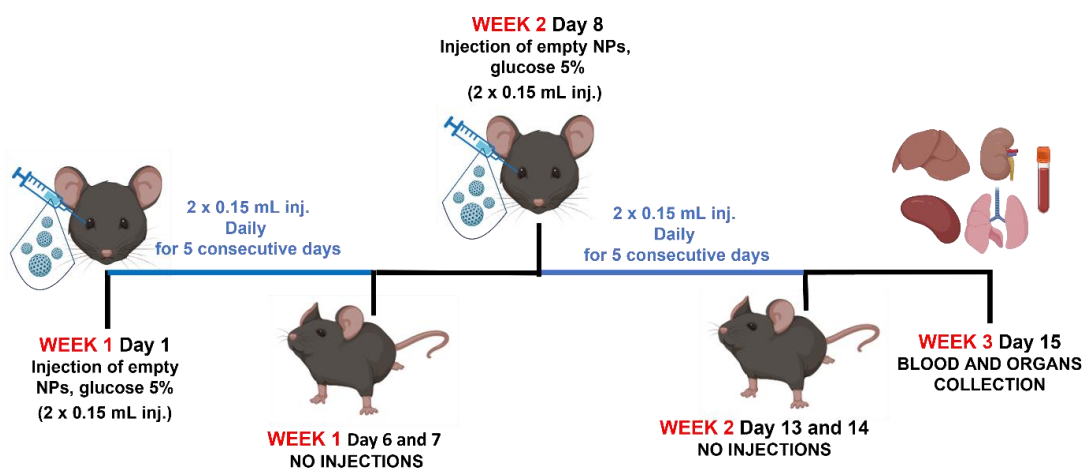


**Figure 6.4:** Timing schematic of *in vivo* toxicity studies. (*Created in BioRender.com*)

200

The results from this preliminary toxicity assay showed that both particles, at the concentration tested, did not cause major changes in the body weight of the animals (**Fig. 6.5**).



## SAFETY ASSESMENT
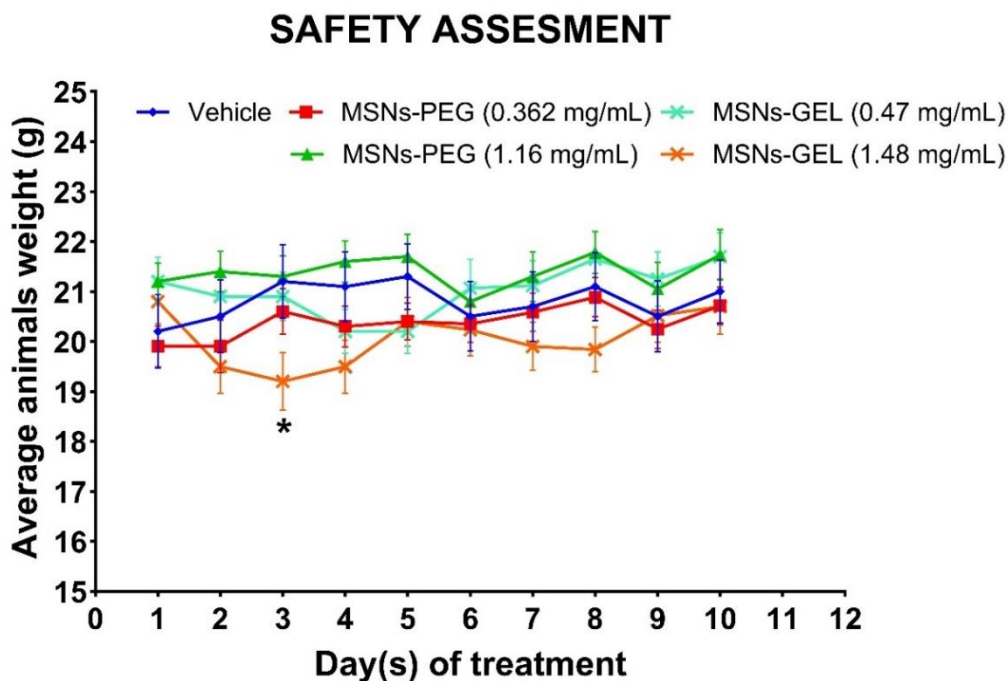
**Figure 6.5:** Average body weight of healthy mice treated with glucose 5%, MSNs-PEG and MSNs-GEL at two different concentrations for 14 days (daily injections for 5 consecutive days followed by 2 days break for a total of 2 weeks). (mean±SEM) The *in vivo* experiments were carried out by Dr Maria Manuela Jesus Guilherme Gaspar; the results were analysed by the candidate. Statistical test: Two-way ANOVA with Dunnett's post-test comparing all treatments versus the negative control (vehicle) on the same day. n=6 (mice per group), $p \leq 0.05$ (*)

Once euthanised, the key organs involved in the metabolic and elimination stages, as well as the lungs, were collected and weighed to determine the tissue index. Tissue index enables the assessment of alterations in a particular organ that may take place, in relation to the total body weight. Variations in organs weight are well recognized as a sensitive marker of organ alterations brought on by chemicals. [549] In this way, tissue index enables the assessment of potential damage to those organs. [331, 550-552] The analysis of tissue index (**Fig. 6.6 A**) showed that the highest dose of MSNs-GEL caused a significant increase in the tissue index of the liver, spleen, and lung (p=0.0055, p<0.0001, p<0.0001, respectively). At the lowest concentration, MSNs-GEL affected the tissue index of the spleen and lung

(p=0.0291, p<0.0001, respectively). No remarkable changes were observed in the kidney for any of the concentrations tested. In contrast, when analysing the tissue index of the same organs in mice that received MSNs-PEG, only the liver's index showed a significant increase in mice treated with the lowest concentration (p=0.0291). No significant changes were observed in the other organs, and in all the organs of mice treated with the highest concentration of MSNs-PEG NPs.

To further assess liver function and potential hepatic effects of the NPs, liver aminotransferases (ALT and AST) were measured in serum. It was observed that, although the levels of AST significantly increased for the highest MSNs-PEG concentration and both MSNs-GEL concentrations, indicating that the NPs may induce liver inflammation (**Fig. 6.16 B**), no significant changes were recorded for ALT. [553-555] Both AST and ALT are found in high concentrations in the liver. However, AST is also present in other organs and tissues such as the heart, skeletal muscle, kidneys, brain, and red blood cells. When there is liver damage or injury, the liver cells release these enzymes into the bloodstream, causing an increase in their serum levels. However, because AST is found in multiple organs, an elevation in AST levels can indicate damage or disease in those organs as well as in the liver. On the other hand, ALT is more specific to the liver, so an increase in ALT serum levels is generally considered a more specific marker of liver damage. [556] The levels of urea in serum for all the NPs tested were similar to those in the control mice, indicating that the NPs do not produce, in principle, renal damage.
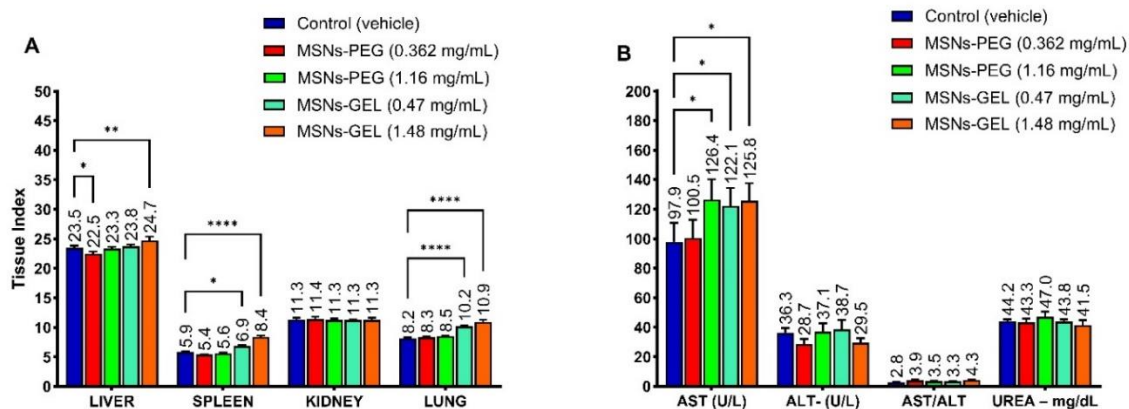
**Figure 6.6:** Tissue indexes of healthy mice after retro-orbital administration of glucose 5% (vehicle), PEG- and GEL-functionalised NPs at two different concentrations for 14 days (daily injections for 5 consecutive days followed by 2 days break for a total of 2 weeks). **B-** Biochemical analysis results after 2 weeks treatment. (mean±SEM) The *in vivo* experiments were carried out by Dr Maria Manuela Jesus Guilherme Gaspar; the results were analysed by the candidate. Statistical test: Two-way ANOVA with Dunnett's post-test comparing all treatments versus the negative control (vehicle). n=6 (mice per group), $p \leq 0.05$ (*), $p \leq 0.01$ (**), or $p \leq 0.0001$ (****)

Histological analysis confirmed the observed results. The organs of mice that received MSNs-PEG did not show significant macroscopic changes compared to the control group. However, mice treated with the highest concentration of MSNs-GEL exhibited splenomegaly (enlarged spleen) and bleeding foci in the lung. Additionally, all mice treated with the different NPs at different concentrations presented a tenuous multifocal lymphocyte infiltrate in the liver that could explain the higher tissue index when compared to the control.

Based on these findings, we can speculate that MSNs-GEL affected lung, spleen, and liver, likely due to their accumulation in these organs. This accumulation may be attributed to macrophages recognizing MSNs-GEL more effectively than MSNs-PEG [557, 558] and sequestering them in the liver and spleen, leading to potential inflammation and toxicity. A slow hepatobiliary excretion process could contribute to the accumulation and potential inflammation. [513] Larger particles are expected to accumulate in the liver [559] and spleen, while smaller particles (5-6 nm) are more likely to be cleared by the kidneys. [560] However, some studies have reported the renal clearance of larger particles, which

were found intact in the urine. [512, 513] Nevertheless, no abnormal parameters were recorded for the kidneys for any of the particles at the concentrations tested.

The higher tissue index of the lung from mice treated with MSNs-GEL could be attributed to an increased oxidative stress caused by the silica component of the NPs. [447-450] This could be due to a non-homogenous gelatine coating or to the degradation of the gelatine layer by MMPs, resulting in the exposure of silanol groups on the surface of the particles. A recent study by Cheng Y. *et al.,* [561] investigated the biodistribution and subacute toxicity of spherical and rod-shaped MSNs in C57/BL6 mice. The authors found that spherical MSNs were mainly distributed in the liver, lung, and spleen after i.v. injection. The toxicity was investigated by injecting the mice with the NPs (100 mg/kg) multiple times over a period of 2 weeks. They observed a significant change in the body weight of the animals when compared to the control group and an increased tissue index for liver, spleen, and lung. They investigated the $H_2O_2$ levels in serum and tissues, and found that these were increased in the serum, as well as in the liver and lung, indicating an increased oxidative stress due to oxidative damage at the accumulation site after the injection of the NPs. These findings could also potentially explain our results. In their work, He Q. and colleagues [294] investigated the *in vivo* biodistribution and excretion of MSNs (with a size range varying from 80 to 360 nm) and their PEG-functionalised counterpart (both by tail-vein injection). According to their findings, both types of particles primarily accumulated in the liver and spleen, with a smaller percentage in the lungs, and with an even smaller amount in the kidney and heart. The authors reported that PEGylated MSNs were always present in lower percentage than their counterpart. Neither of the NPs showed any toxicity, and it was also found that the particles were excreted mainly in the urine 30 minutes post injection, with the bigger NPs being excreted in higher amount as opposed to the smaller and PEGylated ones.

Che E. and colleagues [353] synthesised magnetic MSNs coated with a gelatine layer and investigated their biodistribution after i.v. injection in male Kunming mice. They reported high accumulation of the NPs in the liver and spleen in the absence of an external magnet, demonstrating fast recognition and capture

by the mononuclear phagocytic cells in the reticuloendothelial system (RES). The group also reported some accumulation in the lungs.

The differences observed in our results between MSNs-GEL and MSNs-PEG NPs may be attributed to various factors such as differences in surface properties of the particles, [557, 558] and the dosages administered: 4.4 and 13.9 mg/kg (total daily dose) of body weight of MSNs-PEG; 5.64 and 17.8 mg/kg (total daily dose) of body weight of MSNs-GEL. [255, 514, 562]

## 6.2  Lung cancer model

To test the efficacy of our PTX loaded nano-formulations *in vivo*, a lung cancer model was established by carrying out three separate assays, injecting the mice with different LLC1 concentrations in order to decide which was the most suitable one.

### 6.2.1   First assay

**Fig. 6.7** shows the representative images of histopathological analysis of lung samples from the first group of mice which received 100,000 cells/mL by retro-orbital injection and was sacrificed 15 days post-injection. All four mice's lungs presented several cell clusters of varying dimensions, consisting of pleomorphic cells with large nuclei, evident nucleoli, and several mitoses. These lesions predominantly assumed a subpleural and perivascular location. The microscopic images were compatible with an undifferentiated malignant neoplasm. In the remaining organs, and in the naïve animal no microscopic lesions worthy of record were observed.
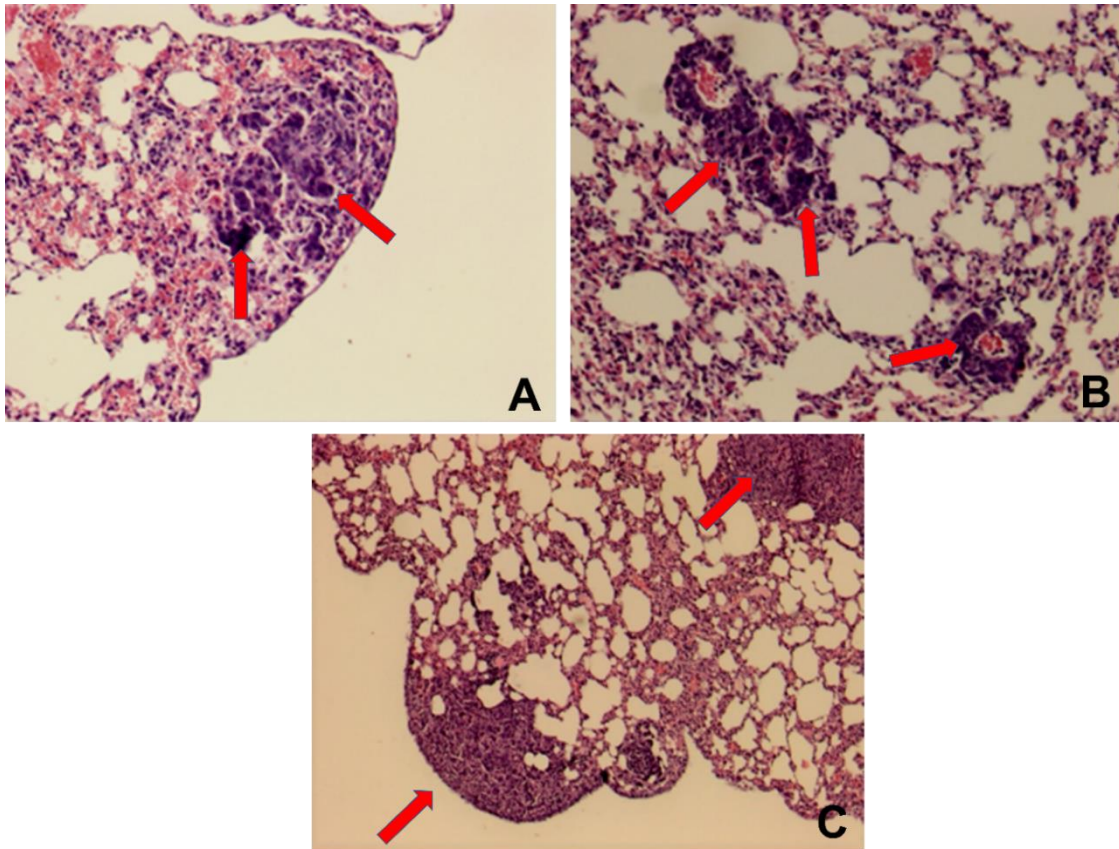
**Figure 6.7: A- B-** and **C-** Representative images of histopathological analysis of lung samples from mice 15 days after retro-orbital injection of 100,000/mL LLC1 cells. Haematoxylin and eosin staining. Original magnification: 100x. Pleomorphic cell clusters indicating the formation of tumour cells are highlighted by red arrows. The *in vivo* experiments were carried out by Dr Maria Manuela Jesus Guilherme Gaspar; the results were analysed by the candidate.

All animals survived the first assay. **Fig 6.8** shows the recorded average body weights of the animals during the 15 days before being euthanised. No significant changes were observed for the duration of the whole experiment, and only a slight reduction on mice weight from days 12-15 post injection was registered.
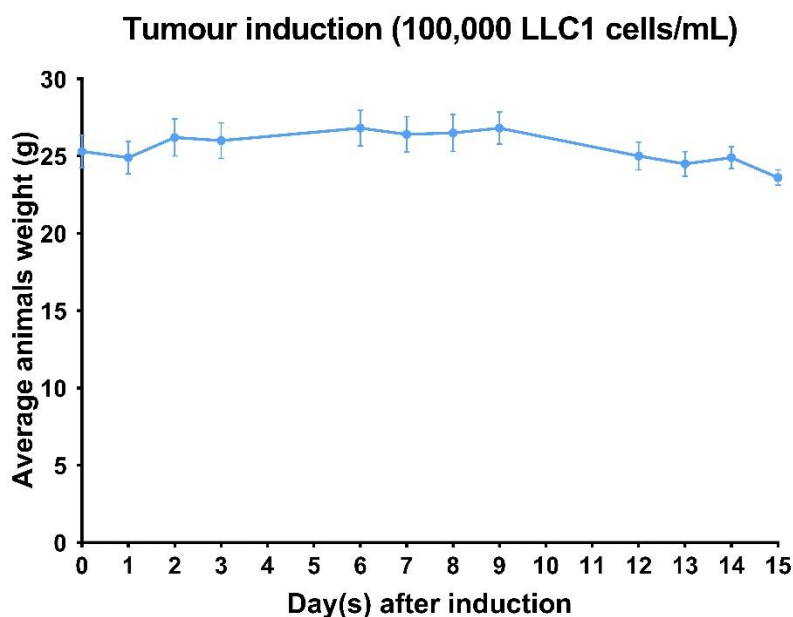
**Figure 6.8:** Mice body weight evolution over 15 days after the animals received 100,000 LLC1 cells/mL retro-orbitally. (mean±SEM) The *in vivo* experiments were carried out by Dr Maria Manuela Jesus Guilherme Gaspar; the results were analysed by the candidate.

**Table 6.2** shows the tissue indexes of liver, spleen, lung, and kidney. It can be noted that no major changes where observed when comparing the tumour bearing mice to the control group.

**Table 6.2:** Tissue Index values for liver, spleen, lung, and kidney. Animals received 100,000 LLC1 cells/mL retro-orbitally and were sacrificed 15 days after tumour induction. (mean±SEM) The *in vivo* experiments were carried out by Dr Maria Manuela Jesus Guilherme Gaspar; the results were analysed by the candidate.

| Mice | Liver | Spleen | Lung | Kidney |
|---|---|---|---|---|
| **Tumour induced** | 21.5 ± 0.1 | 6.3 ± 0.7 | 8.6 ± 0.2 | 10.7 ± 0.4 |
| **Naïve animal** | 22.0 ± 1.0 | 6.1 ± 0.9 | 8.2 ± 0.7 | 10.9 ± 0.8 |

## 6.2.2  Second assay

In the second assay 500,000/mL cells were injected in the mice's retro-orbital area and animals were sacrificed 15 days post tumour induction. From the histological analysis (**Fig. 6.9),** it can be seen that the lungs of the mice presented several cell clusters of variable dimensions, consisting of pleomorphic cells with intense anisokaryosis, and numerous mitoses, some of them atypical. In one of the mice (**Fig. 6.9 B**) several small clusters of pleomorphic cells identical to those observed in the lung were observed in the brain too, indicating the presence of metastases. Two out of five animals died before the end of the experiment.
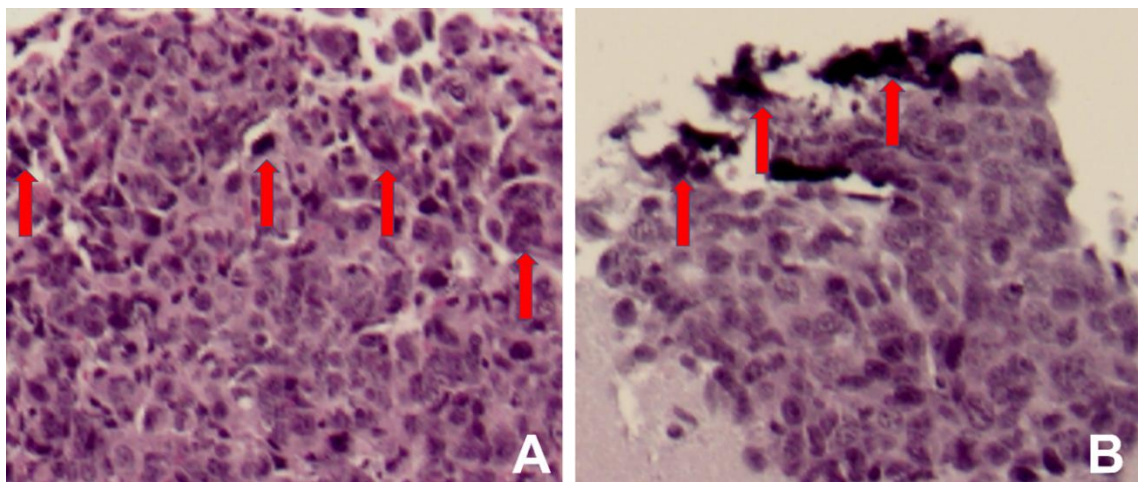


**Figure 6.9:** Representative images of histopathological analysis of **A-** lung and **B-** brain samples from mice 15 days after retro-orbital injection of 500,000/mL LLC1 cells. Haematoxylin and eosin staining. Original magnification: 100x. Pleomorphic cell clusters indicating the formation of tumour cells are highlighted by red arrows. The *in vivo* experiments were carried out by Dr Maria Manuela Jesus Guilherme Gaspar; the results were analysed by the candidate.

As for the first assay, the recorded average body weight of the animals during the 15 days before being euthanised showed no significant changes (**Fig. 6.10**), with only slight changes around the 13th day post tumour cells injection recorded. On the other hand, the calculated tissue index of the induced mice's spleen and lung showed a higher value than the naïve animals (**Table 6.3**).
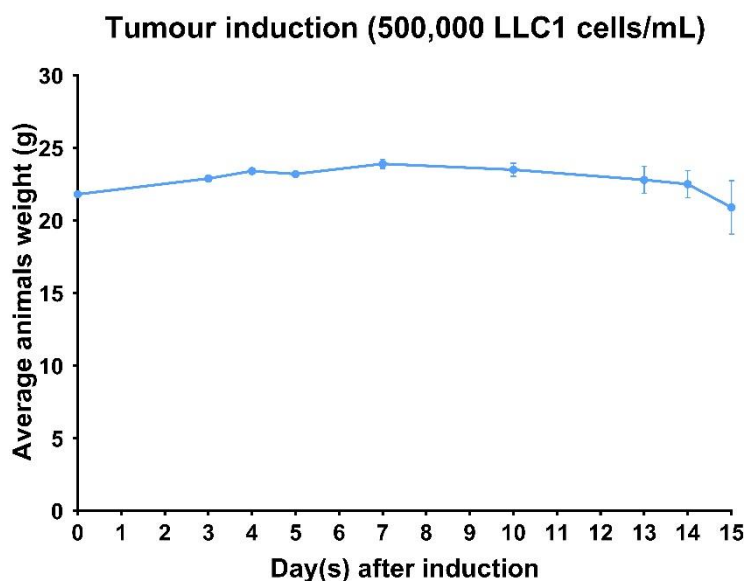
**Figure 6.10:** Mice body weight evolution over 15 days after the animals received 500,000 LLC1 cells/mL retro-orbitally. (mean±SEM) The *in vivo* experiments were carried out by Dr Maria Manuela Jesus Guilherme Gaspar; the results were analysed by the candidate.

**Table 6.3:** Tissue Index values for liver, spleen, lung, and kidney. Animals received 500,000 LLC1 cells/mL retro-orbitally and were sacrificed 15 days after tumour induction. (mean±SEM) The *in vivo* experiments were carried out by Dr Maria Manuela Jesus Guilherme Gaspar; the results were analysed by the candidate.

| Mice | Liver | Spleen | Lung | Kidney |
|---|---|---|---|---|
| **Tumour induced** | 21.1 ± 1.6 | 7.2 ± 1.1 | 9.5 ± 0.9 | 10.9 ± 0.1 |
| **Naïve animal** | 22.0 ± 1.0 | 6.1 ± 0.9 | 8.2 ± 0.7 | 10.9 ± 0.8 |

## 6.2.3 Third assay

The aim of the final assay was to determine the most suitable time span for evaluating the efficacy of the treatment after tumour induction. In this case it was decided to inject 100,000 LLC1 cells/mL retro-orbitally, since the mice did not show brain metastases in the initial assay. Three different groups of mice were injected, and each group was euthanized at different time points: 15 days, 30 days, and 35 days post-injection.

At 15 days post tumour injection (**Fig. 6.11 A**) mice presented several cell clusters of variable dimensions, consisting of pleomorphic cells with intense anisokaryosis, and numerous mitoses, some of them atypical. Similarly, at 30 days post injection (**Fig. 6.11 B**) mice's lung showed the presence of several pleomorphic cell clusters with marked anisokaryosis and numerous mitoses. At 35 days post tumour induction (**Fig. 6.11 C**) histological analysis of the lung highlighted the presence of pleomorphic cells in the interalveolar septa that were available in rare groups with a reduced number of cells compatible with the development of a malignant lesion. In the remaining organs, no microscopic abnormal lesions were observed for any of the mice from the different groups.
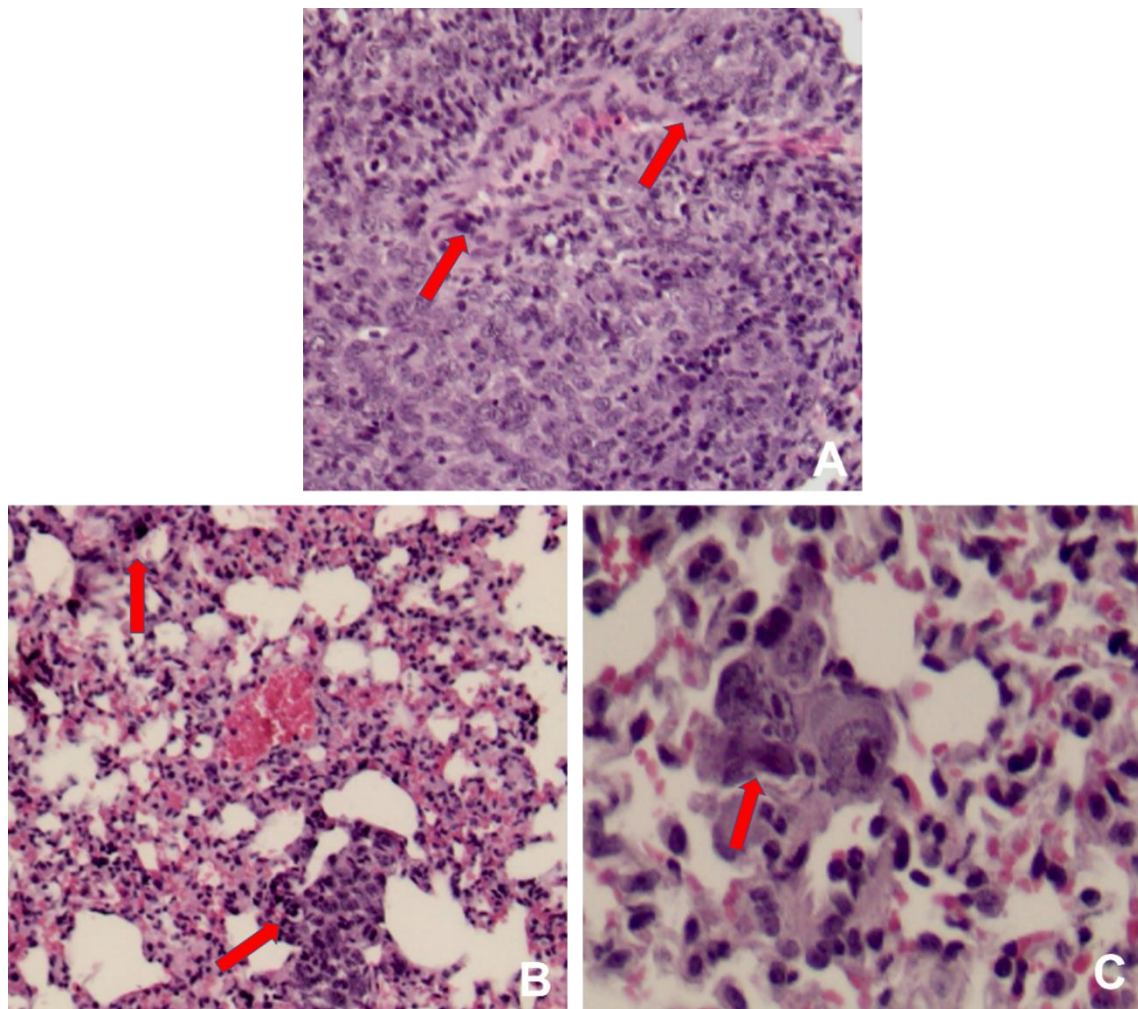


**Figure 6.11:** Representative images of histopathological analysis of lung samples of **A-** mice euthanised after 15 days; **B-** mice euthanised after 30 days; **C-** mice euthanised after 35 days. Haematoxylin and eosin staining. Original magnification **A-** and **B-** 100x; **C-** 200x. Pleomorphic cell clusters indicating the formation of tumour cells are highlighted by

red arrows. The *in vivo* experiments were carried out by Dr Maria Manuela Jesus Guilherme Gaspar; the results were analysed by the candidate.

When looking at the average body weight of the different groups of mice (**Fig. 6.12**), it can be noticed that the mice started to lose weight at around 21 days post tumour cells injection, with two animals dying between the 30th and 35th day. Changes were also recorded for the mice's main vital organs tissue index as showed in **Table 6.4**.



**Figure 6.12:** Mice body weight evolution over 35 days after the animals received 100,000 LLC1 cells/mL retro-orbitally, and they were sacrificed after 15 (**blue**), 30 (**green**), or 35 (**red**) days after tumour induction. (mean±SEM) The *in vivo* experiments were carried out by Dr Maria Manuela Jesus Guilherme Gaspar; the results were analysed by the candidate.

**Table 6.4:** Tissue Index values for liver, spleen, lung, and kidney. Animals received 100,000 LLC1 cells/mL retro-orbitally and where euthanised at 15-, 30- and 35-days post injection. (mean±SEM) The *in vivo* experiments were carried out by Dr Maria Manuela Jesus Guilherme Gaspar; the results were analysed by the candidate.

| Day of sacrifice (after tumour induction) | Liver | Spleen | Lung | Kidney |
|---|---|---|---|---|
| 15th | 21.1 ± 0.7 | 6.0 ± 0.6 | 8.7 ± 0.4 | 11.2 ± 0.4 |
| 30th | 21.0 ± 1.2 | 7.8 ± 1.9 | 9.1 ± 0.8 | 11.2 ± 0.2 |
| 35th | 22.3 ± 1.3 | 6.0 ± 0.5 | 8.1 ± 0.4 | 11.4 ± 0.3 |
| Naïve animals | 22.0 ± 1.0 | 6.1 ± 0.9 | 8.2 ± 0.7 | 10.9 ± 0.8 |

Based on the evaluation of the outcomes from the three separate assays, which considered factors such as the presence/absence of metastasis, weight change, and tissue index of the analysed organs, it was decided to proceed with the injection of 200,000 LLC1 cells retro-orbitally for the efficacy studies. Furthermore, it was determined that 15 days was an appropriate time span with the loaded NPs post-injection since this window allowed for sufficient time for the tumour to establish without significant adverse effects on the animals' overall health.

## 6.3  Efficacy studies

Based on the preliminary studies' results and in order to test the antitumour activity of the PTX loaded NPs, it was determined that the tumour bearing mice would be treated with the highest dose of NPs and, consequently, PTX, but for a duration of one week only (**Fig. 6.13**). The decision was based on the speculation that the observed toxic effects, were mainly due to the high accumulation of the particles in the various organs over the course of two weeks treatment. However, considering that the administration of a total dose of 2.5 mg/kg of PTX for one week would be too low for obtaining a therapeutic effect, it was decided to use the highest dose previously tested (8 mg/kg). Normally, PTX is administered at a dose of 135 or 175 mg/m$^2$ as a 3- or 24-hour infusion, every 3 weeks. [374, 563, 564] Since the drug MTD of 20 mg/kg in mice is equivalent to 60 mg/m$^2$ [565, 566], a dose of 2.5 mg/kg would correspond to only 7.5 mg/m$^2$, which would be considerably lower than the typical clinical doses used in humans.

The lung cancer was induced by injecting 200,000 LLC1 cells into the retro-orbital region of the mice. After two weeks, the animals were randomly divided in six groups of 5 mice each receiving either the vehicle (glucose 5%), PTX in the free form administered in Cr/EL, unloaded NPs or PTX-loaded NPs at the highest concentration, corresponding to an 8 mg/kg weekly PTX dose (for corresponding NPs concentrations please refer to **Appendix 4, Table A4.1**).
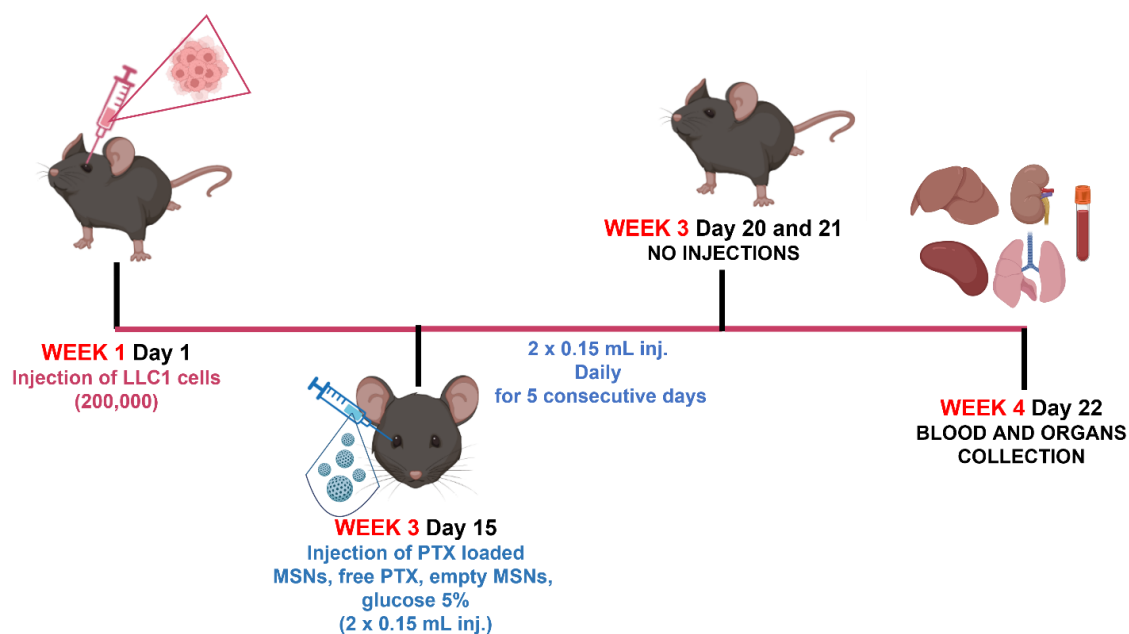


**Figure 6.13:** Timing schematic of *in vivo* efficacy studies. (*Created in BioRender.com*)

The results from the efficacy studies (**Fig. 6.14**) indicated that the group of mice treated solely with PTX (Pos C) experienced a significant mortality rate during the treatment period, with the survival percentage dropping below 50%. In contrast, the mice that received the vehicle (Neg C) and those treated with PTX-loaded and unloaded NPs showed higher survival rates in the order unloaded NPs > loaded NPs > vehicle.

Overall, the mice from the different groups did not show a significant weight loss (**Fig. 6.15 A**) during the whole period (from day 0, tumour induction, to day 23 when they were sacrificed). Significant changes were only observed near the end of the study in mice treated with PTX loaded MSNs-PEG (day 19, p=0.0245) and PTX loaded MSNs-GEL (day 22, p=0.0304), with both groups losing one animal

each. Tissue indexes analysis (**Fig. 6.15 B**) evidenced a significant increase for the spleen's index only for mice treated with empty GEL-functionalised NPs (p= 0.0008) when compared to the control group (glucose 5%), most likely due to a recognition and sequestration of the particles by the RES. This outcome may indicate that the shorter treatment did not cause a toxic accumulation of the particles in the analysed organs. In fact, when comparing the tissue index of the tumour induced mice to the ones of the naïve group (no tumour induced, from the safety assessment studies) it can be seen that the values for liver and spleen significantly increased for all the treatment groups, which could be linked to an inflammatory response and the presence of the tumour mass, rather than a toxic effect caused by the accumulations of the NPs. [567-569] Biochemical analysis confirmed the absence of liver damage overall, with a significant increase (p= 0.0356) in AST only in mice treated with loaded MSNs-PEG. Once again and comparing the results of all the treatment groups to the naïve animal group, the significant increase in values for AST might indicate that the presence of the tumour mass was the cause for liver inflammation. Nevertheless, definite conclusions cannot be drawn without having the results from the histological analysis (in process at the time of submission of this thesis).

One possible explanation for the higher mortality rate observed in the group receiving only PTX is the known toxicity of the vehicle (CrEL). [375-380] Additionally, the lower bioavailability of PTX [361-364] may have hindered its effective delivery to the tumour site. These factors combined likely contributed to the reduced efficacy and increased mortality in the PTX-only group, highlighting the superiority of the NPs in delivering PTX to the tumour site, ensuring higher survival rates and avoiding the toxicity associated with the use of high concentrations of drugs, especially the ones that require the use of toxic vehicles.

The mice treated with PTX-loaded NPs (**Fig. 6.14**) showed a survival rate of 80% at the conclusion of the treatment period, surviving longer compared to the group that received only the vehicle (glucose 5%). This result would suggest that the PTX-loaded NPs effectively delivered the drug to the tumour site by EPR effect. [98, 570]

Zheng J. *et al.,* [387] reported that after i.v. injection of Taxol® (brand name for PTX, 10 mg/kg single injection) in LLC1 tumour-bearing C57BL/6 mice, the drug distributed rapidly in various tissues, with the liver accounting for the majority (56%) of the total amount. 1h post-administration, the drug was found in the lungs and heart, with only a small amount present in the tumour site and plasma. The study also reported a lower survival rate in mice treated with the free drug compared to those treated with different formulations (PEG-conjugated solid lipid NPs), which was attributed to the longer circulation time and higher accumulation of the drug in the tumour site when delivered using alternative formulations. In their work, Jiménez-López J. *et al.,* [458] also observed a higher bioavailability of PTX formulations (PEGylated cationic liposomes) as opposed to the free drug (10 mg/kg of PTX administered every three days for a total of four doses), after administration in C57BL/6 bearing LLC1 tumour mice. In another study, [353] after i.v. administration of Taxol® (10 mg/kg every two days for a total of 6 days) the researchers observed an increase in the tumour weight, as opposed to the group of mice which received the loaded NPs, indicating that the free drug did not effectively inhibit tumour growth. Furthermore, the mice treated with the free drug experienced minimal weight gain 10 days after completing the treatment. The researchers interpreted these results as a potential indication of the toxicity of Taxol® due to its non-selective absorption by healthy tissues.

The lower survival rate (80%) in the mice that received PTX-loaded NPs (**Fig. 6.14**), as opposed to the unloaded NPs treatment group, which presented a 100% survival, could be attributed to the basal leakage observed during the *in vitro* release studies. Although *in vitro* release studies with PTX loaded MSNs will need to be completed in order to understand the release profile of the drug from our NPs and confirm the hypothesis of PTX basal leakage (as observed with safranin-O), it appears that a certain amount of the drug may have been released from the NPs upon administration before the effective removal of the capping systems by the respective stimulus (GSH for MSNs-PEG and MMPs for MSNs-GEL) after reaching the tumour site. As a result, the released drug could have been absorbed by healthy tissues instead of being specifically targeted towards the tumour site. This

unintended distribution of the drug to healthy tissues could have caused adverse effects, leading to the death of some animals in the study.

Further investigation will be necessary to confirm our hypotheses. It is important to reiterate that histological analysis is crucial when evaluating both the safety and efficacy of NPs *in vivo*. The histology results from these studies will provide a better understanding of the effects on tissues, organs and on the tumour mass.

*In vitro* release studies with PTX will also need to be carried out in order to understand the release profile of the drug from our NPs. On top of that, the improvement of PTX loading in the future could potentially reduce the required dosages, avoiding possible toxicities. Additionally, appropriate measures should be taken to minimize the off-target effects of the drug and improve the targeting efficiency of the NPs to enhance the therapeutic outcome, like conjugation with particular ligands or antibodies. [571]
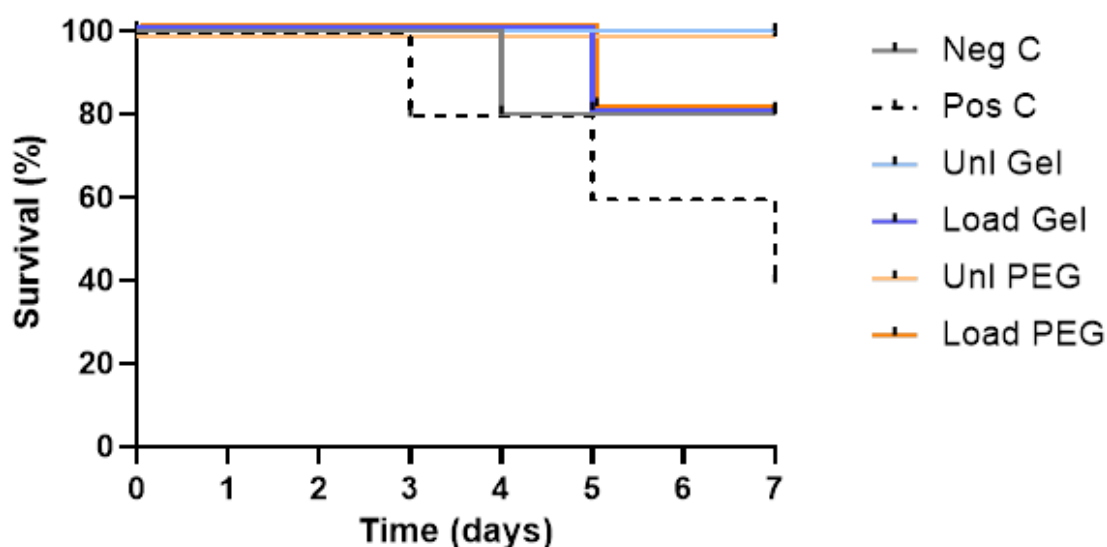


**Figure 6.14:** Animal survival and mortality curves of mice bearing LLC1 tumours following the retro-orbital administration of the vehicle (**Neg C**), PTX (**Pos C**), MSNs-GEL (**Unl Gel**), MSNs-PEG (**Unl PEG**), MSNs+PTX-GEL (**Load Gel**) and MSNs+PTX-PEG (**Load PEG**). The *in vivo* experiments were carried out by Dr Maria Manuela Jesus Guilherme Gaspar; the results were analysed by the candidate.
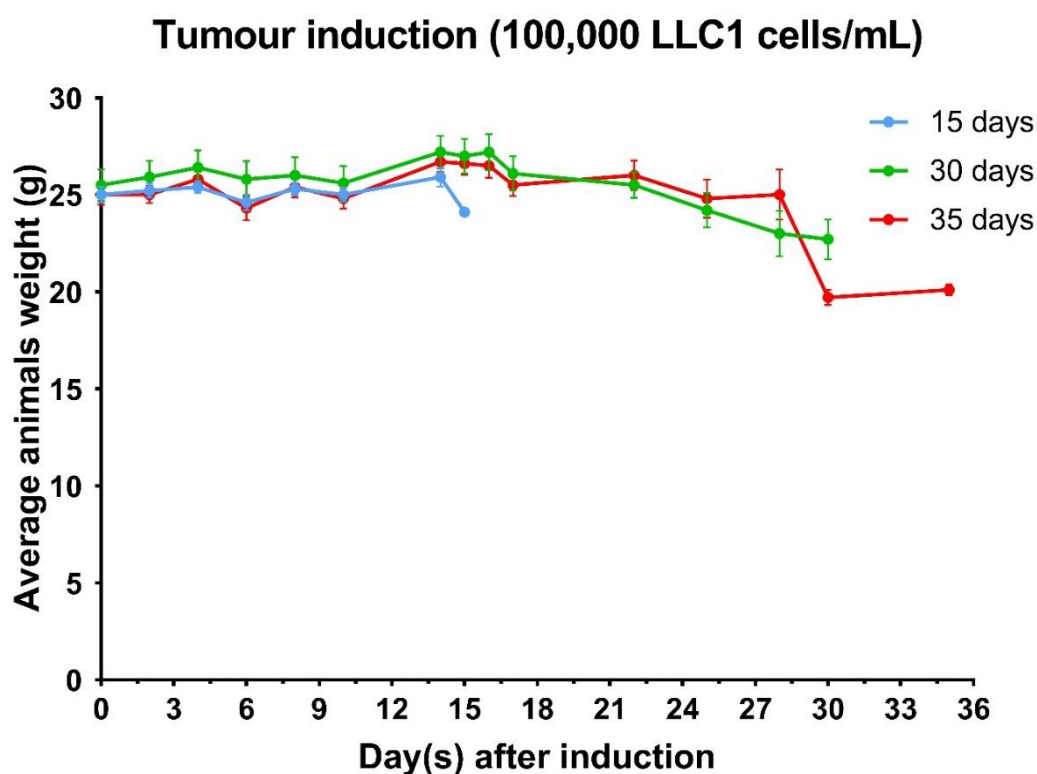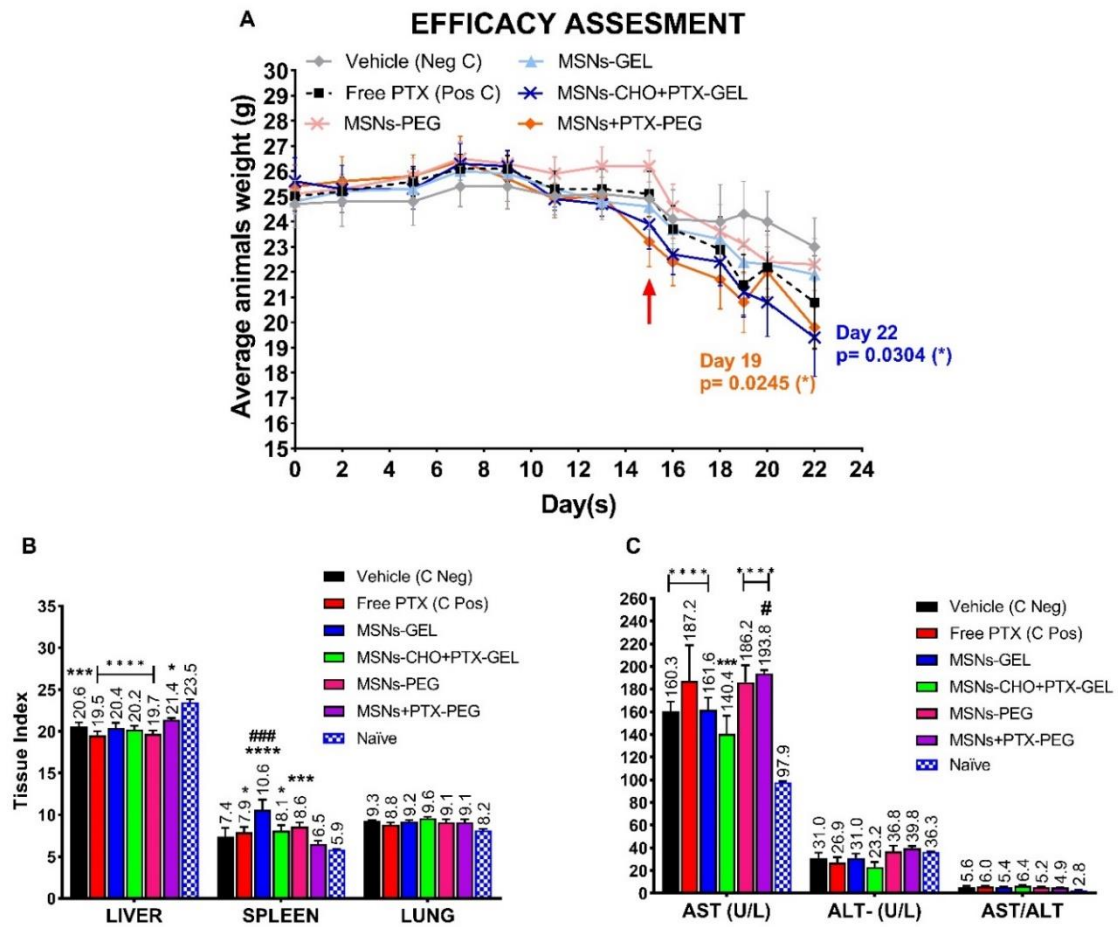
**Figure 6.15: A-** Mice body weight evolution over 22 days after the animals received 200,000 LLC1 cells/mL retro-orbitally (**Day 0**), and the different treatments (**red arrow, day 15**). **B-** Tissue indexes of tumour induced mice after retro-orbital administration of vehicle (Neg C), free drug (Pos C), PEG- and GEL-functionalised NPs both loaded and unloaded, and naïve animals (no tumour induced mice from safety assessment). **C-** Biochemical data from serum analysis of tumour induced mice and naïve animals (no tumour induced mice from safety assessment) after being euthanised. (mean±SEM) The *in vivo* experiments were carried out by Dr Maria Manuela Jesus Guilherme Gaspar; the results were analysed by the candidate. Statistical test: Two-way ANOVA with Dunnett's post-test comparing all treatments versus the negative control (vehicle). n=5 (mice per group), p ≤ 0.05 (#), p ≤ 0.001 (###). Two-way ANOVA with Dunnett's post-test comparing all treatments versus the naïve animals (no tumour induced mice from safety assessment). n=5 (mice per treatment group), n=6 (naïve), p ≤ 0.05 (*), p ≤ 0.001 (***), p ≤ 0.0001 (****)

### 6.3.1 Conclusions

The preliminary *in vivo* studies conducted in C57/BL6 mice with empty NPs yielded positive results in terms of tolerability to the MSNs-PEG, with no significant toxic effect observed. On the other hand, MSNs-GEL exhibited a toxic effect, particularly towards the lungs, possibly due to their accumulation that, based on data available from previous reports, may result in increased oxidative stress.

The results from the *in vivo* efficacy studies indicated that the PTX-loaded NPs were capable of delivering the drug to the tumour site, improving the survival rates when compared to the positive control group (free PTX). The drug delivery with MSNs resulted in a reduction of the toxicity associated with PTX and its vehicle CrEL, commonly used to solubilize PTX for intravenous administration, and also associated with lower bioavailability of the drug in the free form.

Moreover, with the administration of a reduced weekly dose of the PTX-loaded MSNs, no significant signs of toxicity were observed in the analysed vital organs, which was attributed to a lower accumulation of the NPs. Nevertheless, histological analysis will provide a more detailed understanding of the observed results.

.

# 7 CHAPTER 7: *Ex vivo* studies: Hemocompatibility

Understanding the effects of MSNs on blood components is crucial since, although the clinical use of these nanocarriers might most likely include intravenous injections, independently of their route of administration, and mainly due to their small size, they will reach the bloodstream.

Of all withdrawals reported to the FDA, undesirable effects on the blood system account for 11% of the total. [572] Blood compatibility is an important consideration for the safe administration of drug-loaded NPs. While in the circulation, NPs come into contact with a complex physiological milieu (blood cells, proteins, lipoproteins, as well as elements of the coagulation system) and pathophysiological processes can be triggered by interactions with these components. For example, the interaction of nanomaterials with platelets and coagulation factors can potentially lead to thrombi formation and severe side effects, such as thrombosis or embolism, which can be life-threatening. In particular, because of the high surface-to-volume ratio of nanoscale carriers, the degree of contact and their potential harmful repercussions can be greatly intensified. [573, 574]

Urbán P., N.J. Liptrott and S. Breme [573] conducted a comprehensive review of the literature to assess the blood toxicities associated with nanocarriers including lipid-based, polymer-based, and inorganic NPs. They found that a total of 46 papers (out of 147 screened) reported *in vivo* blood toxicities and 153 (out of 515) reported *in vitro* blood incompatibility. Thrombosis was found to be the most frequently observed side effect during preclinical assessment of nanomedicines *in vivo*, accounting for 61% of reported incidents. The remaining reports were linked to changes in haematology (including alterations of complete blood count, leukocyte activation, and haemolysis) and complement activation. Regarding *in vitro* blood toxicities, 23% were caused by platelet disfunction, and 15% were related to unbalanced coagulation processes. The authors reported that the majority of the unwanted effects in both *in vivo* and *in vitro* tests were caused by inorganic NPs, with the main adversities being thrombosis *in vivo* and imbalances in the coagulation cascade and defects in platelets function *in vitro*.

## 7.1 Interaction of Nanoparticles with platelets and plasma proteins

Haemostasis is derived from the Greek words "haem" (blood) and "stasis" (to stop). Haemostasis is an important mechanism that serves to preserve the circulatory system's integrity by preventing blood loss after injury. Platelets are small, disc-shaped elements that circulate in the blood (in quiescent state in the absence of stimuli) and play a crucial role in haemostasis. Platelets become activated when a blood vessel is damaged and adhere to the site of injury, generating a platelet clog. This initial response is essential to prevent blood loss but requires as well of the activation of the coagulation cascade to stop the bleeding. On the other hand, the human body's aggregation and coagulation processes are meticulously regulated by a complex system where antiaggregating, anticoagulant and fibrinolytic factors work together to prevent excessive clotting and the spreading of thrombi. Endothelial cells, which line the inside of blood vessels, also play an important part in haemostasis regulation by releasing factors that limit and/or promote platelet activation and coagulation. When, for example, the activity of coagulation factors is increased, or the activity of naturally occurring inhibitors is decreased, this delicate equilibrium is disrupted, and it can lead to either bleeding disorders or thrombotic disorders. [575-579]

There are studies [245, 328, 580-583] which report that nanomaterials have the potential to quickly interact with platelets and endothelial cells, leading to platelet aggregation and thrombosis. [298]

### 7.1.1 Light transmission aggregometry (LTA)

The potential impact of different MSNs concentration on platelets' function was investigated using light transmission aggregometry.

Light transmission aggregometry (LTA) is a widely used technique for measuring platelets function by recording changes in light transmission after the addition of agonists to platelets under stirring (**Fig. 7.1**). The light aggregometer

has traditionally been regarded as the gold standard for measuring platelet function. However, this technique has certain limitations that can affect its ability to accurately replicate platelet behaviour *in vivo*. Since platelets are stirred to keep them in suspension, the interactions between them are influenced by fluid mechanical shear stress. The platelet suspension's shear stress, however, fluctuates constantly and is not representative of the shear rates found in arterial circulation. This can affect the interactions between platelets and lead to differences in platelet aggregation compared to what occurs *in vivo*. Additionally, platelets are stirred at low shear and only aggregate once agonists are added, which does not closely resemble platelets adhesion, activation, and aggregation in the organism. Lastly, LTA may not be able to detect the microaggregates formation that precede the generation of larger platelets thrombi. [579]
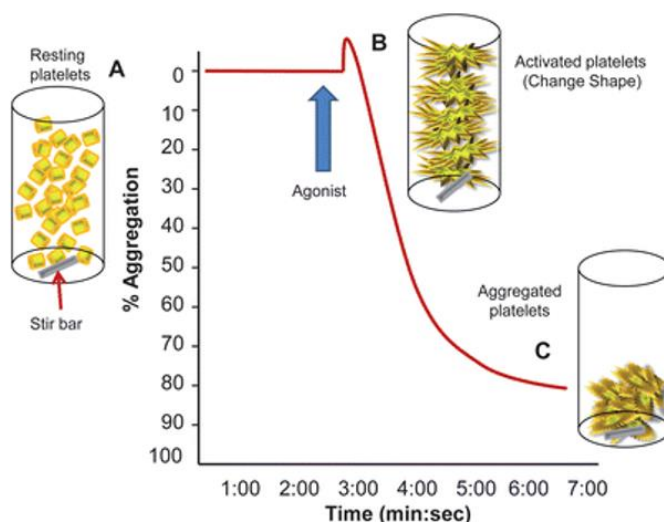


**Figure 7.1:** Fundamentals of light transmission aggregometry used to examine platelets function. **A-** In the absence of aggregation, platelets rich plasma results in 0% light transmission (baseline). **B-** When platelets are activated, the resulting change in shape causes a brief reduction in light transmission. **C-** In the presence of platelets aggregation, the instrument detects an increase in light transmission and calculates the percentage of aggregation. (*Used with permission of Royal Society of Chemistry. Permission conveyed through Copyright Clearance Center, Inc.*) [579]

For evaluating the potential effect that the developed NPs could exert on platelet function, platelet rich plasma (PRP) was incubated in an aggregometer in the presence and absence of bare, PEG- and GEL-functionalised MSNs and their effect of platelet aggregation recorded for 30 minutes.

The overall results obtained from LTA assays (**Fig. 7.2 A** and **B**), indicated that any of the NPs at the concentrations tested, with the exception of GEL-functionalised MSNs at 100 µg/mL, induced significant changes in platelet aggregation when compared to stirred PRP. Therefore, further investigations on gelatine-containing NPs' platelet activation need to be conducted to confirm the absence of a significant thrombogenic activity, especially at higher concentrations, since the amounts used for the *in vivo* studies (the single daily injections) of MSNs-GEL were higher (around 200 µg/mL, see **Appendix 4**) than the highest concentration tested with LTA.

Our results are in line with what has been previously reported in the literature. In their work Yildirim A., E. Ozgur, and M. Bayindir [575] demonstrated that MSNs with different surface properties did not induce platelet activation at concentrations up to 1 mg/mL. The group explained that the fact that the particles were suspended in PBS before being in contact with the platelets, resulted in the medium filling the NPs' pores and therefore significantly diminishing their adsorption capacity when compared to the same in the dry state. [298, 584-587]
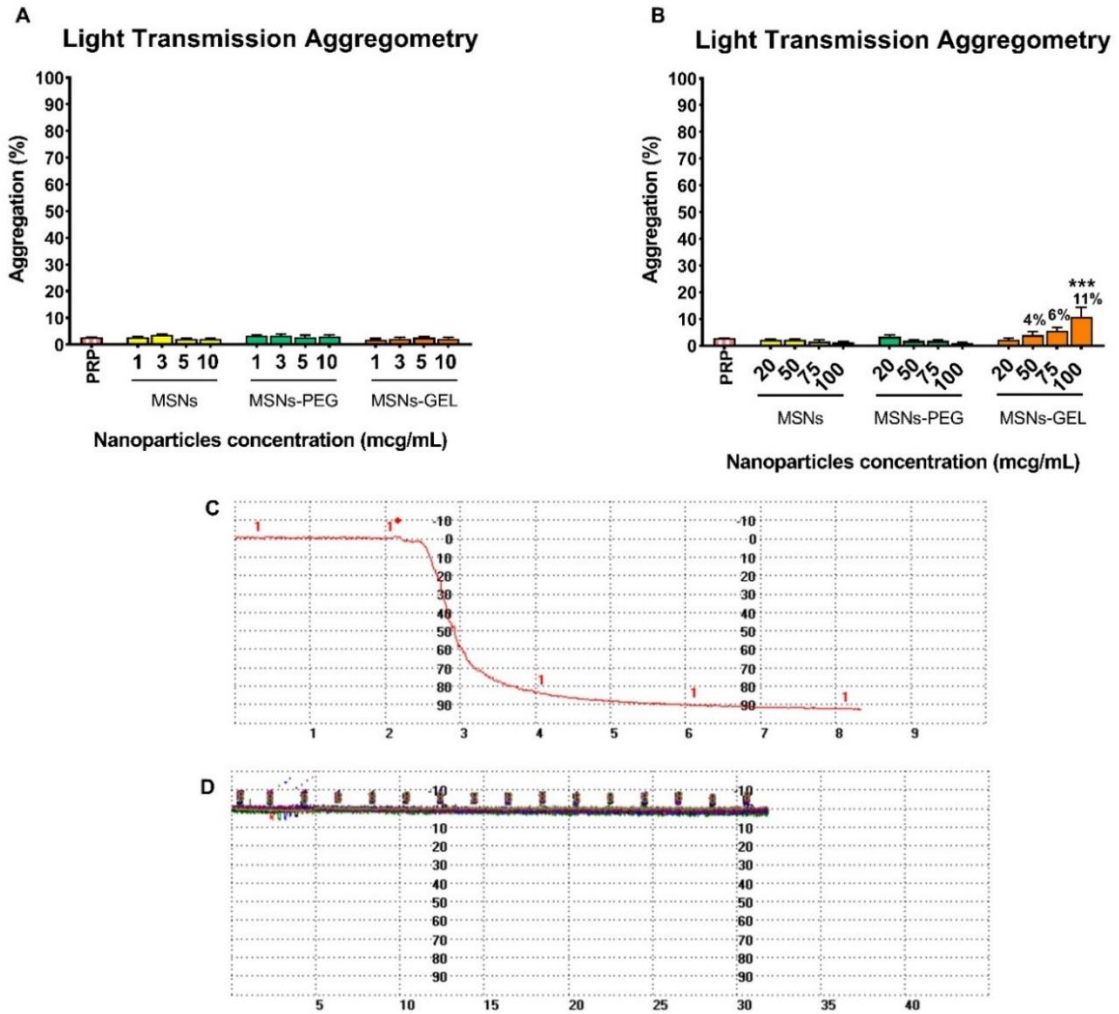
**Figure 7.2:** Light transmission aggregometry **A-** and **B-** Statistical analysis of the interactions between different concentrations of bare, PEG- and GEL-functionalised MSNs, and platelets. **C-** and **D-** Representative traces from collagen + PRP and MSNs + PRP, respectively, from LTA. Collagen was used to confirm that platelet function was preserved after preparation for all the donors tested. Platelet rich plasma (PRP) under stirring was used as control. (mean±SEM) Statistical test: Two-way ANOVA with Dunnett's post-test; n=4 (MSNs and MSNs-PEG), n=7 (MSNs-GEL); $p \leq 0.001$ (***) vs PRP.

## 7.1.2  Quartz Crystal Microbalance with Dissipation (QCM-D)

Results obtained from light transmission aggregometry studies demonstrated that, except for the gelatine-functionalised NPs at the highest concentration tested, the developed NPs did not induce significant platelet aggregation. However, as already mentioned, LTA is not performed under flow conditions and its sensitivity is not enough to detect microaggregates. [328, 579]

Quartz Crystal Microbalance with Dissipation (QCM-D) was then used to investigate the potential effect of the NPs on the formation of platelet micro-aggregation under flow conditions that mimic more closely the ones encountered in the human microvasculature.

QCM measures the mass of a substance bound to the surface of a quartz crystal by detecting the resonance frequency of the crystal, induced by applying an alternating electric field. When a substance binds to the crystal surface, there is an increase in mass that causes a negative shift in the oscillation frequency ($f$), which is proportional to the mass of the material deposited. In this regard, QCM can detect changes in mass with nanogram sensitivity when the layer deposited is very thin and rigid. However, when a soft or thick layer binds to the crystal surface, it causes a dissipation ($D$) shift, and its magnitude depends on the viscoelasticity of the film. Therefore, by simply measuring $f$, the mass deposited on the sensor might be underestimated, especially when investigating platelets aggregation where a thick and viscoelastic layer can be formed on the surface of the sensor. For this reason, using a QCM-D, where it is possible to simultaneously monitor both $f$ and $D$ parameters in real time (**Fig. 7.3**), platelet microaggregates can be detected and therefore, the effect of NPs on platelet aggregation measured with higher sensitivity. [328, 576]
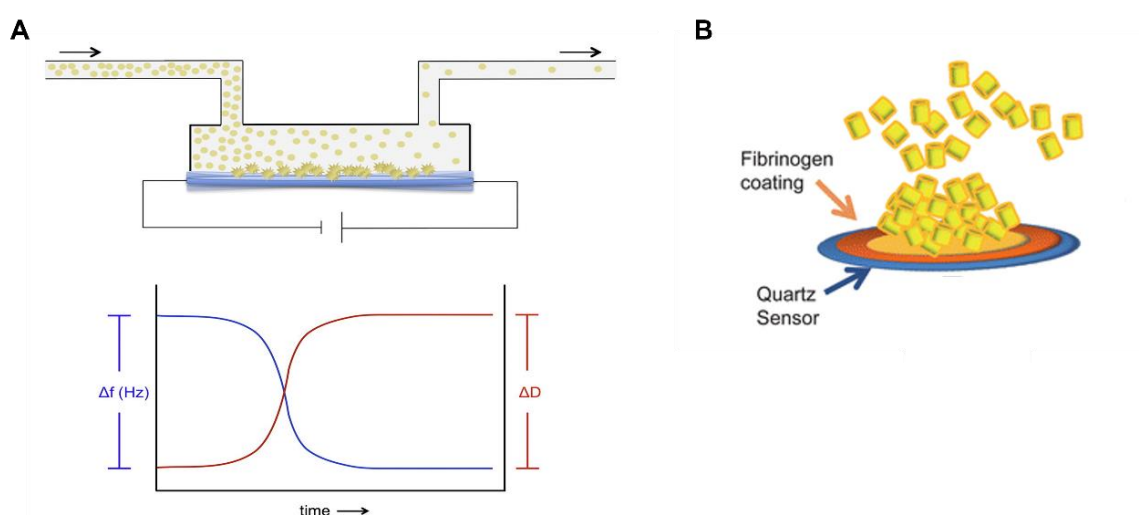


**Figure 7.3: A-** Platelet aggregation on a QCM-D sensor and graphical output described in terms of changes in frequency and energy dissipation over time. *(Adapted from Nanomedicine: Nanotechnology, Biology and Medicine, 2015. 11(1): p. 39-46, with permission from Elsevier)*. **B-** Representation of the deposition of microaggregates on the quartz sensor surface. (*Adapted from Analyst, 2011. **136**(24): p. 5120-5126 and used with*

PRP and PPP in the presence and absence of NPs were perfused on fibrinogen coated crystals as previously described [328, 329] using a QCM-D and changes in *f* and *D* recorded for 30 minutes.

Preliminary investigations using this method, seems to demonstrate that the interactions between bare MSNs and PEG-functionalized MSNs with human platelets at 100 µg/mL under flow conditions do not lead to an increase in platelet accumulation on the surface of the crystals. In fact, when compared to the control (PRP), it seems that less platelet aggregates are deposited on the crystals' surface (**Fig. 7.4 A** and **B**, **Fig. 7.5**, **Fig. 7.6)**.
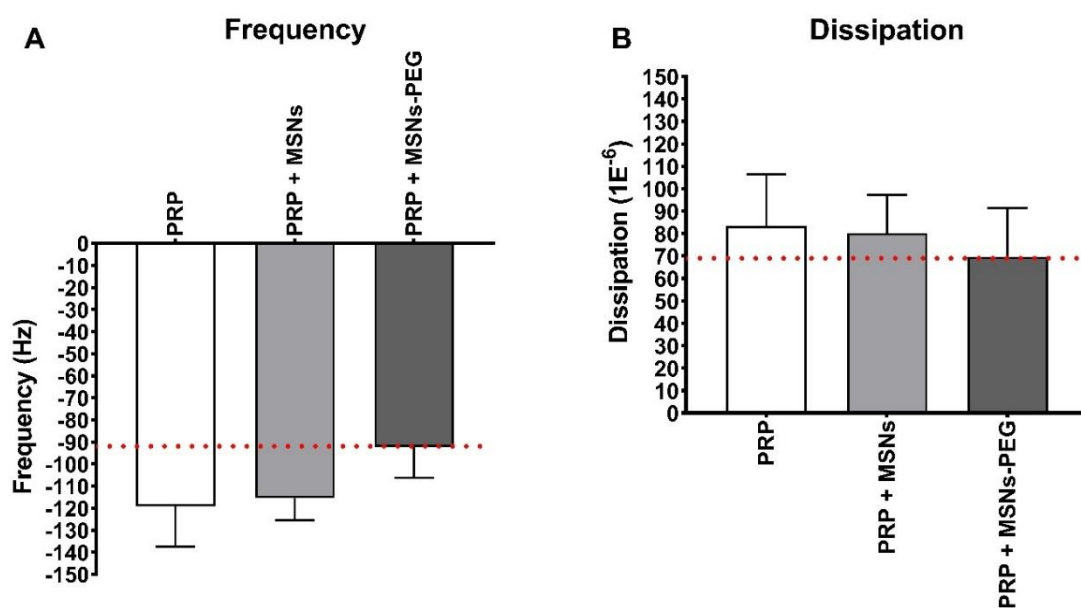


**Figure 7.4:** Quartz crystal microbalance with dissipation. Effects of MSNs and MSNs-PEG on platelet aggregation (PRP). Quantitative analysis of the effect of MSNs and MSNs-PEG on **A-** PRP frequency *f*; **B-** PRP energy dissipation *D*. Data is presented as mean±SEM of 3 independent experiments for MSNs-PEG, and 2 experiments for bare MSNs.
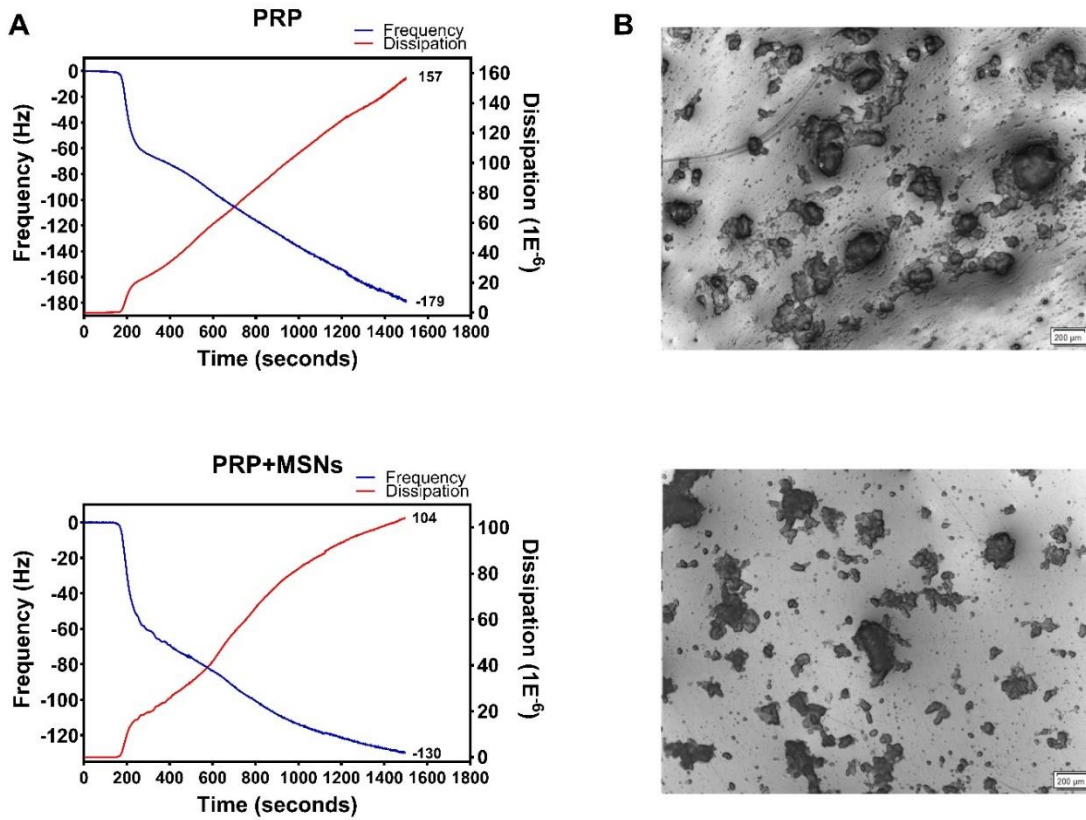
**Figure 7.5: A-** and **C-** Effects of MSNs on platelet aggregation. Traces for frequency *f* and energy dissipation *D* (from the third overtone) recorded by the device from one of the experiments. Frequency is represented as a blue line and its values shown in the left axis. Energy dissipation is represented as a red line and its values are shown in the right axis. PRP: platelet rich plasma. **B-** and **D-** Representative micrographs of the surface of fibrinogen-coated PC-quartz crystals as viewed by optical microscopy (5x objective) taken at the same time-point (after 30 minutes of PRP and PRP + MSNs perfusion). The perfusion of PRP in the presence of MSNs revealed the presence of platelet aggregates similar/smaller to those of the control (PRP).
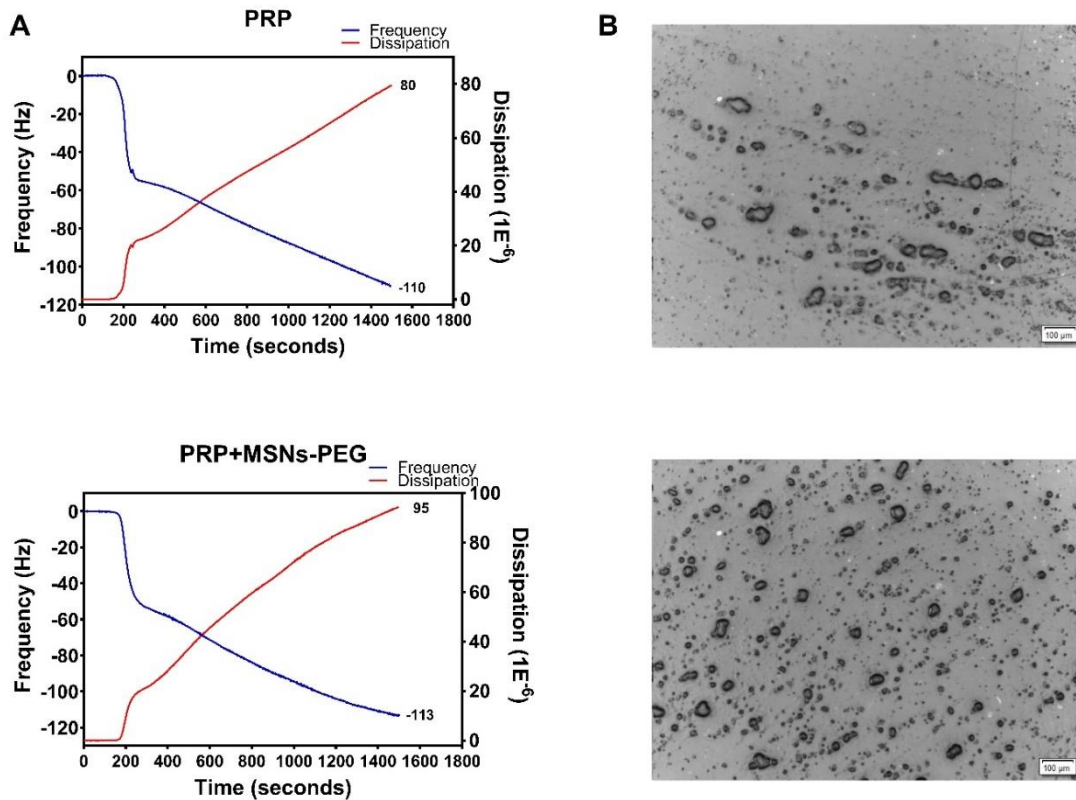
**Figure 7.6: A-** and **C-** Effects of MSNs-PEG on platelet aggregation. Traces for frequency *f* and energy dissipation *D* (from the third overtone) recorded by the device from one of the donors. Frequency is represented as a blue line and its values shown in the left axis. Energy dissipation is represented as a red line and its values are shown in the right axis. PRP: platelet rich plasma. **B-** and **D-** Representative micrographs of the surface of fibrinogen-coated PC-quartz crystals as viewed by optical microscopy (5x objective) taken at the same time-point (after 30 minutes of PRP and PRP with MSNs-PEG perfusion). The perfusion of PRP in the presence of MSNs-PEG revealed the presence of platelet aggregates similar to those of the controls (PRP).

Platelet poor plasma was also perfused through the system, in the presence and in the absence of bare and PEG-functionalized NPs, in order to confirm that the changes observed in f and D were not only attributed to NPs interactions with plasma proteins (**Fig. 7.7 A** and **B, Fig. 7.8**).
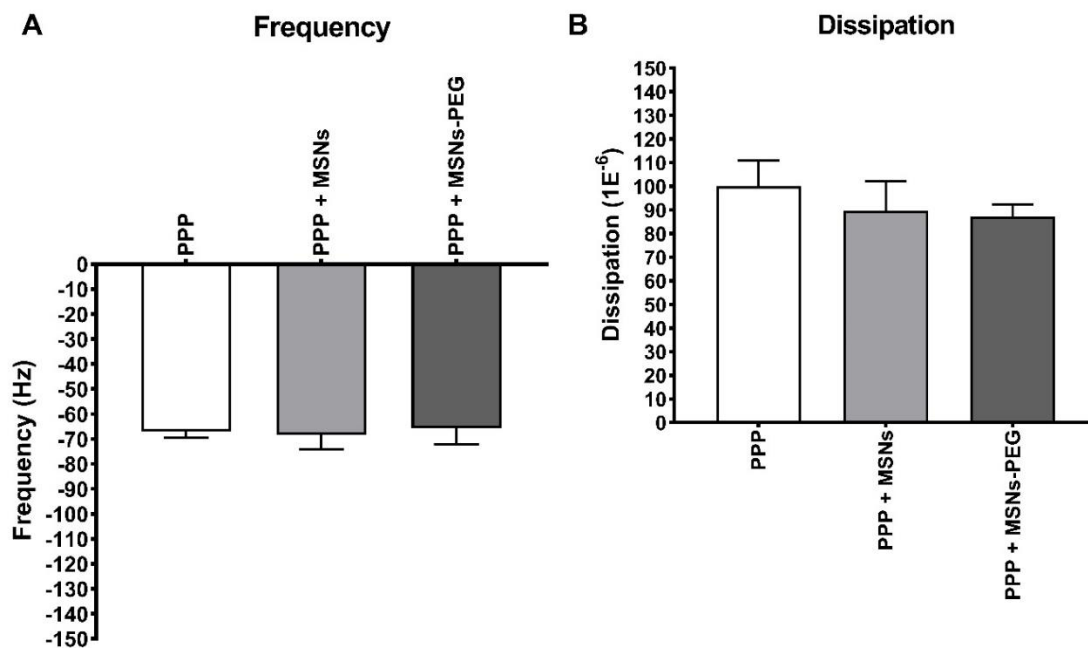
**Figure 7.7:** Quartz crystal microbalance with dissipation. Effects of MSNs and MSNs-PEG on deposition of plasma protein (PPP). Quantitative analysis of the effect of MSNs and MSNs-PEG on **A-** PPP frequency *f*; **B-** PPP energy dissipation *D*. Data is presented as mean±SEM of 3 independent experiments for MSNs-PEG, and 2 experiments for bare MSNs.
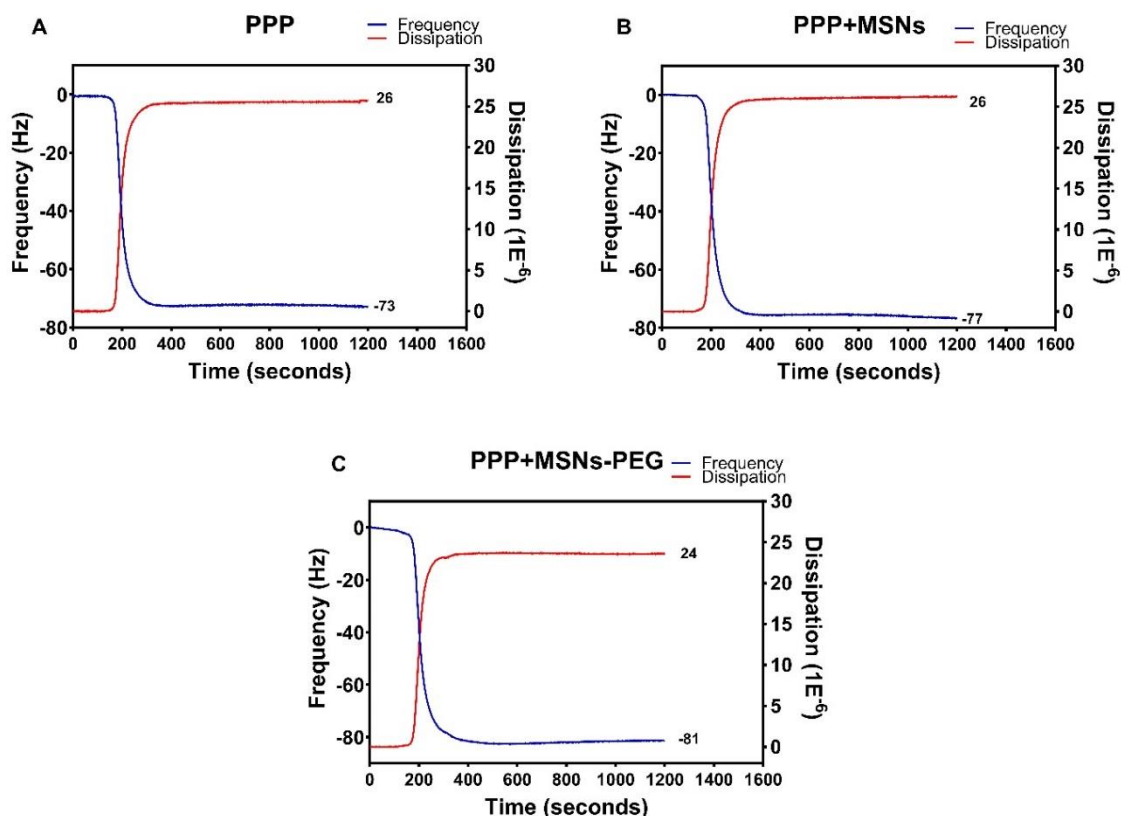
**Figure 7.8:** Effects of MSNs and MSNs-PEG on deposition of plasma proteins. Representative traces for frequency *f* and energy dissipation *D* (from the third overtone) recorded by the device. Frequency is represented as a blue line and its values shown in the left axis. Energy dissipation is represented as a red line and its values are shown in the right axis. PPP: platelet poor plasma.

These results suggest that bare and PEG-functionalized MSNs are blood compatible at the concentrations tested, in agreement with the LTA studies. However, more research is needed in order to carry out statistical analysis and confirm those preliminary results. In addition, experiments for investigating the effect on platelet aggregation induced by GEL-functionalised NPs at the concentrations which have been detected to induce a 11% increase of platelet aggregation with LTA are also warranted.

The research conducted by Santos-Martinez M.J. *et al.*, [328] aimed to evaluate the potential of QCM-D as a method for measuring interactions between NPs and platelets. Specifically, they investigated the interactions of silica and polystyrene NPs of different sizes and concentrations, as well as gold NPs, with

platelets. The researchers compared QCM-D with conventional techniques such as light aggregometry and flow cytometry, to determine whether QCM-D could provide greater sensitivity in detecting platelet aggregation induced by NPs. In their study, platelet aggregation was observed through aggregometry only for the smallest silica NPs (10 nm) at a concentration of 200 µg/mL. However, when QCM-D was used, the researchers observed an increase in dissipation and a decrease in frequency for all NPs and concentrations tested. Based on the results of their study, the group concluded that QCM-D is a viable and sensitive tool for detecting NPs-induced platelet aggregation, surpassing the effectiveness of the other mentioned techniques. In another study, the same group [589] used QCM-D to assess the pharmacological pathways and regulators of NP-induced platelet micro aggregation comparing the results to those obtained by LTA. The effects of silica NPs (10 and 50 nm) and polystyrene NPs (23 nm) were studied, and the results indicated that, when analysed by LTA, none of the NPs used caused platelet aggregation at the concentrations tested in PRP. However, when QCM-D was employed, platelet micro aggregation was induced by all three types of NPs, at concentrations that were not detectable by LTA. These findings suggested once again that QCM-D exhibits greater sensitivity in assessing platelet aggregation in response to NPs compared to LTA.

## 7.2 Interaction of Nanoparticles with red blood cells

### 7.2.1 Haemolysis

Haemolysis involves the deformation of red blood cells' membrane followed by their disintegration and release of their content. It has been previously described that nanomaterials of different compositions can induce haemolysis and lead to deleterious effects. [590-595] Therefore, it is of great importance to confirm that NPs developed for human use do not disrupt red blood cells membrane.

MSNs can cause haemolysis, and several explanations have been proposed to understand the possible mechanisms underlying this effect: [312, 575, 596]

1) The generation of ROS induced by silica. [597]

2) The denaturation of the proteins of the RBC membrane by electrostatic interactions with silicate. [598]

3) The binding affinity of silicate for the positively charged tetraalkylammonium-containing phospholipids abundant in the RBC membrane. [599-601]

A haemolysis assay, based on the measurement of Hb release, was used to determine the potential toxicity of the different MSNs on RBC.

From the results obtained in our study (**Fig. 7.9 A** and **B**) no significant haemolytic activity was observed for the different concentrations of the different MSNs tested. The highest level of haemolysis was recorded for bare MSNs at the highest concentration (100 μg/mL) and equal to 8.1 ± 1.3%. This is in line with what has been previously reported in the literature. Lin Y.-S. and C.L. Haynes [306] reported that nonporous silica NPs caused haemolysis of RBC, which was dose and size dependant, with smaller NPs being more toxic, due to a higher surface area and so displaying more silanol groups. However, MSNs showed a lower haemolytic activity and the authors concluded that the pores' structure can influence the toxicity towards red blood cells. The group demonstrated that the collapse of the pores inside the porous silica NPs after aging in PBS increased the haemolytic activity of the particles, supporting the hypothesis that the pores' structure may play a role in RBC toxicity. Zhao Y. with colleagues [307] investigated the haemolytic activity of MCM-41 and SBA-15 type of MSNs. In this case, they reported that bigger particles (SBA-15 with an average hydrodynamic size of 531 nm) showed higher toxicity towards red blood cells, than smaller ones (MCM-41 with an average hydrodynamic size of 122 nm). Both particles were found to adsorb to the surface of the RBC, but only SBA-15 MSNs lead to a higher local membrane deformation with spiculation, more particles internalization and consequently lysis. To explain these findings, the authors hypothesized that the adsorption of NPs to RBC is governed by two conflicting mechanisms. The first is the release of energy occurring when MSNs surface silanol groups bind to RBC membrane phosphatidylcholine groups; when the cells bind larger MSNs, with greater exterior surface areas, they release more binding energy than smaller ones with smaller

external surface areas. The second is the bending energy required to wrap the MSNs by RBC membranes. Since the flat cell membrane must undergo more changes in orientation to fit smaller particles than bigger ones, this process demands a greater degree of bending energy for smaller particles. Combined, these two processes explain why it was more thermodynamically advantageous to assimilate bigger SBA-15 MSNs, with an exterior surface area of 155.4 $m^2/g$, than smaller MCM-41 MSNs, with an external surface area of 81.6 $m^2/g$. [298, 575]
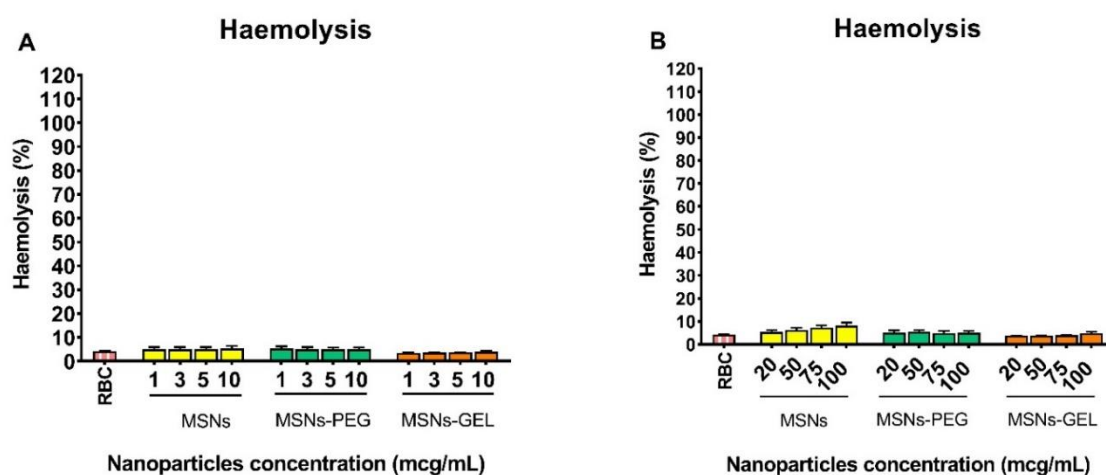


**Figure 7.9: A-** and **B-** Statistical analysis of the effect of bare, PEG- and GEL-functionalised MSNs on red blood cells. Triton X was used as a positive control for red blood cells lysis and taken as 100% of haemolysis. Red blood cells (RBC) in the absence of NPs were used as control. Data is presented as mean±SEM. Statistical test: Two-way ANOVA with Dunnett's post-test; p=0.8994; n=5 (MSNs and MSNs-PEG), n=3 (MSNs-GEL).
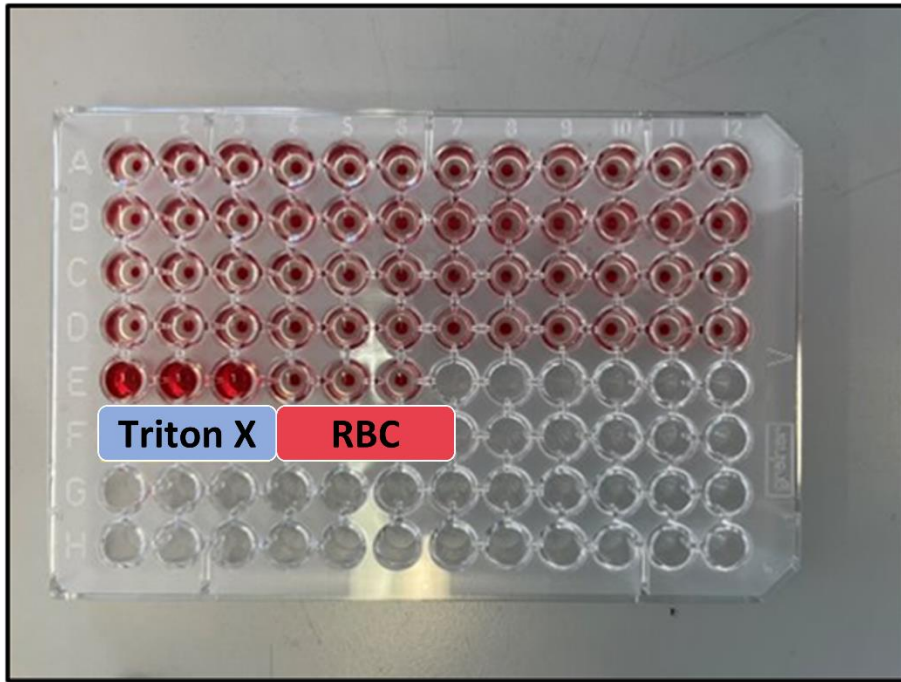
**Figure 7.10:** Photograph of the plate containing RBC treated with MSNs and MSNs-PEG at different concentrations. The released haemoglobin from the damaged cells can be seen from the RBC treated with Triton X, while RBC treated with the NPs look like the negative control (RBC).

## 7.2.2 Conclusions

The preliminary data obtained following the exposure of platelets to MSNs and MSNs-PEG NPs seem to indicate that those NPs do not interfere with platelet function. Neither light transmission aggregometry nor quartz crystal microbalance with dissipation detected platelet aggregation, but more experiments are required for confirming those results.

Gelatine-functionalised MSNs showed significant platelet aggregation at the highest dose tested with LTA, which requires further investigation.

No haemolysis was detected for any of the NPs at the different concentrations tested, confirming that the developed MCM-41 are not toxic towards red blood cells.

# 8   CHAPTER 8: GENERAL CONCLUSIONS AND FUTURE WORK

## 8.1   General conclusions

The central focus of the present study was to develop biocompatible NPs using mesoporous silica as delivery system for contrast agents and/or chemotherapeutic drugs. The goal was to create a library of NPs that can be used to enhance the diagnosis and treatment of various types of cancer using for this purpose lung cancer as a model.

The main objective was to develop nano-systems able to detect abnormal cells with high specificity and sensitivity. In fact, by developing a stimuli-responsive drug delivery system capable of responding quickly to the presence of known specific tumour biomarkers by releasing the loaded cargo, it would be possible to either detect (contrast agent) or treat (chemotherapeutic drug) cancer while avoiding non-targeted cytotoxic drug release.

Overall, the development of biocompatible NPs using mesoporous silica as a delivery system has the potential to significantly improve current detection methods and the efficacy of chemotherapeutic treatments.

### 8.1.1   CHAPTER 3: MESOPOROUS SILICA NANOPARTICLES AS TRIGGERED DRUG DELIVERY SYSTEM

- Multiple batches of MCM-41 type of MSNs were successfully synthesised validating the advantageous physical-chemical properties stated in the literature for this class of materials, including:
    i.   a large surface area (700-1000 $m^2/g$)
    ii.  honeycomb-shaped, uniform pores that are unidirectional and have an average diameter of 2.5 nm, and a volume ranging from 0.6 to 0.9 $cm^3/g$.

- Batches of NPs were synthesised in a reproducible manner by maintaining certain variables constant such as the type of glassware, stirring rate, temperature, pH, and rate of addition of the silica source.

- The resulting particles showed good dispersibility in aqueous solvent, which was further improved after functionalization.

- The NPs were successfully functionalised with either a layer of poly-(ethylene glycol) (PEG)  or gelatine (GEL), proving the possibility of tuning the particles' surface.

- The efficient loading of both paclitaxel (PTX) (25% loading capacity) and doxorubicin hydrochloride (DOX) (16% loading capacity) into the nanocarrier's pores, supported the efficient encapsulation and high loading capacity properties of MSNs, confirming the drug delivery system's ability to encapsulate both hydrophobic and hydrophilic molecules. However, when aldehyde-functionalized NPs were used, the loading capacity was lower than that of the bare MSNs (PTX 12%, DOX 7%); this was explained by the presence of aldehyde groups on the external surface and inside the pores, hindering the loading of the drugs, but confirming the presence of a tuneable outer NP surface and pore channels.

- The responsiveness of the PEG and GEL coating layers to the presence of glutathione (GSH) or Matrix Metalloproteinases (MMPs), respectively, proved the successful development of a stimuli-responsive drug delivery system that could react instantly to the presence of known specific triggers or tissue biomarkers. We showed that both polymers effectively protected the cargo from premature release by capping the pores of the silica structure. The PEG layer, linked to the surface of the MSNs by disulphide bonds, was promptly disrupted in the presence of the reductive agent GSH, allowing for the opening of the pores, and consequently the release of the cargo. Similarly, the GEL shell covering the MSNs was able to protect the cargo until in the presence of MMPs the gelatine layer was digested, exposing the drug allowing its release. Overall, we demonstrated that both systems are an excellent example of a stimuli-responsive drug delivery

system that can be used to target specific areas of the body, such as tumours, allowing for a more selective and effective drug delivery.

### 8.1.2  CHAPTER 4: *In vitro* cell studies

- *In vitro* cytotoxicity tests were used to investigate the compatibility of empty NPs and the cytotoxic effect of PTX-loaded NPs against human (A549) and murine (LLC1) lung cancer cell lines. We demonstrated that aldehyde- (CHO) and GEL-functionalised MSNs were well tolerated by both A549 and LLC1 cells, whereas bare and PEG-functionalized NPs presented some toxicity. LLC1 cells appeared to be more resistant towards silica, with lower viability loss.

- The selectivity of the stimuli-responsive systems was confirmed, after performing *in vitro* release studies, and during *in vitro* cytotoxicity assays: the results showed that the drug-loaded NPs effectively released the drug and killed the cancer cells, as evidenced by a decrease in cell viability. However, the observed cytotoxic effect could not be solely attributed to the release of the drug from the NPs due to the intrinsic toxicity of MSNs.

  i.   In A549 cells the PEG-functionalised NPs confirmed their ability to prevent a burst release, as opposed to cells treated with unfunctionalized NPs where cells viability decreased quicker. The cytotoxic profiles of aldehyde- and GEL-functionalised NPs were comparable, indicating that the GEL layer on the surface of the particles was easily removed. Nonetheless, the selectivity of the stimuli responsive system was proven for both.

  ii.  LLC1 cells were more resistant to PTX-loaded MSNs and MSNs-PEG than A549 cells, with higher concentrations of bare and functionalised loaded MSNs needed to have a harmful impact. LLC1 cells tolerated empty aldehyde- and GEL-functionalized NPs well, and drug release was validated by a decrease in cell viability that was time and concentration dependent. Nonetheless, the cells demonstrated some level of resistance, with their viability being

higher when compared to the ones of A549 cells treated with the same NPs at equal concentrations.

- Flow cytometry and confocal microscopy were used to verify the NPs' cellular uptake by both cell lines. Flow cytometry data indicated that A549 cells internalised more NPs than LLC1. However, LLC1 cells showed an increasing fluorescence intensity over time, whereas the fluorescence decreased over time in the human cell line. It was hypothesised that, due to the higher internalization in A549 cells, 1) a higher interaction between the NPs and the cell membrane could result in membrane lysis and a decrease in cell viability, or 2) the cells reached saturation and particles began to leave the cells, explaining the decrease in fluorescence intensity that was not seen with LLC1.

- MMPs production by A549 and LLC1 cells was verified by gelatine zymography. The enzyme activity was identified in the media from the cells incubated in the presence and in the absence of PMA, and the ability to concentrate the naturally occurring enzyme by repeated centrifugation cycles using protein concentrators was demonstrated. Based on the collected data, it was concluded that, under the same experimental conditions, LLC1 release higher levels of gelatinases than A549 cells. This finding could possibly explain the differences observed in the cytotoxic profiles of MSNs+PTX-PEG and MSNs-CHO+PTX-GEL NPs, which were more pronounced in LLC1 than in A549 cells. This difference was also reflected in the *in vitro* release profiles of GEL-functionalized NPs resuspended in the LLC1 and A549 conditioned media. The amount of MMPs collected in the media from both cell lines was found to be sufficient to conduct release assays with GEL-functionalized NPs, which confirmed further their ability to release their cargo in the presence of MMPs. This also demonstrated that enough concentrations of the enzymes could be obtained using routine laboratory procedures providing experimental conditions that may mimic, to some extent, the ones available in the tumour microenvironment.

### 8.1.3  CHAPTER 5: 3D cells culture *in vitro* studies

- A 3D model of glioblastoma multiforme, which was previously well established by our research group, was employed to evaluate NPs' killing and internalization capabilities in a system that can simulate better than a 2D model the *in vivo* conditions.

  i.  To investigate the potential toxic effect on GBM spheroids, NPs loaded with DOX (the model drug used in earlier toxicity studies with U-87 cells) and functionalised with either PEG or GEL were employed. The findings indicate that both NPs had a greater toxic effect than the free drug, most likely due to an enhanced particle uptake by the cancer cells, and a functional capping system which provided a prolonged release of DOX and its accumulation inside the tumour.

  ii. By confocal imaging the successful internalization and distribution of both types of NPs within the spheroids was confirmed.

Overall, these experiments provided a better understanding of the behaviour of the NPs in a more realistic environment by using a 3D model of glioblastoma multiforme, which can be used to predict how the system might behave *in vivo* once it reaches the tumour region.

### 8.1.4  CHAPTER 6: *In vivo* studies

- Preliminary *in vivo* studies were conducted in C57/BL6 mice in order to assess the safety of MSNs-PEG and MSNs-GEL. The NPs were administered by retro-orbital route at two different concentrations, corresponding to a total weekly dose of 2.5 and 8 mg/kg of PTX, for 2 weeks. The results highlighted that MSNs-PEG were well tolerated by the mice, with no significant toxic effect towards the main vital organs and kidney. MSNs-GEL, on the other hand, resulted in a higher toxic effect, with a significant increase of the lungs, spleen, and liver tissue indexes, indicating a possible

accumulation of the NPs causing an increase of oxidative stress and/or tissue inflammation.

- The *in vivo* efficacy studies demonstrated a higher survival in the group of mice treated with PTX loaded MSNs, when compared to the delivery of the free drug with the toxic CrEL, indicating an improved delivery of the drug to the tumour site.

- The administration of the loaded NPs for a shorter treatment time did not show significant signs of toxicity towards the main vital organs, indicating a possible lower accumulation of the NPs and, therefore, a lower tissue damage.

### 8.1.5  CHAPTER 7: *Ex vivo* studies: HEMOCOMPATIBILITY

- Preliminary studies were conducted in order to assess the blood compatibility of the developed NPs at different concentrations (from 1 to 100 µg/mL), by using two different techniques to evaluate platelets' function in the presence of NPs:
  i.  With light transmission aggregometry, no significant platelet aggregation was detected for any of the NPs tested, with the exception of GEL-functionalised NPs at the highest concentration (100 µg/mL), which induced a 11% increase in platelet aggregation over the control.
  ii. Neither bare, nor PEG-functionalized NPs promoted platelet aggregation when using a quartz crystal microbalance with dissipation. However, more research is needed to confirm those preliminary results and for evaluating the effect of GEL-functionalised NPs.

- The potential haemolytic effect of the different MSNs with red blood cells was also investigated. The findings showed that the NPs were compatible at all the concentrations tested.

Overall, these preliminary results demonstrated that the developed nano-systems are most likely blood compatible. However, further investigations will need to be conducted in order to confirm the obtained results and for addressing the questions raised during these experiments.

## 8.2 FUTURE WORK

1) In order to establish a reproducible loading protocol for hydrophobic molecules like PTX, it may be helpful to explore different methods for the loading of such molecules into the NPs and to optimize the parameters of the loading process, such as the solvent used and the duration of loading. This optimization process aims to obtain a lower variability between batches, as well as reducing the required therapeutic dosages for *in vitro* and *in vivo* studies thanks to a higher encapsulation efficiency.

2) In order to understand the release profile of PTX from our NPs *in vitro* release studies with the drug will need to be carried out.

3) To investigate the basal leaking of cargo from the capped nano-system, further studies should be conducted to identify the factors that contribute to this event and to develop strategies for minimizing it. For this purpose, it may be helpful to investigate the stability of the NPs over time and under different conditions.

4) Although for unravelling the effect of the NPs at cellular level and, for therefore carrying out further mechanistic studies, the use of FBS is not suitable, to better simulate the physiological conditions and determine if the presence of a protein corona on the surface of the NPs may modify their toxicity towards lung cancer cells, future *in vitro* cytotoxicity tests could be conducted after the incubation of NPs with relevant proteins or human plasma or in the presence of FBS.

5) Further investigations using QCM-D analysis need to be performed in order to confirm the effect that the functionalised MSNs may exert on platelet aggregation. Higher concentrations will need to be tested as well, considering the doses needed for the *in vivo* studies.

6) In the future, it would be beneficial to optimize a protocol for the creation of a 3D model of lung cancer. This would indeed provide a more accurate representation of the tumour microenvironment in lung malignancies, and it would aid in answering the questions raised by the *in vitro* tests using 2D models. (Furthermore, additional studies using the 3D model of GBM should be performed to evaluate the toxicity of empty NPs)

7) The nano-system selectivity will need to be tested using patient-derived samples in order to better predict their clinical outcome. By using patient-derived xenograft, the aim would be to preserve the heterogeneity and complexity of the original patients' tumour (genomic features including genetic mutations, gene expression patterns, and molecular characteristics), providing a more representative platform to investigate the tumour behaviour and response to treatments compared to traditional cell models.

8) Further *in vivo* efficacy studies of the loaded NPs will need to be performed in order to confirm the ability of the NPs to accumulate in the lung tumour region and effectively reduce the tumour mass. In addition, further functionalisation of the NPs and conjugation with particular ligands or antibodies for improving the targeting efficiency of the NPs and enhancing the therapeutic outcome could be also explored. It would be interesting to investigate the excretion routes of the particles as well as their biodistribution by using radio-labelled NPs.

# REFERENCES

1. Society, C.C. *Types of tumours* [cited 2022 September 26]; Home/Cancer information /What is cancer?/Types of tumours]. Available from: https://cancer.ca/en/cancer-information/what-is-cancer/types-of-tumours.

2. Institute, N.C. *What Is Cancer?* May 5 2021 [cited 2022 September 16]; Home > About Cancer > Understanding Cancer]. Available from: https://www.cancer.gov/about-cancer/understanding/what-is-cancer#:~:text=Pittsburgh%20Cancer%20Institute-,The%20Definition%20of%20Cancer,up%20of%20trillions%20of%20cells.

3. UK, C.R. *Types of cancer.* 2020 1 July 2020 [cited 2022 09 November]; Home>About> Cancer>What is cancer?>How cancer starts>Types of cancer]. Available from: https://www.cancerresearchuk.org/what-is-cancer/how-cancer-starts/types-of-cancer.

4. Nobili, S., et al., *Natural compounds for cancer treatment and prevention.* Pharmacological Research, 2009. **59**(6): p. 365-378.

5. WHO. *Cancer.* [cited 2022 3 February 2022]; Home/Newsroom/Fact sheets/Detail/Cancer]. Available from: https://www.who.int/news-room/fact-sheets/detail/cancer.

6. Chandra, A., *Overview of Cancer and Medicinal Herbs used for Cancer Therapy.* Asian Journal of Pharmaceutics (AJP), 2018. **12**(01).

7. World Health, O., *Global health estimates 2020: deaths by cause, age, sex, by country and by region, 2000–2019.* 2020, WHO Geneva, Switzerland.

8. Ferlay, J., et al., *Cancer statistics for the year 2020: An overview.* International Journal of Cancer, 2021. **149**(4): p. 778-789.

9. Sung, H., et al., *Global Cancer Statistics 2020: GLOBOCAN Estimates of Incidence and Mortality Worldwide for 36 Cancers in 185 Countries.* CA: A Cancer Journal for Clinicians, 2021. **71**(3): p. 209-249.

10. Kessenbrock, K., V. Plaks, and Z. Werb, *Matrix metalloproteinases: regulators of the tumor microenvironment.* Cell, 2010. **141**(1): p. 52-67.

11. Lemjabbar-Alaoui, H., et al., *Lung cancer: Biology and treatment options.* Biochimica et Biophysica Acta (BBA) - Reviews on Cancer, 2015. **1856**(2): p. 189-210.

12. Rosen RD, S.A. *TNM Classification.* 2022 17 February 2022 27 December 2022]; Available from: https://www.ncbi.nlm.nih.gov/books/NBK553187/.

13. de Groot, P.M., et al., *The epidemiology of lung cancer.* Translational Lung Cancer Research; Vol 7, No 3 (June 2018): Translational Lung Cancer Research (Lung Cancer Screening), 2018.

14. Zappa, C. and S.A. Mousa, *Non-small cell lung cancer: current treatment and future advances.* Translational lung cancer research, 2016. **5**(3): p. 288-300.

15. Mridha, M.F., et al., *A Comprehensive Survey on the Progress, Process, and Challenges of Lung Cancer Detection and Classification.* Journal of Healthcare Engineering, 2022. **2022**: p. 5905230.

16. Thandra, K.C., et al., *Epidemiology of lung cancer.* Contemporary oncology (Poznan, Poland), 2021. **25**(1): p. 45-52.

17. Dela Cruz, C.S., L.T. Tanoue, and R.A. Matthay, *Lung cancer: epidemiology, etiology, and prevention.* Clinics in chest medicine, 2011. **32**(4): p. 605-644.

18. Mattson, M.E., E.S. Pollack, and J.W. Cullen, *What are the odds that smoking will kill you?* American journal of public health, 1987. **77**(4): p. 425-431.

19. Alberg, A.J., et al., *Epidemiology of lung cancer: Diagnosis and management of lung cancer: American College of Chest Physicians evidence-based clinical practice guidelines.* Chest, 2013. **143**(5): p. e1S-e29S.

20. Peto, J., *That the effects of smoking should be measured in pack-years: misconceptions 4.* British journal of cancer, 2012. **107**(3): p. 406-407.

21. Health, U.S.D.o. and S. Human, *The health consequences of involuntary exposure to tobacco smoke: a report of the Surgeon General.* 2006, Atlanta, GA: US Department of Health and Human Services, Centers for Disease ….

22. Hackshaw, A.K., *Lung cancer and passive smoking.* Statistical Methods in Medical Research, 1998. **7**(2): p. 119-136.

23. Kim, A.S., et al. *Exposure to Secondhand Smoke and Risk of Cancer in Never Smokers: A Meta-Analysis of Epidemiologic Studies.* International Journal of Environmental Research and Public Health, 2018. **15**, DOI: 10.3390/ijerph15091981.

24. Schabath, M.B. and M.L. Cote, *Cancer Progress and Priorities: Lung Cancer.* Cancer Epidemiology, Biomarkers & Prevention, 2019. **28**(10): p. 1563-1579.

25. Simons, E., et al., *Maternal second-hand smoke exposure in pregnancy is associated with childhood asthma development.* The Journal of Allergy and Clinical Immunology: In Practice, 2014. **2**(2): p. 201-207.

26. Al-Sayed, E.M. and K.S. Ibrahim, *Second-hand tobacco smoke and children.* Toxicology and Industrial Health, 2014. **30**(7): p. 635-644.

27. Öberg, M., et al., *Worldwide burden of disease from exposure to second-hand smoke: a retrospective analysis of data from 192 countries.* The lancet, 2011. **377**(9760): p. 139-146.

28. Doll, R. and A.B. Hill, *Smoking and Carcinoma of the Lung.* British Medical Journal, 1950. **2**(4682): p. 739.

29. Wynder, E.L. and E.A. Graham, *TOBACCO SMOKING AS A POSSIBLE ETIOLOGIC FACTOR IN BRONCHIOGENIC CARCINOMA: A Study of Six Hundred and Eighty-Four Proved Cases.* Journal of the American Medical Association, 1950. **143**(4): p. 329-336.

30. Costa, F. and R. Soares, *Nicotine: a pro-angiogenic factor.* Life Sciences, 2009. **84**(23-24): p. 785-790.

31. Saccone, S.F., et al., *Cholinergic nicotinic receptor genes implicated in a nicotine dependence association study targeting 348 candidate genes with 3713 SNPs.* Human molecular genetics, 2007. **16**(1): p. 36-49.

32. Benowitz, N.L., *Clinical pharmacology of nicotine: implications for understanding, preventing, and treating tobacco addiction.* Clinical Pharmacology & Therapeutics, 2008. **83**(4): p. 531-541.

33. Hoffmann, D.H.I., *The changing cigarette, 1950-1995.* Journal of Toxicology and Environmental Health Part A, 1997. **50**(4): p. 307-364.

34. Hecht, S.S., *Biochemistry, biology, and carcinogenicity of tobacco-specific N-nitrosamines.* Chemical research in toxicology, 1998. **11**(6): p. 559-603.

35. Hoffmann, D. and I. Hoffmann, *The Changing Cigarette: Chemical.* Risks associated with smoking cigarettes with low machine-measured yields of tar and nicotine, 2001(2): p. 159.

36. Smith, C.J., et al., *"IARC group 2A Carcinogens" reported in cigarette mainstream smoke.* Food and chemical toxicology, 2000. **38**(4): p. 371-383.

37. Smith, C.J., et al., *"IARC group 2B Carcinogens" reported in cigarette mainstream smoke.* Food and chemical toxicology, 2000. **38**(9): p. 825-848.

38. Hecht, S.S., *Tobacco carcinogens, their biomarkers and tobacco-induced cancer.* Nature Reviews Cancer, 2003. **3**(10): p. 733-744.

39. Rajalakshmi, T.R., et al., *DNA adducts-chemical addons.* Journal of pharmacy & bioallied sciences, 2015. **7**(Suppl 1): p. S197-S199.

40. Hwa Yun, B., et al., *DNA adducts: Formation, biological effects, and new biospecimens for mass spectrometric measurements in humans.* Mass spectrometry reviews, 2020. **39**(1-2): p. 55-82.

41. Akopyan, G. and B. Bonavida, *Understanding tobacco smoke carcinogen NNK and lung tumorigenesis.* International journal of oncology, 2006. **29**(4): p. 745-752.

42. Hecht, S.S., *It is time to regulate carcinogenic tobacco-specific nitrosamines in cigarette tobacco.* Cancer Prevention Research, 2014. **7**(7): p. 639-647.

43. Rodenhuis, S. and R.J.C. Slebos, *Clinical significance of ras oncogene activation in human lung cancer.* Cancer research, 1992. **52**(9_Supplement): p. 2665s-2669s.

44. Westra, W.H., et al., *K-ras oncogene activation in lung adenocarcinomas from former smokers evidence that K-ras mutations are an early and irreversible event in the development of adenocarcinoma of the lung.* Cancer, 1993. **72**(2): p. 432-438.

45. Denissenko, M.F., et al., *Preferential formation of benzo [a] pyrene adducts at lung cancer mutational hotspots in P53.* Science, 1996. **274**(5286): p. 430-432.

46. HSE, H.S.E. *Chronic obstructive pulmonary disease (COPD) - Overview*. 15 December 2021 [cited 2022 19 November]; Chronic obstructive pulmonary disease (COPD) - Overview]. Available from: https://www2.hse.ie/conditions/copd/copd-overview/.

47. Ireland, C.S. *What Is COPD.* 2022 [cited 2022 19 November]; What Is COPD]. Available from: https://copd.ie/what-is-copd/.

48. MacNee, W., *Pathogenesis of chronic obstructive pulmonary disease.* Proceedings of the American thoracic society, 2005. **2**(4): p. 258-266.

49. Kuller, L.H., et al., *Relation of forced expiratory volume in one second (FEV1) to lung cancer mortality in the Multiple Risk Factor Intervention Trial (MRFIT).* American journal of epidemiology, 1990. **132**(2): p. 265-274.

50. Hole, D.J., et al., *Impaired lung function and mortality risk in men and women: findings from the Renfrew and Paisley prospective population study.* Bmj, 1996. **313**(7059): p. 711-715.

51.    Wu, A.H., et al., *Previous Lung Disease and Risk of Lung Cancer among Lifetime Nonsmoking Women in the United States.* American Journal of Epidemiology, 1995. **141**(11): p. 1023-1032.

52.    Skillrud, D.M., K.P. Offord, and R.D. Miller, *Higher risk of lung cancer in chronic obstructive pulmonary disease: a prospective, matched, controlled study.* Annals of internal medicine, 1986. **105**(4): p. 503-507.

53.    Tockman, M.S., et al., *Airways obstruction and the risk for lung cancer.* Annals of internal medicine, 1987. **106**(4): p. 512-518.

54.    Anthonisen, N.R., et al., *Effects of Smoking Intervention and the Use of an Inhaled Anticholinergic Bronchodilator on the Rate of Decline of FEV1: The Lung Health Study.* JAMA, 1994. **272**(19): p. 1497-1505.

55.    Turner, M.C., et al., *Chronic obstructive pulmonary disease is associated with lung cancer mortality in a prospective study of never smokers.* American journal of respiratory and critical care medicine, 2007. **176**(3): p. 285-290.

56.    Loganathan, R.S., et al., *Prevalence of COPD in women compared to men around the time of diagnosis of primary lung cancer.* Chest, 2006. **129**(5): p. 1305-1312.

57.    Young, R.P., et al., *COPD prevalence is increased in lung cancer, independent of age, sex and smoking history.* European Respiratory Journal, 2009. **34**(2): p. 380.

58.    Stayner, L., et al., *An epidemiological study of the role of chrysotile asbestos fibre dimensions in determining respiratory disease risk in exposed workers.* Occupational and Environmental Medicine, 2008. **65**(9): p. 613.

59.    Spitz, M.R., et al., *An expanded risk prediction model for lung cancer.* Cancer prevention research (Philadelphia, Pa.), 2008. **1**(4): p. 250-254.

60.    Spitz, M.R., et al., *A Risk Model for Prediction of Lung Cancer.* JNCI: Journal of the National Cancer Institute, 2007. **99**(9): p. 715-726.

61.    Cassidy, A., et al., *The LLP risk model: an individual risk prediction model for lung cancer.* British journal of cancer, 2008. **98**(2): p. 270-276.

62.    Ryberg, D., et al., *Different susceptibility to smoking-induced DNA damage among male and female lung cancer patients.* Cancer research, 1994. **54**: p. 5801-3.

63.    Murthy, V.H., H.M. Krumholz, and C.P. Gross, *Participation in cancer clinical trials: race-, sex-, and age-based disparities.* Jama, 2004. **291**(22): p. 2720-2726.

64.    Cersosimo, R.J., *Lung cancer: A review.* American Journal of Health-System Pharmacy, 2002. **59**(7): p. 611-642.

65.    Zheng, M., *Classification and pathology of lung cancer.* Surgical Oncology Clinics, 2016. **25**(3): p. 447-468.

66.    Jeremic, B., et al., *Hyperfractionated radiation therapy with or without concurrent low-dose daily carboplatin/etoposide for stage III non-small-cell lung cancer: a randomized study.* Journal of Clinical Oncology, 1996. **14**(4): p. 1065-1070.

67.    Schaake-Koning, C., et al., *Effects of concomitant cisplatin and radiotherapy on inoperable non-small-cell lung cancer.* New England Journal of Medicine, 1992. **326**(8): p. 524-530.

68.    Sause, W., et al., *Final results of phase III trial in regionally advanced unresectable non-small cell lung cancer: Radiation Therapy Oncology Group, Eastern Cooperative Oncology Group, and Southwest Oncology Group.* Chest, 2000. **117**(2): p. 358-364.

69. Dillman, R.O., et al., *Improved survival in stage III non-small-cell lung cancer: seven-year follow-up of cancer and leukemia group B (CALGB) 8433 trial.* JNCI: Journal of the National Cancer Institute, 1996. **88**(17): p. 1210-1215.

70. Le Chevalier, T., et al., *Radiotherapy alone versus combined chemotherapy and radiotherapy in nonresectable non-small-cell lung cancer: first analysis of a randomized trial in 353 patients.* JNCI: Journal of the National Cancer Institute, 1991. **83**(6): p. 417-423.

71. da Cunha Santos, G., F.A. Shepherd, and M.S. Tsao, *EGFR mutations and lung cancer.* Annual Review of Pathology: Mechanisms of Disease, 2011. **6**: p. 49-69.

72. Paz-Ares, L., et al., *Maintenance therapy with pemetrexed plus best supportive care versus placebo plus best supportive care after induction therapy with pemetrexed plus cisplatin for advanced non-squamous non-small-cell lung cancer (PARAMOUNT): a double-blind, phase 3, randomised controlled trial.* The Lancet Oncology, 2012. **13**(3): p. 247-255.

73. Ciuleanu, T., et al., *Maintenance pemetrexed plus best supportive care versus placebo plus best supportive care for non-small-cell lung cancer: a randomised, double-blind, phase 3 study.* The Lancet, 2009. **374**(9699): p. 1432-1440.

74. Cappuzzo, F., et al., *Erlotinib as maintenance treatment in advanced non-small-cell lung cancer: a multicentre, randomised, placebo-controlled phase 3 study.* The lancet oncology, 2010. **11**(6): p. 521-529.

75. Senapati, S., et al., *Controlled drug delivery vehicles for cancer treatment and their performance.* Signal Transduction and Targeted Therapy, 2018. **3**(1): p. 7.

76. Tran, S., et al., *Cancer nanomedicine: a review of recent success in drug delivery.* Clinical and translational medicine, 2017. **6**(1): p. 1-21.

77. Saha, R.N., et al., *Nanoparticulate drug delivery systems for cancer chemotherapy.* Molecular membrane biology, 2010. **27**(7): p. 215-231.

78. Louis, D.N., *WHO classification of tumours of the central nervous system.* 2007: WHO.

79. Mariappan, A., et al., *Trends and challenges in modeling glioma using 3D human brain organoids.* Cell Death & Differentiation, 2021. **28**(1): p. 15-23.

80. Bi, J., et al., *Altered cellular metabolism in gliomas—An emerging landscape of actionable co-dependency targets.* Nature Reviews Cancer, 2020. **20**(1): p. 57-70.

81. Lapointe, S., A. Perry, and N.A. Butowski, *Primary brain tumours in adults.* The Lancet, 2018. **392**(10145): p. 432-446.

82. Grochans, S., et al. *Epidemiology of Glioblastoma Multiforme–Literature Review.* Cancers, 2022. **14**, DOI: 10.3390/cancers14102412.

83. Tamimi, A.F. and M. Juweid, *Epidemiology and outcome of glioblastoma.* Exon Publications, 2017: p. 143-153.

84. Oszvald, Á., et al., *Glioblastoma therapy in the elderly and the importance of the extent of resection regardless of age.* Journal of neurosurgery, 2012. **116**(2): p. 357-364.

85. Wu, W., et al., *Glioblastoma multiforme (GBM): An overview of current therapies and mechanisms of resistance.* Pharmacological Research, 2021. **171**: p. 105780.

86. Davis, M.E., *Glioblastoma: overview of disease and treatment.* Clinical journal of oncology nursing, 2016. **20**(5): p. S2.

87.	Sturm, D., et al., *Paediatric and adult glioblastoma: multiform (epi)genomic culprits emerge.* Nature Reviews Cancer, 2014. **14**(2): p. 92-107.

88.	Brennan, C.W., et al., *The somatic genomic landscape of glioblastoma.* cell, 2013. **155**(2): p. 462-477.

89.	Kumari, A., S.K. Yadav, and S.C. Yadav, *Biodegradable polymeric nanoparticles based drug delivery systems.* Colloids and Surfaces B: Biointerfaces, 2010. **75**(1): p. 1-18.

90.	Wertheimer, A.I., et al., *Drug delivery systems improve Pharmaceutical profile and facilitate medication adherence.* Advances in Therapy, 2005. **22**(6): p. 559-577.

91.	Urquhart, J., *Erratic patient compliance with prescribed drug regimens: Target for drug delivery systems.* Clinical Pharmacology & Therapeutics, 2000. **67**(4): p. 331-334.

92.	Wilczewska, A.Z., et al., *Nanoparticles as drug delivery systems.* Pharmacological reports, 2012. **64**(5): p. 1020-1037.

93.	Martínez-Carmona, M., M. Colilla, and M. Vallet-Regí, *Smart Mesoporous Nanomaterials for Antitumor Therapy.* Nanomaterials (Basel, Switzerland), 2015. **5**(4): p. 1906-1937.

94.	Andersson, J., et al., *Influences of Material Characteristics on Ibuprofen Drug Loading and Release Profiles from Ordered Micro- and Mesoporous Silica Matrices.* Chemistry of Materials, 2004. **16**(21): p. 4160-4167.

95.	Scheinberg, D.A., et al., *Conscripts of the infinite armada: systemic cancer therapy using nanomaterials.* Nature Reviews Clinical Oncology, 2010. **7**(5): p. 266-276.

96.	Algar, W.R., et al., *The Controlled Display of Biomolecules on Nanoparticles: A Challenge Suited to Bioorthogonal Chemistry.* Bioconjugate Chemistry, 2011. **22**(5): p. 825-858.

97.	Wicki, A., et al., *Nanomedicine in cancer therapy: Challenges, opportunities, and clinical applications.* Journal of Controlled Release, 2015. **200**: p. 138-157.

98.	Matsumura, Y. and H. Maeda, *A new concept for macromolecular therapeutics in cancer chemotherapy: mechanism of tumoritropic accumulation of proteins and the antitumor agent smancs.* Cancer research, 1986. **46**(12_Part_1): p. 6387-6392.

99.	Shukla, T., et al., *Site-specific drug delivery, targeting, and gene therapy*, in *Nanoarchitectonics in Biomedicine*. 2019, Elsevier. p. 473-505.

100.	Morshed, M. and E.H. Chowdhury, *Gene delivery and clinical applications*, in *Encyclopedia of Biomedical Engineering*. 2019, Elsevier. p. 345-351.

101.	Peer, D., et al., *Nanocarriers as an emerging platform for cancer therapy.* Nano-Enabled Medical Applications, 2020: p. 61-91.

102.	ud Din, F., et al., *Effective use of nanocarriers as drug delivery systems for the treatment of selected tumors.* International journal of nanomedicine, 2017. **12**: p. 7291.

103.	Salmaso, S. and P. Caliceti, *Stealth properties to improve therapeutic efficacy of drug nanocarriers.* Journal of drug delivery, 2013. **2013**.

104.	Frank, M.M. and L.F. Fries, *The role of complement in inflammation and phagocytosis.* Immunology today, 1991. **12**(9): p. 322-326.

105.	Moghimi, S.M., et al., *Coating particles with a block co-polymer (poloxamine-908) suppresses opsonization but permits the activity of dysopsonins in the serum.*

Biochimica et Biophysica Acta (BBA)-Molecular Cell Research, 1993. **1179**(2): p. 157-165.

106. Yan, X., G.L. Scherphof, and J.A.A.M. Kamps, *Liposome opsonization.* Journal of liposome research, 2005. **15**(1-2): p. 109-139.

107. Moghimi, S.M., A.C. Hunter, and J.C. Murray, *Long-circulating and target-specific nanoparticles: theory to practice.* Pharmacological reviews, 2001. **53**(2): p. 283-318.

108. Danhier, F., O. Feron, and V. Préat, *To exploit the tumor microenvironment: Passive and active tumor targeting of nanocarriers for anti-cancer drug delivery.* Journal of Controlled Release, 2010. **148**(2): p. 135-146.

109. López, V., et al., *Janus mesoporous silica nanoparticles for dual targeting of tumor cells and mitochondria.* ACS applied materials & interfaces, 2017. **9**(32): p. 26697-26706.

110. Li, Y., et al., *A dual-targeting nanocarrier based on poly(amidoamine) dendrimers conjugated with transferrin and tamoxifen for treating brain gliomas.* Biomaterials, 2012. **33**(15): p. 3899-3908.

111. Hu, Q., et al., *Tumor Microenvironment and Angiogenic Blood Vessels Dual-Targeting for Enhanced Anti-Glioma Therapy.* ACS Applied Materials & Interfaces, 2016. **8**(36): p. 23568-23579.

112. Zhao, Y., et al., *Dual targeted nanocarrier for brain ischemic stroke treatment.* Journal of Controlled Release, 2016. **233**: p. 64-71.

113. Vallet-Regí, M., et al., *Mesoporous silica nanoparticles for drug delivery: Current insights.* Molecules, 2017. **23**(1): p. 47.

114. Tang, F., L. Li, and D. Chen, *Mesoporous Silica Nanoparticles: Synthesis, Biocompatibility and Drug Delivery.* Advanced Materials, 2012. **24**(12): p. 1504-1534.

115. Shi, Y., M.L. Miller, and A.J. Di Pasqua, *Biocompatibility of Mesoporous Silica Nanoparticles?* Comments on Inorganic Chemistry, 2016. **36**(2): p. 61-80.

116. Fleige, E., M.A. Quadir, and R. Haag, *Stimuli-responsive polymeric nanocarriers for the controlled transport of active compounds: Concepts and applications.* Advanced Drug Delivery Reviews, 2012. **64**(9): p. 866-884.

117. Jhaveri, A., P. Deshpande, and V. Torchilin, *Stimuli-sensitive nanopreparations for combination cancer therapy.* Journal of Controlled Release, 2014. **190**: p. 352-370.

118. Tannock, I.F. and D. Rotin, *Acid pH in Tumors and Its Potential for Therapeutic Exploitation1.* Cancer Research, 1989. **49**(16): p. 4373-4384.

119. Gao, W., J.M. Chan, and O.C. Farokhzad, *pH-Responsive Nanoparticles for Drug Delivery.* Molecular Pharmaceutics, 2010. **7**(6): p. 1913-1920.

120. Liu, R., et al., *pH-responsive nanogated ensemble based on gold-capped mesoporous silica through an acid-labile acetal linker.* Journal of the American Chemical Society, 2010. **132**(5): p. 1500-1501.

121. Gan, Q., et al., *A magnetic, reversible pH-responsive nanogated ensemble based on Fe3O4 nanoparticles-capped mesoporous silica.* Biomaterials, 2011. **32**(7): p. 1932-1942.

122. Xu, C., et al., *Nanoceria-Triggered Synergetic Drug Release Based on CeO2-Capped Mesoporous Silica Host–Guest Interactions and Switchable Enzymatic*

*Activity and Cellular Effects of CeO2.* Advanced Healthcare Materials, 2013. **2**(12): p. 1591-1599.

123. Obata, Y., S. Tajima, and S. Takeoka, *Evaluation of pH-responsive liposomes containing amino acid-based zwitterionic lipids for improving intracellular drug delivery in vitro and in vivo.* Journal of Controlled Release, 2010. **142**(2): p. 267-276.

124. Feng, W., et al., *Polyelectrolyte multilayer functionalized mesoporous silica nanoparticles for pH-responsive drug delivery: layer thickness-dependent release profiles and biocompatibility.* Journal of Materials Chemistry B, 2013. **1**(43): p. 5886-5898.

125. Meng, H., et al., *Autonomous in Vitro Anticancer Drug Release from Mesoporous Silica Nanoparticles by pH-Sensitive Nanovalves.* Journal of the American Chemical Society, 2010. **132**(36): p. 12690-12697.

126. Gao, Y., et al., *A Multifunctional Nanocarrier Based on Nanogated Mesoporous Silica for Enhanced Tumor-Specific Uptake and Intracellular Delivery.* Macromolecular Bioscience, 2012. **12**(2): p. 251-259.

127. Rim, H.P., et al., *pH-Tunable Calcium Phosphate Covered Mesoporous Silica Nanocontainers for Intracellular Controlled Release of Guest Drugs.* Angewandte Chemie International Edition, 2011. **50**(38): p. 8853-8857.

128. Cheng, R., et al., *Glutathione-responsive nano-vehicles as a promising platform for targeted intracellular drug and gene delivery.* Journal of Controlled Release, 2011. **152**(1): p. 2-12.

129. Kirpotin, D., et al., *Liposomes with detachable polymer coating: destabilization and fusion of dioleoylphosphatidylethanolamine vesicles triggered by cleavage of surface-grafted poly(ethylene glycol).* FEBS Letters, 1996. **388**(2): p. 115-118.

130. Wang, Y.-C., et al., *Redox-Responsive Nanoparticles from the Single Disulfide Bond-Bridged Block Copolymer as Drug Carriers for Overcoming Multidrug Resistance in Cancer Cells.* Bioconjugate Chemistry, 2011. **22**(10): p. 1939-1945.

131. Ma, X., et al., *Functional Silica Nanoparticles for Redox-Triggered Drug/ssDNA Co-delivery.* Advanced Healthcare Materials, 2012. **1**(6): p. 690-697.

132. Zhang, J., et al., *Mesoporous silica nanoparticles with redox-responsive surface linkers for charge-reversible loading and release of short oligonucleotides.* Dalton transactions, 2014. **43**(10): p. 4115-4126.

133. Nadrah, P., et al., *Poly (propylene imine) dendrimer caps on mesoporous silica nanoparticles for redox-responsive release: smaller is better.* Physical Chemistry Chemical Physics, 2013. **15**(26): p. 10740-10748.

134. Lai, C.-Y., et al., *A Mesoporous Silica Nanosphere-Based Carrier System with Chemically Removable CdS Nanoparticle Caps for Stimuli-Responsive Controlled Release of Neurotransmitters and Drug Molecules.* Journal of the American Chemical Society, 2003. **125**(15): p. 4451-4459.

135. Yang, J., et al., *Modulating the cellular microenvironment with disulfide-containing nanoparticles as an auxiliary cancer treatment strategy.* Journal of Materials Chemistry B, 2016. **4**(22): p. 3868-3873.

136. de la Rica, R., D. Aili, and M.M. Stevens, *Enzyme-responsive nanoparticles for drug release and diagnostics.* Advanced Drug Delivery Reviews, 2012. **64**(11): p. 967-978.

137. Agostini, A., et al., *Dual Enzyme-Triggered Controlled Release on Capped Nanometric Silica Mesoporous Supports.* ChemistryOpen, 2012. **1**(1): p. 17-20.

138. van Rijt, S.H., et al., *Protease-mediated release of chemotherapeutics from mesoporous silica nanoparticles to ex vivo human and mouse lung tumors.* ACS nano, 2015. **9**(3): p. 2377-2389.

139. Singh, N., et al., *Bioresponsive Mesoporous Silica Nanoparticles for Triggered Drug Release.* Journal of the American Chemical Society, 2011. **133**(49): p. 19582-19585.

140. Park, C., et al., *Enzyme Responsive Nanocontainers with Cyclodextrin Gatekeepers and Synergistic Effects in Release of Guests.* Journal of the American Chemical Society, 2009. **131**(46): p. 16614-16615.

141. Baeza, A., et al., *Hybrid Enzyme-Polymeric Capsules/Mesoporous Silica Nanodevice for In Situ Cytotoxic Agent Generation.* Advanced Functional Materials, 2014. **24**(29): p. 4625-4633.

142. Mas, N., et al., *Towards the Development of Smart 3D "Gated Scaffolds" for On-Command Delivery.* Small, 2014. **10**(23): p. 4859-4864.

143. Xu, J.-H., et al., *Gelatin–mesoporous silica nanoparticles as matrix metalloproteinases-degradable drug delivery systems in vivo.* Microporous and mesoporous materials, 2013. **182**: p. 165-172.

144. Dicheva, B.M. and G.A. Koning, *Targeted thermosensitive liposomes: an attractive novel approach for increased drug delivery to solid tumors.* Expert opinion on drug delivery, 2014. **11**(1): p. 83-100.

145. Chen, K.-J., et al., *A Thermoresponsive Bubble-Generating Liposomal System for Triggering Localized Extracellular Drug Delivery.* ACS Nano, 2013. **7**(1): p. 438-446.

146. Needham, D., et al., *A New Temperature-sensitive Liposome for Use with Mild Hyperthermia: Characterization and Testing in a Human Tumor Xenograft Model1.* Cancer Research, 2000. **60**(5): p. 1197-1201.

147. Aznar, E., et al., *Finely Tuned Temperature-Controlled Cargo Release Using Paraffin-Capped Mesoporous Silica Nanoparticles.* Angewandte Chemie International Edition, 2011. **50**(47): p. 11172-11175.

148. Schlossbauer, A., et al., *A Programmable DNA-Based Molecular Valve for Colloidal Mesoporous Silica.* Angewandte Chemie International Edition, 2010. **49**(28): p. 4734-4737.

149. Martelli, G., et al., *Coiled-coil peptide motifs as thermoresponsive valves for mesoporous silica nanoparticles.* Chemical communications, 2013. **49**(85): p. 9932-9934.

150. Ferris, D.P., et al., *Light-Operated Mechanized Nanoparticles.* Journal of the American Chemical Society, 2009. **131**(5): p. 1686-1688.

151. Mal, N.K., M. Fujiwara, and Y. Tanaka, *Photocontrolled reversible release of guest molecules from coumarin-modified mesoporous silica.* Nature, 2003. **421**(6921): p. 350-353.

152. Martínez-Carmona, M., et al., *Mesoporous silica nanoparticles grafted with a light-responsive protein shell for highly cytotoxic antitumoral therapy.* Journal of Materials Chemistry B, 2015. **3**(28): p. 5746-5752.

153. Martínez-Carmona, M., et al., *A novel visible light responsive nanosystem for cancer treatment.* Nanoscale, 2017. **9**(41): p. 15967-15973.

154. Han, G., et al., *Light-regulated release of DNA and its delivery to nuclei by means of photolabile gold nanoparticles.* Angewandte Chemie, 2006. **118**(19): p. 3237-3241.

155. Nishiyama, N., et al., *Light-induced gene transfer from packaged DNA enveloped in a dendrimeric photosensitizer.* Nature Materials, 2005. **4**(12): p. 934-941.

156. Fomina, N., et al., *UV and Near-IR Triggered Release from Polymeric Nanoparticles.* Journal of the American Chemical Society, 2010. **132**(28): p. 9540-9542.

157. Sirsi, S.R. and M.A. Borden, *State-of-the-art materials for ultrasound-triggered drug delivery.* Advanced Drug Delivery Reviews, 2014. **72**: p. 3-14.

158. Wang, J., et al., *High-Frequency Ultrasound-Responsive Block Copolymer Micelle.* Langmuir, 2009. **25**(22): p. 13201-13205.

159. Paris, J.L., et al., *Polymer-Grafted Mesoporous Silica Nanoparticles as Ultrasound-Responsive Drug Carriers.* ACS Nano, 2015. **9**(11): p. 11023-11033.

160. Paris, J.L., et al., *Vectorization of ultrasound-responsive nanoparticles in placental mesenchymal stem cells for cancer therapy.* Nanoscale, 2017. **9**(17): p. 5528-5537.

161. Rapoport, N., Z. Gao, and A. Kennedy, *Multifunctional Nanoparticles for Combining Ultrasonic Tumor Imaging and Targeted Chemotherapy.* JNCI: Journal of the National Cancer Institute, 2007. **99**(14): p. 1095-1106.

162. Schroeder, A., et al., *Ultrasound triggered release of cisplatin from liposomes in murine tumors.* Journal of Controlled Release, 2009. **137**(1): p. 63-68.

163. Saint-Cricq, P., et al., *Magnetic field activated drug delivery using thermodegradable azo-functionalised PEG-coated core–shell mesoporous silica nanoparticles.* Nanoscale, 2015. **7**(31): p. 13168-13172.

164. Baeza, A., et al., *Magnetically Triggered Multidrug Release by Hybrid Mesoporous Silica Nanoparticles.* Chemistry of Materials, 2012. **24**(3): p. 517-524.

165. Thomas, C.R., et al., *Noninvasive Remote-Controlled Release of Drug Molecules in Vitro Using Magnetic Actuation of Mechanized Nanoparticles.* Journal of the American Chemical Society, 2010. **132**(31): p. 10623-10625.

166. Zhu, Y., et al., *Dipolar Molecules as Impellers Achieving Electric-Field-Stimulated Release.* Journal of the American Chemical Society, 2010. **132**(5): p. 1450-1451.

167. Ge, J., et al., *Drug release from electric-field-responsive nanoparticles.* ACS nano, 2012. **6**(1): p. 227-233.

168. Laurent, S., et al., *Magnetic fluid hyperthermia: Focus on superparamagnetic iron oxide nanoparticles.* Advances in Colloid and Interface Science, 2011. **166**(1): p. 8-23.

169. G. Kong, M.W.D., *Review Hyperthermia and liposomes.* International Journal of Hyperthermia, 1999. **15**(5): p. 345-370.

170. Estrela, J.M., A. Ortega, and E. Obrador, *Glutathione in Cancer Biology and Therapy.* Critical Reviews in Clinical Laboratory Sciences, 2006. **43**(2): p. 143-181.

171. Meister, A., *Glutathione metabolism and its selective modification.* Journal of biological chemistry, 1988. **263**(33): p. 17205-17208.

172.    Forman, H.J., H. Zhang, and A. Rinna, *Glutathione: overview of its protective roles, measurement, and biosynthesis.* Molecular aspects of medicine, 2009. **30**(1-2): p. 1-12.

173.    Kennedy, L., et al. *Role of Glutathione in Cancer: From Mechanisms to Therapies.* Biomolecules, 2020. **10**, DOI: 10.3390/biom10101429.

174.    Gamcsik, M.P., et al., *Glutathione levels in human tumors.* Biomarkers : biochemical indicators of exposure, response, and susceptibility to chemicals, 2012. **17**(8): p. 671-691.

175.    Blair, S.L., et al., *Glutathione Metabolism in Patients with Non-Small Cell Lung Cancers.* Cancer Research, 1997. **57**(1): p. 152-155.

176.    Bachhawat, A.K. and S. Yadav, *The glutathione cycle: Glutathione metabolism beyond the γ-glutamyl cycle.* IUBMB Life, 2018. **70**(7): p. 585-592.

177.    Vernier, M., et al., *Estrogen-related receptors are targetable ROS sensors.* Genes & Development, 2020. **34**(7-8): p. 544-559.

178.    Godwin, A.K., et al., *High resistance to cisplatin in human ovarian cancer cell lines is associated with marked increase of glutathione synthesis.* Proceedings of the National Academy of Sciences, 1992. **89**(7): p. 3070-3074.

179.    Mulcahy, R.T., S. Untawale, and J.J. Gipp, *Transcriptional up-regulation of gamma-glutamylcysteine synthetase gene expression in melphalan-resistant human prostate carcinoma cells.* Molecular pharmacology, 1994. **46**(5): p. 909-914.

180.    Hochwald, S.N., et al., *Elevation of glutathione and related enzyme activities in high-grade and metastatic extremity soft tissue sarcoma.* Annals of Surgical Oncology, 1997. **4**(4): p. 303-309.

181.    Lewis, A.D., J.D. Hayes, and C.R. Wolf, *Glutathione and glutathione-dependent enzymes in ovarian adenocarcinoma cell lines derived from a patient before and after the onset of drug resistance: intrinsic differences and cell cycle effects.* Carcinogenesis, 1988. **9**(7): p. 1283-1287.

182.    Kuo, M.T., et al., *Frequent coexpression of MRP/GS-X pump and γ-glutamylcysteine synthetase mRNA in drug-resistant cells, untreated tumor cells, and normal mouse tissues.* Biochemical Pharmacology, 1998. **55**(5): p. 605-615.

183.    Oguri, T., et al., *Expression of γ-glutamylcysteine synthetase (γ-GCS) and multidrug resistance-associated protein (MRP), but not human canalicular multispecific organic anion transporter (cMOAT), genes correlates with exposure of human lung cancers to platinum drugs.* British Journal of Cancer, 1998. **77**(7): p. 1089-1096.

184.    Traverso, N., et al., *Role of Glutathione in Cancer Progression and Chemoresistance.* Oxidative Medicine and Cellular Longevity, 2013. **2013**: p. 972913.

185.    Hadler-Olsen, E., J.-O. Winberg, and L. Uhlin-Hansen, *Matrix metalloproteinases in cancer: their value as diagnostic and prognostic markers and therapeutic targets.* Tumor Biology, 2013. **34**(4): p. 2041-2051.

186.    Merchant, N., et al., *Matrix metalloproteinases: their functional role in lung cancer.* Carcinogenesis, 2017. **38**(8): p. 766-780.

187.    Laronha, H. and J. Caldeira, *Structure and Function of Human Matrix Metalloproteinases.* Cells, 2020. **9**(5): p. 1076.

188. Gialeli, C., A.D. Theocharis, and N.K. Karamanos, *Roles of matrix metalloproteinases in cancer progression and their pharmacological targeting.* The FEBS Journal, 2011. **278**(1): p. 16-27.

189. van Hinsbergh, V.W.M., M.A. Engelse, and P.H.A. Quax, *Pericellular Proteases in Angiogenesis and Vasculogenesis.* Arteriosclerosis, Thrombosis, and Vascular Biology, 2006. **26**(4): p. 716-728.

190. Deryugina, E.I. and J.P. Quigley, *Matrix metalloproteinases and tumor metastasis.* Cancer and Metastasis Reviews, 2006. **25**(1): p. 9-34.

191. Gouyer, V., et al., *Tissue inhibitor of metalloproteinase 1 is an independent predictor of prognosis in patients with nonsmall cell lung carcinoma who undergo resection with curative intent.* Cancer, 2005. **103**(8): p. 1676-1684.

192. Hsu, C.-P., G.-H. Shen, and J.-L. Ko, *Matrix metalloproteinase-13 expression is associated with bone marrow microinvolvement and prognosis in non-small cell lung cancer.* Lung Cancer, 2006. **52**(3): p. 349-357.

193. Li, L., et al., *Expression and clinical significance of matrix metalloproteinase (MMP)-26 protein in non-small cell lung cancer.* Ai Zheng= Aizheng= Chinese Journal of Cancer, 2009. **28**(1): p. 60-63.

194. J, S., et al., *Expression of MMP-7, MMP-9, TIMP-1 and TIMP-2 mRNA in Lung Tissue of Patients with Non-small Cell Lung Cancer (NSCLC) and Benign Pulmonary Disease.* Anticancer Research, 2009. **29**(7): p. 2513.

195. Qian, Q., et al., *The role of matrix metalloproteinase 2 on the survival of patients with non-small cell lung cancer: a systematic review with meta-analysis.* Cancer investigation, 2010. **28**(6): p. 661-669.

196. Peng, W.-J., et al., *Prognostic value of matrix metalloproteinase 9 expression in patients with non-small cell lung cancer.* Clinica Chimica Acta, 2012. **413**(13): p. 1121-1126.

197. Liu, D., et al., *Overexpression of matrix metalloproteinase-7 (MMP-7) correlates with tumor proliferation, and a poor prognosis in non-small cell lung cancer.* Lung cancer, 2007. **58**(3): p. 384-391.

198. Liu, H., et al., *Predictive value of MMP-7 expression for response to chemotherapy and survival in patients with non-small cell lung cancer.* Cancer science, 2008. **99**(11): p. 2185-2192.

199. Leinonen, T., et al., *Expression of matrix metalloproteinases 7 and 9 in non-small cell lung cancer: Relation to clinicopathological factors, β-catenin and prognosis.* Lung Cancer, 2006. **51**(3): p. 313-321.

200. Ylisirniö, S., M. Höyhtyä, and T. Turpeenniemi-Hujanen, *Serum matrix metalloproteinases -2, -9 and tissue inhibitors of metalloproteinases -1, -2 in lung cancer--TIMP-1 as a prognostic marker.* Anticancer research, 2000. **20**(2B): p. 1311-1316.

201. Hoikkala, S., et al., *Tissue MMP-2 and MMP-9 [corrected] are better prognostic factors than serum MMP-2/TIMP-2--complex or TIMP-1 [corrected] in stage [corrected] I-III lung carcinoma.* Cancer letters, 2006. **236**(1): p. 125-132.

202. Mercer, B.A., et al., *Extracellular regulated kinase/mitogen activated protein kinase is up-regulated in pulmonary emphysema and mediates matrix metalloproteinase-1 induction by cigarette smoke.* Journal of Biological Chemistry, 2004. **279**(17): p. 17690-17696.

203. Pritchard, S.C., et al., *Expression of matrix metalloproteinases 1, 2, 9 and their tissue inhibitors in stage II non-small cell lung cancer: implications for MMP inhibition therapy.* Oncology reports, 2001. **8**(2): p. 421-424.

204. Schütz, A., et al., *Differential Expression and Activity Status of MMP-1, MMP-2 and MMP-9 in Tumor and Stromal Cells of Squamous Cell Carcinomas of the Lung.* Tumor Biology, 2002. **23**(3): p. 179-184.

205. Houghton, A.M., *Matrix metalloproteinases in destructive lung disease.* Matrix biology, 2015. **44**: p. 167-174.

206. Togawa, D., et al., *Highly activated matrix metalloproteinase-2 secreted from clones of metastatic lung nodules of nude mice injected with human fibrosarcoma HT1080.* Cancer Letters, 1999. **146**(1): p. 25-33.

207. Ke, Z., et al., *MMP-2 mediates ethanol-induced invasion of mammary epithelial cells over-expressing ErbB2.* International Journal of Cancer, 2006. **119**(1): p. 8-16.

208. Nawrocki, B., et al., *Expression of matrix metalloproteinases and their inhibitors in human bronchopulmonary carcinomas: Quantificative and morphological analyses.* International Journal of Cancer, 1997. **72**(4): p. 556-564.

209. Wilson, C.L. and L.M. Matrisian, *Matrilysin: An epithelial matrix metalloproteinase with potentially novel functions.* The International Journal of Biochemistry & Cell Biology, 1996. **28**(2): p. 123-136.

210. Zheng, S., et al., *Expression of KISS1 and MMP-9 in non-small cell lung cancer and their relations to metastasis and survival.* Anticancer research, 2010. **30**(3): p. 713-718.

211. El-Badrawy, M.K., et al., *Matrix Metalloproteinase-9 Expression in Lung Cancer Patients and Its Relation to Serum MMP-9 Activity, Pathologic Type, and Prognosis.* Journal of Bronchology & Interventional Pulmonology, 2014. **21**(4).

212. Houghton, A.M., et al., *Macrophage Elastase (Matrix Metalloproteinase-12) Suppresses Growth of Lung Metastases.* Cancer Research, 2006. **66**(12): p. 6149-6155.

213. Acuff, H.B., et al., *Analysis of Host- and Tumor-Derived Proteinases Using a Custom Dual Species Microarray Reveals a Protective Role for Stromal Matrix Metalloproteinase-12 in Non–Small Cell Lung Cancer.* Cancer Research, 2006. **66**(16): p. 7968-7975.

214. Hofmann, H.-S., et al., *Matrix Metalloproteinase-12 Expression Correlates with Local Recurrence and Metastatic Disease in Non–Small Cell Lung Cancer Patients.* Clinical Cancer Research, 2005. **11**(3): p. 1086-1092.

215. Qu, P., et al., *Matrix Metalloproteinase 12 Overexpression in Lung Epithelial Cells Plays a Key Role in Emphysema to Lung Bronchioalveolar Adenocarcinoma Transition.* Cancer Research, 2009. **69**(18): p. 7252-7261.

216. Dehan, E., et al., *Chromosomal aberrations and gene expression profiles in non-small cell lung cancer.* Lung cancer, 2007. **56**(2): p. 175-184.

217. Knäuper, V., et al., *Activation of progelatinase B (proMMP-9) by active collagenase-3 (MMP-13).* European journal of biochemistry, 1997. **248**(2): p. 369-373.

218. Yu, X., et al., *Matrix metalloproteinase 13: a potential intermediate between low expression of microRNA-125b and increasing metastatic potential of non–small cell lung cancer.* Cancer genetics, 2015. **208**(3): p. 76-84.

219. Thomas, P., et al., *Differential expression of matrix metalloproteinases and their inhibitors in non-small cell lung cancer.* The Journal of Pathology, 2000. **190**(2): p. 150-156.

220. Zhang, Y., et al., *Non-small cell lung cancer invasion and metastasis promoted by MMP-26.* Molecular Medicine Reports, 2011. **4**(6): p. 1201-1209.

221. van Elk, M., et al., *Nanomedicines for advanced cancer treatments: Transitioning towards responsive systems.* International Journal of Pharmaceutics, 2016. **515**(1): p. 132-164.

222. Abdullah, L.N. and E.K.-H. Chow, *Mechanisms of chemoresistance in cancer stem cells.* Clinical and translational medicine, 2013. **2**(1): p. 3-3.

223. López-Noriega, A., et al., *Hyperthermia-Induced Drug Delivery from Thermosensitive Liposomes Encapsulated in an Injectable Hydrogel for Local Chemotherapy.* Advanced Healthcare Materials, 2014. **3**(6): p. 854-859.

224. Narayan, R., et al., *Mesoporous Silica Nanoparticles: A Comprehensive Review on Synthesis and Recent Advances.* Pharmaceutics, 2018. **10**(3): p. 118.

225. Niculescu, V.-C., *Mesoporous Silica Nanoparticles for Bio-Applications.* Frontiers in Materials, 2020. **7**.

226. Patra, J.K., et al., *Nano based drug delivery systems: recent developments and future prospects.* Journal of nanobiotechnology, 2018. **16**(1): p. 1-33.

227. Xia, T., et al., *Polyethyleneimine coating enhances the cellular uptake of mesoporous silica nanoparticles and allows safe delivery of siRNA and DNA constructs.* ACS nano, 2009. **3**(10): p. 3273-3286.

228. Prabhakar, N., et al., *Stimuli-responsive hybrid nanocarriers developed by controllable integration of hyperbranched PEI with mesoporous silica nanoparticles for sustained intracellular siRNA delivery.* International journal of nanomedicine, 2016. **11**: p. 6591.

229. Desai, D., et al., *Lipid bilayer-gated mesoporous silica nanocarriers for tumor-targeted delivery of zoledronic acid in vivo.* Molecular Pharmaceutics, 2017. **14**(9): p. 3218-3227.

230. Han, N., et al., *Hybrid Lipid-Capped Mesoporous Silica for Stimuli-Responsive Drug Release and Overcoming Multidrug Resistance.* ACS Applied Materials & Interfaces, 2015. **7**(5): p. 3342-3351.

231. Zhang, C., et al., *Applications and Biocompatibility of Mesoporous Silica Nanocarriers in the Field of Medicine.* Frontiers in pharmacology, 2022. **13**: p. 829796-829796.

232. Daraee, H., et al., *Application of liposomes in medicine and drug delivery.* Artificial Cells, Nanomedicine, and Biotechnology, 2016. **44**(1): p. 381-391.

233. Liu, P., G. Chen, and J. Zhang, *A review of liposomes as a drug delivery system: current status of approved products, regulatory environments, and future perspectives.* Molecules, 2022. **27**(4): p. 1372.

234. Ghasemiyeh, P. and S. Mohammadi-Samani, *Solid lipid nanoparticles and nanostructured lipid carriers as novel drug delivery systems: Applications,*

*advantages and disadvantages.* Research in pharmaceutical sciences, 2018. **13**(4): p. 288.

235. Shirodkar, R.K., et al., *Solid Lipid Nanoparticles and Nanostructured Lipid Carriers: Emerging Lipid Based Drug Delivery Systems.* Pharmaceutical Chemistry Journal, 2019. **53**(5): p. 440-453.

236. Sur, S., et al., *Recent developments in functionalized polymer nanoparticles for efficient drug delivery system.* Nano-Structures & Nano-Objects, 2019. **20**: p. 100397.

237. Lu, X.-Y., et al., *Chapter 7 - Polymer Nanoparticles*, in *Progress in Molecular Biology and Translational Science*, A. Villaverde, Editor. 2011, Academic Press. p. 299-323.

238. Chis, A.A., et al., *Applications and limitations of dendrimers in biomedicine.* Molecules, 2020. **25**(17): p. 3982.

239. Noriega-Luna, B., et al., *Applications of Dendrimers in Drug Delivery Agents, Diagnosis, Therapy, and Detection.* Journal of Nanomaterials, 2014. **2014**: p. 507273.

240. Wang, J., et al., *Dendrimer-based drug delivery systems: history, challenges, and latest developments.* Journal of Biological Engineering, 2022. **16**(1): p. 18.

241. Dobrovolskaia, M.A. and S.E. McNeil, *Immunological properties of engineered nanomaterials.* Nature nanotechnology, 2007. **2**(8): p. 469-478.

242. Poland, C.A., et al., *Carbon nanotubes introduced into the abdominal cavity of mice show asbestos-like pathogenicity in a pilot study.* Nature nanotechnology, 2008. **3**(7): p. 423-428.

243. Bergamaschi, E., et al. *Occupational Exposure to Carbon Nanotubes and Carbon Nanofibres: More Than a Cobweb.* Nanomaterials, 2021. **11**, DOI: 10.3390/nano11030745.

244. Jia, G., et al., *Cytotoxicity of carbon nanomaterials: single-wall nanotube, multi-wall nanotube, and fullerene.* Environmental science & technology, 2005. **39**(5): p. 1378-1383.

245. Radomski, A., et al., *Nanoparticle-induced platelet aggregation and vascular thrombosis.* British journal of pharmacology, 2005. **146**(6): p. 882-893.

246. Holmannova, D., et al. *Carbon Nanoparticles and Their Biomedical Applications.* Applied Sciences, 2022. **12**, DOI: 10.3390/app12157865.

247. Debnath, S.K. and R. Srivastava, *Drug delivery with carbon-based nanomaterials as versatile nanocarriers: progress and prospects.* Frontiers in Nanotechnology, 2021. **3**: p. 644564.

248. Hiemenz, J.W. and T.J. Walsh, *Lipid Formulations of Amphotericin B: Recent Progress and Future Directions.* Clinical Infectious Diseases, 1996. **22**(Supplement_2): p. S133-S144.

249. *Kaposi's sarcoma: DaunoXome approved.* AIDS Treat News, 1996(246): p. 3-4.

250. Barenholz, Y.C., *Doxil®—The first FDA-approved nano-drug: Lessons learned.* Journal of controlled release, 2012. **160**(2): p. 117-134.

251. Batist, G., et al., *Myocet (liposome-encapsulated doxorubicin citrate): a new approach in breast cancer therapy.* Expert opinion on pharmacotherapy, 2002. **3**(12): p. 1739-1751.

252. Junghanns, J.-U.A.H. and R.H. Müller, *Nanocrystal technology, drug delivery and clinical applications.* International journal of nanomedicine, 2008. **3**(3): p. 295-309.

253. Rosen, H. and T. Abribat, *The rise and rise of drug delivery.* Nature Reviews Drug Discovery, 2005. **4**(5): p. 381-385.

254. Lesniak, A., et al., *Nanoparticle adhesion to the cell membrane and its effect on nanoparticle uptake efficiency.* Journal of the American Chemical Society, 2013. **135**(4): p. 1438-1444.

255. Farjadian, F., et al., *Mesoporous silica nanoparticles: Synthesis, pharmaceutical applications, biodistribution, and biosafety assessment.* Chemical Engineering Journal, 2019. **359**: p. 684-705.

256. Alothman, Z.A. *A Review: Fundamental Aspects of Silicate Mesoporous Materials.* Materials, 2012. **5**, 2874-2902 DOI: 10.3390/ma5122874.

257. Tangestaninejad, S., et al., *Alkene epoxidation catalyzed by molybdenum supported on functionalized MCM-41 containing N–S chelating Schiff base ligand.* Catalysis Communications, 2009. **10**(6): p. 853-858.

258. Klein, L.C., *A review of:"Sol-Gel Science-The Physics and Chemistry of Sol-Gel Processing" Edited by C. Jeffrey Brinker and George W. Scherer.* MATERIAL AND MANUFACTURING PROCESS, 1994. **9**(5): p. 1007-1008.

259. Sayari, A., *Periodic mesoporous materials: synthesis, characterization and potential applications.* Studies in Surface Science and Catalysis, 1996. **102**: p. 1-46.

260. Feng, Y., et al., *The application of mesoporous silica nanoparticle family in cancer theranostics.* Coordination Chemistry Reviews, 2016. **319**: p. 86-109.

261. Meynen, V., P. Cool, and E.F. Vansant, *Verified syntheses of mesoporous materials.* Microporous and mesoporous materials, 2009. **125**(3): p. 170-223.

262. Beck, J.S., et al., *A new family of mesoporous molecular sieves prepared with liquid crystal templates.* Journal of the American Chemical Society, 1992. **114**(27): p. 10834-10843.

263. Huo, Q., D.I. Margolese, and G.D. Stucky, *Surfactant control of phases in the synthesis of mesoporous silica-based materials.* Chemistry of Materials, 1996. **8**(5): p. 1147-1160.

264. Trewyn, B.G., et al., *Synthesis and functionalization of a mesoporous silica nanoparticle based on the sol–gel process and applications in controlled release.* Accounts of chemical research, 2007. **40**(9): p. 846-853.

265. Vartuli, J.C., et al., *Development of a formation mechanism for M41S materials*, in *Studies in Surface Science and Catalysis*, J. Weitkamp, et al., Editors. 1994, Elsevier. p. 53-60.

266. Sharma, R.K., S. Das, and A. Maitra, *Surface modified ormosil nanoparticles.* Journal of Colloid and Interface Science, 2004. **277**(2): p. 342-346.

267. Roy, I., et al., *Ormosil nanoparticles as a sustained-release drug delivery vehicle.* RSC Advances, 2014. **4**(96): p. 53498-53504.

268. Shi, S., F. Chen, and W. Cai, *Biomedical applications of functionalized hollow mesoporous silica nanoparticles: focusing on molecular imaging.* Nanomedicine, 2013. **8**(12): p. 2027-2039.

269. Zhou, Y., et al., *Hollow mesoporous silica nanoparticles as nanocarriers employed in cancer therapy: A review.* Frontiers of Materials Science, 2020. **14**(4): p. 373-386.

270. Degnan, T.F., W.J. Roth, and J.C. Vartuli, *Mesoporous Materials (M41S): From Discovery to Application.* Dekker Encyclopedia of Nanoscience and Nanotechnology, 2004. **3**: p. 1797.

271. Kresge, C.T., et al., *Ordered mesoporous molecular sieves synthesized by a liquid-crystal template mechanism.* Nature, 1992. **359**(6397): p. 710-712.

272. Vallet-Regi, M., et al., *A New Property of MCM-41: Drug Delivery System.* Chemistry of Materials, 2001. **13**(2): p. 308-311.

273. Wang, Y., et al., *Mesoporous silica nanoparticles in drug delivery and biomedical applications.* Nanomedicine: Nanotechnology, Biology and Medicine, 2015. **11**(2): p. 313-327.

274. Giret, S., M. Wong Chi Man, and C. Carcel, *Mesoporous-Silica-Functionalized Nanoparticles for Drug Delivery.* Chemistry – A European Journal, 2015. **21**(40): p. 13850-13865.

275. Ahmadi, E., et al., *Synthesis and surface modification of mesoporous silica nanoparticles and its application as carriers for sustained drug delivery.* Drug Delivery, 2014. **21**(3): p. 164-172.

276. Hu, Q., et al., *Synthesis and hydrophobic adsorption properties of microporous/mesoporous hybrid materials.* Journal of Hazardous Materials, 2009. **164**(2): p. 1205-1212.

277. Huang, X., N.P. Young, and H.E. Townley, *Characterization and comparison of mesoporous silica particles for optimized drug delivery.* Nanomaterials and Nanotechnology, 2014. **4**(Godište 2014): p. 4-2.

278. Lee, C.-H., et al., *Intracellular pH-Responsive Mesoporous Silica Nanoparticles for the Controlled Release of Anticancer Chemotherapeutics.* Angewandte Chemie International Edition, 2010. **49**(44): p. 8214-8219.

279. Stöber, W., A. Fink, and E. Bohn, *Controlled growth of monodisperse silica spheres in the micron size range.* Journal of Colloid and Interface Science, 1968. **26**(1): p. 62-69.

280. Lin, Y.-S., K.R. Hurley, and C.L. Haynes, *Critical Considerations in the Biomedical Use of Mesoporous Silica Nanoparticles.* The Journal of Physical Chemistry Letters, 2012. **3**(3): p. 364-374.

281. Mellaerts, R., et al., *Increasing the oral bioavailability of the poorly water soluble drug itraconazole with ordered mesoporous silica.* European Journal of Pharmaceutics and Biopharmaceutics, 2008. **69**(1): p. 223-230.

282. Slowing, I.I., B.G. Trewyn, and V.S.Y. Lin, *Mesoporous Silica Nanoparticles for Intracellular Delivery of Membrane-Impermeable Proteins.* Journal of the American Chemical Society, 2007. **129**(28): p. 8845-8849.

283. Li, X., J. Zhang, and H. Gu, *Adsorption and Desorption Behaviors of DNA with Magnetic Mesoporous Silica Nanoparticles.* Langmuir, 2011. **27**(10): p. 6099-6106.

284. Li, X., et al., *The packaging of siRNA within the mesoporous structure of silica nanoparticles.* Biomaterials, 2011. **32**(35): p. 9546-9556.

285. Gao, F., et al., *Monodispersed Mesoporous Silica Nanoparticles with Very Large Pores for Enhanced Adsorption and Release of DNA.* The Journal of Physical Chemistry B, 2009. **113**(6): p. 1796-1804.

286. Kim, M.-H., et al., *Facile Synthesis of Monodispersed Mesoporous Silica Nanoparticles with Ultralarge Pores and Their Application in Gene Delivery.* ACS Nano, 2011. **5**(5): p. 3568-3576.

287. Zhao, Y., et al., *Mesoporous Silica Nanoparticle-Based Double Drug Delivery System for Glucose-Responsive Controlled Release of Insulin and Cyclic AMP.* Journal of the American Chemical Society, 2009. **131**(24): p. 8398-8400.

288. Chen, A.M., et al., *Co-delivery of Doxorubicin and Bcl-2 siRNA by Mesoporous Silica Nanoparticles Enhances the Efficacy of Chemotherapy in Multidrug-Resistant Cancer Cells.* Small, 2009. **5**(23): p. 2673-2677.

289. Kim, J., et al., *Magnetic Fluorescent Delivery Vehicle Using Uniform Mesoporous Silica Spheres Embedded with Monodisperse Magnetic and Semiconductor Nanocrystals.* Journal of the American Chemical Society, 2006. **128**(3): p. 688-689.

290. Lin, Y.-S., et al., *Multifunctional Composite Nanoparticles: Magnetic, Luminescent, and Mesoporous.* Chemistry of Materials, 2006. **18**(22): p. 5170-5172.

291. Kim, J., et al., *Multifunctional uniform nanoparticles composed of a magnetite nanocrystal core and a mesoporous silica shell for magnetic resonance and fluorescence imaging and for drug delivery.* Angewandte Chemie-International Edition, 2008. **47**(44): p. 8438-8441.

292. Wu, S.H., et al., *Multifunctional mesoporous silica nanoparticles for intracellular labeling and animal magnetic resonance imaging studies.* ChemBioChem, 2008. **9**(1): p. 53-57.

293. Lee, C.H., et al., *Near-infrared mesoporous silica nanoparticles for optical imaging: characterization and in vivo biodistribution.* Advanced Functional Materials, 2009. **19**(2): p. 215-222.

294. He, Q., et al., *In vivo Biodistribution and Urinary Excretion of Mesoporous Silica Nanoparticles: Effects of Particle Size and PEGylation.* Small, 2011. **7**(2): p. 271-280.

295. Huang, X., et al., *The Shape Effect of Mesoporous Silica Nanoparticles on Biodistribution, Clearance, and Biocompatibility in Vivo.* ACS Nano, 2011. **5**(7): p. 5390-5399.

296. Lu, J., et al., *Biocompatibility, biodistribution, and drug-delivery efficiency of mesoporous silica nanoparticles for cancer therapy in animals.* Small, 2010. **6**(16): p. 1794-1805.

297. Meng, H., et al., *Use of size and a copolymer design feature to improve the biodistribution and the enhanced permeability and retention effect of doxorubicin-loaded mesoporous silica nanoparticles in a murine xenograft tumor model.* ACS nano, 2011. **5**(5): p. 4131-4144.

298. Asefa, T. and Z. Tao, *Biocompatibility of Mesoporous Silica Nanoparticles.* Chemical Research in Toxicology, 2012. **25**(11): p. 2265-2284.

299. Tarn, D., et al., *Mesoporous Silica Nanoparticle Nanocarriers: Biofunctionality and Biocompatibility.* Accounts of Chemical Research, 2013. **46**(3): p. 792-801.

300. Fadeel, B. and A.E. Garcia-Bennett, *Better safe than sorry: Understanding the toxicological properties of inorganic nanoparticles manufactured for biomedical applications.* Advanced Drug Delivery Reviews, 2010. **62**(3): p. 362-374.

301. Feliu, N. and B. Fadeel, *Nanotoxicology: no small matter.* Nanoscale, 2010. **2**(12): p. 2514-2520.

302. Lu, F., et al., *Size effect on cell uptake in well-suspended, uniform mesoporous silica nanoparticles.* Small, 2009. **5**(12): p. 1408-1413.

303. Chithrani, B.D., A.A. Ghazani, and W.C.W. Chan, *Determining the size and shape dependence of gold nanoparticle uptake into mammalian cells.* Nano letters, 2006. **6**(4): p. 662-668.

304. Osaki, F., et al., *A quantum dot conjugated sugar ball and its cellular uptake. On the size effects of endocytosis in the subviral region.* Journal of the American Chemical Society, 2004. **126**(21): p. 6520-6521.

305. He, Q., et al., *Intracellular Localization and Cytotoxicity of Spherical Mesoporous Silica Nano- and Microparticles.* Small, 2009. **5**(23): p. 2722-2729.

306. Lin, Y.-S. and C.L. Haynes, *Impacts of Mesoporous Silica Nanoparticle Size, Pore Ordering, and Pore Integrity on Hemolytic Activity.* Journal of the American Chemical Society, 2010. **132**(13): p. 4834-4842.

307. Zhao, Y., et al., *Interaction of Mesoporous Silica Nanoparticles with Human Red Blood Cell Membranes: Size and Surface Effects.* ACS Nano, 2011. **5**(2): p. 1366-1375.

308. Hudson, S.P., et al., *The biocompatibility of mesoporous silicates.* Biomaterials, 2008. **29**(30): p. 4045-4055.

309. Lu, J., et al., *Biocompatibility, Biodistribution, and Drug-Delivery Efficiency of Mesoporous Silica Nanoparticles for Cancer Therapy in Animals.* Small, 2010. **6**(16): p. 1794-1805.

310. Verma, A. and F. Stellacci, *Effect of surface properties on nanoparticle–cell interactions.* small, 2010. **6**(1): p. 12-21.

311. Nel, A.E., et al., *Understanding biophysicochemical interactions at the nano–bio interface.* Nature materials, 2009. **8**(7): p. 543-557.

312. Slowing, I.I., et al., *Mesoporous Silica Nanoparticles for Reducing Hemolytic Activity Towards Mammalian Red Blood Cells.* Small, 2009. **5**(1): p. 57-62.

313. Sheibani, S., et al., *Nanoscale characterization of the biomolecular corona by cryo-electron microscopy, cryo-electron tomography, and image simulation.* Nature Communications, 2021. **12**(1): p. 573.

314. Sharifi, S., G. Caracciolo, and M. Mahmoudi, *Biomolecular Corona Affects Controlled Release of Drug Payloads from Nanocarriers.* Trends in Pharmacological Sciences, 2020. **41**(9): p. 641-652.

315. Pozzi, D., et al., *The biomolecular corona of nanoparticles in circulating biological media.* Nanoscale, 2015. **7**(33): p. 13958-13966.

316. Geng, Y., et al., *Shape effects of filaments versus spherical particles in flow and drug delivery.* Nature Nanotechnology, 2007. **2**(4): p. 249-255.

317. Champion, J.A. and S. Mitragotri, *Role of target geometry in phagocytosis.* Proceedings of the National Academy of Sciences, 2006. **103**(13): p. 4930-4934.

318. Trewyn, B.G., et al., *Biocompatible mesoporous silica nanoparticles with different morphologies for animal cell membrane penetration.* Chemical Engineering Journal, 2008. **137**(1): p. 23-29.

319. Huang, X., et al., *The effect of the shape of mesoporous silica nanoparticles on cellular uptake and cell function.* Biomaterials, 2010. **31**(3): p. 438-448.

320. Lee, S., H.-S. Yun, and S.-H. Kim, *The comparative effects of mesoporous silica nanoparticles and colloidal silica on inflammation and apoptosis.* Biomaterials, 2011. **32**(35): p. 9434-9443.

321. Maurer-Jones, M.A., Y.-S. Lin, and C.L. Haynes, *Functional Assessment of Metal Oxide Nanoparticle Toxicity in Immune Cells.* ACS Nano, 2010. **4**(6): p. 3363-3373.

322. Yu, T., A. Malugin, and H. Ghandehari, *Impact of Silica Nanoparticle Design on Cellular Toxicity and Hemolytic Activity.* ACS Nano, 2011. **5**(7): p. 5717-5728.

323. Townson, J.L., et al., *Re-examining the Size/Charge Paradigm: Differing in Vivo Characteristics of Size- and Charge-Matched Mesoporous Silica Nanoparticles.* Journal of the American Chemical Society, 2013. **135**(43): p. 16030-16033.

324. Giménez, C., et al., *Gated Mesoporous Silica Nanoparticles for the Controlled Delivery of Drugs in Cancer Cells.* Langmuir, 2015. **31**(12): p. 3753-3762.

325. Jia, L., et al., *In vitro and in vivo evaluation of paclitaxel-loaded mesoporous silica nanoparticles with three pore sizes.* International Journal of Pharmaceutics, 2013. **445**(1): p. 12-19.

326. Roomi, M.W., et al., *Patterns of MMP-2 and MMP-9 expression in human cancer cell lines.* Oncology reports, 2009. **21**(5): p. 1323-1333.

327. Medina, C., et al., *Increased activity and expression of matrix metalloproteinase-9 in a rat model of distal colitis.* American Journal of Physiology-Gastrointestinal and Liver Physiology, 2003. **284**(1): p. G116-G122.

328. Santos-Martinez, M.J., et al., *The use of quartz crystal microbalance with dissipation (QCM-D) for studying nanoparticle-induced platelet aggregation.* International journal of nanomedicine, 2012: p. 243-255.

329. Santos-Martinez, M.J., et al., *Pegylation increases platelet biocompatibility of gold nanoparticles.* Journal of biomedical nanotechnology, 2014. **10**(6): p. 1004-1015.

330. Dos Santos, C. and L. Erthal, *Design and development of a hydrogel formulation with nanoparticles for the treatment of glioblastoma multiforme.* 2021.

331. Matos, C.P., et al., *New iron(III) anti-cancer aminobisphenolate/phenanthroline complexes: Enhancing their therapeutic potential using nanoliposomes.* International Journal of Pharmaceutics, 2022. **623**: p. 121925.

332. Kazemzadeh, P., et al., *Structure-Property Relationship for Different Mesoporous Silica Nanoparticles and its Drug Delivery Applications: A Review.* Frontiers in Chemistry, 2022. **10**.

333. Rosenholm, J.M., C. Sahlgren, and M. Lindén, *Towards multifunctional, targeted drug delivery systems using mesoporous silica nanoparticles–opportunities & challenges.* Nanoscale, 2010. **2**(10): p. 1870-1883.

334. Ramimoghadam, D., M.Z.B. Hussein, and Y.H. Taufiq-Yap, *The effect of sodium dodecyl sulfate (SDS) and cetyltrimethylammonium bromide (CTAB) on the properties of ZnO synthesized by hydrothermal method.* International journal of molecular sciences, 2012. **13**(10): p. 13275-13293.

335. Goworek, J., et al., *Thermal degradation of CTAB in as-synthesized MCM-41.* Journal of thermal analysis and calorimetry, 2009. **96**: p. 375-382.

336. Hauck, T.S., A.A. Ghazani, and W.C.W. Chan, *Assessing the Effect of Surface Chemistry on Gold Nanorod Uptake, Toxicity, and Gene Expression in Mammalian Cells.* Small, 2008. **4**(1): p. 153-159.

337. Alkilany, A.M., et al., *Cellular Uptake and Cytotoxicity of Gold Nanorods: Molecular Origin of Cytotoxicity and Surface Effects.* Small, 2009. **5**(6): p. 701-708.

338. Niidome, T., et al., *PEG-modified gold nanorods with a stealth character for in vivo applications.* Journal of Controlled Release, 2006. **114**(3): p. 343-347.

339. Qiu, Y., et al., *Surface chemistry and aspect ratio mediated cellular uptake of Au nanorods.* Biomaterials, 2010. **31**(30): p. 7606-7619.

340. Vigderman, L., P. Manna, and E.R. Zubarev, *Quantitative Replacement of Cetyl Trimethylammonium Bromide by Cationic Thiol Ligands on the Surface of Gold Nanorods and Their Extremely Large Uptake by Cancer Cells.* Angewandte Chemie International Edition, 2012. **51**(3): p. 636-641.

341. Silva, A.M., et al., *Soft cationic nanoparticles for drug delivery: Production and cytotoxicity of solid lipid nanoparticles (SLNs).* Applied Sciences, 2019. **9**(20): p. 4438.

342. Yasun, E., et al., *BSA modification to reduce CTAB induced nonspecificity and cytotoxicity of aptamer-conjugated gold nanorods.* Nanoscale, 2015. **7**(22): p. 10240-10248.

343. Wang, L., et al., *Selective Targeting of Gold Nanorods at the Mitochondria of Cancer Cells: Implications for Cancer Therapy.* Nano Letters, 2011. **11**(2): p. 772-780.

344. Yildirim, A., et al., *Cytotoxicity of multifunctional surfactant containing capped mesoporous silica nanoparticles.* RSC advances, 2016. **6**(38): p. 32060-32069.

345. Wang, L., et al., *Surface chemistry of gold nanorods: origin of cell membrane damage and cytotoxicity.* Nanoscale, 2013. **5**(18): p. 8384-8391.

346. Mourdikoudis, S., R.M. Pallares, and N.T.K. Thanh, *Characterization techniques for nanoparticles: comparison and complementarity upon studying nanoparticle properties.* Nanoscale, 2018. **10**(27): p. 12871-12934.

347. Kumar, A. and C.K. Dixit, *Methods for characterization of nanoparticles*, in *Advances in nanomedicine for the delivery of therapeutic nucleic acids*. 2017, Elsevier. p. 43-58.

348. Thommes, M., et al., *Physisorption of gases, with special reference to the evaluation of surface area and pore size distribution (IUPAC Technical Report).* Pure and applied chemistry, 2015. **87**(9-10): p. 1051-1069.

349. Oliveira, D.M. and A.S. Andrada, *Synthesis of ordered mesoporous silica MCM-41 with controlled morphology for potential application in controlled drug delivery systems.* Cerâmica, 2019. **65**: p. 170-179.

350. De La Torre, C., et al., *Gated mesoporous silica nanoparticles using a double-role circular peptide for the controlled and target-preferential release of doxorubicin in CXCR4-expresing lymphoma cells.* Advanced Functional Materials, 2015. **25**(5): p. 687-695.

351. von Baeckmann, C., et al., *On the importance of the linking chemistry for the PEGylation of mesoporous silica nanoparticles.* Journal of Colloid and Interface Science, 2021. **589**: p. 453-461.

352. Cui, Y., et al., *Mesoporous Silica Nanoparticles Capped with Disulfide-Linked PEG Gatekeepers for Glutathione-Mediated Controlled Release.* ACS Applied Materials & Interfaces, 2012. **4**(6): p. 3177-3183.

353. Che, E., et al., *Paclitaxel/gelatin coated magnetic mesoporous silica nanoparticles: Preparation and antitumor efficacy in vivo.* Microporous and Mesoporous Materials, 2015. **204**: p. 226-234.

354. Elzoghby, A.O., *Gelatin-based nanoparticles as drug and gene delivery systems: Reviewing three decades of research.* Journal of Controlled Release, 2013. **172**(3): p. 1075-1091.

355. Zou, Z., et al., *Programmed packaging of mesoporous silica nanocarriers for matrix metalloprotease 2-triggered tumor targeting and release.* Biomaterials, 2015. **58**: p. 35-45.

356. Kommareddy, S., D.B. Shenoy, and M.M. Amiji, *Gelatin nanoparticles and their biofunctionalization.* Nanotechnologies for the life sciences: Online, 2007.

357. Martínez-Carmona, M., et al., *Selective topotecan delivery to cancer cells by targeted pH-sensitive mesoporous silica nanoparticles.* RSC advances, 2016. **6**(56): p. 50923-50932.

358. Esfahani, M.K., et al. *PEGylated Mesoporous Silica Nanoparticles (MCM-41): A Promising Carrier for the Targeted Delivery of Fenbendazole into Prostrate Cancer Cells.* Pharmaceutics, 2021. **13**, DOI: 10.3390/pharmaceutics13101605.

359. Ahsan, S.M. and C.M. Rao, *The role of surface charge in the desolvation process of gelatin: implications in nanoparticle synthesis and modulation of drug release.* International journal of nanomedicine, 2017. **12**: p. 795-808.

360. Liao, Y.-T., et al., *Gelatin-functionalized mesoporous silica nanoparticles with sustained release properties for intracameral pharmacotherapy of glaucoma.* Journal of Materials Chemistry B, 2017. **5**(34): p. 7008-7013.

361. Martin, V., *Overview of Paclitaxel (TAXOL®).* Seminars in Oncology Nursing, 1993. **9**(4, Supplement 2): p. 2-5.

362. Nicolaou, K.C., W.-M. Dai, and R.K. Guy, *Chemistry and Biology of Taxol.* Angewandte Chemie International Edition in English, 1994. **33**(1): p. 15-44.

363. Goldspiel, B.R., *Pharmaceutical issues: preparation, administration, stability, and compatibility with other medications.* Annals of pharmacotherapy, 1994. **28**(5_suppl): p. S23-S26.

364. Panchagnula, R., *Pharmaceutical aspects of paclitaxel.* International Journal of Pharmaceutics, 1998. **172**(1): p. 1-15.

365. Yang, T., et al., *Preparation and evaluation of paclitaxel-loaded PEGylated immunoliposome.* Journal of Controlled Release, 2007. **120**(3): p. 169-177.

366. Hu, F.-Q., et al., *Shell cross-linked stearic acid grafted chitosan oligosaccharide self-aggregated micelles for controlled release of paclitaxel.* Colloids and Surfaces B: Biointerfaces, 2006. **50**(2): p. 97-103.

367. Rossi, J., et al., *Long-circulating poly (ethylene glycol)-coated emulsions to target solid tumors.* European journal of pharmaceutics and biopharmaceutics, 2007. **67**(2): p. 329-338.

368. Li, R., J.S. Eun, and M.-K. Lee, *Pharmacokinetics and biodistribution of paclitaxel loaded in pegylated solid lipid nanoparticles after intravenous administration.* Archives of pharmacal research, 2011. **34**: p. 331-337.

369. Desai, S., A. Poddar, and K. Sawant, *Formulation of cyclodextrin inclusion complex-based orally disintegrating tablet of eslicarbazepine acetate for improved oral bioavailability.* Materials Science and Engineering: C, 2016. **58**: p. 826-834.

370. Riekes, M.K., et al., *Enhanced solubility and dissolution rate of amiodarone by complexation with β-cyclodextrin through different methods.* Materials Science and Engineering: C, 2010. **30**(7): p. 1008-1013.

371. Mishra, B., J. Sahoo, and P.K. Dixit, *Enhanced bioavailability of cinnarizine nanosuspensions by particle size engineering: Optimization and physicochemical investigations.* Materials Science and Engineering: C, 2016. **63**: p. 62-69.

372. Liggins, R.T. and H.M. Burt, *Polyether–polyester diblock copolymers for the preparation of paclitaxel loaded polymeric micelle formulations.* Advanced drug delivery reviews, 2002. **54**(2): p. 191-202.

373. Lee, M.-K., S.-J. Lim, and C.-K. Kim, *Preparation, characterization and in vitro cytotoxicity of paclitaxel-loaded sterically stabilized solid lipid nanoparticles.* Biomaterials, 2007. **28**(12): p. 2137-2146.

374. Kim, S.C., et al., *In vivo evaluation of polymeric micellar paclitaxel formulation: toxicity and efficacy.* Journal of Controlled Release, 2001. **72**(1): p. 191-202.

375. Onetto, N., et al., *Overview of Taxol safety.* Journal of the National Cancer Institute. Monographs, 1993(15): p. 131-139.

376. Lorenz, W., et al., *Histamine release in dogs by Cremophor El® and its derivatives: Oxethylated oleic acid is the most effective constituent.* Agents and actions, 1977. **7**(1): p. 63-67.

377. Dye, D. and J. Watkins, *Suspected anaphylactic reaction to Cremophor EL.* British medical journal, 1980. **280**(6228): p. 1353.

378. Spencer, C.M. and D. Faulds, *Paclitaxel: a review of its pharmacodynamic and pharmacokinetic properties and therapeutic potential in the treatment of cancer.* Drugs, 1994. **48**(5): p. 794-847.

379. Szebeni, J., C.R. Alving, and F.M. Muggia, *Complement Activation by Cremophor EL as a Possible Contributor to Hypersensitivity to Paclitaxel: an In Vitro Study.* JNCI: Journal of the National Cancer Institute, 1998. **90**(4): p. 300-306.

380. Weiss, R.B., et al., *Hypersensitivity reactions from taxol.* Journal of Clinical Oncology, 1990. **8**(7): p. 1263-1268.

381. Ibrahim, N.K., et al., *Phase I and Pharmacokinetic Study of ABI-007, a Cremophor-free, Protein-stabilized, Nanoparticle Formulation of Paclitaxel1.* Clinical Cancer Research, 2002. **8**(5): p. 1038-1044.

382. Ibrahim, N.K., et al., *Multicenter phase II trial of ABI-007, an albumin-bound paclitaxel, in women with metastatic breast cancer.* Journal of clinical oncology, 2005. **23**(25): p. 6019-6026.

383. Gradishar, W.J., et al., *Phase III Trial of Nanoparticle Albumin-Bound Paclitaxel Compared With Polyethylated Castor Oil–Based Paclitaxel in Women With Breast Cancer.* Journal of Clinical Oncology, 2005. **23**(31): p. 7794-7803.

384. Nyman, D.W., et al., *Phase I and Pharmacokinetics Trial of ABI-007, a Novel Nanoparticle Formulation of Paclitaxel in Patients With Advanced Nonhematologic Malignancies.* Journal of Clinical Oncology, 2005. **23**(31): p. 7785-7793.

385. Desai, N., et al., *Increased antitumor activity, intratumor paclitaxel concentrations, and endothelial cell transport of cremophor-free, albumin-bound paclitaxel, ABI-007, compared with cremophor-based paclitaxel.* Clinical Cancer Research, 2006. **12**(4): p. 1317-1324.

386. Vishnu, P. and V. Roy, *Safety and efficacy of nab-paclitaxel in the treatment of patients with breast cancer.* Breast Cancer: Basic and Clinical Research, 2011. **5**: p. BCBCR-S5857.

387. Zheng, J., et al., *Targeted Paclitaxel Delivery to Tumors Using Cleavable PEG-Conjugated Solid Lipid Nanoparticles.* Pharmaceutical Research, 2014. **31**(8): p. 2220-2233.

388. He, Y., et al., *Mesoporous silica nanoparticles as potential carriers for enhanced drug solubility of paclitaxel.* Materials science &amp; engineering. C, Materials for biological applications, 2017. **78**: p. 12-17.

389. Fang, R., et al., *Nanoscale Drug Delivery Systems: A Current Review on the Promising Paclitaxel Formulations for Future Cancer Therapy.* Nano, 2015. **10**(05): p. 1530004.

390. Cai, S., et al., *Micelles of Different Morphologies—Advantages of Worm-like Filomicelles of PEO-PCL in Paclitaxel Delivery.* Pharmaceutical Research, 2007. **24**(11): p. 2099-2109.

391. Wang, J., et al., *Rational Design of Multifunctional Dendritic Mesoporous Silica Nanoparticles to Load Curcumin and Enhance Efficacy for Breast Cancer Therapy.* ACS Applied Materials & Interfaces, 2016. **8**(40): p. 26511-26523.

392. Sarkar, A., et al., *Targeted delivery of quercetin loaded mesoporous silica nanoparticles to the breast cancer cells.* Biochimica et Biophysica Acta (BBA) - General Subjects, 2016. **1860**(10): p. 2065-2075.

393. Li, J., et al., *Effects of pore size on in vitro and in vivo anticancer efficacies of mesoporous silica nanoparticles.* RSC advances, 2018. **8**(43): p. 24633-24640.

394. Jafari, S., et al., *Mesoporous silica nanoparticles for therapeutic/diagnostic applications.* Biomedicine & Pharmacotherapy, 2019. **109**: p. 1100-1111.

395. Niroumand, U., et al., *The Effect of Size, Morphology and Surface Properties of Mesoporous Silica Nanoparticles on Pharmacokinetic Aspects and Potential Toxicity Concerns.* Frontiers in Materials. **10**: p. 237.

396. Djayanti, K., et al. *Mesoporous Silica Nanoparticles as a Potential Nanoplatform: Therapeutic Applications and Considerations.* International Journal of Molecular Sciences, 2023. **24**, DOI: 10.3390/ijms24076349.

397. Popat, A., et al., *Mesoporous silica nanoparticles for bioadsorption, enzyme immobilisation, and delivery carriers.* Nanoscale, 2011. **3**(7): p. 2801-2818.

398. Kioni, P.N., et al., *Synthesis and characterization of ordered mesoporous silica nanoparticles with tunable physical properties by varying molar composition of reagents.* 2011.

399. Tian, Z., Y. Xu, and Y. Zhu, *Aldehyde-functionalized dendritic mesoporous silica nanoparticles as potential nanocarriers for pH-responsive protein drug delivery.* Materials Science and Engineering: C, 2017. **71**: p. 452-459.

266

400.    Melguizo, C., et al., *Enhanced antitumoral activity of doxorubicin against lung cancer cells using biodegradable poly (butylcyanoacrylate) nanoparticles.* Drug design, development and therapy, 2015. **9**: p. 6433.

401.    Velusamy, P., et al., *A pH stimuli thiol modified mesoporous silica nanoparticles: Doxorubicin carrier for cancer therapy.* Journal of the Taiwan Institute of Chemical Engineers, 2018. **87**: p. 264-271.

402.    Zhang, M. and L. Jiang, *Doxorubicin hydrochloride-loaded mesoporous silica nanoparticles inhibit non-small cell lung cancer metastasis by suppressing VEGF-mediated angiogenesis.* Journal of biomedical nanotechnology, 2016. **12**(11): p. 1975-1986.

403.    Nguyen, T.N., et al. *Optical Properties of Doxorubicin Hydrochloride Load and Release on Silica Nanoparticle Platform*. Molecules, 2021. **26**, DOI: 10.3390/molecules26133968.

404.    Roik, N.V., L.A. Belyakova, and M.O. Dziazko, *Adsorption of antitumor antibiotic doxorubicin on MCM-41-type silica surface.* Adsorption Science & Technology, 2017. **35**(1-2): p. 86-101.

405.    Zou, Z., et al., *Natural gelatin capped mesoporous silica nanoparticles for intracellular acid-triggered drug delivery.* Langmuir, 2013. **29**(41): p. 12804-12810.

406.    Xie, Z., et al., *The properties of mesoporous silica nanoparticles functionalized with different PEG-chain length via the disulfide bond linker and drug release in glutathione medium.* Journal of Biomaterials Science, Polymer Edition, 2016. **27**(1): p. 55-68.

407.    Iyer, R., et al., *Glutathione-responsive biodegradable polyurethane nanoparticles for lung cancer treatment.* Journal of Controlled Release, 2020. **321**: p. 363-371.

408.    Wang, K., et al., *Novel shell-cross-linked micelles with detachable PEG corona for glutathione-mediated intracellular drug delivery.* Soft Matter, 2013. **9**(3): p. 692-699.

409.    Iizasa, T., et al., *Elevated Levels of Circulating Plasma Matrix Metalloproteinase 9 in Non-Small Cell Lung Cancer Patients1.* Clinical Cancer Research, 1999. **5**(1): p. 149-153.

410.    Zucker, S., et al., *Mr 92,000 Type IV Collagenase Is Increased in Plasma of Patients with Colon Cancer and Breast Cancer1.* Cancer Research, 1993. **53**(1): p. 140-146.

411.    Zhang, Y., et al., *Detection of circulating vascular endothelial growth factor and matrix metalloproteinase-9 in non-small cell lung cancer using Luminex multiplex technology.* Oncology Letters, 2014. **7**(2): p. 499-506.

412.    Fiorelli, A., et al., *Correlation between matrix metalloproteinase 9 and 18F-2-fluoro-2-deoxyglucose-positron emission tomography as diagnostic markers of lung cancer†.* European Journal of Cardio-Thoracic Surgery, 2012. **41**(4): p. 852-860.

413.    Jumper, C., E. Cobos, and C. Lox, *Determination of the serum matrix metalloproteinase-9 (MMP-9) and tissue inhibitor of matrix metalloproteinase-1 (TIMP-1) in patients with either advanced small-cell lung cancer or non-small-cell lung cancer prior to treatment.* Respiratory Medicine, 2004. **98**(2): p. 173-177.

414.    Shah, S.A., et al., *Differential matrix metalloproteinase levels in adenocarcinoma and squamous cell carcinoma of the lung.* The Journal of Thoracic and Cardiovascular Surgery, 2010. **139**(4): p. 984-990.

415. Jin, Y., et al., *Protein expression and significance of VEGF, EGFR and MMP-9 in non-small cell lung carcinomas.* Asian Pac J Cancer Prev, 2011. **12**(6): p. 1473-1476.

416. Rosellini, E., et al., *Preparation and characterization of alginate/gelatin blend films for cardiac tissue engineering.* Journal of Biomedical Materials Research Part A, 2009. **91A**(2): p. 447-453.

417. Treuel, L. and G.U. Nienhaus, *Toward a molecular understanding of nanoparticle–protein interactions.* Biophysical reviews, 2012. **4**: p. 137-147.

418. Walczyk, D., et al., *What the cell "sees" in bionanoscience.* Journal of the American Chemical Society, 2010. **132**(16): p. 5761-5768.

419. Leszczynski, J., *Nano meets bio at the interface.* Nature Nanotechnology, 2010. **5**(9): p. 633-634.

420. Moreau, J.W., et al., *Extracellular proteins limit the dispersal of biogenic nanoparticles.* Science, 2007. **316**(5831): p. 1600-1603.

421. Gref, R., et al., *'Stealth' corona-core nanoparticles surface modified by polyethylene glycol (PEG): influences of the corona (PEG chain length and surface density) and of the core composition on phagocytic uptake and plasma protein adsorption.* Colloids and Surfaces B: Biointerfaces, 2000. **18**(3): p. 301-313.

422. Gessner, A., et al., *Functional groups on polystyrene model nanoparticles: influence on protein adsorption.* Journal of Biomedical Materials Research Part A: An Official Journal of The Society for Biomaterials, The Japanese Society for Biomaterials, and The Australian Society for Biomaterials and the Korean Society for Biomaterials, 2003. **65**(3): p. 319-326.

423. Gessner, A., et al., *Nanoparticles with decreasing surface hydrophobicities: influence on plasma protein adsorption.* International journal of pharmaceutics, 2000. **196**(2): p. 245-249.

424. Thode, K., et al., *Determination of plasma protein adsorption on magnetic iron oxides: sample preparation.* Pharmaceutical research, 1997. **14**: p. 905-910.

425. Lundqvist, M., et al., *Nanoparticle size and surface properties determine the protein corona with possible implications for biological impacts.* Proceedings of the National Academy of Sciences, 2008. **105**(38): p. 14265-14270.

426. Cedervall, T., et al., *Detailed Identification of Plasma Proteins Adsorbed on Copolymer Nanoparticles.* Angewandte Chemie International Edition, 2007. **46**(30): p. 5754-5756.

427. Faunce, T.A., J. White, and K.I. Matthaei, *Integrated research into the nanoparticle–protein corona: a new focus for safe, sustainable and equitable development of nanomedicines.* 2008.

428. Casals, E., et al., *Time Evolution of the Nanoparticle Protein Corona.* ACS Nano, 2010. **4**(7): p. 3623-3632.

429. Casals, E., et al., *Hardening of the nanoparticle–protein corona in metal (Au, Ag) and oxide (Fe3O4, CoO, and CeO2) nanoparticles.* Small, 2011. **7**(24): p. 3479-3486.

430. Gunawan, C., et al., *Nanoparticle–protein corona complexes govern the biological fates and functions of nanoparticles.* Journal of Materials Chemistry B, 2014. **2**(15): p. 2060-2083.

431. Izak-Nau, E., et al., *Altered characteristics of silica nanoparticles in bovine and human serum: the importance of nanomaterial characterization prior to its toxicological evaluation.* Particle and fibre toxicology, 2013. **10**(1): p. 1-12.

432. Monopoli, M.P., et al., *Physical−Chemical Aspects of Protein Corona: Relevance to in Vitro and in Vivo Biological Impacts of Nanoparticles.* Journal of the American Chemical Society, 2011. **133**(8): p. 2525-2534.

433. Pisani, C., et al., *The timeline of corona formation around silica nanocarriers highlights the role of the protein interactome.* Nanoscale, 2017. **9**(5): p. 1840-1851.

434. von Roemeling, C., et al., *Breaking down the barriers to precision cancer nanomedicine.* Trends in biotechnology, 2017. **35**(2): p. 159-171.

435. Desai, N., *Challenges in development of nanoparticle-based therapeutics.* The AAPS journal, 2012. **14**(2): p. 282-295.

436. Aljabali, A.A., et al. *Nanomaterials and Their Impact on the Immune System.* International Journal of Molecular Sciences, 2023. **24**, DOI: 10.3390/ijms24032008.

437. Harris, J.M. and R.B. Chess, *Effect of pegylation on pharmaceuticals.* Nature reviews Drug discovery, 2003. **2**(3): p. 214-221.

438. Walkey, C.D. and W.C.W. Chan, *Understanding and controlling the interaction of nanomaterials with proteins in a physiological environment.* Chemical Society Reviews, 2012. **41**(7): p. 2780-2799.

439. Shahabi, S., et al., *Enhancing Cellular Uptake and Doxorubicin Delivery of Mesoporous Silica Nanoparticles via Surface Functionalization: Effects of Serum.* ACS Applied Materials & Interfaces, 2015. **7**(48): p. 26880-26891.

440. Shannahan, J., *The biocorona: a challenge for the biomedical application of nanoparticles.* Nanotechnology reviews, 2017. **6**(4): p. 345-353.

441. Lesniak, A., et al., *Effects of the Presence or Absence of a Protein Corona on Silica Nanoparticle Uptake and Impact on Cells.* ACS Nano, 2012. **6**(7): p. 5845-5857.

442. Iso, I., *10993–5: 2009 Biological evaluation of medical devices—part 5: tests for in vitro cytotoxicity.* International Organization for Standardization, Geneva, 2009: p. 34.

443. Bakand, S., et al., *In vitro cytotoxicity of formaldehyde and glutaraldehyde mixtures in human cells.* 2006.

444. Beauchamp, R.O., et al., *A critical review of the toxicology of glutaraldehyde.* Critical Reviews in Toxicology, 1992. **22**(3-4): p. 143-174.

445. Islam, N., I. Dmour, and M.O. Taha, *Degradability of chitosan micro/nanoparticles for pulmonary drug delivery.* Heliyon, 2019. **5**(5): p. e01684.

446. Azami, M., M. Rabiee, and F. Moztarzadeh, *Glutaraldehyde crosslinked gelatin/hydroxyapatite nanocomposite scaffold, engineered via compound techniques.* Polymer composites, 2010. **31**(12): p. 2112-2120.

447. Ros, R.O.S., *Serial review: role of reactive oxygen and nitrogen species (ROS/RNS) in lung injury and diseases.* Free radical biology & medicine, 2003. **34**(12): p. 1507-1516.

448. Wang, J.J., B.J.S. Sanderson, and H. Wang, *Cytotoxicity and genotoxicity of ultrafine crystalline SiO2 particulate in cultured human lymphoblastoid cells.* Environmental and Molecular Mutagenesis, 2007. **48**(2): p. 151-157.

449. Di Pasqua, A.J., et al., *Cytotoxicity of mesoporous silica nanomaterials.* Journal of Inorganic Biochemistry, 2008. **102**(7): p. 1416-1423.

450. Lin, W., et al., *In vitro toxicity of silica nanoparticles in human lung cancer cells.* Toxicology and Applied Pharmacology, 2006. **217**(3): p. 252-259.

451. Tao, Z., et al., *Mesoporosity and Functional Group Dependent Endocytosis and Cytotoxicity of Silica Nanomaterials.* Chemical Research in Toxicology, 2009. **22**(11): p. 1869-1880.

452. Gehrke, H., et al., *In vitro toxicity of amorphous silica nanoparticles in human colon carcinoma cells.* Nanotoxicology, 2013. **7**(3): p. 274-293.

453. Kostiv, U., et al., *Physico-chemical characteristics, biocompatibility, and MRI applicability of novel monodisperse PEG-modified magnetic Fe 3 O 4 &SiO 2 core–shell nanoparticles.* RSC advances, 2017. **7**(15): p. 8786-8797.

454. Stayton, I., et al., *Study of uptake and loss of silica nanoparticles in living human lung epithelial cells at single cell level.* Analytical and Bioanalytical Chemistry, 2009. **394**(6): p. 1595-1608.

455. Zhang, L., et al., *Doxorubicin-loaded polypeptide nanorods based on electrostatic interactions for cancer therapy.* Journal of Colloid and Interface Science, 2016. **464**: p. 126-136.

456. Carvalho, C., et al., *Doxorubicin: the good, the bad and the ugly effect.* Current medicinal chemistry, 2009. **16**(25): p. 3267-3285.

457. Alqahtani, F.Y., et al., *Paclitaxel.* Profiles of Drug Substances, Excipients, and Related Methodology, 2019. **44**: p. 205-238.

458. Jiménez-López, J., et al., *Paclitaxel antitumor effect improvement in lung cancer and prevention of the painful neuropathy using large pegylated cationic liposomes.* Biomedicine & Pharmacotherapy, 2021. **133**: p. 111059.

459. Mo, Y. and L.-Y. Lim, *Paclitaxel-loaded PLGA nanoparticles: Potentiation of anticancer activity by surface conjugation with wheat germ agglutinin.* Journal of Controlled Release, 2005. **108**(2): p. 244-262.

460. Torres, K. and S.B. Horwitz, *Mechanisms of Taxol-induced cell death are concentration dependent.* Cancer research, 1998. **58**(16): p. 3620-3626.

461. Marupudi, N.I., et al., *Paclitaxel: a review of adverse toxicities and novel delivery strategies.* Expert Opinion on Drug Safety, 2007. **6**(5): p. 609-621.

462. Fonseca, C., S. Simões, and R. Gaspar, *Paclitaxel-loaded PLGA nanoparticles: preparation, physicochemical characterization and in vitro anti-tumoral activity.* Journal of Controlled Release, 2002. **83**(2): p. 273-286.

463. Lu, H., et al., *Paclitaxel nanoparticle inhibits growth of ovarian cancer xenografts and enhances lymphatic targeting.* Cancer Chemotherapy and Pharmacology, 2007. **59**(2): p. 175-181.

464. Lopes, N.M., et al., *Cell kill kinetics and cell cycle effects of taxol on human and hamster ovarian cell lines.* Cancer Chemotherapy and Pharmacology, 1993. **32**(3): p. 235-242.

465. Yakisich, J.S., et al., *Chemoresistance of Lung and Breast Cancer Cells Growing Under Prolonged Periods of Serum Starvation.* Journal of Cellular Physiology, 2017. **232**(8): p. 2033-2043.

466. Orr, G.A., et al., *Mechanisms of Taxol resistance related to microtubules.* Oncogene, 2003. **22**(47): p. 7280-7295.

467. Replogle, J.M., et al., *Aneuploidy increases resistance to chemotherapeutics by antagonizing cell division.* Proceedings of the National Academy of Sciences, 2020. **117**(48): p. 30566-30576.

468. Chen, J.-G. and S.B. Horwitz, *Differential Mitotic Responses to Microtubule-stabilizing and -destabilizing Drugs1.* Cancer Research, 2002. **62**(7): p. 1935-1938.

469. White, E.Z., et al., *Serum deprivation initiates adaptation and survival to oxidative stress in prostate cancer cells.* Scientific Reports, 2020. **10**(1): p. 12505.

470. Park, E.-J. and K. Park, *Oxidative stress and pro-inflammatory responses induced by silica nanoparticles in vivo and in vitro.* Toxicology Letters, 2009. **184**(1): p. 18-25.

471. Sydlik, U., et al., *Ultrafine carbon particles induce apoptosis and proliferation in rat lung epithelial cells via specific signaling pathways both using EGF-R.* American Journal of Physiology-Lung Cellular and Molecular Physiology, 2006. **291**(4): p. L725-L733.

472. Allalunis-Turner, M.J., F.Y.F. Lee, and D.W. Siemann, *Comparison of Glutathione Levels in Rodent and Human Tumor Cells Grown in Vitro and in Vivo1.* Cancer Research, 1988. **48**(13): p. 3657-3660.

473. Morstyn, G., et al., *Heterogeneity in the radiation survival curves and biochemical properties of human lung cancer cell lines.* Journal of the National Cancer Institute, 1984. **73**(4): p. 801-807.

474. Mitchell, J.B., et al., *The relationship of SR-2508 sensitizer enhancement ratio to cellular glutathione levels in human tumor cell lines.* International Journal of Radiation Oncology* Biology* Physics, 1986. **12**(7): p. 1143-1146.

475. Silva, M.M., et al., *The balance between NRF2/GSH antioxidant mediated pathway and DNA repair modulates cisplatin resistance in lung cancer cells.* Scientific reports, 2019. **9**(1): p. 17639-17639.

476. Shin, H., et al., *Quantifying the level of nanoparticle uptake in mammalian cells using flow cytometry.* Nanoscale, 2020. **12**(29): p. 15743-15751.

477. Fritsch-Decker, S., et al., *Silica Nanoparticles Provoke Cell Death Independent of p53 and BAX in Human Colon Cancer Cells.* Nanomaterials (Basel, Switzerland), 2019. **9**(8): p. 1172.

478. Morishige, T., et al., *Suppression of nanosilica particle-induced inflammation by surface modification of the particles.* Archives of Toxicology, 2012. **86**(8): p. 1297-1307.

479. dos Santos, T., et al., *Quantitative Assessment of the Comparative Nanoparticle-Uptake Efficiency of a Range of Cell Lines.* Small, 2011. **7**(23): p. 3341-3349.

480. Toth, M. and R. Fridman, *Assessment of Gelatinases (MMP-2 and MMP-9 by Gelatin Zymography.* Methods in molecular medicine, 2001. **57**: p. 163-174.

481. Kodate, M., et al., *Expression of matrix metalloproteinase (gelatinase) in T1 adenocarcinoma of the lung.* Pathology international, 1997. **47**(7): p. 461-469.

482. Blanco-Prieto, S., et al., *Relevance of matrix metalloproteases in non-small cell lung cancer diagnosis.* BMC cancer, 2017. **17**(1): p. 1-8.

483. Habanjar, O., et al. *3D Cell Culture Systems: Tumor Application, Advantages, and Disadvantages.* International Journal of Molecular Sciences, 2021. **22**, DOI: 10.3390/ijms222212200.

484. Salinas-Vera, Y.M., et al., *Three-Dimensional 3D Culture Models in Gynecological and Breast Cancer Research.* Frontiers in Oncology, 2022. **12**.

485. Wanigasekara, J., et al., *Advances in 3D culture systems for therapeutic discovery and development in brain cancer.* Drug Discovery Today, 2023. **28**(2): p. 103426.

486. Petersen, O.W., et al., *Interaction with basement membrane serves to rapidly distinguish growth and differentiation pattern of normal and malignant human breast epithelial cells.* Proceedings of the National Academy of Sciences, 1992. **89**(19): p. 9064-9068.

487. Mó, I., et al., *The importance of spheroids in analyzing nanomedicine efficacy.* Nanomedicine, 2020. **15**(15): p. 1513-1525.

488. Paolillo, M., S. Comincini, and S. Schinelli *In Vitro Glioblastoma Models: A Journey into the Third Dimension.* Cancers, 2021. **13**, DOI: 10.3390/cancers13102449.

489. Erthal, L.C.S., et al., *Nanocomposite formulation for a sustained release of free drug and drug-loaded responsive nanoparticles: an approach for a local therapy of glioblastoma multiforme.* Scientific Reports, 2023. **13**(1): p. 5094.

490. de la Torre, C., et al., *In Situ-Forming Gels Loaded with Stimuli-Responsive Gated Mesoporous Silica Nanoparticles for Local Sustained Drug Delivery.* Pharmaceutics, 2023. **15**(4): p. 1071.

491. Janjua, T.I., et al., *Facile synthesis of lactoferrin conjugated ultra small large pore silica nanoparticles for the treatment of glioblastoma.* Nanoscale, 2021. **13**(40): p. 16909-16922.

492. Mo, J., et al., *Tailoring Particle Size of Mesoporous Silica Nanosystem To Antagonize Glioblastoma and Overcome Blood–Brain Barrier.* ACS Applied Materials & Interfaces, 2016. **8**(11): p. 6811-6825.

493. Vehlow, A. and N. Cordes, *Invasion as target for therapy of glioblastoma multiforme.* Biochimica et Biophysica Acta (BBA) - Reviews on Cancer, 2013. **1836**(2): p. 236-244.

494. Hagemann, C., et al., *A complete compilation of matrix metalloproteinase expression in human malignant gliomas.* World journal of clinical oncology, 2012. **3**(5): p. 67-79.

495. Rao, J.S., *Molecular mechanisms of glioma invasiveness: the role of proteases.* Nature Reviews Cancer, 2003. **3**(7): p. 489-501.

496. Forsyth, P.A., et al., *Gelatinase-A (MMP-2), gelatinase-B (MMP-9) and membrane type matrix metalloproteinase-1 (MT1-MMP) are involved in different aspects of the pathophysiology of malignant gliomas.* British journal of cancer, 1999. **79**(11): p. 1828-1835.

497. Sawaya, R.E., et al., *Expression and localization of 72 kDa type IV collagenase (MMP-2) in human malignant gliomas in vivo.* Clinical & experimental metastasis, 1996. **14**: p. 35-42.

498. Lampert, K., et al., *Expression of matrix metalloproteinases and their tissue inhibitors in human brain tumors.* The American journal of pathology, 1998. **153**(2): p. 429-437.

499. Nakano, A., et al., *Matrix metalloproteinases and tissue inhibitors of metalloproteinases in human gliomas.* Journal of neurosurgery, 1995. **83**(2): p. 298-307.

500. Raithatha, S.A., et al., *Localization of gelatinase-A and gelatinase-B mRNA and protein in human gliomas.* Neuro-oncology, 2000. **2**(3): p. 145-150.

501. Lakka, S.S., et al., *Inhibition of cathepsin B and MMP-9 gene expression in glioblastoma cell line via RNA interference reduces tumor cell invasion, tumor growth and angiogenesis.* Oncogene, 2004. **23**(27): p. 4681-4689.

502. Lakka, S.S., et al., *Adenovirus-mediated expression of antisense MMP-9 in glioma cells inhibits tumor growth and invasion.* Oncogene, 2002. **21**(52): p. 8011-8019.

503. Rao, J.S., et al., *Role of plasminogen activator and of 92-KDa type IV collagenase in glioblastoma invasion using an in vitro matrigel model.* Brain Tumor Invasiveness, 1994: p. 41-50.

504. Kesanakurti, D., et al., *Role of MMP-2 in the regulation of IL-6/Stat3 survival signaling via interaction with α5β1 integrin in glioma.* Oncogene, 2013. **32**(3): p. 327-340.

505. Kesanakurti, D., et al., *Functional cooperativity by direct interaction between PAK4 and MMP-2 in the regulation of anoikis resistance, migration and invasion in glioma.* Cell death & disease, 2012. **3**(12): p. e445-e445.

506. Badiga, A.V., et al., *MMP-2 siRNA inhibits radiation-enhanced invasiveness in glioma cells.* PloS one, 2011. **6**(6): p. e20614.

507. Zengin, E., et al., *Alterations in lipid peroxidation and antioxidant status in different types of intracranial tumors within their relative peritumoral tissues.* Clinical neurology and neurosurgery, 2009. **111**(4): p. 345-351.

508. Wright, A.J., et al., *Ex-vivo HRMAS of adult brain tumours: metabolite quantification and assignment of tumour biomarkers.* Molecular cancer, 2010. **9**(1): p. 1-18.

509. Opstad, K.S., et al., *Detection of elevated glutathione in meningiomas by quantitative in vivo 1H MRS.* Magnetic Resonance in Medicine: An Official Journal of the International Society for Magnetic Resonance in Medicine, 2003. **49**(4): p. 632-637.

510. Lynch, I., A. Salvati, and K.A. Dawson, *What does the cell see?* Nature Nanotechnology, 2009. **4**(9): p. 546-547.

511. Bhavsar, D., V. Patel, and K. Sawant, *Systematic investigation of in vitro and in vivo safety, toxicity and degradation of mesoporous silica nanoparticles synthesized using commercial sodium silicate.* Microporous and Mesoporous Materials, 2019. **284**: p. 343-352.

512. Mamaeva, V., C. Sahlgren, and M. Lindén, *Mesoporous silica nanoparticles in medicine—Recent advances.* Advanced Drug Delivery Reviews, 2013. **65**(5): p. 689-702.

513. Kumar, R., et al., *In Vivo Biodistribution and Clearance Studies Using Multimodal Organically Modified Silica Nanoparticles.* ACS Nano, 2010. **4**(2): p. 699-708.

514. He, Q. and J. Shi, *Mesoporous silica nanoparticle based nano drug delivery systems: synthesis, controlled drug release and delivery, pharmacokinetics and biocompatibility.* Journal of Materials Chemistry, 2011. **21**(16): p. 5845-5855.

515. MacCuaig, W.M., et al. *Toxicity Assessment of Mesoporous Silica Nanoparticles upon Intravenous Injection in Mice: Implications for Drug Delivery*. Pharmaceutics, 2022. **14**, DOI: 10.3390/pharmaceutics14050969.

516. Song, Y.-Y., et al., *Graphene oxide coating core–shell silver sulfide@ mesoporous silica for active targeted dual-mode imaging and chemo-photothermal synergistic therapy against tumors.* Journal of Materials Chemistry B, 2018. **6**(29): p. 4808-4820.

517. Sweeney, S.K., et al., *Peptide-mediated targeting mesoporous silica nanoparticles: a novel tool for fighting bladder cancer.* Journal of biomedical nanotechnology, 2017. **13**(2): p. 232-242.

518. Kwon, D., et al., *Extra-large pore mesoporous silica nanoparticles for directing in vivo M2 macrophage polarization by delivering IL-4.* Nano letters, 2017. **17**(5): p. 2747-2756.

519. Dréau, D., et al., *Mucin-1-antibody-conjugated mesoporous silica nanoparticles for selective breast cancer detection in a mucin-1 transgenic murine mouse model.* Journal of biomedical nanotechnology, 2016. **12**(12): p. 2172-2184.

520. Wang, H.-q., et al., *Construction of ICG encapsulated W18O49@ MSN as a fluorescence carrier for real-time tracked photothermal therapy.* Materials Science and Engineering: C, 2017. **80**: p. 102-109.

521. Zeng, C., et al., *Intraoperative identification of liver cancer microfoci using a targeted near-infrared fluorescent probe for imaging-guided surgery.* Scientific Reports, 2016. **6**(1): p. 21959.

522. Desai, D., et al., *Targeted modulation of cell differentiation in distinct regions of the gastrointestinal tract via oral administration of differently PEG-PEI functionalized mesoporous silica nanoparticles.* International Journal of Nanomedicine, 2016. **11**: p. 299.

523. Croissant, J.G., et al., *Protein-gold clusters-capped mesoporous silica nanoparticles for high drug loading, autonomous gemcitabine/doxorubicin co-delivery, and in-vivo tumor imaging.* Journal of Controlled Release, 2016. **229**: p. 183-191.

524. Valdovinos, H., et al., *Positron Emission Tomography Imaging of Intrinsically Titanium-45 Radiolabeled Mesoporous Silica Nanoparticles*. 2016, Soc Nuclear Med.

525. Liu, X., et al., *In vitro and in vivo evaluation of puerarin-loaded PEGylated mesoporous silica nanoparticles.* Drug development and industrial pharmacy, 2016. **42**(12): p. 2031-2037.

526. Yahya Hanafi-Bojd, M., et al., *Co-delivery of epirubicin and siRNA using functionalized mesoporous silica nanoparticles enhances in vitro and in vivo drug efficacy.* Current drug delivery, 2016. **13**(7): p. 1176-1182.

527. Zheng, H., et al., *Organosilane and polyethylene glycol functionalized magnetic mesoporous silica nanoparticles as carriers for CpG immunotherapy in vitro and in vivo.* PLoS One, 2015. **10**(10): p. e0140265.

528. Wu, Q., et al., *In vivo evaluation of an anticancer drug delivery system based on heparinized mesoporous silica nanoparticles.* Rsc Advances, 2015. **5**(50): p. 40103-40110.

529. Xu, X., et al., *Polymeric micelle-coated mesoporous silica nanoparticle for enhanced fluorescent imaging and pH-responsive drug delivery.* Chemical Engineering Journal, 2015. **279**: p. 851-860.

530. Li, Z., et al., *Mesoporous silica nanoparticles with pH-sensitive nanovalves for delivery of moxifloxacin provide improved treatment of lethal pneumonic tularemia.* ACS nano, 2015. **9**(11): p. 10778-10789.

531. Dai, L., et al., *Facile synthesis of yolk–shell silica nanoparticles for targeted tumor therapy.* Journal of Materials Chemistry B, 2015. **3**(42): p. 8303-8313.

532. Hu, H., et al., *The rational design of NAMI-A-loaded mesoporous silica nanoparticles as antiangiogenic nanosystems.* Journal of Materials Chemistry B, 2015. **3**(30): p. 6338-6346.

533. Liu, J., et al., *Enzyme responsive mesoporous silica nanoparticles for targeted tumor therapy in vitro and in vivo.* Nanoscale, 2015. **7**(8): p. 3614-3626.

534. Zhang, Q., et al., *Biocompatible, uniform, and redispersible mesoporous silica nanoparticles for cancer-targeted drug delivery in vivo.* Advanced Functional Materials, 2014. **24**(17): p. 2450-2461.

535. Li, Q.-L., et al., *Mesoporous silica nanoparticles coated by layer-by-layer self-assembly using cucurbit [7] uril for in vitro and in vivo anticancer drug release.* Chemistry of Materials, 2014. **26**(22): p. 6418-6431.

536. Xie, M., et al., *Negative-charge-functionalized mesoporous silica nanoparticles as drug vehicles targeting hepatocellular carcinoma.* International journal of pharmaceutics, 2014. **474**(1-2): p. 223-231.

537. Chen, F., et al., *Engineering of hollow mesoporous silica nanoparticles for remarkably enhanced tumor active targeting efficacy.* Scientific reports, 2014. **4**(1): p. 5080.

538. Chen, Y., et al., *In vivo distribution and antitumor activity of doxorubicin-loaded N-isopropylacrylamide-co-methacrylic acid coated mesoporous silica nanoparticles and safety evaluation.* European Journal of Pharmaceutics and Biopharmaceutics, 2013. **85**(3): p. 406-412.

539. Chen, F., et al., *In vivo tumor targeting and image-guided drug delivery with antibody-conjugated, radiolabeled mesoporous silica nanoparticles.* ACS nano, 2013. **7**(10): p. 9027-9039.

540. Chen, F., et al., *In vivo tumor targeting with dual-labeled mesoporous silica nanoparticles.* 2014, Soc Nuclear Med.

541. Lin, D., et al., *Intracellular cleavable poly (2-dimethylaminoethyl methacrylate) functionalized mesoporous silica nanoparticles for efficient siRNA delivery in vitro and in vivo.* Nanoscale, 2013. **5**(10): p. 4291-4301.

542. Meng, H., et al., *Codelivery of an optimal drug/siRNA combination using mesoporous silica nanoparticles to overcome drug resistance in breast cancer in vitro and in vivo.* ACS nano, 2013. **7**(2): p. 994-1005.

543. Lu, J., et al., *In vivo tumor suppression efficacy of mesoporous silica nanoparticles-based drug-delivery system: enhanced efficacy by folate modification.* Nanomedicine: Nanotechnology, Biology and Medicine, 2012. **8**(2): p. 212-220.

544. Yan, H., et al., *Functional mesoporous silica nanoparticles for photothermal-controlled drug delivery in vivo.* Angewandte Chemie International Edition, 2012. **51**(33): p. 8373-8377.

545. Cao, X., et al., *In vitro release and in vitro–in vivo correlation for silybin meglumine incorporated into hollow-type mesoporous silica nanoparticles.* International Journal of Nanomedicine, 2012: p. 753-762.

546. Falah, M., M. Rayan, and A. Rayan, *A novel paclitaxel conjugate with higher efficiency and lower toxicity: a new drug candidate for cancer treatment.* International Journal of Molecular Sciences, 2019. **20**(19): p. 4965.

547. He, Z., et al., *A high capacity polymeric micelle of paclitaxel: Implication of high dose drug therapy to safety and in vivo anti-cancer activity.* Biomaterials, 2016. **101**: p. 296-309.

548. Kim, J.-H., et al., *Tumor-targeted delivery of paclitaxel using low density lipoprotein-mimetic solid lipid nanoparticles.* Molecular pharmaceutics, 2015. **12**(4): p. 1230-1241.

549. Michael, B., et al., *Evaluation of organ weights for rodent and non-rodent toxicity studies: a review of regulatory guidelines and a survey of current practices.* Toxicologic pathology, 2007. **35**(5): p. 742-750.

550. Nave, M., et al., *Nanoformulations of a potent copper-based aquaporin inhibitor with cytotoxic effect against cancer cells.* Nanomedicine, 2016. **11**(14): p. 1817-1830.

551. Piao, Y., Y. Liu, and X. Xie, *Change trends of organ weight background data in Sprague Dawley rats at different ages.* Journal of toxicologic pathology, 2013. **26**(1): p. 29-34.

552. Lopes, J., et al. *Safety of Gold Nanoparticles: From In Vitro to In Vivo Testing Array Checklist.* Pharmaceutics, 2023. **15**, DOI: 10.3390/pharmaceutics15041120.

553. Laboratories, C.R. *C57BL/6 Mouse Hematology.* 2008-2012 [cited 2023 23 June]; Available from: https://www.criver.com/sites/default/files/resources/doc_a/C57BL6MouseClinical PathologyData.pdf.

554. Medicine, U.-D.o.L.A. *SERUM CHEMISTRY REFERENCE RANGE - MOUSE*.* 2013 [cited 2023 23 June]; Available from: https://labs.dgsom.ucla.edu/dlam/files/view/docs/diagnostic-lab-services/private/serum_chemistry_reference_ranges_mice.pdf.

555. Kurtz, D.M. and G.S. Travlos, *The clinical chemistry of laboratory animals.* 2017: CRC Press.

556. Giannini, E.G., R. Testa, and V. Savarino, *Liver enzyme alteration: a guide for clinicians.* CMAJ : Canadian Medical Association journal = journal de l'Association medicale canadienne, 2005. **172**(3): p. 367-379.

557. Li, Y.-P., et al., *PEGylated PLGA nanoparticles as protein carriers: synthesis, preparation and biodistribution in rats.* Journal of controlled release, 2001. **71**(2): p. 203-211.

558. Bazile, D., et al., *Stealth Me. PEG-PLA nanoparticles avoid uptake by the mononuclear phagocytes system.* Journal of pharmaceutical sciences, 1995. **84**(4): p. 493-498.

559. Nagayama, S., et al., *Time-dependent changes in opsonin amount associated on nanoparticles alter their hepatic uptake characteristics.* International journal of pharmaceutics, 2007. **342**(1-2): p. 215-221.

560. Burns, A.A., et al., *Fluorescent silica nanoparticles with efficient urinary excretion for nanomedicine.* Nano letters, 2009. **9**(1): p. 442-448.

561. Cheng, Y., et al., *Shape and Shear Stress Impact on the Toxicity of Mesoporous Silica Nanoparticles: In Vitro and In Vivo Evidence.* Molecular Pharmaceutics, 2023.

562. Wu, S.-H., Y. Hung, and C.-Y. Mou, *Mesoporous silica nanoparticles as nanocarriers.* Chemical Communications, 2011. **47**(36): p. 9972-9985.

563. Krämer, I. and A. Heuser, *Paclitaxel-Pharmaceutical and pharmacological issues.* EHP-AMERONGEN-, 1995. **1**: p. 37-41.

564. Mylan Pharmaceuticals, I. *Paclitaxel Injection.* 2002 [cited 2023 17 June]; Available from: https://www.accessdata.fda.gov/drugsatfda_docs/nda/2002/75278_Paclitaxel.cfm#:~:text=Approval%20Date%3A%201%2F25%2F2002.

565. Saadh, M.J., et al., *A guide for estimating the maximum safe starting dose and conversion it between animals and humans.* Syst. Rev. Pharm, 2020. **11**: p. 98-101.

566. Nair, A.B. and S. Jacob, *A simple practice guide for dose conversion between animals and human.* Journal of basic and clinical pharmacy, 2016. **7**(2): p. 27.

567. Cuenca, A.G., et al., *Novel Role for Tumor-Induced Expansion of Myeloid-Derived Cells in Cancer Cachexia.* The Journal of Immunology, 2014. **192**(12): p. 6111-6119.

568. Geppert, J., et al. *Aging Aggravates Cachexia in Tumor-Bearing Mice.* Cancers, 2022. **14**, DOI: 10.3390/cancers14010090.

569. Ferrara, M., et al., *Cancer cachexia as a multiorgan failure: Reconstruction of the crime scene.* Frontiers in Cell and Developmental Biology, 2022: p. 1746.

570. Muggia, F.M., *Doxorubicin-polymer conjugates: further demonstration of the concept of enhanced permeability and retention.* Clinical cancer research, 1999. **5**(1): p. 7-8.

571. Liong, M., et al., *Multifunctional inorganic nanoparticles for imaging, targeting, and drug delivery.* ACS nano, 2008. **2**(5): p. 889-896.

572. Onakpoya, I.J., C.J. Heneghan, and J.K. Aronson, *Post-marketing withdrawal of 462 medicinal products because of adverse drug reactions: a systematic review of the world literature.* BMC medicine, 2016. **14**(1): p. 1-11.

573. Urbán, P., N.J. Liptrott, and S. Bremer, *Overview of the blood compatibility of nanomedicines: A trend analysis of in vitro and in vivo studies.* WIREs Nanomedicine and Nanobiotechnology, 2019. **11**(3): p. e1546.

574. Sobot, D., S. Mura, and P. Couvreur, *Nanoparticles: Blood Components Interactions*, in *Encyclopedia of Polymeric Nanomaterials*, S. Kobayashi and K. Müllen, Editors. 2021, Springer Berlin Heidelberg: Berlin, Heidelberg. p. 1-10.

575. Yildirim, A., E. Ozgur, and M. Bayindir, *Impact of mesoporous silica nanoparticle surface functionality on hemolytic activity, thrombogenicity and non-specific protein adsorption.* Journal of Materials Chemistry B, 2013. **1**(14): p. 1909-1920.

576. Santos-Martínez, M.J., et al., *FORUM EKSPERTÓW A nanoscale resolution assay of flow-induced platelet microaggregation.* Kardiochirurgia i Torakochirurgia Polska/Polish Journal of Thoracic and Cardiovascular Surgery, 2011. **7**(4): p. 365-375.

577. Palta, S., R. Saroa, and A. Palta, *Overview of the coagulation system.* Indian journal of anaesthesia, 2014. **58**(5): p. 515-523.

578. Tomaszewski, K.A., M.W. Radomski, and M.J. Santos-Martinez, *Nanodiagnostics, nanopharmacology and nanotoxicology of platelet–vessel wall interactions.* Nanomedicine, 2015. **10**(9): p. 1451-1475.

579. Santos-Martínez, M.J., et al., *Analysis of platelet function: role of microfluidics and nanodevices.* Analyst, 2011. **136**(24): p. 5120-5126.

580. Corbalan, J.J., et al., *Amorphous silica nanoparticles trigger nitric oxide/peroxynitrite imbalance in human endothelial cells: inflammatory and cytotoxic effects.* International journal of nanomedicine, 2011: p. 2821-2835.

581. Corbalan, J.J., et al., *Amorphous silica nanoparticles aggregate human platelets: potential implications for vascular homeostasis.* International journal of nanomedicine, 2012: p. 631-639.

582. Bihari, P., et al., *Single-walled carbon nanotubes activate platelets and accelerate thrombus formation in the microcirculation.* Toxicology, 2010. **269**(2-3): p. 148-154.

583. Semberova, J., et al., *Carbon nanotubes activate blood platelets by inducing extracellular Ca2+ influx sensitive to calcium entry inhibitors.* Nano letters, 2009. **9**(9): p. 3312-3317.

584. Wu, H., et al., *A Hollow-Core, Magnetic, and Mesoporous Double-Shell Nanostructure: In Situ Decomposition/Reduction Synthesis, Bioimaging, and Drug-Delivery Properties.* Advanced Functional Materials, 2011. **21**(10): p. 1850-1862.

585. Dai, C., et al., *Degradable, antibacterial silver exchanged mesoporous silica spheres for hemorrhage control.* Biomaterials, 2009. **30**(29): p. 5364-5375.

586. Alam, H.B., et al., *Application of a Zeolite Hemostatic Agent Achieves 100% Survival in a Lethal Model of Complex Groin Injury in Swine.* Journal of Trauma and Acute Care Surgery, 2004. **56**(5).

587. Ostomel, T.A., Q. Shi, and G.D. Stucky, *Oxide Hemostatic Activity.* Journal of the American Chemical Society, 2006. **128**(26): p. 8384-8385.

588. Gaffney, A.M., et al., *Blood biocompatibility of surface-bound multi-walled carbon nanotubes.* Nanomedicine: Nanotechnology, Biology and Medicine, 2015. **11**(1): p. 39-46.

589. Santos-Martinez, M.J., et al., *Pharmacological characterization of nanoparticle-induced platelet microaggregation using quartz crystal microbalance with dissipation: comparison with light aggregometry.* International journal of nanomedicine, 2015. **10**: p. 5107.

590. Choi, J., et al., *Physicochemical Characterization and In Vitro Hemolysis Evaluation of Silver Nanoparticles.* Toxicological Sciences, 2011. **123**(1): p. 133-143.

591. Saha, K., D.F. Moyano, and V.M. Rotello, *Protein coronas suppress the hemolytic activity of hydrophilic and hydrophobic nanoparticles.* Materials Horizons, 2014. **1**(1): p. 102-105.

592. Chen, L.Q., et al., *Nanotoxicity of Silver Nanoparticles to Red Blood Cells: Size Dependent Adsorption, Uptake, and Hemolytic Activity.* Chemical Research in Toxicology, 2015. **28**(3): p. 501-509.

593. Singh, N., S.K. Sahoo, and R. Kumar, *Hemolysis tendency of anticancer nanoparticles changes with type of blood group antigen: An insight into blood*

*nanoparticle interactions.* Materials Science and Engineering: C, 2020. **109**: p. 110645.

594. Aseichev, A.V., et al., *Effects of Gold Nanoparticles on Erythrocyte Hemolysis.* Bulletin of Experimental Biology and Medicine, 2014. **156**(4): p. 495-498.

595. Barshtein, G., D. Arbell, and S. Yedgar, *Hemolytic Effect of Polymeric Nanoparticles: Role of Albumin.* IEEE Transactions on NanoBioscience, 2011. **10**(4): p. 259-261.

596. Gerashchenko, B.I., et al., *Probing the silica surfaces by red blood cells.* Cytometry, 2002. **49**(2): p. 56-61.

597. Nash, T., A.C. Allison, and J.S. Harington, *Physico-chemical properties of silica in relation to its toxicity.* Nature, 1966. **210**(5033): p. 259-261.

598. Diociaiuti, M., et al., *Morphological and Functional Alterations of Human Erythrocytes Induced by SiO2Particles: An Electron Microscopy and Dielectric Spectroscopy Study.* Environmental research, 1999. **80**(3): p. 197-207.

599. Yawata, Y., *Cell membrane: the red blood cell as a model.* 2006: John Wiley & Sons.

600. Depasse, J. and J. Warlus, *Relation between the toxicity of silica and its affinity for tetraalkylammonium groups. Comparison between Si02 and Ti02.* Journal of Colloid and Interface Science, 1976. **56**(3): p. 618-621.

601. Stodghill, S.P., A.E. Smith, and J.H. O'Haver, *Thermodynamics of micellization and adsorption of three alkyltrimethylammonium bromides using isothermal titration calorimetry.* Langmuir, 2004. **20**(26): p. 11387-11392.
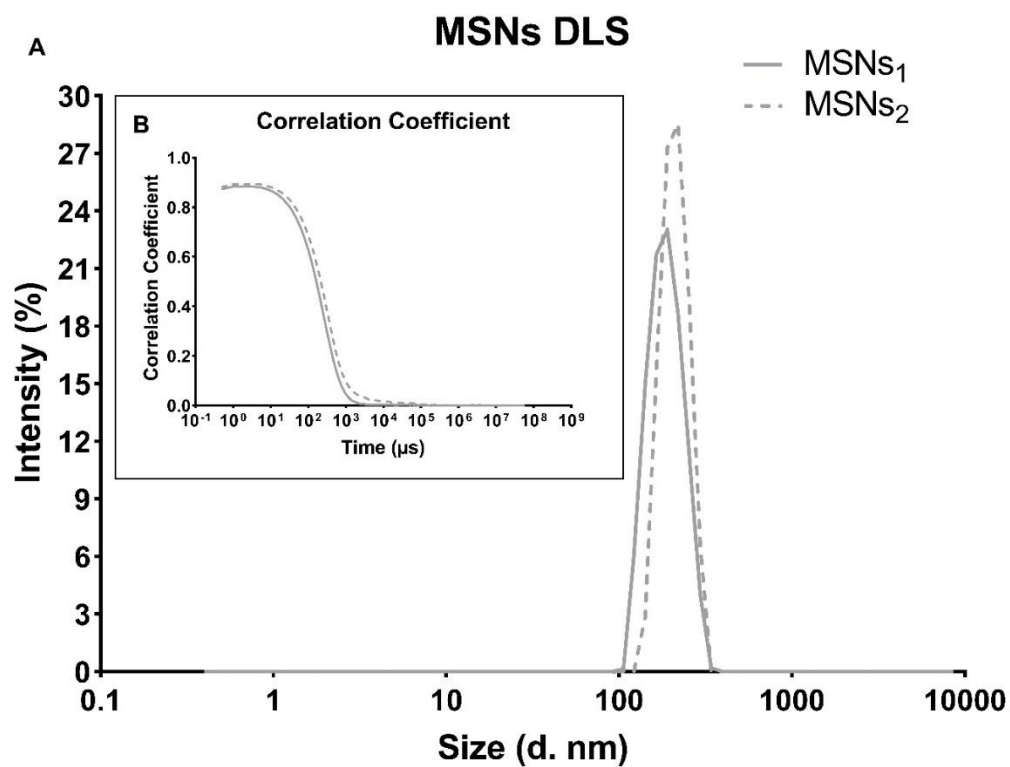
# APPENDICES

## Appendix 1



**Figure A1. 1: A-** Size distribution (3 measurements) by intensity (%), and **B-** Raw correlation data (3 measurements) measured by dynamic light scattering of the synthesised MCM-41 type of MSNs.
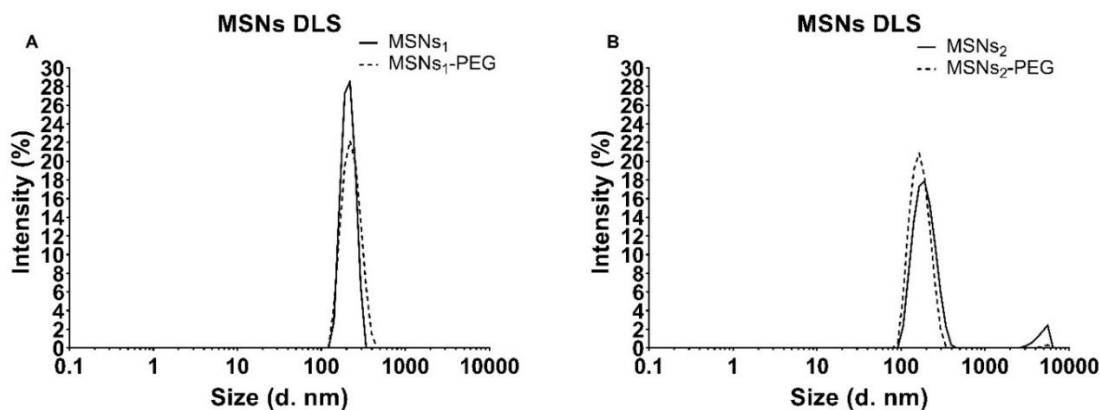
**Figure A1. 2: A-** and **B-** Size distribution (3 measurements) by intensity (%), measured by dynamic light scattering of the synthesised MCM-41 type of MSNs before (MSNs) and after (MSNs-PEG) PEGylation. (mean±SEM).
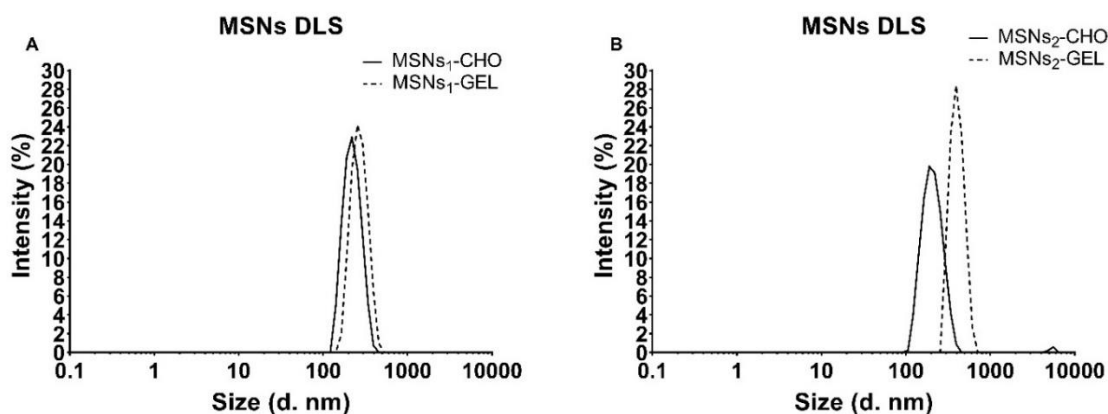


**Figure A1. 3: A-** and **B-** Size distribution (3 measurements) by intensity (%), measured by dynamic light scattering of the synthesised MCM-41 type of MSNs before (MSNs-CHO) (3 measurements) and after (MSNs-GEL) (5 measurements) functionalization with gelatine. (mean±SEM)

# Appendix 2

**Table A2. 1:** Equivalences of the free drug concentrations used for the *in vitro* cytotoxicity assays.

| DOX (µM) | DOX (µg/mL) | PTX (µM) | PTX (µg/mL) |
|----------|-------------|----------|-------------|
| 0.2 | 0.1 | 0.06 | 0.05 |
| 0.9 | 0.5 | 0.12 | 0.1 |
| 1.7 | 1 | 0.6 | 0.5 |
| 9 | 5 | 1.2 | 1 |
| 17 | 10 | 3.5 | 3 |
| 43 | 25 | 7.2 | 6 |

**Table A2. 2:** Equivalences between concentrations of loaded- MSNs and MSNs-PEG, and amount of drug loaded for the *in vitro* cytotoxicity assays.

| MSNs+PTX (µg/mL) | PTX loaded (µM) | MSNs+PTX-PEG (µg/mL) | PTX loaded (µM) |
|------------------|-----------------|----------------------|-----------------|
| 1.5 | 0.6 | 4.5 | 0.6 |
| 3 | 1.2 | 9 | 1.2 |
| 9 | 3.5 | 25 | 3.5 |
| 18 | 7.2 | 50 | 7.2 |
| 25 | 10 | 71 | 10 |
| 30 | 12 | 87 | 12 |
| 50 | 20 | 147 | 20 |
| 124 | 50 | 365 | 50 |
| 149 | 60 | 436 | 60 |

**Table A2. 3:** Equivalences between concentrations of loaded- MSNs-CHO and MSNs-GEL, and amount of drug loaded for the *in vitro* cytotoxicity assays.

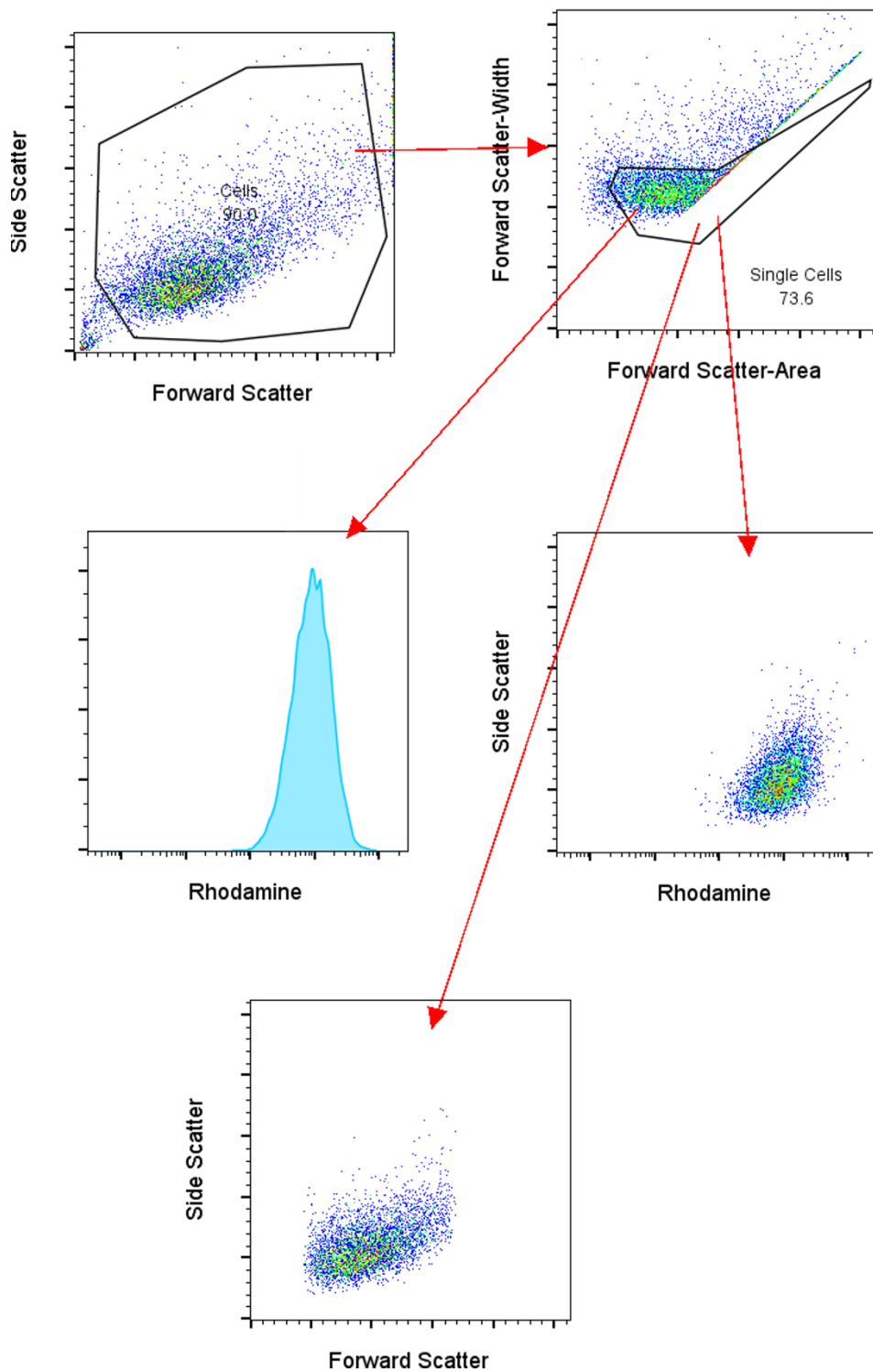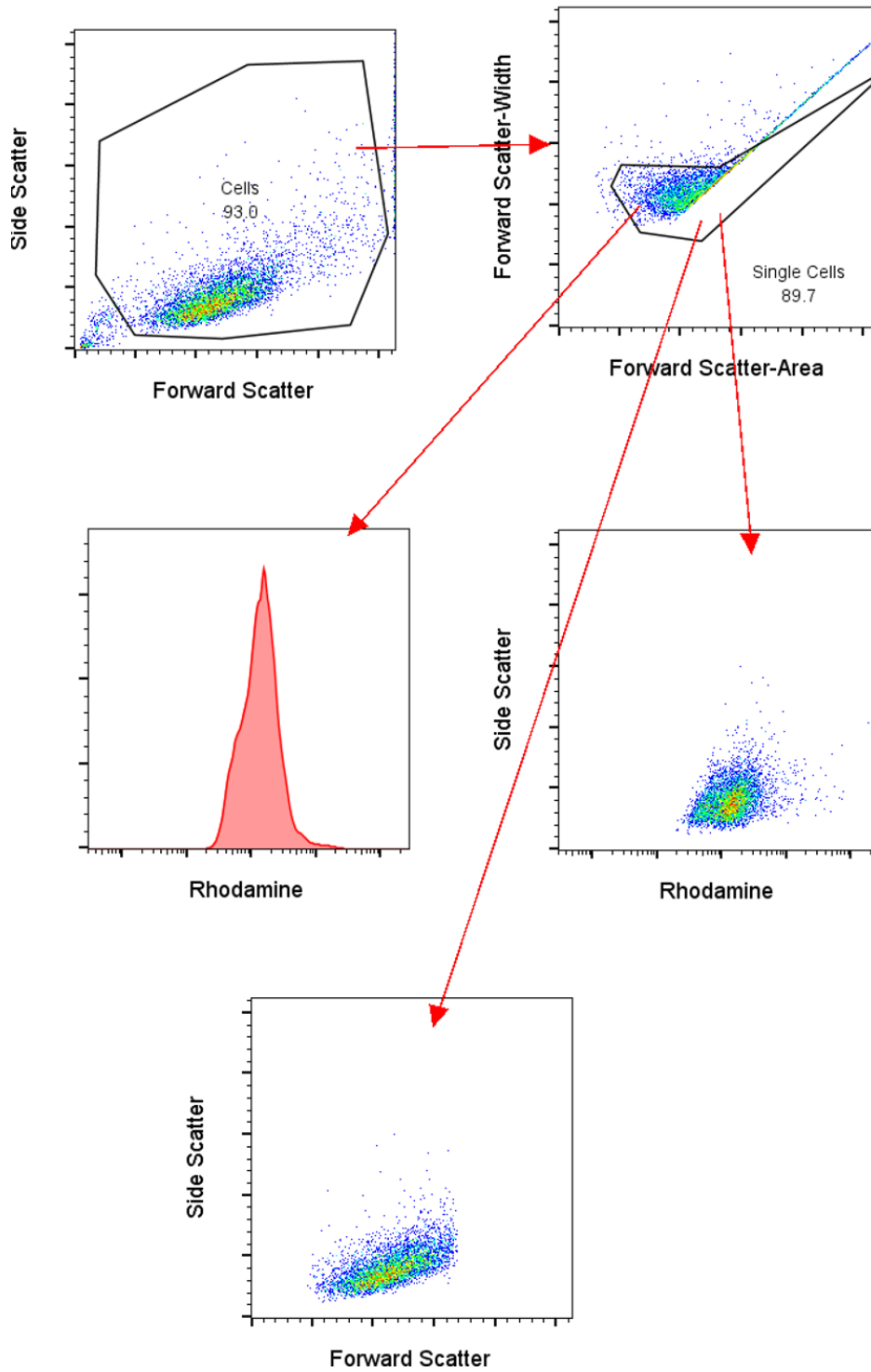| MSNs-CHO+PTX (µg/mL) | PTX loaded (µM) | MSNs-CHO+PTX-GEL (µg/mL) | PTX loaded (µM) |
|---|---|---|---|
| 5 | 0.6 | 6 | 0.6 |
| 10 | 1.2 | 11 | 1.2 |
| 28 | 3.5 | 32 | 3.5 |
| 58 | 7.2 | 67 | 7.2 |

**Figure A2. 1:** Representation of cell debris exclusion with a gate on Forward Scatter Channel (FSC) vs Side Scatter Channel (SSC), with doublets subsequently excluded via FSC-A vs FSC-W for A549 cells.
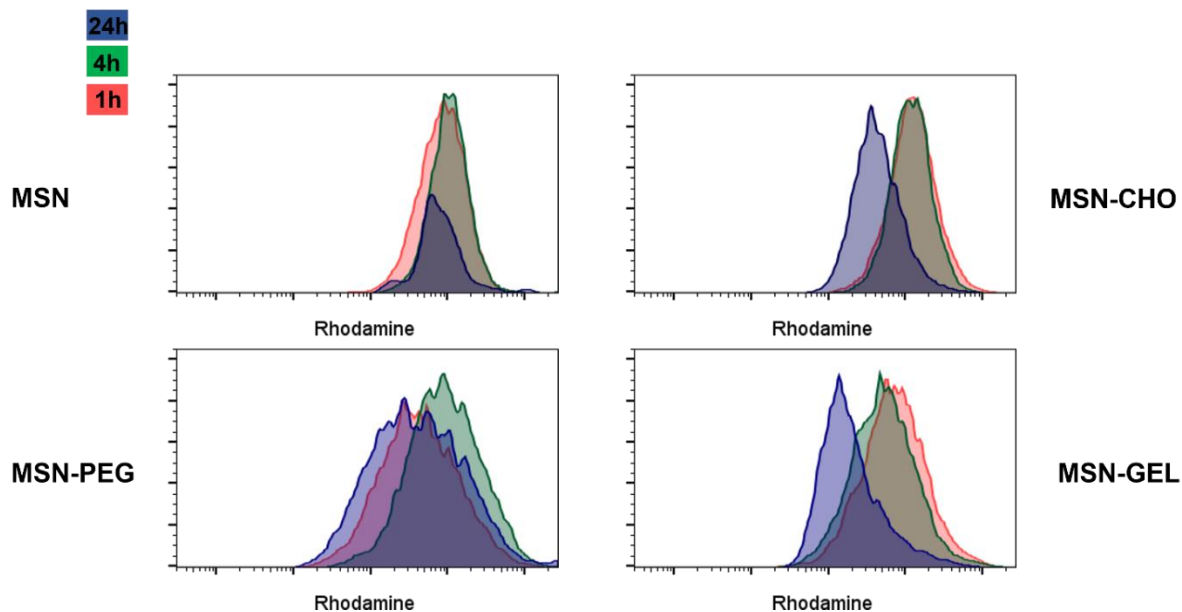
**Figure A2. 2:** Representation of cell debris exclusion with a gate on Forward Scatter Channel (FSC) vs Side Scatter Channel (SSC), with doublets subsequently excluded via FSC-A vs FSC-W for LLC1 cells.

**Figure A2. 3:** Representative graphs from the Flow cytometer analysis of A549 cellular fluorescence after treatment with different RhBITC functionalised NPs at 1, 4 and 24 h. (Replicate 1)
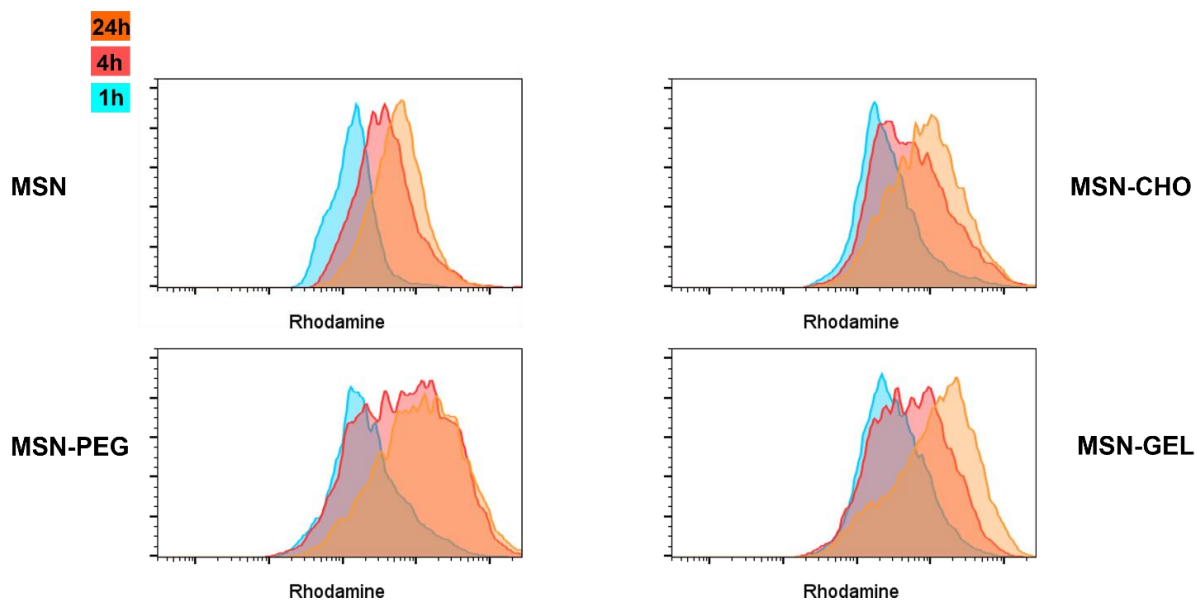


**Figure A2. 4:** Representative graphs from the Flow cytometer analysis of LLC1 cellular fluorescence after treatment with different RhBITC functionalised NPs at 1, 4 and 24 h. (Replicate 1)
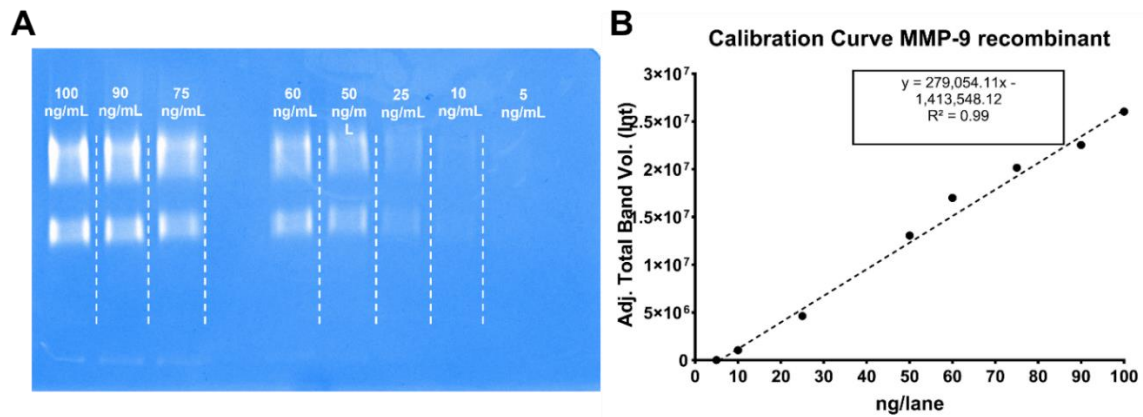
**Figure A2. 5: A-** Gelatine zymogram of different concentrations of commercial recombinant MMP-9. **B-** Calibration curve obtained by plotting commercial recombinant MMP-9 concentrations, against the intensity of the Adj. Total Band Volumes obtained from the gel.
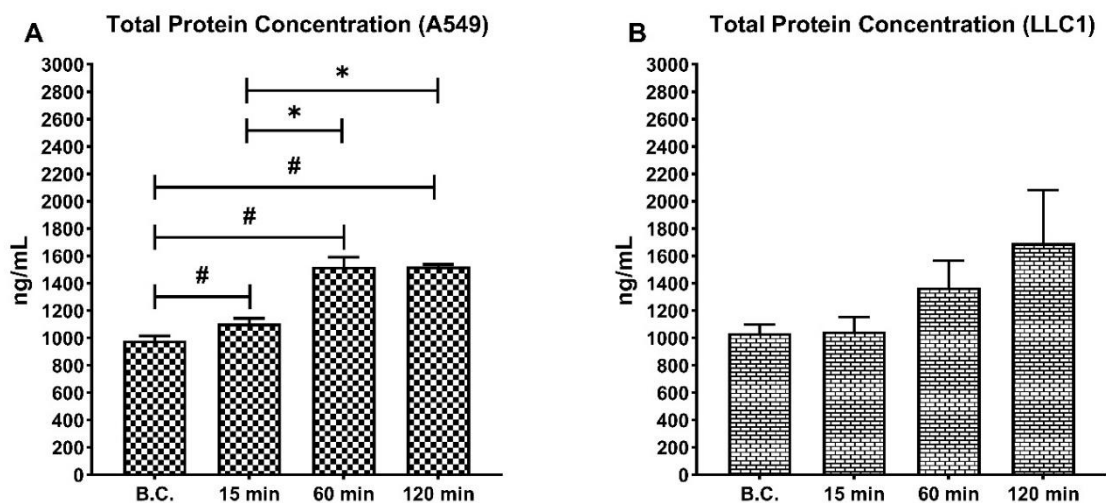


**Figure A2. 6:** Total protein concentration in **A-** A549 cells conditioned media before (**B.C.**) and after (**15**, **60** and **120 min**) centrifugation (media±SEM); and **B-** LLC1 cells conditioned media before (**B.C.**) and after (**15**, **60** and **120 min**) centrifugation (media±SEM). Statistical test: One-way ANOVA with Tukey's multiple comparison post-test comparing all time points to the control (**B.C.**), $p \leq 0.05$ (#); and comparing all time points between each other, $p \leq 0.05$ (*). **B-** p=0.1659
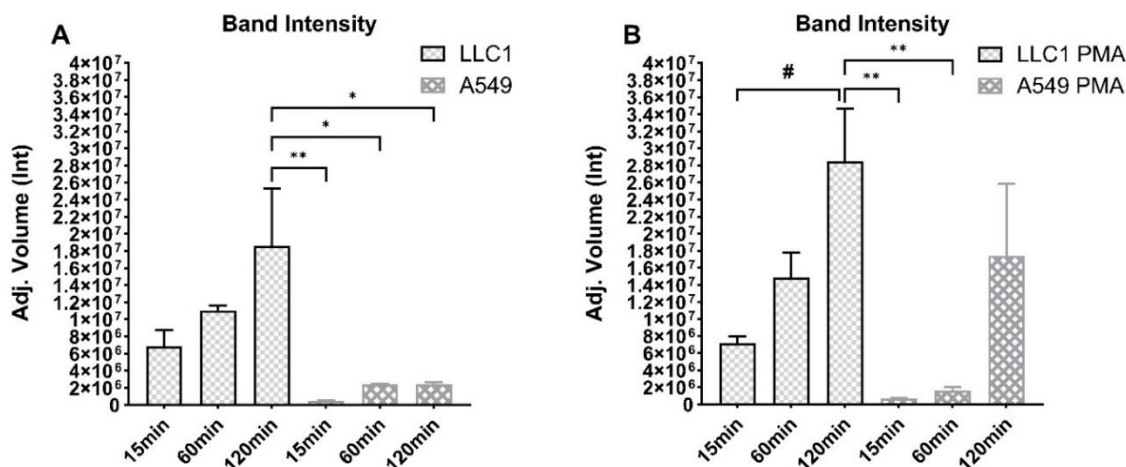
288

**Figure A2. 7: A-** Statistical analysis of the differences between MMP-9 band intensities, quantified by gelatine zymography, in A549 and LLC1 conditioned media before (**B.C.**) and after (**15**, **60** and **120 min**) centrifugation (media±SEM); **B-** Statistical analysis of the differences between MMP-9 band intensities, quantified by gelatine zymography, in A549 and LLC1 stimulated media before (**B.C.**) and after (**15**, **60** and **120 min**) centrifugation (media±SEM). Statistical test: Two-way ANOVA with Tukey's multiple comparison post-test showing differences between the different time points, $p \leq 0.05$ (*), $p \leq 0.01$ (**); and the different cell lines, $p \leq 0.05$ (#)

**Table A2. 4**: List of buffers, solutions and gels prepared prior to performing the zymography assay.

| Resolving buffer - 500 mL | <ul><li>91g of Tris base</li><li>300 mL of dd H2O</li><li>Adjust pH to 8.8</li><li>Bring to volume with dd $H_2O$ (500 mL)</li><li>Filter using a 0.45 µM filter</li><li>Store at 4°C</li></ul> |
|---|---|
| Stacking Buffer – 100 mL | <ul><li>Tris Base 6.05 g</li><li>40 mL of dd $H_2O$</li><li>Adjust to pH 6.8</li><li>Bring to volume with dd $H_2O$ (100 mL)</li><li>Filter using a 0.45 µM filter</li><li>Add 0.4 g of SDS</li></ul> |

| | |
|---|---|
| | • Store at 4°C |
| **2M Tris HCl pH 7.6 (for zymography buffer) - 1 L** | • 242.18 g (2M) of Tris base<br>• 500 mL of dd $H_2O$<br>• Adjust to pH 7.6<br>• Bring to volume with dd $H_2O$ (1 L) |
| **Zymography Buffer - 2 L** | • 50 mL of 2M Tris HCl<br>• 18 g of NaCl<br>• 1.47 g of $CaCl_2$<br>• 1 g $NaN_3$<br>• Bring to volume with dd $H_2O$ (2 L) |
| **Triton Buffer (2.5%) – 1 L** | • 25 mL of Triton 100x<br>• 975 mL of dd $H_2O$ |
| **Tank Buffer - 1 L** | • Tris base 30.2 g<br>• Glycine 144 g<br>• SDS 10 g<br>• 700 mL of dd $H_2O$<br>• Adjust to pH 8.3<br>• Bring to volume with dd $H_2O$ (1 L) |
| **Staining solution** | • 250 mg of Coomassie blue G-250 2<br>• 50 mL of methanol<br>• 100 mL of acetic acid<br>• 650 mL of dd $H_2O$ |

| | |
|---|---|
| **Distaining solution** | • 40 mL of methanol<br>• 80 mL of acetic acid<br>• 880 mL of dd H2O |
| **Stacking gel FOR 4 GELS** | • 1.3 mL of acrylamide 30%<br>• 2.5 mL of stacking buffer<br>• 6 mL of dd $H_2O$<br>• 50 µL of APS<br>• 10 µL of TEMED |
| **Separating gel for zymography (8%) (4 GELS)** | • 4 mL of acrylamide 30%<br>• 3.75 mL of 4x Tris pH 8.8 (resolving buffer)<br>• 1.5 mL of gelatine (2% with SDS 1%)<br>• 5.75 mL of dd $H_2O$<br>• 50 µL of APS (0.1 g APS + 960 µL dd $H_2O$)<br>• 10 µL TEMED |

# Appendix 3
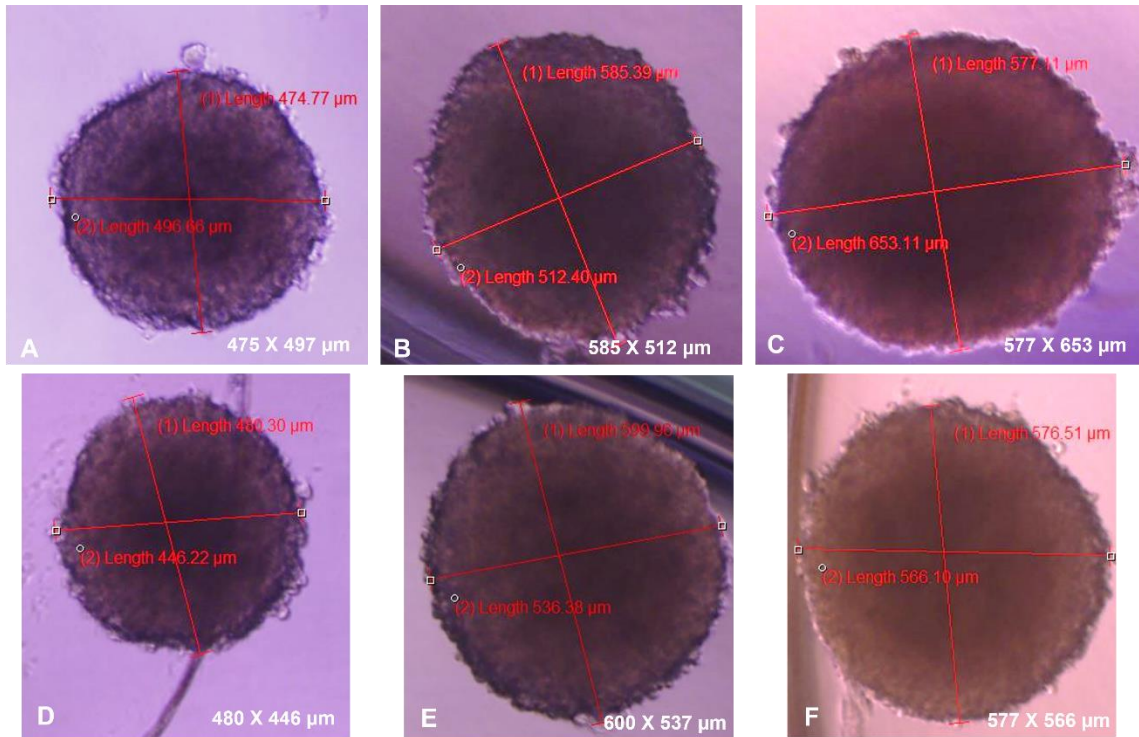


**Figure A.3 1:** U-87 control spheroids (no treatment) growth at **A- and D-** day 5, **B- and E** day 6, **C- and F** day 7 of treatment with respective measurements. (Representative image of U-87 control spheroids growth in one of the wells from the Nunclon Sphera low attachment 96-well plate) The pictures were taken by Dr Amelia Ultimo and Ph.D. students Mila Djisalov and Teodora Knezic; the results were analysed by the candidate.
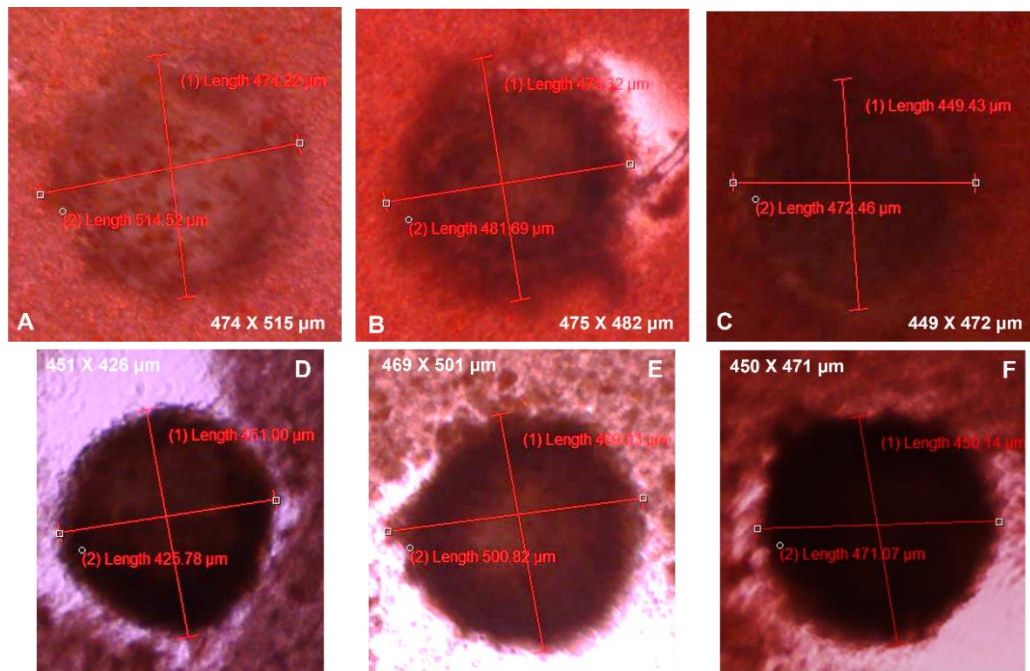
**Figure A.3 2:** U-87 control spheroids growth at **A-** day 5, **B-** day 6, **C-** day 7 of treatment with MSNs+DOX-PEG (0.01 µg/mL) with respective measurements. U-87 control spheroids growth at **D-** day 5, **E-** day 6, **F-** day 7 of treatment with MSNs-CHO+DOX-GEL (0.01 µg/mL) with respective measurements. (Representative image of U-87 control spheroids growth in one of the wells from the Nunclon Sphera low attachment 96-well plate) The pictures were taken by Dr Amelia Ultimo and Ph.D. students Mila Djisalov and Teodora Knezic; the results were analysed by the candidate.
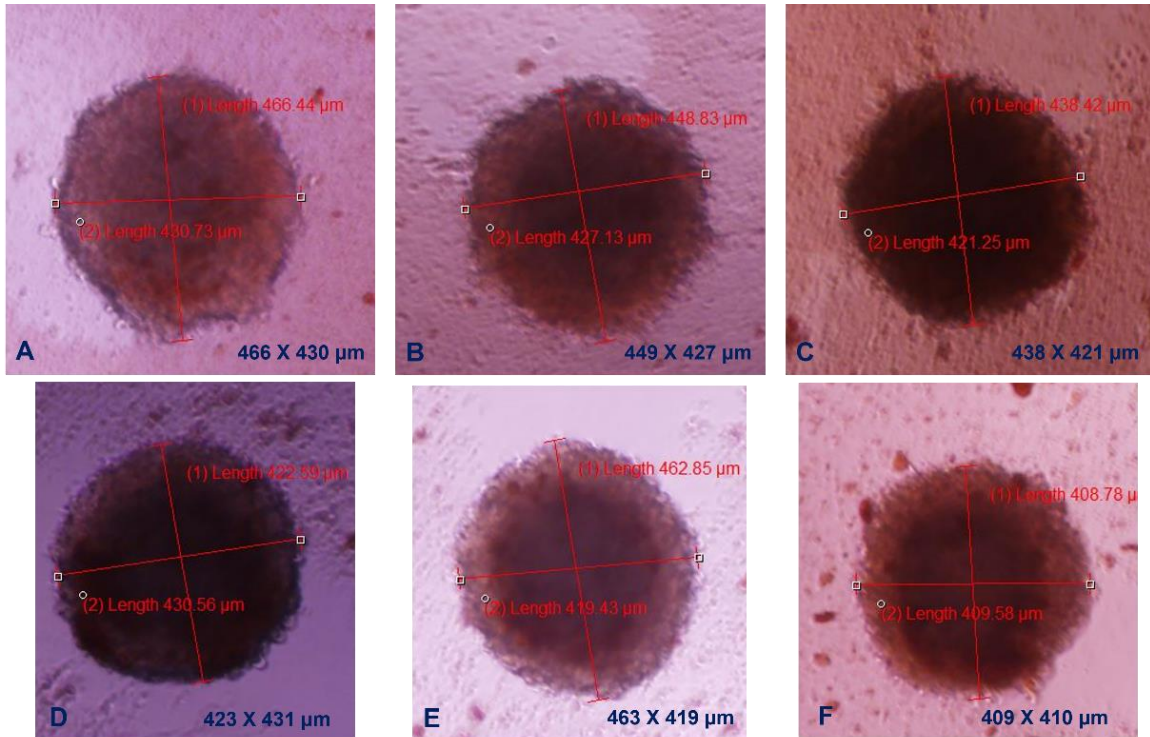
**Figure A.3 3:** U-87 control spheroids growth at **A-** day 5, **B-** day 6, **C-** day 7 of treatment with MSNs+DOX-PEG (10 µg/mL) with respective measurements. U-87 control spheroids growth at **D-** day 5, **E-** day 6, **F-** day 7 of treatment with MSNs-CHO+DOX-GEL (10 µg/mL) with respective measurements. (Representative image of U-87 control spheroids growth in one of the wells from the Nunclon Sphera low attachment 96-well plate) The pictures were taken by Dr Amelia Ultimo and Ph.D. students Mila Djisalov and Teodora Knezic; the results were analysed by the candidate.

# Appendix 4

**Table A4. 2:** Calculations for MSNs formulations preparation for *in vivo* studies.

| MSN-PEG | | MSN-GEL | |
|---|---|---|---|
| (PTX 115 µg/mg NPs) | | (PTX 90 µg/mg NPs) | |
| **LOWER [  ]** | **HIGHER [  ]** | **LOWER [  ]** | **HIGHER [  ]** |
| 2.5 mg/kg PTX weekly | 8 mg/kg PTX weekly | 2.5 mg/kg PTX weekly | 8 mg/kg PTX weekly |
| **-** 2.5 mg x 0.025 kg mice = 0.0625 mg or 62.5 µg PTX weekly | **-** 8 mg x 0.025 kg mice = 0.2 mg or 200 µg PTX weekly | **-** 2.5 mg x 0.025 kg mice = 0.0625 mg or 62.5 µg PTX weekly | **-** 8 mg x 0.025 kg mice = 0.2 mg or 200 µg PTX weekly |
| **-** 0.543 mg PEG NPs needed weekly | **-** 1.74 mg PEG NPs needed weekly | **-** 0.70 mg GEL NPs needed weekly | **-** 2.22 mg GEL NPs needed weekly |
| **-** 0.15 mL injections, twice daily, for five days = 1.5mL total | **-** 0.15 mL injections, twice daily, for five days = 1.5mL total | **-** 0.15 mL injections, twice daily, for five days = 1.5mL total | **-** 0.15 mL injections, twice daily, for five days = 1.5mL total |
| **-** 0.543 mg : 1.5 mL = 0.362 mg/mL NPs to be prepared | **-** 1.74 mg : 1.5 mL = 1.16 mg/mL NPs to be prepared | **-** 0.70 mg : 1.5 mL = 0.47 mg/mL NPs to be prepared | **-** 2.22 mg : 1.5 mL = 1.48 mg/mL NPs to be prepared |
| **-** 0.15mL x 2 daily = 0.11 mg NPs daily = 4.4 mg NPs/kg | **-** 0.15mL x 2 daily = 0.348 mg NPs daily = 13.92 mg NPs/kg | **-** 0.15mL x 2 daily = 0.141 mg NPs daily = 5.64 mg NPs/kg | **-** 0.15mL x 2 daily = 0.444 mg NPs daily = 17.8 mg NPs/kg |
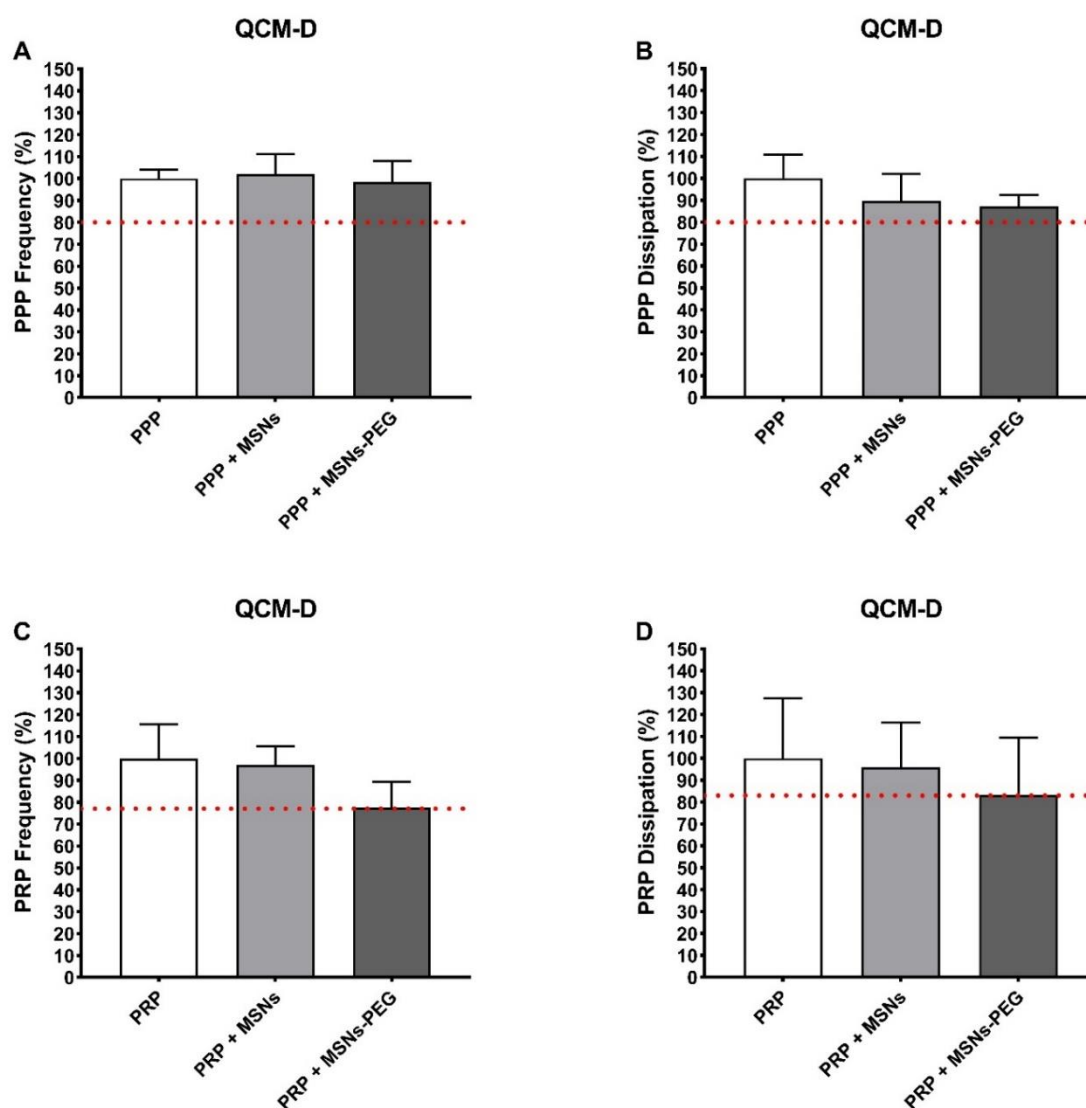
**Figure A5. 1:** Quartz crystal microbalance with dissipation. Effects of MSNs and MSNs-PEG on deposition of plasma proteins (PPP) and platelet aggregation (PRP). **A-** PPP frequency *f*; **B-** PPP energy dissipation *D*; **C-** PRP frequency *f* and **D-** PRP energy dissipation *D*. Data is presented as mean±SEM of 3 independent experiments for MSNs-PEG, and 2 experiments for bare MSNs. The maximal changes in frequency (negative shift) and dissipation (positive shift) for the control (PPP and PRP) are considered as 100%.